Diss. ETH No. 21667

Vibration Assisted Guillotining of Stacked Thin Material

A thesis submitted to the
ETH ZURICH

to attain the degree of
DOCTOR OF SCIENCES of ETH ZURICH
(Dr. sc. ETH Zurich)

presented by
KARL-ROBERT DEIBEL
MSc ETH, Zurich
born March 2nd 1985
citizen of Germany

accepted on the recommendation of
Prof. Dr. Konrad Wegener, examiner
Prof. Dr. Pavel Hora, co-examiner

2014

Acknowledgments

I wish to acknowledge the many following people, who invaluably helped throughout my dissertation at ETH Zurich and at other times.

Foremost, I graciously thank my supervisor, Prof. Dr. Konrad Wegener, head of IWF, for offering me a position at his renowned institute, giving me the opportunity to further my knowledge and research in manufacturing and production. Even through challenging times, his council provided much insight and inspiration in various fields. Our great collaboration since my undergraduate and graduate studies have brought fruitful results in research and in the classroom. My gracious thanks also go to Prof. Dr. Pavel Hora, head of IVP, for his provoking interest in my research, and for his continuous guidance and stimulating suggestions throughout my dissertation.

I am grateful for the intriguing works of my students, who allowed me to supervise them for their Bachelor Theses, Semester Projects, and Master Theses: Peter Bolt, Nils Furrer, Fabian Kaiser, Sarah Lämmlein, Nino Lemann, Linus Meier, Simon Müller, Christian Raemy, Maria Schneider, Dennis Stone, Raffael Wäspi, and Remo Zimmermann. Through their invaluable contributions, a profound base for my work and other fields were build. They represent the best mechanical engineers.

Many thanks go to my colleagues at the IWF, who contributed to my work by either giving supportive advice or technical help: Dr. Sascha Weikert for his knowledge on modeling and dynamic systems, his insights in design, and the great time as office colleagues; Dr. Wolfgang Knapp for his support in matters of metrology; Dr. Nikolaus Rüttimann for his extraordinary council in simulation, optimization, and material failure; Dr. Bastian Migge for discussion on optimization algorithms and proper research papers; Daniel Spescha for carrying out various experimental modal analyses.

Special thanks go the Michael Gebhardt, doctoral student in the field of metrology, for his great companionship throughout the time at the IWF. The joined trip to NAMRC in Madison, Wisconsin, USA, and the following days in Troy, Montana, where an essential part of this work was created, were one of the greatest time during my research. Approximately 5640 km were driven from Madison, Wisconsin to Troy, Montana to Las Vegas, Nevada to San Francisco, California, USA. Special thanks also go to Dr. Markus Ess for in-depth support in numerical simulation, advice in performing research, and being a great colleague since our time as graduate students at ETH Zurich.

Many thanks go to Konrad Rudin for the wonderful time as a fellow student during undergraduate, graduate, and doctoral years. The advice on control system was invaluable. I would like to place special emphasize on the adventurous scuba diving activities.

I owe thanks to Jens Boos, laboratory supervisor, for great help in creating measurement setups, data recording, high-speed video recording, and many other experimental works. I am grateful for the sedulous help of Samuel Staub, laboratory supervisor of IVP, in carrying out proper tensile tests, compression tests, and cutting tests. Thanks go to Sandro Wigger and Albert Weber for manufacturing the many tools and unique parts for my measurement setup. Many thanks also go to the Institute of Mechanical Systems for

allowing me to use the Laser-Vibrometers.

All the people at and related to IWF provided a comfortable working environment I wish to return to. I extend my thanks to Claus Dold, Marcel Henerichs, Michal Kuffa, Dr. Fredy Kuster, Umang Maradia, Raoul Roth, Nicolas Schaal, Josef Stirnimann, Stefan Thoma, Robert Transchel, Robert Voss, Christian Walter, Dr. Eduardo Weingärtner, and Lukas Weiss for all the work and non-work related discussions over the years and the fun times.

I appreciate the supportive insights of Dr. Anna Kubik throughout the beginning of my thesis. I graciously thank Prof. Dr. Thomas Rösgen for the inspiring council and guidance at ETH Zurich. My thanks go to the Jiu-Jitsukas of Ju-Jitsu at ASVZ and their contribution to an exceptional atmosphere outside of work. My grateful thanks go to Moya Müller, who supported me through the ups and downs during writing and long hours at the office.

I dedicate this work to my brothers and my parents, who have always encouraged me to do what it takes.

Karl-R. Deibel, February 2014

To my brothers and parents

Contents

List of Symbols

The list of symbols is divided in a list of commonly used subscripts that can be used in combination with any of the below-mentioned symbols. The list of subscripts can be found after the latin and greek symbols.

Symbol	Unit	Description
a	mm	Crack length
$\overset{*}{a}_i$	–	Fitting parameter for i
a_v	µm	Vibration amplitude
A	m^2	Area
b	mm	Length
$\overset{*}{b}_i$	–	Fitting parameter for i
B	µm	Sheet thickness
c	$\mathrm{m\,s^{-1}}$	Displacement propagation velocity within a solid
$\overset{*}{c}_i$	–	Fitting parameter for i
d	$\mathrm{N\,s\,m^{-1}}$	Damping
d_b	$\mathrm{N\,s\,m^{-1}}$	Damping between top sheet and blade
d_f	$\mathrm{N\,s\,m^{-1}}$	Damping of force sensor
$\boldsymbol{D}$	$\mathrm{N\,s\,m^{-1}}$	Damping matrix
e_{fr}	$\mathrm{N\,mm^{-1}}$	Specific cutting force in cutting direction
E	$\mathrm{N\,m^{-2}}$	Young's modulus
f	–	Fitness function
F	N	Force
F_b	N	Force between top sheet and blade
F_{crit}	N	Critical force
F_C	N	Cutting force in cutting direction
F_d	N	Damping force

Symbol	Unit	Description
F_{exp}	N	Force during compression experiments
F_{EF}	N	Normal force against cutting edge
F_{fr}	N	Plastic deformation force
F_F	N	Friction force
F_G	N	Force of gravity
F_i	N	Force in direction i
F_K	N	Compression force
F_L	N	Lateral cutting force
F_N	N	Normal force
F_R	N	Resulting force or total force
F_s	N	Static force
F_S	N	Output in the frequency domain
F_{US}	N	Dynamic force
G	MPa	Shear modulus
$\boldsymbol{g}$	–	Equality constraint vector
$\mathcal{G}$	$\mathrm{N\,mm^{-1}}$	Energy release rate
h_g	mm	Hole length
h_s	µm	Height of sheet
$\boldsymbol{h}$	–	Inequality constraint vector
j	–	Imaginary unit
J	$\mathrm{N\,mm^{-1}}$	J integral
k	$\mathrm{N\,m^{-1}}$	Stiffness
k_b	$\mathrm{N\,m^{-1}}$	Stiffness between top sheet and blade
k_f	$\mathrm{N\,m^{-1}}$	Stiffness of force sensor
k_0	$\mathrm{N\,m^{-1}}$	Static stiffness
$\boldsymbol{K}$	$\mathrm{N\,m^{-1}}$	Stiffness matrix
K_i	$\mathrm{MPa\,mm^{-1/2}}$	Stress intensity factor of mode i
K_p	–	Gain
K_{ell}	–	Complete elliptic integral first kind

Symbol	Unit	Description
l	m	Deformation of material
L	m	Contact length between knife and workpiece
m	kg	Mass
M	–	Shear stress friction parameter
$\boldsymbol{M}$	kg	Mass matrix
n_c	–	Number of cut sheets
n_n	–	Number of sheets
$o(t)$	–	Input in the time domain
$\hat{o}(t)$	–	Four series or transform
$O(s)$	–	Input in the frequency domain
$\mathcal{O}$	–	Taylor series
p	$\mathrm{N\,m^{-2}}$	Pressure
P	N	Mode I loading
P_V	N	External applied loads
$q(t)$	–	Single pulse function
Q	N	Mode II loading
r	mm	Radius
r_c	–	Cut ratio
r_{con}	–	Contact ratio
R	N	Mode III loading
s	–	Complex argument
$\boldsymbol{s}$	MPa	Stress vector
t	s	Time
t_a	s	Contact time start
t_c	s	Contact time
T	s	Period
T_w	s	Period of resonance
u	m	Displacement
	m	Nodal displacement
$\boldsymbol{u}$	m	Displacement vector

Symbol	Unit	Description
$\dot{u}$	$\mathrm{m\,s^{-1}}$	Velocity
$\boldsymbol{\dot{u}}$	$\mathrm{m\,s^{-1}}$	Velocity vector
$\ddot{u}$	$\mathrm{m\,s^{-2}}$	Acceleration
$\boldsymbol{\ddot{u}}$	$\mathrm{m\,s^{-2}}$	Acceleration vector
u_C	m	Displacement in cutting direction
u_L	m	Displacement in lateral direction
U	J	Elastic deformation energy
v_c	$\mathrm{m\,s^{-1}}$	Cutting speed or feed rate
v_i	$\mathrm{m\,s^{-1}}$	Velocity in direction i
v_R	$\mathrm{m\,s^{-1}}$	Resulting velocity
v_r	$\mathrm{m\,s^{-1}}$	Relative velocity
v_v	$\mathrm{m\,s^{-1}}$	Blade velocity
V	$\mathrm{m^3}$	Volume
w	m	Sheet width or stack width
w_g	m	Hole width
W	J	Work
W_F	J	Friction work
W_s	N m	Surface energy
x	m	Position or coordinate
x_b	m	Knife position
$\dot{x}_b$	$\mathrm{m\,s^{-1}}$	Knife velocity
$\ddot{x}_b$	$\mathrm{m\,s^{-2}}$	Knife acceleration
x_c	mm	Cutting depth
x_v	m	Blade position
$\mathcal{X}$	–	Transfer function
y	m	Position or coordinate
$\boldsymbol{y}$	–	Design variable vector
z	m	Position or coordinate
$\boldsymbol{z}$	–	Transformed variable vector
z_{press}	mm	Compression

Greek Symbol	Unit	Description
α	$^\circ$	Tilt angle of single sheet or stack
β	$^\circ$	Cutting angle
β_c	$^\circ$	Cutting angle
β_f	$^\circ$	Face angle
γ	$^\circ$	Transformed slice-push ratio
ϵ	–	Nominal strain
ε	–	Compression ratio
ζ	–	Slice-push ratio
η	–	Normalized time
λ	–	Decay constant
μ	–	Coefficient of friction
μ_b	–	Coefficient of friction between cutting edge and workpiece
μ_{pp}	–	Coefficient of friction between paper sheets
ν	–	Poisson ratio
ξ	–	Tool-workpiece relative speed
ϖ	–	Relation between friction and cutting angle
ρ	$\mathrm{kg\,m^{-3}}$	Density
σ	MPa	Tensile stress
σ_0	MPa	Yield stress
ς	–	Damping coefficient
τ	MPa	Shear stress
τ_F	MPa	Shear stress caused by friction
φ	$^\circ$	Angle of guides or angle of knife
	–	Azimuthal coordinate
ψ	–	Design variable
ω	Hz	Frequency
ω_0	Hz	Resonance frequency
Δ	m	Difference between the centerline of the tools vibration and the height of the unstrained material

Greek Symbol	**Unit**	**Description**
Π	J	Potential energy
$\boldsymbol{\Upsilon}$	–	Transformation matrix
$\Lambda(t)$	–	Pulse
Ψ	–	Penalty factor

Subscript	**Description**
b	Blade
$crit$	Critical
el	Elastic
f	Feed forward direction
F	Coulomb friction
h	Horizontal direction
L	Lateral direction
p	Paper
pl	Plastic
t	Transversal direction
v	Vertical direction
x	X-direction
y	Y-direction
z	Z-direction
X	X-direction
Y	Y-direction
Z	Z-direction

Abbreviation	Description
CD	Cross Direction
CFRP	Carbin Fiber Reinforced Polymers
CNC	Computerized Numerical Control
DENT	Double-Edge-Notched-Tension
DIN	Deutsches Institut für Normung
DOE	Design of Experiments
EA	Evolutionary Algorithms
EOM	Equation of Motion
FEM	Finite Element Method
FFT	Fast Fourier Transform
GA	Genetic Algorithms
MD	Machine Direction
NIMBUS	Nondifferentiable Interactive Multiobjective Optimization System
ODE	Ordinary Differential Equation
SIF	Stress Intensity Factor
$TWCR$	Tool-Workpiece Contact Ratio
$TWRS$	Tool-Workpiece Relative Speed
UVA	Ultrasonic Vibration Assisted

Abstract

Cutting stacked thin material, is a separation process that requires in-depth process perfection and optimized tools. Reducing cutting forces can be of key interest in perfecting the cutting process and expanding its capabilities. For the pulp and paper industry, the guillotining of stacked sheets is an essential finishing process. Adding vibrations to the cutting edge may significantly improve the separation process by reducing cutting forces. With two sources of energy acting together at the tool-workpiece interface, this becomes a hybrid process. In this dissertation, one numerical and two analytical models are developed to predict cutting forces during longitudinal vibration assisted cutting and lateral vibration assisted cutting of stacked thin material. While the first is a discontinuous conventional process, the latter adds a slicing motion to the conventional push cutting. The resulting cutting forces of these two hybrid processes are discussed in detail. It is shown that the force reduction due to longitudinal vibration is mainly a phony effect, because the specific energy necessary for material separation stays unchanged. Thus, the cutting forces at the tool-workpiece interface are not reduced. However, the increased damping force between the cutting knife and workpiece causes the stacked material to fail at lower compression. The force reduction occurring during lateral vibration is valid from an energy and fracture mechanic point of view. Reduced friction effects between cutting edge and sheet material are the significant contributors towards overall force reduction during slicing. The energy based model considers the cutting process without any leading crack as a combination of push cutting and slicing. Cutting and friction forces are overcome by the energy provided from both translatory motions. On the contrary, the fracture mechanics model considers the slice-push cutting with a leading crack during sideways cutting of stacked sheets. It is shown that the slicing motion helps overcoming friction effects, but material failure is only due to mode I, leaving the slicing motion without any effect on the separation process. All three models are capable of closely predicting the cutting forces during the separation process of stacked thin paper material. To test the vibration assisted cutting processes at high frequency, two cutting knives for ultrasonic vibration assisted cutting are designed with a newly developed optimization methodology. The new optimization methodology allows the design of complex tools requiring a specific resonance mode at a specific resonance frequency. Finally, the presented models are verified through experiments, which highlights their accuracy.

Kurzfassung

Schneiden von dünnen gestapelten Materialien ist ein Trennprozess, der tiefgehende Prozesskenntnisse und optimierte Werkzeuge voraussetzt. Guillotinieren von gestapelten Papierlagen gilt als zentraler Endprozess in der Papierindustrie. Die Einsatzmöglichkeiten des Schneidprozesses werden durch die Reduktion von Schneidkräften erweitert. Die Überlagerung von Vibrationen an der Schneidkante kann den Trennprozess signifikant beeinflussen und so eine Reduktion von Schneidkräften bewirken. Durch das Zusammenspiel zweier Energiequellen an der Werkzeug-Werkstück Schnittstelle entsteht ein Hybridprozess. In dieser Dissertation werden drei Modelle, ein dynamisches und zwei analytische, entwickelt, um die auftretenden Schneidkräfte beim longitudinalen vibrationsunterstütztem Schneiden und lateralen vibrationsunterstütztem Schneiden vorherzusagen. Während das erste Modell eine Abbildung eines diskontinuierlichen konventionellen Prozesses ist, fügt das zweite Modell eine weitere translatorische Bewegung dem konventionellen Drückschneiden bei. Die resultierenden Schneidkräfte dieser Hybridprozesse werden im Detail in der Dissertation diskutiert. Es stellt sich dabei heraus, dass die Schneidkraftreduktion beim longitudinalen vibrationsunterstützten Schneiden eine Täuschung ist, da die spezifische Energie unverändert bleibt. Aus diesem Grund wird die effektive Schneidkraft an der Werkzeug-Werkstück Schnittstelle nicht reduziert. Allerdings führt die hohe Relativgeschwindigkeit und deren Dämpfungskraft zum verfrühten Versagen des Materials, wodurch die vorangehende Kompression reduziert wird. Die Schneidkraftreduktion beim lateralen vibrationsunterstützten Schneiden ist eine tatsächliche Reduktion in Anbetracht der notwendigen Trennenergie bzw. Bruchenergie. Die Reduktion der Reibeffekte zwischen Schneidkante und Bogenmaterial liefert dabei einen signifikanten Beitrag zur gesamten Schneidkraftreduktion während des Ziehschneidens. Das analytische, auf Energie basierende Modell betrachtet den Ziehdrückschneidprozess ohne Rissausbreitung als eine Kombination aus Drückschneiden und Ziehschneiden, wobei beide translatorische Bewegungen die notwendige Energie für das Trennen des Materials liefern. Im Gegensatz dazu prognostiziert das bruchmechanische Modell ein Versagen des Werkstücks unter Rissausbreitung beim seitlichen Schneiden. Es wird gezeigt, dass die Ziehbewegung die Reibung reduzieren kann, aber das Material ausschliesslich auf Grund von Modus I versagt, wodurch die Ziehbewegung keinen Einfluss auf den Trennprozess hat. Alle drei Modelle sind fähig die auftretenden Schneidkräfte sehr genau vorherzusagen. Um das vibrationsunterstützte Schneiden bei hohen Frequenzen experimentell zu testen, müssen zwei Schneidmesser für den Resonanzbetrieb mittels eines neu entwickelten Optimierungsprozesses ausgelegt werden. Die neue Optimierungsmethodik für Ultraschallbauteile erlaubt die Konstruktion von neuen komplexen Bauteilen im Resonanzbetrieb. Zum Schluss werden die entwickelten Modelle mittels experimenteller Verifikation getestet, wodurch deren Genauigkeit hervorgehoben wird.

1 Introduction

1.1 Ultrasonic Applications in Manufacturing

Applications of Ultrasound were first researched in 1927 to test the effects of high power waves on glass, wood, oil, water, and living matter [1]. It was found that a piezoelectric oscillator operating at 50 000 V with a vibration frequency of 300 kHz was capable of easily cutting into glass and wood, cause an oil bath to support a plate of 150 g, and create high temperatures when holding it in one's fingers. Testing on living matter showed red blood corpuscles to be destroyed, and small fish and frogs be killed by an exposure of one or two minutes. A twenty minute exposure of mice did not prove to be fatal, but the animals were barely capable of moving, though recovery was quickly. A blood corpuscles count proved to be very low, indicating fear. The piezoelectric transducer used in the experiments is based on the studies on submarine detection done by Paul Langevin in 1917 [2]. The principles of this transducer are still used today. Regarding manufacturing, Farrer [3] invented ultrasonic erosion in 1948, which up to today is used to cut materials such as glass, ceramics, semiconductor materials, diamond, hard alloys and others, which are difficult to cut by conventional machining [4]. A rod, vibrating at its longitudinal resonance mode, is used in combination with abrasive slurry to cut into those materials. A fundamental review was done by Rozenberg et al. [5] on ultrasonic cutting and machine tool applications. Cutting forces, cutting rate, and surface finish are discussed for various materials when using ultrasonic machining. The key factors of vibration assisted machining are vibration frequency, vibration amplitude, cutting rate, and workpiece material properties.

Processes in which fracture is caused at a specific static force are the majority in the field of ultrasonic application. The observed static force is significantly reduced to fulfill the conventional machining process, making this effect the key advantage of ultrasonic vibration assisted machining. However, this decrease in forces is observed solely on the fact that today no measurement equipment is capable of recording the actual process as it is pointed out in [4]. Hence, most observations on force reduction are based on the average force during one vibration cycle. Material properties are not altered due to ultrasound. This is also addressed by Brehl et al. [6] in the review on vibration assisted machining. Numerous advantages of ultrasonic machining are improved surface finishes, better accuracy, reduced burr, increased tool life, and improved machinability.

When using vibrations to enhance conventional processes of machining, it is commonly called vibration assisted machining. In case of using vibrations in the ultrasonic range, which is above the maximum audible frequency of $\sim 18\,\text{kHz}$ [7, 8], it may also be called ultrasonic assisted machining. Since two sources of energy are combined at the tool workpiece interface, vibration assisted machining may be categorized as a hybrid process.

1.2 Motivation

In the pulp and paper industry, the cutting of paper is a key finishing process used for all types of products. Not only is paper cut as single sheets, but also as stacks of a few or hundreds of sheets. These stacks may be cut with a simple cutting knife or a more complex shaped cutting punch. The former is mostly used for books or other stacks that need to be trimmed, while the latter is commonly used in the creation of various labels or thin material with complex shapes. Key challenges are proper cutting properties to reduce wear, cutting forces, friction forces, and improved cutting quality for a various range of paper products with and without printing. Here, vibration assisted cutting and guillotining presents a new process allowing substantial advantages that have already been well researched for the cutting of metal. Therefore, this work deals with the basis of vibration assisted guillotining of stacked thin materials. A structural optimization methodology for ultrasonic devices, and three process models of vibration assisted cutting of stacks are presented. Through the optimization methodology, more complex devices may be designed with maximum performance and less time consuming manual work. The process models can be used to better understand the effects of vibration assistance and its advantages. Finally, experimental verification underline the effectiveness of the hybrid processes.

2 State of the Art and Scope

2.1 Definition of Cutting and Guillotining

According to DIN 8588 [9] and [10], splitting is a manufacturing process in which material is separated without the formation of chips (while chips may occur during the cutting process, they are physically not essential for separation of material). It is a sub-category of cutting in the classification of the different manufacturing processes. Splitting can be divided up into different manufacturing sub-processes, such as shearing, knife edge cutting, cutting with two approaching blades (bite cutting), cleaving, tearing, and breaking as shown in Figure 2.1. Today, cutting and shearing are the most commonly used processes in the metal, food, textile, polymer, and paper industry. In surgery, the cutting of tissue and bone material is also widely done with knife edge cutting and sawing.

The polymer and paper industry further distinguishes knife edge cutting into rotary slitting with circular knives and guillotining with straight knives [15, 16]. The rotary cutting methods are mostly used for continuous slitting and cutting of single layers as it is done in big paper mills. They are also realized as a shearing process. Guillotining is used to cut a single sheet or stack of thin material layers at once as it is shown in Figure 2.2. It is a common finishing process in the label industry and bookbinding. In the label industry, finished printed sheets are stacked as a block of approximately 1000 pieces and then guillotined and die-cut according to the printed patterns [17]. There are four different guillotining methods that can be categorized as following [15]:

1. Parallel Vertical Cut
2. Parallel Slide Cut
3. Swinging Vertical Cut
4. Swinging Slide Cut

As shown in Figure 2.3a, the knife moves from top to bottom with the dead center sliding along a straight line for the parallel vertical cut. The parallel slide cut can be defined as two separate motions in y- and z-direction (Figure 2.3b). The swing cut (Figure 2.3c) adds a rotary movement around the x-direction or normal vector of the knife. While the parallel cut brings the entire cutting edge of the knife in contact with one single layer of the stack and cutting it at once, the swing cut allows continuous knife edge cutting of a single layer during the guillotining process. The advantage of the swinging cut is the lower total cutting force, because the knife is only partially in contact with the layer. This is commonly used for cutting sheet metal as discussed in [18]. The sliding movement of the knife adds a sawing-like effect to the process, which is discussed later. Regarding the Swinging Slide Cut (Figure 2.3d), it consists of two translatory and one rotary movements of the knife edge, combining the advantages of sliding and swinging. It is the most common

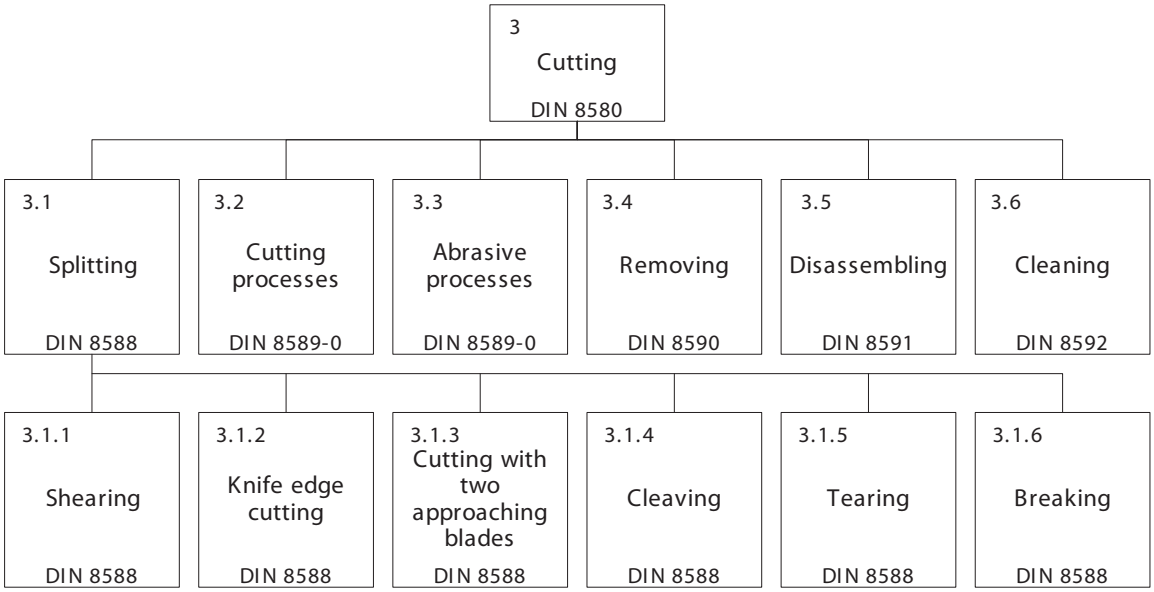

Figure 2.1: Definition of cutting manufacturing processes. Translation from [9] and [11] according to [12–14].

process used in guillotining of paper stacks, since the cut material is easier pushed away by the knife [19]. All four guillotining methods must ensure that the knife is parallel to the work table at the lowest point, to ensure a complete cutting operation on all layers of the stack.

DIN 8869 [20] specifies the parts of a asymmetrical knife used in knife edge cutting and guillotining of paper. Most important are the rake face angle and cutting angle, of which the cutting angle is usually larger than the rake face angle, e.g. 24° and 22° or 19° and 17°. Length of the cutting face is usually approximately 1.5 mm. Modern knives include a clearance angle to reduce friction on the flat side of the asymmetrical knife.

2.2 Cutting and Guillotining of stacked thin Material

2.2.1 Overall process

The overall guillotining (or cutting) process of a single thin sheet can be described as following [21]:

1. Phase I: contact between cutting knife and sheet material
2. Phase II: compression of material until critical cutting force is reached
3. Phase III: cutting of material
4. Phase IV: cutting knife emerges from material.

Summarizing the discussions in [19, 21–35], there has been numerous research done on the cutting and slitting of thin materials considering various factors, such as cutting force, friction force, compression, tensile and compression stress, wear, cutting quality, material

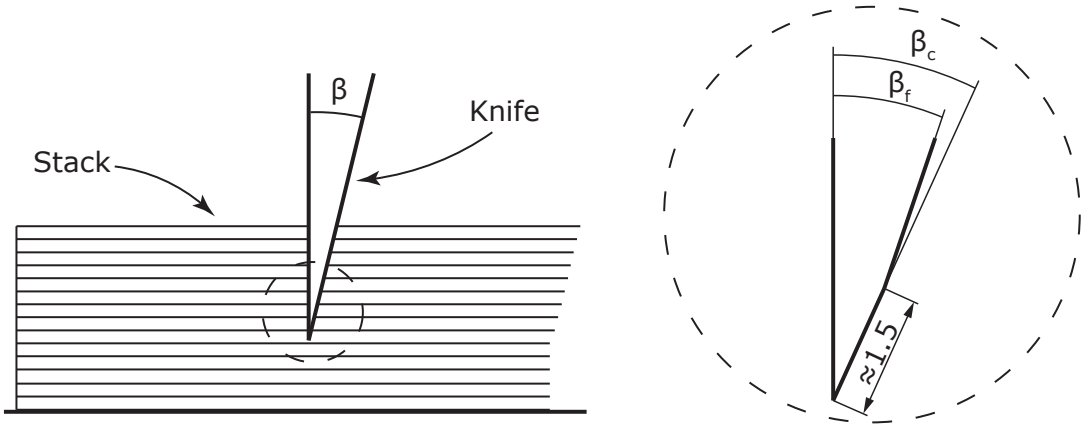

Figure 2.2: Schematic diagram of guillotining of stacked thin material. β_c is the cutting angle and β_f is the rake face angle.

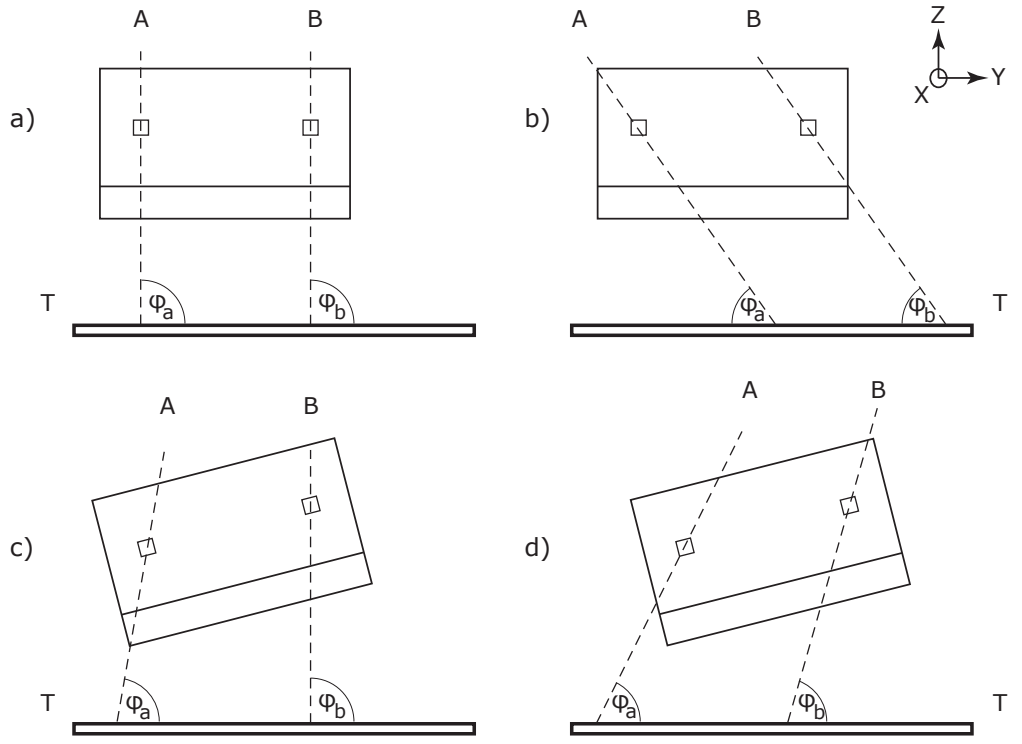

Figure 2.3: Four different guillotining methods, with a) parallel vertical cut ($\varphi_a = \varphi_b = 90°$), b) parallel slide cut ($\varphi_a = \varphi_b < 90°$), c) swinging vertical cut ($\varphi_a < \varphi_b = 90°$), and d) swinging slide cut ($\varphi_a < \varphi_b < 90°$). φ_a and φ_b are the angles of the guides (A and B) relative to the table (T).

parameters, cutting tool geometry, cutting tool material, etc. These factors have an impact on the cutting process and are partly dependent on each other. Rösner and Schulz [22] qualitatively describe in detail the cutting of paper as a combination of several effects in the splitting process:

- Compression: The contact between cutting knife and sheet material causes high localized pressure causing fibers to be separated, cut, or ripped apart.
- Sawing: It only occurs during slicing motion of the knife. Due to the roughness of the cutting edge, it has micro saw-tooths that cause fibers to be sawed. This effect increases with the amount of slicing motion.
- Tearing: It can be observed that some sheets are ripped apart before the cutting edge reaches them. This is caused by tensile stresses inside the paper stack and is described as a leading crack [36].
- Notch effect: During the cutting of a single sheet, the tear resistance is decreased by the increasing notch caused by the cutting edge. This effect is related to the ripping effect.
- Thermal effect: Friction at the cutting edge causes the blade and sheet material to heat up, which aids the cutting of fibers. This effect is negligible.
- Shearing effect: When using a counter-knife opposite the cutting knife, shearing forces are acting upon the sheet material. However this effect is only visible when cutting single or small number of sheets.

These effects also apply to guillotining of non-fibrous thin sheet materials. In the following, the essential cutting process parameters are discussed.

Cutting forces result from the separation, ripping and cutting of fibers at the cutting edge, and friction along the cutting blade. Forces occurring during the cutting of thin material are related to the cutting angle, rake face angle, clearance angle, sharpness and cleanness of the cutting blade. The cutting angle affects the cutting forces and is defined by the material being cut. For soft materials the cutting angle should be very slim, whereas for hard materials it should be more "blunt" [19]. A slimmer angle causes lower friction and compression forces during sheet separation, but it wears down easier. The cutting angle also affects how much the edge is being deformed due to the resistance of the sheet material. As a result, the cutting angle and knife edge sharpness affect the cutting quality. Proper sharpening and cleanness of the cutting edge are essential for cutting forces and quality of guillotining stacks. Regarding the plane side of asymmetrical knives, a small clearance angle should be observed to reduce friction between the compressed stack and the down sliding cutting knife [19, 23–25]. The size of the cutting edge radius also affects cutting forces with an increasing radius causing increased cutting forces at a constant cutting angle [26]. A table for various materials and the corresponding appropriate cutting angles can be found in [37].

Cutting forces are also related to tool wear and material properties as investigated in [26–28]. With increasing wear at the cutting edge, cutting forces increase. Wear of guillotining knives for cutting of polymer sheets depends on cutting angles, cutting forces,

and cutting speed [38]. A relationship between cutting force and specific material parameters was found in [29]. It was observed that the force necessary for cutting paper and board are correlated to area density (linear), thickness (linear), lateral bending stiffness (logarithmic), and transversal bending stiffness (logarithmic), as well as bursting strength (linear). The correlation between shearing angle and cutting force was examined in [30]. An optimal (= lowest cutting forces) shearing angle between 6° to 8° was found.

The cutting of fibrous food materials was researched in [39]. Increasing the cutting speed reduced cutting forces and improved cutting quality, because the increased momentum of the cutting knife and inertia of the workpiece promote initial failure of the material. The slicing cut process decreases the vertical cutting force as previously described and investigated in [35]. At a higher sliding speed, the cutting force decreases, due to the sawing and thermal effect from friction at the cutting edge.

Prior to guillotining a stack of sheet material, the stack needs to be compressed to remove air between the layers, in order to prevent single layers from moving relative to each other. The compressed stack can then be regarded as a firm block along the cutting line, thus preventing the penetrating knife to further press down the stack [15]. When the knife further compresses the stack, the top sheets of the stack are pulled out in x-direction due to the bending of the sheets as shown in Figure 2.4. Especially soft materials with high air volume between single sheets need to be compressed to avoid the negative cutting qualities of bending and relative movement. However, high compression reduces the sliding ability between cut sheets [19]. As a rule of thumb: soft materials require high compression while hard materials require low compression. Recent research done by Desch [40] in his dissertation regarding the effective cutting angle when guillotining paper stacks shows that the bending of the paper material influences the effective cutting angle during the separation process. A geometric model describes the effective cutting angle based on the knife's motion and resulting cutting forces. The effects of the paper compression are also highlighted. Detailed analysis of the pressure distribution is carried out to obtain a clear understanding of the compression forces within the stack. It is shown that the compression area, which depends on the material used, slightly expands below the applied load (reduction of pressure), but the effect is asymptotic.

These compression forces cause tensile and compression stress inside the stack, which lead to weakening and partly tearing of sheet material. Through the compression force, caused by the cutting edge pressing onto the thin material, compression stress is present below the knife edge, resulting in bending and tensile stress in the sheet material in the vicinity of the compression. The cutting angle causes additional compression stress at the cutting edge, which also results in tensile stress in the sheet stack. A larger cutting angle causes a more flat stress distribution in the material. Figure 2.4 shows the occurring stresses within the stack in detail. The cutting edge radius also influences the compression forces, with a smaller radius causing a more narrow stress distribution. Once the air volume is pressed out, these tensile stresses result in tearing forces acting upon a single sheet, leading to partly or fully splitting of a single sheet. It was observed that a more narrow compression stress distribution causes higher localized tensile stress, which in return reduces the force necessary for the cutting of the material [22, 26, 31, 32, 35, 41, 42]. FEM simulations show that during the compression phase, materials like paperboard create a hull-like effect around the penetrating cutting edge, thereby causing high compression stress, which increases the cutting force and can lead to failure of the knife [31]. This phenomenon explains the increase in cutting force for thicker material when parallel cutting.

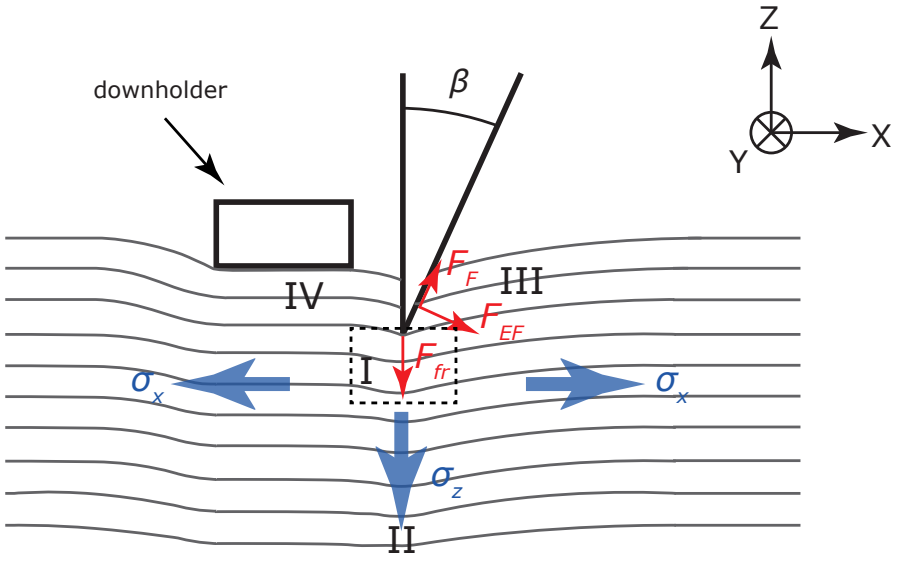

Figure 2.4: Forces and stress during the guillotining process. Cutting and friction forces cause compressive stress underneath the cutting edge, resulting in tensile stress along the sheets.

Cutting quality of a single thin sheet is dependent on various factors, such as cutting angle, and material properties [33, 34]. The most appropriate cutting angle depends on the material being cut. Materials with high deformation should be cut with a large cutting angle, while materials with lower deformation should be cut with a narrower cutting angle, because they are more susceptible to cracks and tearing that decrease cutting quality. The importance of correct cutting parameters regarding cutting quality is discussed for shearing of paper in [34]. Wear of the cutting edge is also directly related to the cutting quality - higher wear results in lower cutting quality. Blunt cutting tools increase the tearing effect during cutting of paper [28].

For the cutting an entire stack of thin material, the macroscopic cutting quality needs to be considered. Depending on cutting forces, fixture of the cutting knife, stack compression, and material parameters, the cutting quality of the entire stack can suffer from two errors: undercut and overcut [43, 44]. Both errors describe how much the stack deviates from being perpendicular to the ideal cutting plane. They are caused by incorrect compression of the stack and incorrect cutting parameters.

2.2.2 Essential material parameters of paper

Many of the previously described cutting process parameters are dependent on the material properties of the sheets being cut. It is therefore necessary to analyze the essential material parameters. For cutting of a paper stack, these are compression strength, compressibility, and bending stiffness [45–49]. Detailed research was done on the compression strength of paper, corrugated board, and boxes in [48]. It was found that the internal material matrix is mainly responsible for the compression strength.

Compressibility is defined as a thickness change during or after applying pressure. It is dependent on how much load is applied to paper material, how long this load is lasting, and what the initial temperature was. After removing the load, the recovered thickness

depends on the initial load applied, the duration of the applied load, and the time of recovery [46, 50]. Compressibility has a logarithmic relationship to the time a load is applied. The behavior of paper and board stacks during the compression phase of knife edge cutting is discussed in [51]. Paper and board stacks were tested and a logarithmic correlation between stack height and load were found. In addition, the residual tensile strength was examined and it is also logarithmic correlated to the applied load. However, the tensile strength is mostly reduced when the air is already pressed out and pores within the material are greatly reduced. Then the compression stress is significantly weakening the structure. High compressed paper produces better cutting quality as well. The energy necessary for compressing a sheet or stack of paper depends not only on the paper matrix, but also on the energy needed to remove the air in the pores and between sheets [52].

Schaffrath et al. [53] suggested a model for the compression behavior of paper in z-direction at low pressures. The model describes the total deformation of a single sheet of paper as a combination of the deformations of the outer and inner structures, with the outer structure being the surface roughness of the paper, and the inner structure being the paper matrix. The deformation of the inner structure is described as the pressure-deformation of a linear elastic material block according to Hooke's law. For the deformation of the outer structure, Hooke's law is used as well, but the deformation is not based on the height, but the average surface roughness. A single sheet of paper can therefore be described as a series of three springs. This model is further applied by Schaffrath et al. [54] to study the behavior of a stack of paper. One key finding is that with an increasing number of sheets in the stack, the deformation does not linearly correlate with the applied constant load. A stack of 20 paper sheets was found to be stiffer than a single sheet. The surface roughness of the paper sheet plays a dominant role in the compressibility of a stack of paper.

Relations between strength properties of fiber constituents and a complete paper are discussed in [55], with analyzing mathematical equations relating material properties. Complete force-deformation behavior is analyzed for single- and multi-axial loading in [56]. It is shown that the force-deformation behavior of paper is nonlinear dependent on the direction and type of loading. As a result, two-dimensional nonlinear constitutive equations are formulated and tested on FEM of shearing of paper. Further material properties for paper are presented in [49, 57, 58]. Detailed research on physical properties of paper were performed in Paetow's dissertation [59]. Various topics related to strain-stress behavior of paper material are discussed. Most important is the investigation on the nonlinear orthotropic behavior.

2.3 Modeling of Cutting and Guillotining

2.3.1 General Cutting Model

Atkins et al. [60] models the cutting of thin slices of material by regarding the total energy balance of the process. Under the assumption that very little elastic strain is stored when cutting thin slices, the total energy necessary for cutting with a parallel vertical cut is the sum of the specific cutting energy and work of friction. It is defined by

$$F_C \cdot \mathrm{d}u_C = e_{fr} \cdot w \cdot \mathrm{d}u + W_F \tag{2.1}$$

with F_C being the total force necessary for cutting, $\mathrm{d}u_C$ being the tool displacement in cutting direction, e_{fr} being the specific cutting energy in cutting direction, w being the

width of the material, and W_F the work needed to overcome friction. This equation is only valid if the motion of the tool and the reached cutting depth are controlled by the cutting device, and no leading crack occurs. It should be pointed out that the tool edge radius, cutting angle, and clearance angle are not considered here. If the cut material requires energy for overcoming bending stiffness, this would need to be added to the above equation. With an empirically found specific cutting energy, the total work necessary to cut a specific material can be calculated with equation (2.1) when disregarding friction effects.

As already discussed earlier, the parallel vertical cut can be superimposed with a slicing motion. Under the assumption that the specific cutting energy remains constant

$$e_{fr} \cdot w \cdot \mathrm{d}u = constant \tag{2.2}$$

and the basic energy balance in equation (2.1) holds true, the model for the vertical slide cut, slice-push cutting, defines the total energy necessary for cutting is provided by the vertical (push) and slicing cutting motion. Regarding floppy materials with no friction, the total energy necessary is

$$e_{fr} \cdot w \cdot \mathrm{d}u = F_Z \cdot \mathrm{d}u_Z + F_Y \cdot \mathrm{d}u_Y \tag{2.3}$$

with F_Z being the vertical force (in cutting direction), $\mathrm{d}u_Z$ being the tool displacement in vertical direction, F_Y being the lateral (horizontal) force, and $\mathrm{d}u_Y$ being the tool displacement in lateral direction [60]. The resulting force is given by

$$F_R = \sqrt{F_Z^2 + F_Y^2} \tag{2.4}$$

and the resulting displacement as

$$u_R = \sqrt{u_Z^2 + u_Y^2} \tag{2.5}$$

so equation (2.3) can be rewritten as

$$e_{fr} \cdot w \cdot \mathrm{d}u = \left(\sqrt{F_Z^2 + F_Y^2}\right)\left(\sqrt{u_Z^2 + u_Y^2}\right) \tag{2.6}$$

Since the vertical slide cut combines push cutting and slicing, a dimensionless slice-push ratio is defined as

$$\zeta = \frac{\mathrm{d}u_Y}{\mathrm{d}u_Z} \tag{2.7}$$

hence with equation (2.3) and $\mathrm{d}u_Z = \mathrm{d}u$ we obtain the two forces based on the resulting force

$$\frac{F_Z}{e_{fr}w} = \frac{1}{(1+\zeta^2)} \tag{2.8}$$

$$\frac{F_Y}{e_{fr}w} = \frac{\zeta}{(1+\zeta^2)} \tag{2.9}$$

The dimensionless resulting force can be calculated with

$$\frac{F_R}{e_{fr}w} = \sqrt{\frac{1}{(1+\zeta^2)}} \tag{2.10}$$

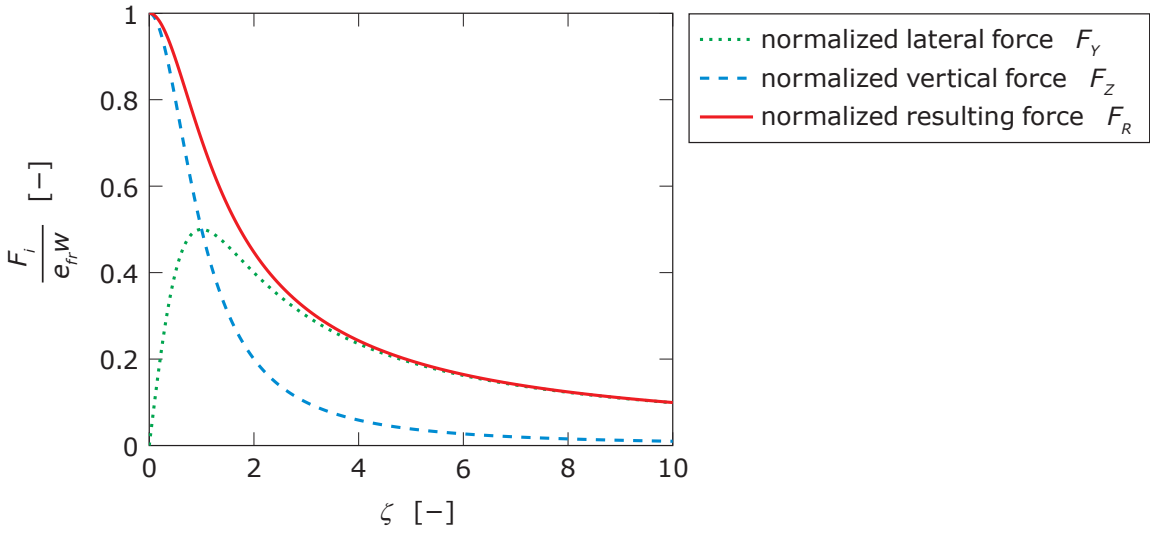

Figure 2.5: Frictionless normalized cutting forces as a function of ζ [60].

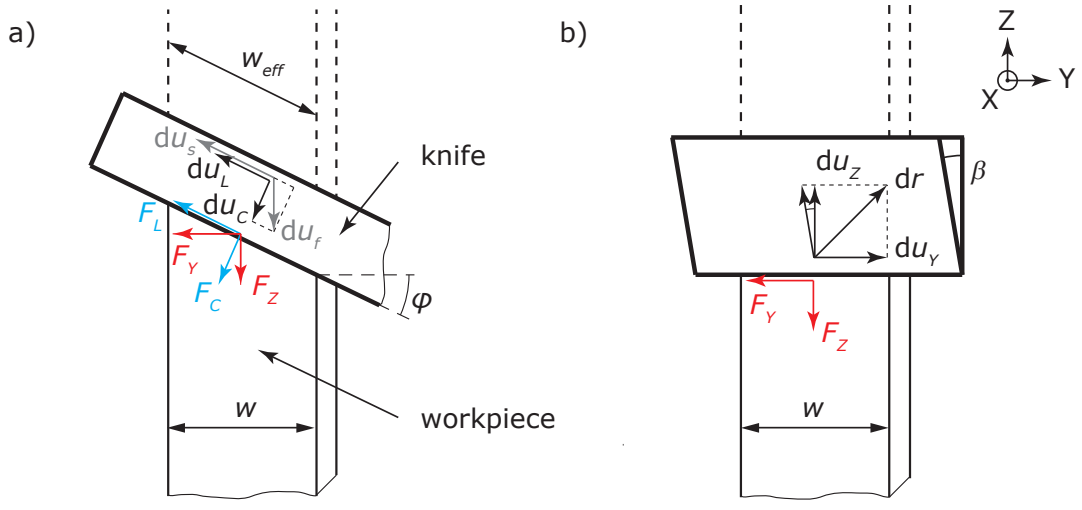

Figure 2.6: Model for forces between knife and workpiece [60, 61]. a) shows cutting with angled knife and b) shows cutting without angled knife.

Figure 2.5 graphically shows the correlation between ζ and the respective forces.

When the cutting knife is slightly angled as it would be in a swinging vertical or sliding cut, the forces parallel F_Z and perpendicular F_Y to the feed direction are

$$F_Z = F_C \cos\varphi - F_L \sin\varphi \tag{2.11}$$

$$F_Y = F_C \sin\varphi + F_L \cos\varphi \tag{2.12}$$

with φ being the tilt angle of the cutting knife as shown in Figure 2.6. Considering the tilt angle, the slice-push ratio and forces in z- and y-direction become

$$\zeta = \frac{\mathrm{d}u_L}{\mathrm{d}u_C} = \frac{\mathrm{d}u_s - \mathrm{d}u_f \sin\varphi}{\mathrm{d}u_f \cos\varphi} \tag{2.13}$$

$$\frac{F_Z}{e_{fr} w} = \frac{\cos\varphi - \zeta \sin\varphi}{(1+\zeta^2)\cos\varphi} \tag{2.14}$$

$$\frac{F_Y}{e_{fr} w} = \frac{\sin\varphi + \zeta \cos\varphi}{(1+\zeta^2)\cos\varphi} \tag{2.15}$$

With $\varphi = 0$, equations (2.8) and (2.9) are again obtained. The reduction in pushing force due to splitting the total cutting force in pushing and slicing was observed for guillotining of paper stacks in [35]. A reduction in pushing force reduces the compressive stress in the paper stack as well.

So far the frictionless vertical or swinging slide cut is considered. As a next step, the model is extended with the Coulomb friction effect. When assuming an asymmetrical cutting knife with the cutting angle β as shown in Figure 2.6, the material slides over the knife after being cut, causing a normal force acting upon the rake face. Equation (2.3) can be rewritten to include Coulomb friction of an asymmetrical cutting knife as

$$e_{fr} \cdot w \cdot \mathrm{d}u + \mu F_N \mathrm{d}r = F_Z \cdot \mathrm{d}u_Z + F_Y \cdot \mathrm{d}u_Y \tag{2.16}$$

where μ is the friction coefficient, $\mathrm{d}r$ is the resulting moving direction, and F_N is the normal force. The resulting moving direction $\mathrm{d}r$ can be calculated from

$$\mathrm{d}r = \sqrt{\mathrm{d}u_Y^2 + \left(\frac{\mathrm{d}u_Z}{\cos\beta}\right)^2} = \frac{\mathrm{d}u_Z}{\cos\beta}\sqrt{(\zeta\cos\beta)^2 + 1} \tag{2.17}$$

and the friction term is expanded to

$$\mu F_N \mathrm{d}r = \frac{\mu}{\cos\beta}\left(\frac{F_Z}{\sin\beta + \mu\cos\beta}\right)\sqrt{\zeta^2\cos^2\beta + 1}\mathrm{d}u_Z \tag{2.18}$$

With equations (2.16) and $F_Y = \zeta F_Z$ [60] the forces in z- and y-direction become

$$\frac{F_Z}{e_{fr} w} = \frac{1}{1+\zeta^2 - \frac{\mu}{(\mu\cos\beta + \sin\beta)\cos\beta}\sqrt{(\zeta\cos\beta)^2+1}} \tag{2.19}$$

$$\frac{F_Y}{e_{fr} w} = \frac{\zeta}{1+\zeta^2 - \frac{\mu}{(\mu\cos\beta + \sin\beta)\cos\beta}\sqrt{(\zeta\cos\beta)^2+1}} \tag{2.20}$$

(as in [60] with slight differences). Thus, the cutting forces in push and slice direction depend on the friction coefficient μ, the slice-push ratio ζ, and the cutting angle β. In case a symmetrical cutting knife is used, the friction coefficient μ is simply multiplied by a factor of 2.

2.3.2 General Guillotining Friction Model

When considering the vertical guillotine cut of paper, the force necessary for moving the cutting knife through the stacked material can be expressed by

$$F_C = f(F_{fr}, F_{EF}, F_F) \tag{2.21}$$
$$F_F = F_{EF}\mu_b \tag{2.22}$$

where F_C is the total cutting force acting against the knife, F_{fr} is the force necessary for cutting, F_{EF} is the force necessary for displacement of cut sheets, and F_F is the Coulomb friction force resulting from F_{EF} and blade-paper friction coefficient μ_b (see Figure 2.4) [16, 27, 42]. To analyze the forces acting against the cutting knife, the stack cutting process is divided into four sections [62]:

I. Immediate proximity of the cutting edge: sheets are being cut by the cutting knife. Paper sheets are under very high loading with compression and tensile stress as discussed earlier.

II. Directly under section I: stresses are lower and sheets are less deformed. It can be regarded as an elastic substructure for section I. (As previously mentioned, detailed research was later done by Desch [40].)

III. Finished cut paper sheets: friction forces occur between sheets and cutting knife and cause bending and displacement of the sheets.

IV. Cut sheets at the plane side of the cutting knife: sheets are bent due to the initial compression before cutting until the clearance angle is reached and bending is relaxed.

To formulate the equilibrium of forces, it is assumed that the process is quasistatic, the paper is homogeneous, fibers are neglected, and no deformation of cutting knife and guides occurs. Regarding section III and Figure 2.7, the following equilibrium of forces of normal and friction forces for the n^{th} sheet is defined by

$$F_{EFn} = F_{Gn}\frac{\mu_{pp}}{\cos\beta - \mu_b\sin\beta - \mu_{pp}\sin\beta - \mu_b\mu_{pp}\cos\beta} \tag{2.23}$$
$$F_{Npn} = nF_{Gn}\frac{\cos\beta - \mu_b\sin\beta}{\cos\beta - \mu_b\sin\beta - \mu_{pp}\sin\beta - \mu_b\mu_{pp}\cos\beta} \tag{2.24}$$
$$F_{Fpn} = F_{Npn}\mu_{pp} \tag{2.25}$$

where F_{EFn} is the displacement force, F_{Gn} is the gravity force acting on each sheet ($F_{G1} = F_{G2} = ... = F_{Gn}$), μ_{pp} is the friction coefficient between paper sheets, F_{Npn} is the normal force between sheets, and F_{Fpn} is the friction force between sheets. It becomes clear that the displacement force F_{EFn} acting against the sheets is independent from the number of sheets. On the blade side, the sum of F_{EFn} results in the total force F_{EF} acting against the blade. However F_{Npn} increases linearly with the number of cut sheets.

When looking closer at the overlap of section I and III of the cutting process, the straight cut sheets as shown in Figure 2.7 do not seem completely correct. The bending of the sheets at the cutting knife due to the compression has to be considered. Therefore, a tilt angle α is introduced as shown in Figure 2.8. α is mainly dependent on material

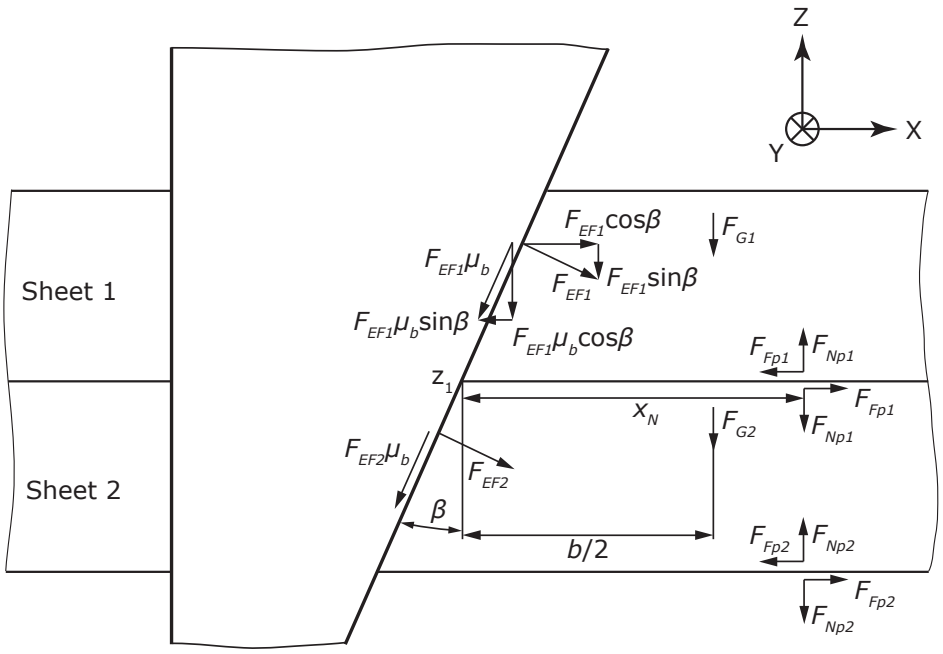

Figure 2.7: Model for forces of friction between knife edge and paper, and friction between paper sheets [62].

properties and cutting edge sharpness. Thus, the equilibrium of forces of normal and friction forces for the n^{th} sheet has to be rewritten as [62]

$$F_{EFn} = F_{Gn}\frac{\sin\alpha+\mu_{pp}\cos\alpha}{\left[\begin{array}{l}(\cos\beta-\mu_b\sin\beta)(\cos\alpha-\mu_{pp}\sin\alpha)\\ \quad-(\sin\beta+\mu_b\cos\beta)(\sin\alpha+\mu_{pp}\cos\alpha)\end{array}\right]} \tag{2.26}$$

$$F_{Npn} = nF_{Gn}\frac{\cos\beta-\mu_b\sin\beta}{\left[\begin{array}{l}(\cos\beta-\mu_b\sin\beta)(\cos\alpha-\mu_{pp}\sin\alpha)\\ \quad-(\sin\beta+\mu_b\cos\beta)(\sin\alpha+\mu_{pp}\cos\alpha)\end{array}\right]} \tag{2.27}$$

$$F_{Fpn} = F_{Npn}\mu_{pp} \tag{2.28}$$

2.4 Fracture Mechanics

In contrast to energy based approaches for determining the necessary force for separating a material, fracture mechanics may be used to model the failure behavior of materials. Fracture mechanics uses continuum mechanics to study the propagation of cracks on a macroscopic level [63]. The study of linear fracture mechanics focuses on the failure behavior caused by a crack within ideal elastic brittle materials. Loading occurs at the flanks of the crack and is the main contributor towards crack propagation. There are three modes that may describe crack opening as shown in Figure 2.9 [64]. A cracked body can be loaded in any of the three shown modes or a combination of two or all three modes.

One key factor of linear fracture mechanics is the energy release rate. It defines how much energy is necessary to create a new area during the separation process by overcoming

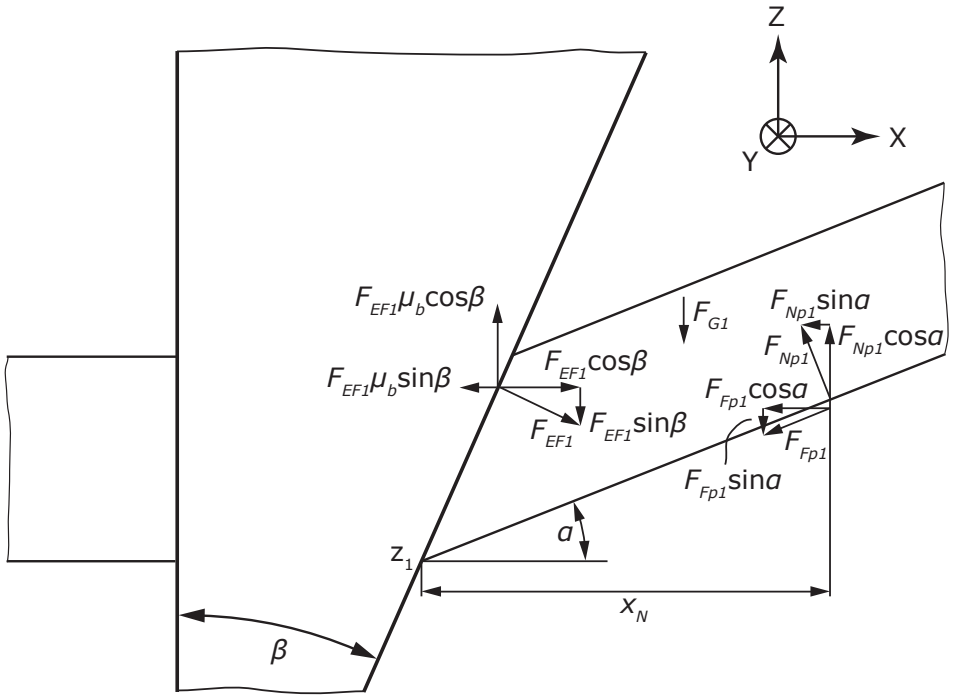

Figure 2.8: Model for forces of friction between knife edge and paper, and friction between paper sheets, while considering the bent down paper. The bending of the cut sheets is represented by the angle α [62]. Further considerations done in [62] are outlined in A.14.

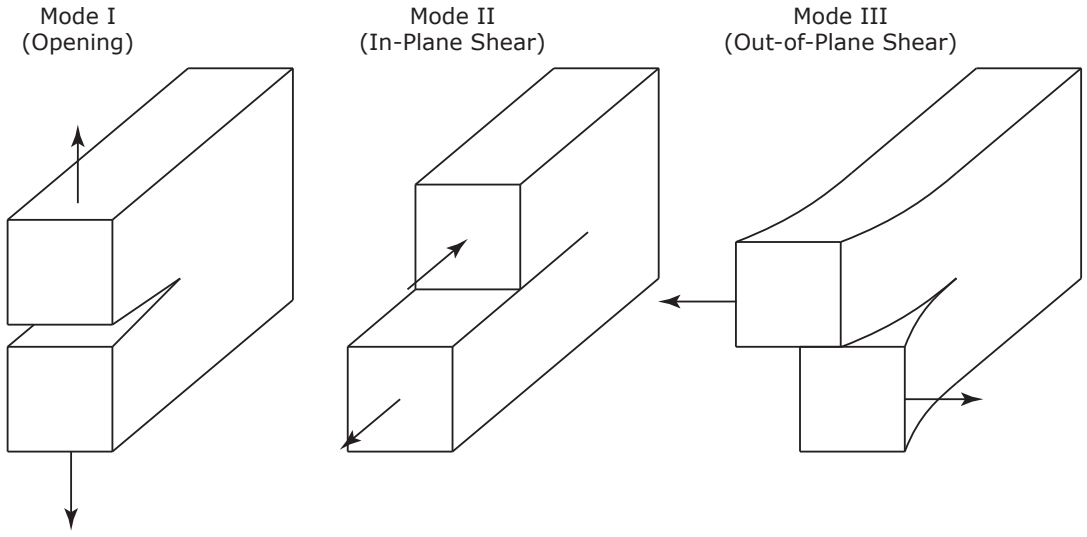

Figure 2.9: The three modes of loading that can be applied to a crack [64].

the bonding energy between atoms. For the infinitesimal increase in crack area $\mathrm{d}A$, the released potential energy $\mathrm{d}\Pi$ is necessary, thus defining the energy release rate $\mathcal{G}$ as

$$\mathcal{G} = -\frac{\mathrm{d}\Pi}{\mathrm{d}A} \tag{2.29}$$

which is also called the Griffith energy balance [64]. The potential energy $\mathrm{d}\Pi$, which is equal to the surface energy W_s necessary to create a new area, is the difference between elastic deformation energy U and the potential of the externally applied loads P_V

$$\Pi = U - P_V \tag{2.30}$$

where the elastic deformation energy is calculated as the product of stress $\boldsymbol{\sigma}$ and strain $\boldsymbol{\epsilon}$, integrated over the volume of the material,

$$U = \iiint\limits_V \left(\int\limits_0^{\boldsymbol{\epsilon}} \boldsymbol{\sigma} \mathrm{d}\boldsymbol{\epsilon} \right) \mathrm{d}V \tag{2.31}$$

The potential of the externally applied loads is simply calculated from the acting force F and the displacement of its contact u,

$$P_V = \boldsymbol{F}^T \boldsymbol{u} \tag{2.32}$$

Next, the concept of the stress intensity factors is very briefly introduced. A cracked workpiece undergoing external loading experiences stress concentration near crack tips, which can lead to further failure at a specific critical level. In linear fracture mechanics, this stress field is usually circular around the crack tip. The stress distribution around the crack tip depends on the radius, where infinitely high stress occurs at radius zero (singularity at $r = 0$ is proportional to $\sqrt{r}^{-1}$). However, this cannot be calculated analytically, but is described with the stress intensity factors (SIF). For the three types of crack modes described previously, these SIF are

$$K_I = \lim_{r \to 0} \sqrt{2\pi r} \sigma_{yy}(\varphi = 0) \tag{2.33}$$

$$K_{II} = \lim_{r \to 0} \sqrt{2\pi r} \tau_{xy}(\varphi = 0) \tag{2.34}$$

$$K_{III} = \lim_{r \to 0} \sqrt{2\pi r} \tau_{yz}(\varphi = 0) \tag{2.35}$$

where r is the radius and φ is the azimuthal coordinate [63, 64]. Their relationship to the energy release rate $\mathcal{G}$ and J contour integral J are well described in [63, 64], and will not be further introduced here. Critical values of the SIF are also called fracture toughness. With these very basic principles, cutting processes for various materials have been investigated. In regard to slice-push cutting, the following works present the research base for this dissertation.

Since the surface energy W_s depends on the material and is regarded as constant, it is argued and shown that a force reduction may be obtained by increasing the slicing motion. Detailed observations are made for cutting food materials using ultrasonic vibration assisted cutting knives in Zahn's [65] dissertation. Mechanics of wire cheese cutting and estimation of fracture toughness depending on wire thickness and cutting force were

discussed in [66]. Neder [67] discusses in his dissertation the cutting of prepreg material. Since the fibers are much tougher than the surrounding matrix material, the resistance to cutting of prepreg is mainly caused by the fibers. He concludes that the slicing motion adds additional shear stress to the fibers of the material. Thus, the fibers are cut more easily due to the additional displacement and its resulting normal and shear stress, complementing the tensile stress from the pushing motion of the cutting knife.

Zhou et al. [68, 69] and Reyssat et al. [70] discuss the slice-push cutting process on bio materials. They both conclude that the slice-push motion creates a three-dimensional state of stress within the workpiece, and thus the resulting equivalent stress is higher than when solely cutting with a pushing motion. Consequently, the material fails earlier and the desired crack is created. However, this approach only explains the initial cutting phase and not the process occurring at the crack tip after the onset of cutting. Similar observations were done by Feiler in his dissertation [71] regarding brittle materials and using the maximum shear stress theory. Guillotine cutting of soft tissue were done in [72] to study the mechanics when cutting with a knife.

In [73] a fracture mechanics energy-based approach was used to model the forces of cutting with scissors. It splits up the process in two phases: deformation and sharp cutting. The model uses the fracture toughness to calculate the cutting forces. McCarthy et al. [74, 75] performed a detailed investigation on the cutting of soft materials regarding blade sharpness. The findings relate the energy required to initiate a cut to the fracture toughness of the tested material and the indentation depth required to penetrate the material, which depends on the sharpness of the knife. From the model, it is found that a maximum stress criterion is a good indicator for predicting the onset of cutting. Blade sharpness is most sensitive to the tip radius. Fracture characteristics in cutting of liver with a surgical blade with regard to cutting force and fracture resistance are studied in [76]. In [77], the friction occurring during cutting and machining is found to increase resulting cutting forces.

Stress intensity factors and other fracture mechanics parameters of paper were researched in [78]. Single edge notch, double edge notch, and center notch samples were used to determine the SIF. It was found that the material parameters significantly impact the fracture toughness as well as humidity, temperature, and printing. However, the critical SIF may determine the force at which the paper material fails.

2.5 Vibration Assisted Cutting and Guillotining

2.5.1 Definition

Vibration Assisted Cutting is a process in which the conventional cutting process is superimposed with vibrations at the cutting edge. Such oscillations can be generated through forced vibrations or resonance vibrations. Forced vibrations are usually applied between 1 Hz to 2000 Hz, while resonance vibrations are usually applied in the ultrasonic range of 20 kHz to 100 kHz. The displacement of a vibrating tool can be described by

$$x_v(t) = v_c t + a_v \sin(\omega t) \tag{2.36}$$

where $x(t)$ is the displacement of the cutting edge, v_c is the cutting velocity of the conventional process, a_v is the vibration amplitude, ω is the vibration frequency, and t is the

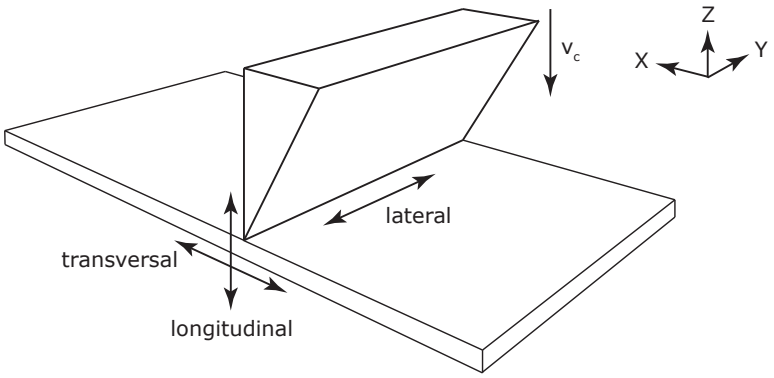

Figure 2.10: The three modes of vibration assisted cutting: longitudinal, transversal, and lateral.

time. Thus the tool vibration speed is

$$v_v(t) = v_c + a_v\omega\cos(\omega t) \tag{2.37}$$

As a result, tool-workpiece relative speed $TWRS$ can be defined by

$$TWRS = \xi = \frac{v_c}{a_v\omega\cos(\omega t)} \tag{2.38}$$

Three types of vibration assistance modes are described by the tool-workpiece relative speed (ξ) [79]:

1. $\xi > 1$: Relative velocity between tool and workpiece periodically changes, but the tool never stops or breaks contact with the workpiece
2. $\xi = 1$: Relative velocity between tool and workpiece periodically reaches 0, but the tool never breaks contact with the workpiece
3. $\xi < 1$: The tool periodically breaks contact with the workpiece. The duration of contact during one vibration cycle is defined by the tool-workpiece contact ratio $TWCR$ [79].

$TWCR$ can be calculated by

$$TWCR = \frac{t_c}{T} \tag{2.39}$$

where t_c is the contact duration during one cycle with the vibration period T. From equation (2.38), it becomes clear that vibration assisted cutting depends on three basic parameters: frequency, amplitude, and conventional cutting velocity.

Figure 2.10 shows the three basic vibration modes that can be used individually or in combination for vibration assisted cutting: longitudinal, transversal, and lateral. At the cutting edge, a longitudinal mode has a maximum displacement in cutting direction, a transversal mode has a maximum displacement perpendicular to the cutting direction and cutting edge, and a lateral mode has a maximum displacement perpendicular to the cutting direction and parallel to the cutting edge.

While in literature the terms ´´vibration assisted cutting" or ´´ultrasonic cutting" and ´´ultrasonic assisted cutting" usually refer to cutting processes according to DIN 8589-0

(see Figure 2.1), it may also refer to splitting processes which cut material without relying on the formation of chips. In the following, the application of vibration (low frequency or ultrasonic) in splitting is discussed.

2.5.2 Influences of Ultrasonics on Forces

Loading Forces

Considering an ideal elastic-plastic material, the loading of such a material results in elastic and plastic deformation. While elastic deformation obeys Hook's law, the plastic deformation occurs at a specific force with no hardening effect. The static force necessary for the deformation in the elastic region of the material is calculated with

$$F_s = k_0 \delta l = \epsilon E A \tag{2.40}$$

where $k_0 = \frac{E_Y A}{L}$ is the static stiffness, δl is the deformation of the material, A and L are the cross-sectional area and length of the material, E is Young's Modulus, and ϵ is the deformation or strain. The force at which plastic deformation occurs is declared as F_{fr}. Assuming such a material under oscillating loading (as in equation (2.36)), F_s occurs during the steady-state periodic regime of deformation [4]. The specimen under loading is assumed to be short and thus an elastic wave will propagate along it much faster than the period of loading, i.e. $\frac{L}{c} \ll T = 2\pi\omega$, where c is the speed of sound in the material. As a result, the dynamic force $F_{US} = F_{US}(x_v, v_v)$ depends on the displacement x_v and speed v_v of the oscillation, represented as

$$F_{US} = F_{US}(x_v, v_v) \begin{cases} 0 & x_v \leq \Delta, v_v > 0, \\ k_0(x_v - \Delta) & \Delta \leq x_v \leq \Delta + \frac{F_{fr}}{k_0}, v_v > 0, \\ F_{fr} & \Delta + \frac{F_{fr}}{k_0} \leq x_v \leq x_{vmax}, v_v > 0, \\ F_{fr} + k_0(x_v - x_{vmax}) & x_{vmax} - \frac{F_{fr}}{k_0} \leq x_v \leq x_{vmax}, v_v < 0, \\ 0 & x_v \leq x_{vmax} - \frac{F_{fr}}{k_0}, v_v < 0 \end{cases} \tag{2.41}$$

where Δ is the distance between the centerline of the tool oscillation cycle and the height of the unstrained material [4], and x_{vmax} is the maximum deformation during one cycle. x_{vmax} can be calculated from

$$x_{vmax} = a_v \left(\sqrt{1 - \left(\frac{v_v}{a_v \omega} \right)^2} + \frac{v_v}{a_v \omega} \arccos\left(-\frac{v_v}{a_v \omega} \right) \right) \tag{2.42}$$

Using the theorem of momentum, the relation between static force (measured) and the dynamic force resulting from the motion of the tool during one period $T = \frac{2\pi}{\omega}$, F_s is obtained from

$$F_s = \frac{1}{T} \int_{t_a}^{t_a+T} F_{US}(t) \mathrm{d}t = \frac{1}{T} \int_{t_a}^{t_a+T} F_{US}(x_v(t), v_v(t)) \mathrm{d}t \tag{2.43}$$

where t_a is the beginning of the contact between material and tool. It becomes clear that F_s depends on the material's static stiffness, vibration amplitude and frequency, and cutting speed. Further detailed analysis can be found in [4].

Friction Forces

The effects of longitudinal ultrasonic vibration on friction forces is discussed in various contributions [4, 80, 81]. Considering the Coulomb friction model and continuous contact, the net friction force can be calculated by

$$\bar{F}_F = \frac{1}{T}\int_0^T \bar{F}_F(t)\mathrm{d}t = \frac{1}{2\pi}\int_0^{2\pi} \bar{F}_F(\eta)\mathrm{d}\eta \tag{2.44}$$

with $\eta = \omega t$ being the normalized time, and $\bar{F}_F$ being the average friction force. Next, the instantaneous friction force $\tilde{F}_F$ as a function of the relative velocity

$$v_{rel} = v_c - \tilde{v}(\eta) = \hat{v}(\xi - \cos(\eta)) \tag{2.45}$$

the normal force F_N, and friction coefficient μ is calculated to

$$\tilde{F}_F(\eta) = \mu F_N \mathrm{sgn}(v_{rel}(\eta)) = \mu F_N \mathrm{sgn}(\xi - \cos(\eta)) \tag{2.46}$$

where

$$\xi = \frac{v_c}{\hat{v}} \tag{2.47}$$

is the velocity ratio between the base velocity (or cutting velocity) and the velocity of the ultrasonic vibration

$$\tilde{v}(t) = \hat{v}\cos(\omega t) = a_v \omega \cos(\omega t). \tag{2.48}$$

Thus, the instantaneous friction force can be integrated resulting in the average friction force

$$\bar{F}_F = \begin{cases} F_F & \text{if} \quad \xi \geq 1, \\ \frac{2}{\pi}\sin^{-1}(\xi) F_F & \text{if} \quad -1 < \xi < 1, \\ -F_F & \text{if} \quad \xi \leq 1. \end{cases} \tag{2.49}$$

It becomes clear that the Coulomb friction force is mainly reduced due to the oscillating movement parallel to the macroscopic motion.

2.5.3 Application of Vibration Assisted Cutting

Food Industry

A very wide field of application and research in ultrasonic assisted cutting is in the food industry. It is used for cutting of cheese, bakery products, sweets, and sandwiches. Soft and sticky materials like cheese or sweets easily stick to cutting knives, thereby causing bad cutting quality and contamination of the knife. Soft foods like cakes or sandwiches easily deform during cutting, resulting in an unpleasant form. These disadvantages can be avoided by using ultrasonic assisted cutting with guillotining knives. Key advantages are the reduction in cutting forces, friction forces, deformation of products during cutting, and improved cutting quality [65, 82–84]. Detailed analysis of the correlation between cutting force and generator power for various food products were done in [85–87]. It is shown that the reduction in cutting force directly correlates to the increased generator power used to excite the cutting tool. It is shown that the energy demand for the cutting of food products is reduced. In Zahn's dissertation [65], the difference between vertical straight cutting and slicing of foods is examined.

Medical Applications

Ultrasonic medical devices are used for cutting, coagulating, and dissecting tissue material [88]. The main advantages are high precision during cutting [89], formation of cavitation causing separation of layers, increase of pressure and temperature causing improved sealing of vessels and coaptation, and reduced deformation of tissue during cutting. A further increase in temperature causes coagulation (denaturation of proteins). Coagulation and coaptation result in hemostasis. While many ultrasonic surgical tools are based on longitudinal excitation, a surgical scalpel (micro-cutter) based on a concept for silicon ultrasonic tools that is excited transversely was introduced in [90].

Textile Industry and Prepregs

Through the use of ultrasonic assistance for cutting of textile materials, smoother cuts with welded synthetic fibers can be achieved. The ultrasonic vibrations cause high local friction forces at the edges of the material, which result in thermal energy. However, it was observed that the cutting blade does not significantly heat up during the process [91, 92]. The high thermal energy can be used to weld loose fibers together while cutting [93]. Thus, the ultrasonic cutting of textile material can be realized as a single cutting and welding process at high feed rates.

Carbon fiber reinforced polymers (CFRP) are increasingly used for structural parts in aeronautics. They mainly consist of a polymer (mostly epoxy) matrix in which fiber components (often carbon fibers) and other components are embedded. When using a with epoxy pre-impregnated weave to manufacture the CFRP part, the material needs to be cut into the appropriate form before curing. Using conventional cutting has proven to be problematic due to the high viscosity of the epoxy and the pulling out of fibers during the cutting process. Ultrasonic assisted cutting of CFRP has proven to significantly reduce cutting forces and improve cutting quality [94–97]. A reduction in wear and cutting forces, and improved cutting quality of prepregs was well studied in Neder's dissertation [67]. It is shown that the fiber failure is changing when using ultrasonic blades due to different stress components within the fibers. Cutting mechanisms also change when machining carbon fiber reinforced carbon [98]. Due to the high frequency vibration, the carbon fibers are not pulled out during turning of carbon fiber reinforced carbon, resulting in a much improved cutting quality.

Paper Industry

There is very little work on vibration assisted cutting or guillotining of paper done in research. In 1975, Downey [99] investigated the cutting and slitting of paper. When slitting continuous moving paper with a blade, frictional heating accelerates the wear of the cutting edge by tempering the hard structure. To solve this problem, a continuously moving blade was considered. It was shown that for vibrations of 10 Hz, 20 Hz, 40 Hz and 100 Hz with an amplitude of 2.54 mm at 0.75 $\mathrm{m\,s^{-1}}$ paper feed rate, the cutting quality could be significantly improved. Damping caused by the paper limited the vibration amplitude. The paper edge exhibited periodic crests of torn fiber which coincided with the minimal motion of the blade during the oscillation cycle. These crests of torn fiber were similar to the experimental results of static cutting with the same setup. Similar experiments were done for cutting of a paper stack with a guillotine knife under forced vibrations, where

the vibrating bladed subdivided the entire stack into smaller parts, thus improving cutting performance [100].

Studies on ultrasonic assisted cutting of wood were done in [101, 102]. It was observed that for dry and wet spruce and beech cutting forces were reduced. Differences in roughness and surface quality were not observed. However, small rolls of wood fiber were visible on the surface, probably due to the slightly angled cutting tool.

2.6 Structural Optimization of Ultrasonic Devices

The design of ultrasonic devices has been studied for various applications. Two very common methods used to design such devices are analytical calculations, and FEM. The two methods have been compared by designing of tool holders [103], and acoustic horns [104]. More challenging is the design of a horn with a longitudinal-torsional composite mode [105]. The longitudinal-torsional composite mode allows advanced applications for machining with rotary movements such as drilling. A design of a longitudinal-torsional vibration converter is introduced in [106]. Various designs for ultrasonic assisted drills were done in [107–110]. A study on the design of transducers for ultrasonic assisted wire bonding has been discussed in [111], with the goal of matching experimental results with simulation results. Ultrasonic assisted cutting tools were designed in [112–115]. The cutting tools are excited with a longitudinal vibration.

Another method for designing ultrasonic devices is the utilization of structural optimization. Many optimization methods have been applied for finding shapes that proved good results for ultrasonic vibration applications. Through structural optimization, the optimal shape and configuration of ultrasonic devices is sought to improve performance. Key properties are resonance frequency, electric impedance, electromechanical coupling coefficient, and vibration amplitudes. A multiobjective optimization with the nondifferentiable interactive multiobjective optimization system (NIMBUS) was used to appropriately tune a Langevin-type transducer with three objective functions corresponding to three practical objectives in the transducer design [116]. The results from FEM calculation were used for evaluating the transducer performance through the objective function (see section 3.2). Genetic Algorithms were used in a multiobjective optimization with two conflicting objective functions, maximum vibration amplitude and minimal electrical input power, to find Pareto-optimal solutions for a Langevin transducer design [117]. Structural optimization using full factorial and Doehlert design (response surface) of design of experiments (DOE) were used to optimize a standing wave ultrasonic linear motor [118]. The resulting sensitivity analysis showed the critical dimensional parameters of the motor and an optimal design was found. Based on equation (A.42), an ultrasonic horn was designed by optimizing the contact stiffness between horn and tool while minimizing the volume of the structure [119]. Porto et al. [120] used three different genetic algorithms to optimize the length of a surgical ultrasonic transducer to maximize the vibration amplitude.

2.7 Scope of this work

Regarding the previous state of art in vibration assisted cutting, cutting of paper stacks, and structural optimization of ultrasonic devices, the scope of this work is defined. The

many advantages of vibration assisted cutting have been well researched for cutting processes of metal, ceramic, glass, food, biological, and composite materials. Forced vibrations at low frequencies have been tested for slitting of single paper sheets. It has been claimed that momentum leads to earlier failure of materials during ultrasonic vibration assisted machining. A detailed dynamic model discussing longitudinal vibration assisted cutting of stacked material does not exist. Models predicting cutting when slice-push cutting have been established with simple Coulomb fiction. However, there is no analytical model explaining the cutting and friction forces occurring during cutting of stacked paper material. For ultrasonic assisted machining, various types of devices have been designed and some strategies for the utilization of optimization algorithms have been defined. The combination of genetic algorithms and FEM has been established and used for axis-symmetrical horns. No general strategy for the optimization of devices requiring a specific resonance mode at a specific resonance frequency has been developed.

In this work, the vibration assisted cutting of paper stacks is investigated. High frequency vibrations generated by a piezoelectrical transducer are superimposed onto the cutting edge of a cutting knife and the impact on cutting and friction forces is analyzed. Two cases of vibration assisted cutting are examined: parallel vertical cutting with longitudinal vibration at the cutting edge, and parallel vertical cutting with lateral vibration at the cutting edge. The vibration direction of the parallel vertical cutting with longitudinal vibration is in the same direction as the feed of the macroscopic motion, while the vibration direction of the parallel vertical cutting with lateral vibration is perpendicular to the feed.

The four scientific contributions of this work are: development of a methodology for the optimization of ultrasonic devices, which allows the designing the tools used in the experimental verification; development of a dynamic numerical model of longitudinal vibration assisted guillotining of stacked thin material; development of an analytical energy based model of cutting and friction forces during slice-push cutting of stacked thin material; and development of an analytical fracture mechanics model of cutting and friction forces during slice-push cutting of sideways oriented stacked thin material. Finally, these models are experimentally verified for the two previously mentioned cutting processes.

In order to make an analysis at resonance operation for these processes possible, specific cutting knives need to be designed. Since there are no known cutting knives or intuitive solutions, two new kinds of cutting knives are created. This is realized by developing a new optimization methodology for structural optimization of ultrasonic devices. The resulting cutting knives are then used for experimental testing and process model verification.

Next, a model of longitudinal vibration assisted guillotining of stacks is developed. The model combines the quasi-static cutting model of stacked thin material with the dynamic force model of ultrasonic assisted machining. A physical model of the stack is defined with specific material parameters that are empirically obtained through various experiments. Eventually, the presented model is experimentally verified.

In respect of slice-push cutting, two models are presented. The first model uses an energy based approach to determine the cutting forces when increasing the slice-push ratio. It uses the specific cutting force, compression force, and friction effects to model the process. The second model uses basics of fracture mechanics to model the same cutting forces when slice-push cutting a stack of sheets sideways (rotated 90°). The fracture mechanics model relies on the fracture toughness, which is experimentally determined. Finally, both models are experimentally verified using simple slice-push cutting. The energy based model is also tested on lateral vibration assisted cutting of stacked thin paper sheets.

3 Cutting Knife Design with Optimization Methodology

3.1 Manual Multi-Step Design using FEM - Intuitive Design Process

In order to superimpose high frequency vibrations on a specific area, the tool needs to be excited at a resonance frequency. Tuning of such ultrasonic devices can be done based on the theory of longitudinal and torsional rods [121]. Simple geometries can be found using this approach (see example in Appendix A.10 for the analytical calculation), but more complex shapes cannot be designed effectively and the analytical method is replaced by FEM. Following, the design process with FEM for complex shapes is introduced as it is done for many designs discussed in section 2.6.

The manual or intuitive design process for complex ultrasonic devices was well outlined in the dissertation of McCulloch [122]. It is based on analyzing the displacement solution of an FEM modal and/or harmonic analysis as shown in Figure 3.1 (see Appendix A.11 for FEM equations). The procedure starts with an intuitive concept on how the geometry should be set up, and can be based on equation (A.42). Next, a 3D model is created and tested with FEM modal and/or harmonic analysis. The mode shape and resonant frequency are visually assessed to determine if the model satisfies the stated requirements, e.g. the proper mode shape at the correct excitation frequency. Once the FEM design procedure is done, the found geometry is being manufactured to start the experimental design process. An experimental modal analysis and/or velocity or displacement measurements with a laser vibrometer are carried out to test the effective mode shape and resonance frequency of the device. If the experimentally determined mode shape and frequency correlate with the FEM results, the device can be tested in the appropriate area of application. Finally, it is determined if the device is suitable for operation or if the initial concept needs to be reconsidered. The downside of the presented design process is that it is very time consuming the more complex the geometry of the ultrasonic device becomes. In addition, there can be multiple geometric features that separately have an effect on the resulting mode shape and resonant frequency, requiring multivariate testing. It is therefore beneficial to create a methodology that automates the manual design process.

3.2 Introduction to Structural Optimization

Structural optimization is based on the motivation to improve a given product in regard to its performance. It is a key aspect of product development. Before the invention of optimization methods for structural problems, the improvements were done based on experience, testing, and intuition. The commonly known trial and error method was used

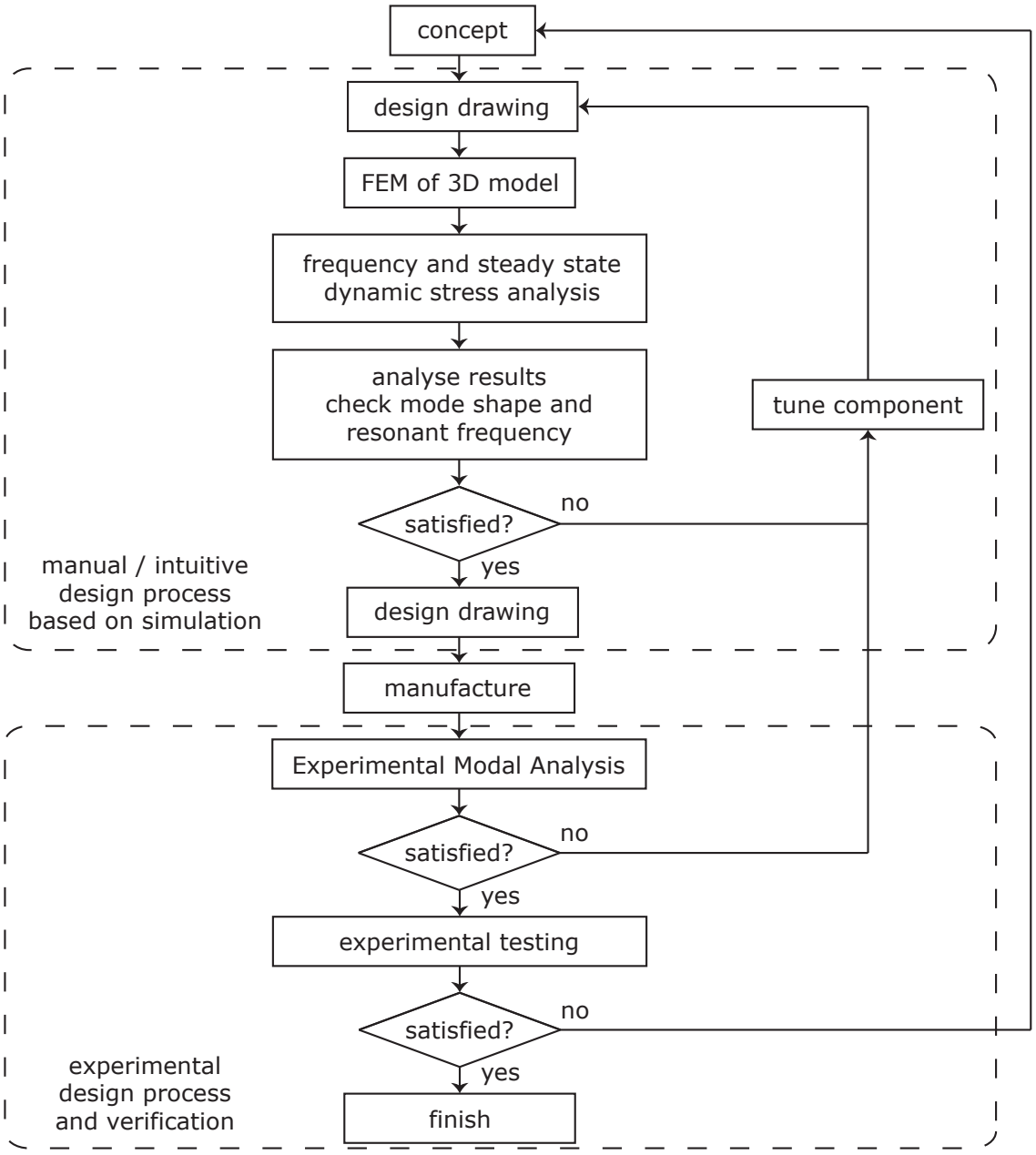

Figure 3.1: Manual / intuitive design procedure for ultrasonic devices. Based on the schematic introduced by [122].

to find the sensitivity of the performance of a specific product. The time needed for one design improvement cycle depends on the time of building a new design and testing its performance during service. With the introduction of FEM, the time necessary for one design improvement cycle could be significantly reduced due to the ability of testing the design in a virtual environment before building a prototype or product. By analyzing the structure via FEM, the decision maker is capable of testing different properties, getting clues to how the design may be improved. However, this process is still based on manual and intuitive decisions, and with increasing complexity of the problem very time consuming.

Fully automated optimization procedures allow the decision maker to work more effectively and reduce the time necessary for one improvement cycle. Testing and evaluating the product's performance is done by the procedure, while the human decision maker focuses on planning and deciding. Planning and deciding include choosing the optimization method, overall procedure, as well as defining the criteria for performance evaluation.

Structural optimization relies on an appropriate definition of design variables that describe the configuration of the product to be optimized. These design variables are either continuous, discrete, or both. Such variables may be geometric shapes, material properties, constructive layout, topology, and supports. Geometric shapes are usually described either by nodal coordinates or lengths. In case of curved or free form surfaces, the geometry is given by spans, supportive points, splines, and thickness distribution. Geometric shape variables are usually continuous. Material properties are defined by variables such as specific weight, Young's modulus, mechanical strength, etc, which are usually discrete values. Constructive layout is the determination of the most suitable layout of all existing solutions. Topology is the arrangement or linking of elements in a structure that can be modified by discrete steps only. Supports design variables define the support or loading conditions that are either continuous or discrete [123]. The design variables are denoted by $\psi_i,\ i = 1, .., n$, composed into a vector $\boldsymbol{\psi}$, which lies in the design space, an n-dimensional Euclidean space:

$$\boldsymbol{\psi}^T = [\psi_1, \psi_2, \psi_3, ..., \psi_i, ..., \psi_n] \tag{3.1}$$

Optimizing a structure by some automated numerical procedure is complex and requires proper organization. The concept presented in the next section was defined by Eschenauer [123] and decomposes the task of optimizing a structure into manageable subtasks so that it can be solved in a straightforward manner. Although the concept seems to have been developed with regard to optimization algorithms labeled as mathematical programming, it is also valid when other solution techniques such as genetic algorithms are used [124].

3.2.1 Objective Function (Fitness Function)

In order to determine whether or not a specific structure meets certain objectives, an objective function, also called cost function, criterion function, performance measure, or fitness function, is formulated. The objective function serves as a mathematical representation of one or multiple structural performance criteria such as displacement, stress, thermal behavior, etc. It is a scalar measure that represents the performance of a given value of the design variables. The optimization algorithm uses this objective function to orientate itself in the search space and know whether one solution is better or worse to other solutions in the objective space.

Regarding the use of genetic algorithms in this dissertation, the objective function is from now on called fitness function.

3.2.2 Constraining Functions

Regarding all possible designs resulting from totality of the continuous or discrete range of the design variables, not all designs may be acceptable or valid in terms of the design and performance requirements. To exclude such design solutions from the search for the optimal solution, constraining functions are formulated. The constraining functions are the mathematical representations of the boundaries in the search space. Geometrical constraints impose explicit restrictions on the design variables due to manufacturing limitations, physical illogical configurations, aesthetics, etc. Behavioral constraints restrict structural response associated with loading conditions and are thus implicit in terms of the design variables [123]. Constraints are expressed in the form of equality and/or inequality constraining functions:

$$h_i(\boldsymbol{\psi}) = 0 \qquad (i = 1, ..., k) \tag{3.2}$$

$$g_j(\boldsymbol{\psi}) \leq 0 \qquad (j = 1, ..., l) \tag{3.3}$$

Inequality constraints divide the design space into feasible and infeasible regions or surfaces. The feasible or admissible region contains all valid values for the design variables $\boldsymbol{\psi}$.

3.2.3 Formulation the Optimization Problem

The goal of the optimization is to find the set of design variables that correspond to an extreme value of the fitness function, while satisfying the constraining functions. Finding the extreme value of the fitness function is usually done by maximizing or minimizing it. For most problems, a minimization of the fitness function is done, thus resulting in the mathematical formulation of the optimization problem as

$$\min_{\boldsymbol{\psi} \in \Re^n} \{f(\boldsymbol{\psi}) \mid \boldsymbol{h}(\boldsymbol{\psi}) = \mathbf{0},\ \boldsymbol{g}(\boldsymbol{\psi}) \leq \mathbf{0}\} \tag{3.4}$$

with $\Re^n$ being an n-dimensional set of real numbers, $f(\boldsymbol{\psi})$ being the fitness function, $\boldsymbol{h}(\boldsymbol{\psi})$ being the vector of inequality constraints, and $\boldsymbol{g}(\boldsymbol{\psi})$ being the vector of equality constraints.

3.2.4 Eschenauer's Three-Columns Concept

Figure 3.2 shows the Three-Columns Concept according to [123], which generally allows any structural optimization problem to be solved. The three columns are the structural model, the optimization model, and the optimization algorithm. To perform a computerized optimization process, the real structure needs to be transferred to a structural model. The structural model describes mathematically or numerically the physical behavior of the real structure, such as the response to applied static and dynamic loads, eigenfrequencies, weight, etc.. Next, the optimization algorithm is chosen based on the problem to be solved. The optimization algorithm solves the generally nonlinear and constraint optimization problem by an iterative process from an initial design vector $\boldsymbol{\psi}_0$. It stops once a predefined criteria is satisfied. Finally, the optimization model connects the structural model with the optimization algorithm. As explained in [124], the evaluation model

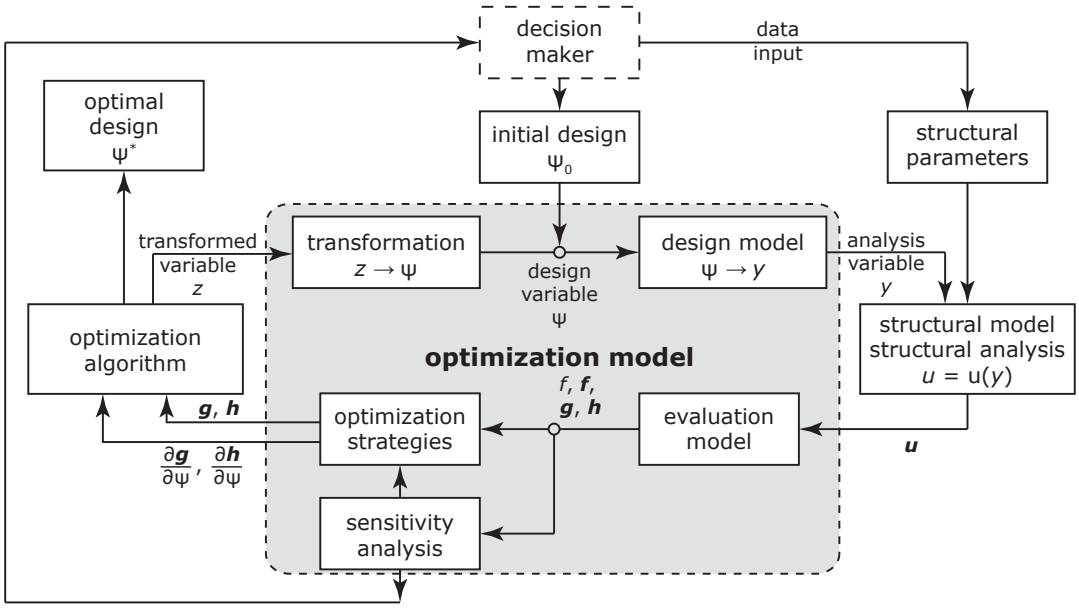

Figure 3.2: Structure of an optimization loop, with structural model, optimization model, and optimization algorithm [123].

performs the design evaluation in terms of the optimization objective and the state (e.g. violated or not) of existing constraints from the values of the state variables and other information from the structural model. The evaluation of the structural model is based on the state variable vector $\boldsymbol{u}$ (e.g. displacement) or some other variables influenced by the design. Variable definitions and transformations in the optimization model are called parameterization. The analysis variables $\boldsymbol{y}$ are chosen from the structural parameters (e.g. nodal points). The shape of the structure is defined by the design variables $\boldsymbol{\psi}$. The design model describes the mathematical relation between the analysis variables $\boldsymbol{y}$ and the design variables $\boldsymbol{y}$. Dependent on the optimization algorithm, the design variables $\boldsymbol{\psi}$ may need to be transformed into transformation variables $\boldsymbol{z}$ meeting the special requirements of the algorithm.

There are two basic methods of optimization algorithms: direct and indirect. An optimization algorithm using a direct search method requires only the values of the objective function, whereas an indirect search method needs additional information in form of the first or higher order derivate of the objective function. Direct search methods can be further subdivided into stochastic and deterministic, while indirect search methods are all deterministic.

3.2.5 Stochastic Search Methods

In mathematical search methods, the objective function must be smooth and convex, and the search space should be continuous and homogeneous. However, there are many structural optimization problems that do not meet these requirements. Hence, the stochastic search methods provide good possibilities to overcome the limitation of mathematical search methods, because no perfect knowledge on the objective is necessary to set the search direction. A random choice is made regarding the search direction as the algo-

rithm iterates towards a solution [125]. Stochastic search methods are inspired by biology or physics or other, such as Evolutionary Algorithms, Simulated Annealing, Ant Colony Optimization and Swarm Optimization. Methods like Tabu Search or Neural Networks imitate learning mechanisms. In this dissertation, two assumptions are stated as in [124]:

1. Pointwise sampling of the search space allows to get a kind of a problem landscape at least locally

2. Better solutions can be found close to already visited good solutions.

These two assumptions show the two opponent search strategies named exploration and exploitation. Exploration uses a wide search within the unknown search space while exploitation uses an already known good solution to test the surrounding region for better solutions. Thus, exploitation will drive the algorithm to an optimum, which can be a local or global one, while exploration checks for distant better solutions. In a stochastic optimization, both search strategies should be applied in balance to avoid a premature convergence in a local optimum. There is no optimal setup for the amount of exploration versus exploitation for finding the global optimum, but it depends on the fitness function.

Regarding the performance of stochastic search methods, it is said that two arbitrary optimization algorithms have the same average performance (i.e., cannot work better than blind random search) over all optimization problems. This is stated in the No Free Lunch Theorem [126]. However, one optimization algorithm might be superior to another for a specific optimization problem. It means that an algorithm cannot have both wide applicability and uniformly high efficiency [125]. While Genetic Algorithms (introduced in the next section) are widely applied to various optimization problems, there is no proof that they are superior to other optimization methods.

3.2.6 Genetic Algorithms

Genetic Algorithms (GA) are a branch of Evolutionary Algorithms (EA) that use biological principles as they occur in nature, such as reproduction, recombination, mutation, section, and isolation, as a search heuristic. They function as a global search method. In nature, an individual must evolve within a specific environment by reproduction, inheritance, variation, and selection. GAs reproduce individuals by either direct cloning of parents, recombination of genetic material from both parents, or reproduction with mutation to allow inheritance with variation. This way, the reproduction represents the exploitation while the mutation acts as the exploration part of the global search. As it is in nature, GAs use selection to determine which individuals reproduce and with whom. It exerts evolutionary pressure to guide the evolution in a specific direction of the search space by defining how genetic material is inherited and how much offspring an individual can have. But it can also be used as an operator for extinction.

An individual in the GA is expressed through genes, which make up the genotype of that individual. It is essentially the vector of the design variables $\boldsymbol{\psi}$. The genes may be expressed as bit strings, special encoding, or floating point numbers. The genotype expresses the phenotype of the individual. In structural optimization, the phenotype is the overall physical behavior of the entire structure, while the genotype describes the physical layout of the structure (e.g. position of beams, thickness of elements, material properties, lengths, etc).

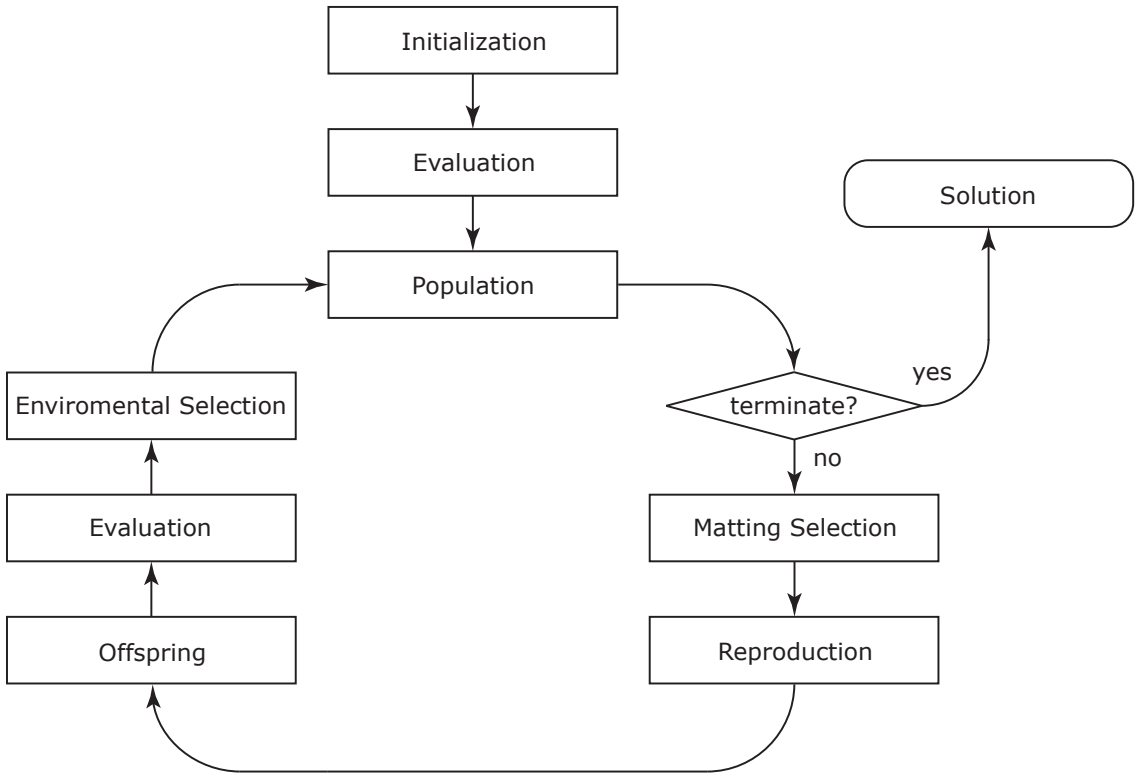

Figure 3.3: General Genetic Algorithm (GA) procedure.

Figure 3.3 shows the basic GA procedure. At the beginning, a group of individuals is being initialized to start the evolution. The initial population serves as a head start in the evolutionary process by creating a random population from the entire search space. This feeds the GA with some amount of knowledge at the beginning of the evolutionary process. The starting point for this initial population maybe an already known or a randomly created individual. Next, the initial population will be evaluated according to the fitness function. These resulting fitness scores will be assigned to the individual respectively. Based on the values of the fitness function and the matting selection method, the reproduction process is started. The matting selection method decides which individuals may produce offspring for the next generation. This operation is based on the principle ´´survival of the fittest," because parents are chosen based on their fitness values. However, this should not be overdone due to the reduction in diversity and premature convergence. Once the parents of the next population are selected, the reproduction process is started. Within the reproduction process, the inheritance and variation of the next generation is decided. Some individuals of the next population may be direct clones, some individuals may be a recombination of genetic material of the parents, and some individuals may have a certain number of mutations in their genetic material. Specific functions are used for the recombination and mutation processes. The newly created population now has similar genetic material as the previous one with a certain percentage of completely new solutions due to the mutation. The new genotypes express similar and different phenotypes than the previous population. Again, the new generation will be evaluated based on the fitness function. Depending on the algorithm, an environmental selection may now take place to decimate a certain amount of the population. Finally, the evolutionary process is repeated

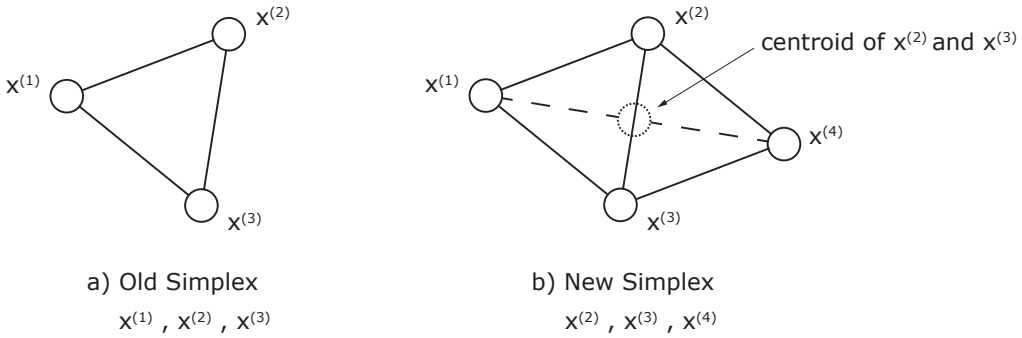

Figure 3.4: Simplex setup and construction of new simplex [128]. Vertices x^1, x^2, and x^3 make up the initial simplex and x^2, x^3, and x^4 make up the new simplex resulting from copying x^1 at the centroid of x^2 and x^3.

until specific termination criteria are met. These termination criteria may be a maximum number of generations, a minimum change in the fitness function of the best individual over a certain amount of generations, specific individual, time, or combination of the previous.

3.2.7 Simplex Search Method

The Simplex Search Method is a direct deterministic local search method developed by Spendley, Hext, and Himsworth [127], and outlined in [128]. The simplex search method uses the idea of locally exploring a base point with a specific pattern. It defines the search direction of a N dimensional objective function by evaluating $N+1$ function values. When placing the $N+1$ points for obtaining the function values equidistantly to each other, they form a regular simplex. For example, the equilateral triangle (see Figure 3.4) is a simplex in two dimensions, and a tetrahedron is a simplex in three dimensions. In order to search for the minimum of the objective function, the values of the vertices are evaluated and the vertex with the highest values is reflected through the centroid of the remaining vertices as shown in Figure 3.4. As a result, a new simplex is created and the process is continued until the algorithm to stalls due to either the same vertex to be reflected back and forth for a certain amount of iterations (cycling) or the minimum is straddled. In case of cycling, the size of the simplex can be reduced to allow smaller steps, or if straddling occurs, the second highest function values is used in the reflection to form the new simplex, or the algorithm is terminated. Termination criteria may be a limited number of iterations, smallest simplex size, or the standard deviation of the function values at the vertices gets small enough. Further details are provided in [128]. Overall, the simplex search method is very efficient in searching for local optimal solutions and will be used in the following chapter to improve the final solution of the Genetic Algorithm.

3.3 Structural Optimization of Ultrasonic Cutting Knives

Some parts of the following content have been published by the author in [B.iv]. In order to efficiently optimize the structure of ultrasonic cutting knives, the optimization procedure with respect to the Three-Columns Concept (Figure 3.2) needs to be defined. First, a structural model is created in section 3.3.2, which can be changed with specific

design variables. Next, the optimization model is set up by calculating the fitness function resulting from the analysis of the structural model (section 3.3.4). Finally, an optimization algorithm is chosen to perform the optimization (section 3.3.5).

The methodology for structural optimization of ultrasonic devices is shown in Figure 3.5. It starts with the decision maker's initial design, which is based on a basic guess on physical performance, specific boundary conditions, and operative requirements. The initial design is then parameterized according to eligible structural variations that are also selected by the decision maker. Thus, a changeable structure is created with parameters determining each possible solution. Next, the optimization algorithm is set up with respect to the optimization problem. Since the decision maker does not know more than the initial design (as explained later), the Genetic Algorithm is used. To start the optimization, the decision maker provides an initial guess on the parameter values and defines how the fitness function is calculated. Through the FEM analysis, the physical performance of the structure is assessed. It should be pointed that out that the FEM solution is not based on the static analysis of the structure, but rather on a quasi-static nodal solution from the dynamic analysis, such as modal analysis or harmonic analysis. However, a static analysis may be included if required by the fitness function. From the results of the FEM analysis, the fitness function of the tested structure is determined, which is then used by the optimization algorithm to guide the optimization. Once the genetic algorithm stops the optimization, because one of the termination criteria is met, the best solution is returned. Since the genetic algorithm is used as a global search method, but minor changes of the parameter values may have a significant influence on the dynamic characteristics of the solution, a local search with the simplex method is done based on the best solution from the genetic algorithm. The simplex search creates a simplex around the input solution and performs its operations with very small changes to the parameter values. Finally, the best solution is returned to the decision maker, who then has to experimentally verify it.

The previous described methodology can be implemented with the help of MATLAB and ANSYS. A procedure similar to [129] is used. The optimization algorithm is provided by MATLAB, while ANSYS performs the necessary FEM calculations based on an input file created by MATLAB and passes an output file back to MATLAB, which is then used for the fitness function.

3.3.1 Starting Designs

The decision maker derived the starting designs for two ultrasonic cutting knives based on known shapes and their physical properties. The starting design for the asymmetrical cutting knife using a longitudinal resonance mode for operation is based on the design of symmetrical ultrasonic cutting knives. Symmetrical cutting knives are basically a series of bars (can be calculated as in Appendix A.10) with a longitudinal vibration mode, connected at specific points. This is done by regularly cutting elongated holes into the knife along its width. An example for a longitudinal mode is shown in Figure 3.6. Since an asymmetrical cutting knife is not symmetric in two planes as it is with symmetrical knives, the starting design will be made up from four elongated holes and variational thickness on one side (the plane side of the asymmetrical knife is obviously kept plane). It will be symmetrical along the plane perpendicular to the width of the knife.

The starting design for the symmetrical cutting knife using a higher order bending mode is based on the bending mode of a bar as shown in Figure 3.6. When stacking

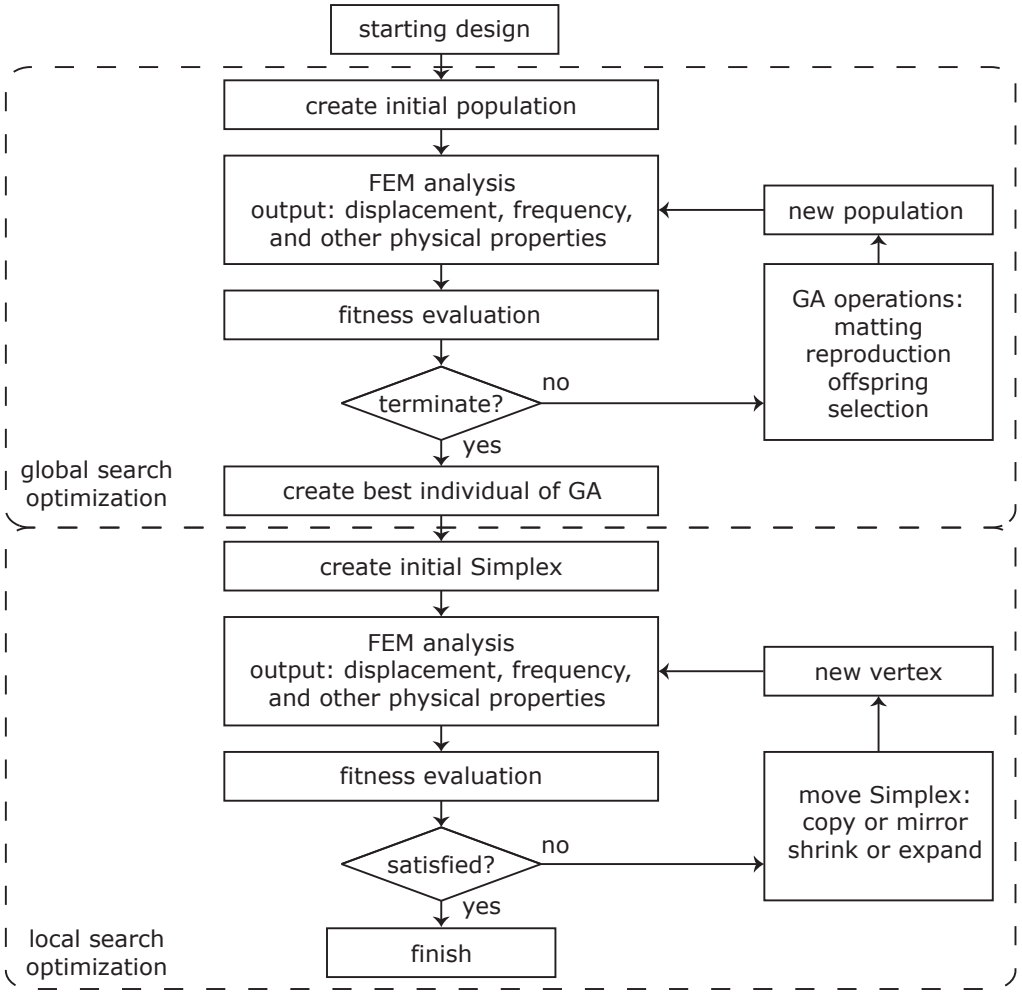

Figure 3.5: Methodology for shape optimization of ultrasonic devices. Global and local search methods are used to replace the intuitive design strategy as shown in Figure 3.1. The nodal results of the FEM analysis are evaluated by a set of fitness functions, in order to find the most appropriate design.

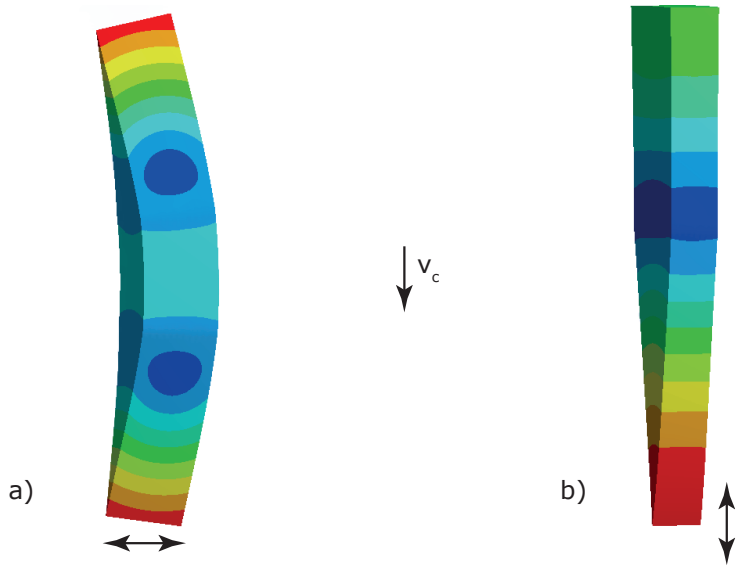

Figure 3.6: Principle idea for the starting designs: a) Bending mode that can be used for lateral vibration while cutting; b) Longitudinal mode used for longitudinal vibration while cutting. Colors show total displacement of the resonance mode with blue being the lowest and red the highest amplitude.

several bars and connecting them at specific points, a bending mode across the width of the cutting knife can be obtained. This is done by placing elongated holes along the width of the knife. To ensure a proper bending mode operation, this cutting knife will be symmetrical along three planes resulting in two cutting edges. Schematic diagrams of both knives are shown in the next section.

3.3.2 Parameterization of Device Shape (Genotype)

As explained earlier, the design that shall be optimized needs to be parameterized in order to allow adjustments of specific structural parts. Through variables, the structure can take on various solutions that will be used by the optimization algorithm. There are three basic types of variables in shape optimization: bits, real numbers, and combination of the previous. While bit variables allow certain structural components to be simply placed and removed, real number variables allow components to be changed in size, length, or any other geometrical definition. Bit variables take on either the 0 or 1 value, and real number variables take on any number within a specified range. To begin with the optimization loop, the structural model is defined. Here, two types of ultrasonic cutting knives are parameterized to allow specific design variables (genes) to change the physical properties (phenotype) of the knives. Design variables are chosen by the decision maker based on eligibility to change the geometric shape without violating application essential boundary conditions, such as cutting angle, threads, mounting size, etc. Material properties are tightly fixed to the application and will therefore not be changed.

Regarding the cutting knife for lateral ultrasonic vibration assisted cutting, the structure is parameterized as shown in Figure 3.7. The basic idea of this type of structure is to create lateral ultrasonic vibrations along the cutting edge. A longitudinal excitation

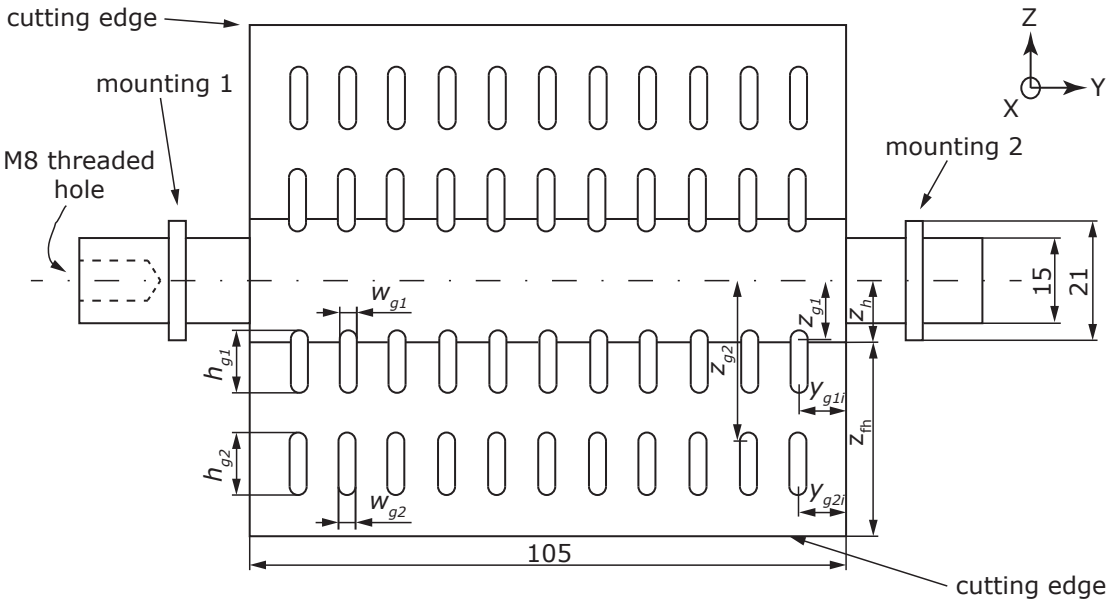

Figure 3.7: Parameterization of the symmetrical ultrasonic cutting knife with lateral vibration. Parameters used by optimization algorithm to alter the structure are shown.

is fed in along Y-direction (M8 threaded hole), which results in a higher order bending mode. Through the strategic placement of elongated holes perpendicular to the cutting edge, the structure is made pliable along the Y-direction. Thus, the entire structure will obtain an almost uniform bending mode with maximum amplitude at the cutting edge. To appropriately mount the knife, the two mounting rings are used to fix it. To find the proper structure with such a uniform bending mode, there are seven parameters that may be altered by the optimization algorithm. These are partial height of the structure (z_h), positions of the rows of elongated holes (z_{g1}, z_{g2}), and height (h_{g1}, h_{g2}) and width (w_{g1}, w_{g2}) of the holes. Since the cutting angle is $\beta = 24°$, the height of the cutting edge (z_{fh}) depends on the width of the cutting knife (for this specific knife a width of 15 mm is chosen). Therefore, the total height of the structure is $z_h + z_{fh}$. The number of holes per row are not altered for this optimization, but kept constant. However, the number of holes effects the uniformity of the lateral displacement at the cutting edge depending on its length. The entire structure is symmetrical along the X-Y-plane (= two cutting edges) and X-Z-plane (except for the cylindrical connections).

For the cutting knife for longitudinal ultrasonic vibration assisted cutting, the structure is parameterized as shown in Figure 3.8. The basic idea of this structure is more complex than the previous one. The longitudinal mode is created by exciting the structure in Z-direction (M8 threaded hole). The parameters for the optimization are chosen based on the boundary conditions of the application. Since this cutting knife is used for asymmetrical cutting of workpieces, one side of the knife needs to be flat. Thus, the opposite side may be used for structural modifications. This is done by point-wise changing the thickness ($x_{101}, ..., x_{606}$) of specific points, which are used as keypoints for connecting splines. In addition, the segmented height of the knife (z_{hi}), y-z-positions ($y_{g1}, y_{g2}, z_{g1}, z_{g2}$) of four elongated holes, and their width (w_{g1}, w_{g2}) and height (h_{g1}, h_{g2}) can be altered by optimization algorithm. The height z_{be} is kept constant at 14 mm to allow proper displacement

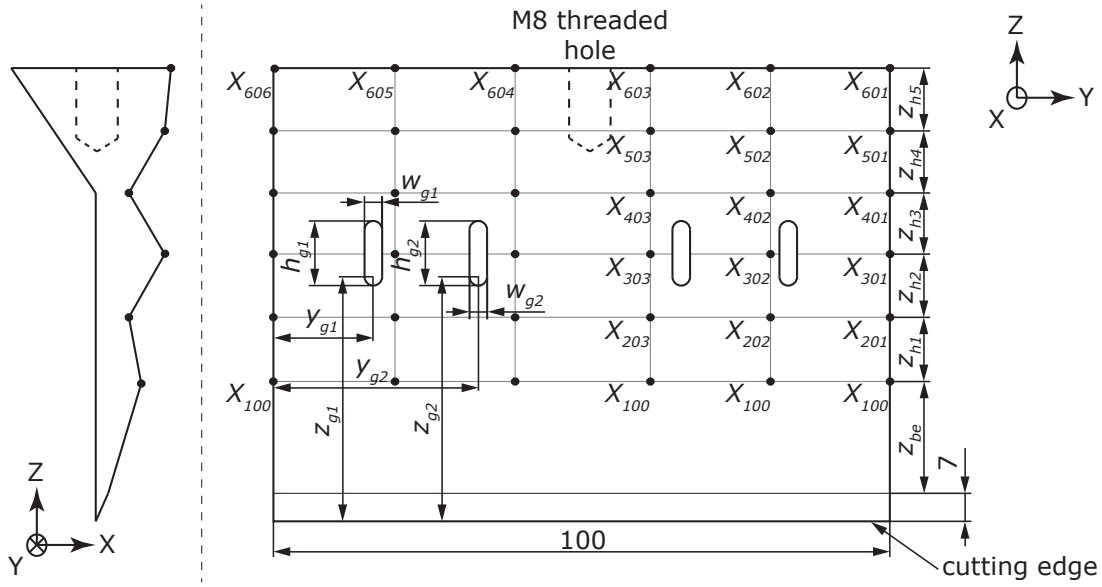

Figure 3.8: Parameterization of the asymmetrical ultrasonic cutting knife with longitudinal vibration. Parameters used by the optimization algorithm are shown.

of the cut material. The entire structure is only symmetrical along the X-Z-plane.

3.3.3 Material Parameters

The material used for the cutting knives is 1.2379 tool-steel (X155CrVMo12-1). It is crucial to match the appropriate material properties to the material used in the FEM simulation of the optimization. For example, if the Young's modulus is set as $E = 200\,\mathrm{GPa}$ instead of $E = 210\,\mathrm{GPa}$, the resonance frequency goes up about 850 Hz when solving for a rod. Here, the following material parameters are used: Young's modulus is set as $E = 210\,\mathrm{GPa}$, density $\rho = 7850\,\mathrm{kg\,m^{-3}}$, Poisson ratio of 0.3, and damping ratio of 1 %.

3.3.4 Fitness Functions

For designing the structure of the ultrasonic cutting knives, the FEM results of a modal analysis and harmonic response analysis are evaluated based on the displacements of the nodes at the specific structure parts and the respective resonance frequency. Since nodal displacements are used to visually inspect the mode shape (see Figure 3.1), they will be used here to mathematically characterize the mode shape by describing the nodal motion at specific areas of the structure.

First, the longitudinal mode of a cutting knife is optimized. The z-direction is the cutting direction, thus the longitudinal mode will occur in z-direction. Therefore, the global fitness function is made up from the following set of dimensionless functions. At the cutting edge, the displacement resulting from the vibration mode should occur in z-direction, while the displacements in y-direction and x-direction should be minimal. This

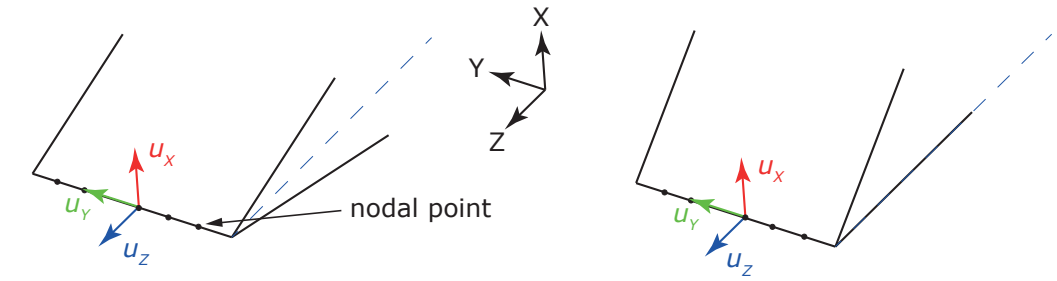

a) symmetrical cutting edge b) asymmetrical cutting edge

Figure 3.9: Nodal displacements at the cutting edge.

is obtained through the sum of the displacements as

$$f_1 = \frac{\sum_{i=0}^{n} |u_{xi}| + \sum_{i=0}^{n} |u_{yi}|}{\sum_{i=0}^{n} |u_{zi}|} \stackrel{!}{=} min \tag{3.5}$$

where u_x is the nodal displacement in x-direction, u_y is the nodal displacement in y-direction, and u_z is the nodal displacement in z-direction for n number of nodal points along the cutting edge. With this function, undesired solutions will have a higher fitness value than the longitudinal mode. To ensure an even displacement across all nodes at the functional area, the cutting edge, the sum of difference between the displacement of a single node and the average displacement in z-direction. This is stated by

$$f_2 = \frac{\sum_{i=0}^{n} (|u_{zi}| - |\bar{u}_z|)}{|\bar{u}_z|} \stackrel{!}{=} min \tag{3.6}$$

with

$$\bar{u}_z = \frac{1}{n} \sum_{i=0}^{n} u_{zi} \tag{3.7}$$

being the average displacement in z-direction. When using a frequency specific generator to excite the transducer at a given frequency, the cutting knife should have the correct resonance mode near the operating frequency. This condition is stated by

$$f_3 = \frac{|\omega_s - \omega_t|}{\omega_t} \stackrel{!}{=} min \tag{3.8}$$

where ω_s is the frequency of the mode and ω_t is the targeted frequency, which is 35 kHz for this ultrasonic device.

Second, the mode shape for exciting the cutting edge in lateral direction needs to be found. Here, the lateral direction is in y-direction, thus equations (3.5), (3.6), and (3.7)

are rewritten to

$$f_1 = \frac{\sum_{i=0}^{n} |u_{xi}| + \sum_{i=0}^{n} |u_{zi}|}{\sum_{i=0}^{n} |u_{yi}|} \stackrel{!}{=} min \tag{3.9}$$

$$f_2 = \frac{\sum_{i=0}^{n} (|u_{yi}| - |\bar{u}_y|)}{|\bar{u}_y|} \stackrel{!}{=} min \tag{3.10}$$

$$\bar{u}_y = \frac{1}{n} \sum_{i=0}^{n} u_{yi} \tag{3.11}$$

Equation (3.8) is kept the same for the second optimization. Finally, the complete fitness function is obtained by adding the separate fitness functions

$$f = \sum_{i=1}^{3} \Psi_i f_i \stackrel{!}{=} min \tag{3.12}$$

Even though the fitness functions are dimensionless, the value ranges of each fitness function are slightly different. Value ranges have an impact on the optimization, because large changes to the fitness functions are prioritized. To equalize the value ranges and control the relevance of each function, a penalty factor Ψ is introduced. Here, the penalty factors are chosen as $\Psi_1 = 100$, $\Psi_2 = 10$, and $\Psi_3 = 100$ for both structural optimizations.

3.3.5 Optimization Algorithm

As discussed earlier, the optimization algorithm is picked according to the optimization model and overall problem by the decision maker. It requires to have a general idea about the design space and fitness function. Regarding the so far presented structural optimization, the optimization algorithm has to be suitable for the following criteria:

- There is no information about the gradient of the previously stated fitness function. The search direction has to be picked randomly.
- The initial design is defined by boundary conditions, but values are picked randomly, because the decision maker does not know where to start.
- The fitness function is globally discontinuous, because it changes with the values of the displacements and frequency, which are dependent on the response of the structure. This response can be very different for neighboring solutions. For example, a longitudinal mode will have neighboring bending modes.
- Small changes in the structure can also be continuous regarding changes in displacements and frequency. This is obvious when examining a longitudinal mode that is near its resonance frequency. For example, a rod with its length close to the calculated length for its longitudinal mode (see Appendix A.10) will show the appropriate displacements in the harmonic analysis but incorrect frequency in the modal analysis. Thus, very small adjustments of the design variables is necessary.

- The sensitivity of each design variable is different.
- A good known solution can help guide the search towards better solutions.

It becomes clear that a global search method and a subsequent local search method are most suitable for these kind of problems. Using good known and randomly new picked solutions to guide the optimization is the most appropriate approach in this case. Hence, Genetic Algorithms followed by Simplex Search Method are used by the decision maker. It should be pointed out that other global search methods such as Simulated Annealing or Swarm Optimization are also very suitable. As discussed in the no free lunch theorem, a purely stochastic search, such as the Monte Carlo simulation, will also provide good solutions, but the knowledge from past iterations is not used. In the following section, the settings and functions used in the genetic algorithm is explained.

3.3.6 Genetic Algorithm and Simplex Search Settings

The two step structural optimization starts with the Genetic Algorithm (GA) and is followed by the simplex method. Each of the two optimization algorithms has separate settings for the search. Especially the GA provides a great variety of search parameters that all impact the performance of the algorithm. The GA of MATLAB is used for the optimization and is set up as following:

- Initial Population is picked randomly within the value range of each parameter.
- Maximum Generation Size is 20 for the lateral cutting knife optimization and 60 for the longitudinal knife optimization.
- Population Size is 200 for the lateral cutting knife optimization and 1200 for the longitudinal knife optimization to allow great variety among children.
- Four Elite Children will be copied from one generation to the next generation. With this, the four best solutions will be kept from one generation to the other.
- Parents are chosen using stochastic universal sampling, with more fit parents having a better chance of being picked.
- 40 % of the children are obtained through mutation and the remaining 60 % from crossover (reproduction).
- Mutation is done using uniform mutations at multiple points at the genotype. Mutated genes are uniformly distributed over the defined range. If a mutant does not meet the inequality constraints, it is discarded and the mutation is repeated.
- The crossover fraction is 0.3 and reproduced children are created as the weighted arithmetic mean of two parents.
- Terminating Conditions: If the cumulative change in the fitness value does not change at least $1.0 \cdot 10^{-4}$, or the maximum of generations is reached, or no change in the fitness value (stall) is observed for 10 successive generations.

When considering the parameterization of the lateral vibration cutting knife (Figure 3.7), it becomes clear that there are some structural configurations that are unwanted or illegal. In order to keep the optimization algorithm search within a legal search space, the following constraining functions are defined. The rows of holes may not be at or closer than 4 mm to the cutting edge, as stated by

$$-z_h + z_{g1} + 0.5w_{g1} + h_{g1} \leq \frac{x_t}{\arctan\beta} + 4 \tag{3.13}$$

and

$$-z_h + z_{g2} + 0.5w_{g2} + h_{g2} \leq \frac{x_t}{\arctan\beta} + 4 \tag{3.14}$$

Since the cutting knife is symmetrical, the rows of holes should not overlap as defined by

$$-z_{g1} + w_{g1} \leq 0 \tag{3.15}$$

and

$$-z_{g2} + w_{g2} \leq 0 \tag{3.16}$$

Lastly, the rows on each side should not overlap each other, thus z_{g2} shall always be larger than the first row position and length, as stated by

$$z_{g1} + 0.5w_{g1} + h_{g1} - z_{g2} \leq 1 \tag{3.17}$$

The value 1 is used here to avoid unnecessary small mesh elements between the rows of holes, but 0 would be mathematically correct as well. Regarding the cutting knife for longitudinal vibration, a similar set of equality constraints need to be defined.

$$\begin{aligned} y_{g1} + 0.5w_{g1} - y_{g2} + 0.5w_{g2} &\leq 0 && (3.18)\\ z_{g1} + w_{g1} + h_{g1} - (z_{be} + 5z_h + 7) &\leq 0 && (3.19)\\ z_{g2} + w_{g2} + h_{g2} - (z_{be} + 5z_h + 7) &\leq 0 && (3.20)\\ x_{100} - (z_{be} + 7)\tan\beta &\leq 0 && (3.21) \end{aligned}$$

Next, the parameter range for each knife structure is defined. Each parameter may be altered by the optimization algorithm within the specified range. For the lateral vibration knife, Table 3.1, and for the longitudinal vibration knife, Table 3.2 list the parameters and their ranges.

3.3.7 Results

The results of the structural optimization are shown in Figure 3.10 and Figure 3.11, with the development of the GA fitness functions shown in Figure 3.12. Amplitude values are not listed, because the results are from the modal analysis and therefore unrealistic. Regarding the total nodal displacement visible in the solutions, it is shown that the optimization methodology seems to work very well. Figure 3.10 shows the lateral motion at the cutting edge, which allows the designed geometry to be used for lateral ultrasonic vibration assisted cutting. However, the amplitude along the cutting edge is not completely uniform. This could be solved by increasing the number of holes per row, while sacrificing the stability of the knife. Figure 3.11 shows the longitudinal motion at the cutting edge, which enables

Parameter	Value Range	Unit
z_h	[7.5 ; 30]	[mm]
z_{g1}	[20 ; 200]	[mm]
z_{g2}	[0 ; 40]	[mm]
w_{g1}	[2 ; 5]	[mm]
w_{g2}	[2 ; 5]	[mm]
h_{g1}	[5 ; 16]	[mm]
h_{g2}	[5 ; 16]	[mm]

Table 3.1: Parameters defining the shape of the knife for lateral vibration and their value range. Mounting width and relative height are $3\,\mathrm{mm}$.

Parameter	Value Range	Unit
z_{hi}	[7 ; 15]	[mm]
z_{g1}	[18 ; 80]	[mm]
z_{g2}	[18 ; 80]	[mm]
y_{g1}	[10 ; 40]	[mm]
y_{g2}	[10 ; 40]	[mm]
w_{g1}	[2 ; 5]	[mm]
w_{g2}	[2 ; 5]	[mm]
h_{g1}	[5 ; 16]	[mm]
h_{g2}	[5 ; 16]	[mm]
x_{100}	[14 ; 19]	[mm]
$x_{201} - x_{303}$	[5 ; 19]	[mm]
$x_{401} - x_{502}$	[5 ; 19]	[mm]
x_{503}	[11 ; 19]	[mm]
$x_{601} - x_{602}$	[5 ; 19]	[mm]
x_{603}	[14 ; 19]	[mm]

Table 3.2: Parameters defining the shape of the knife with longitudinal vibration and their value range.

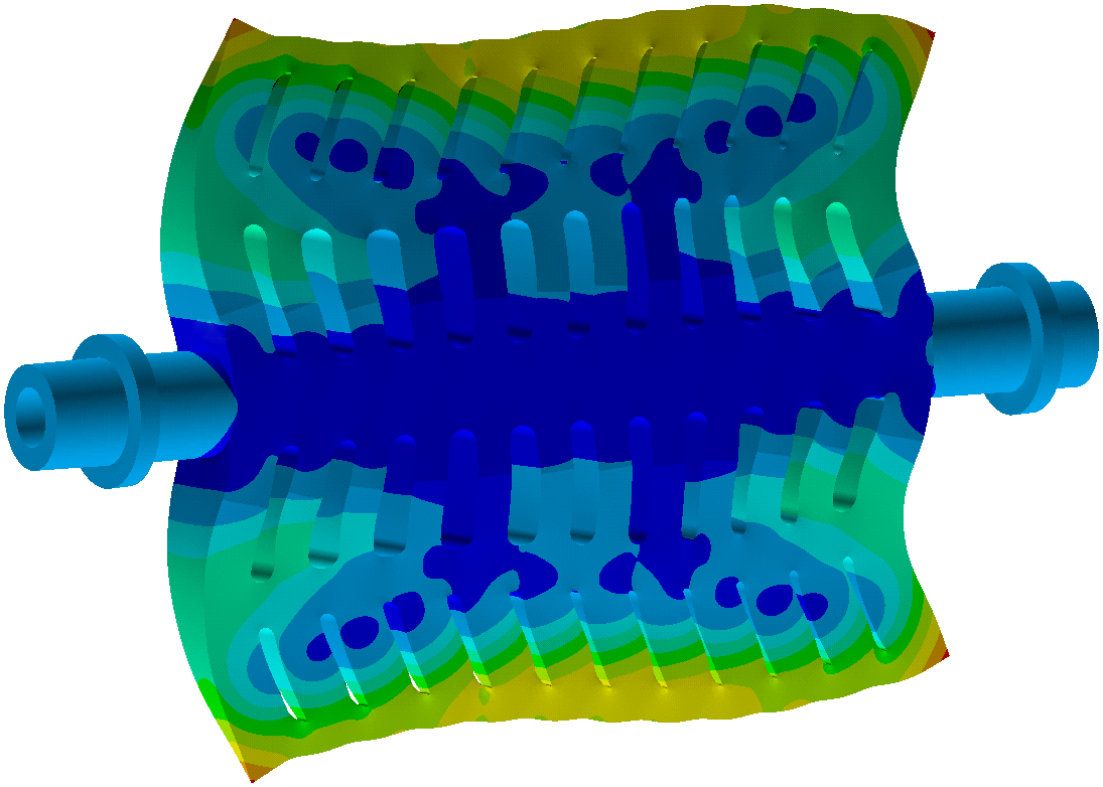

Figure 3.10: Solution for the cutting knife for lateral ultrasonic vibration assisted cutting. 11 holes per row. Colors indicate total nodal displacement for the mode shape (modal analysis) with dark blue being the lowest value ($3.6\,\mu m$) and orange the highest ($28.3\,\mu m$), with linear distribution between.

the designed geometry to be used for longitudinal vibration assisted cutting. Here, the amplitude is also not completely uniform across the cutting edge and a slight bending mode is visible. Due to the very complex design requirements of this cutting knife, improvement is very limited.

Additional CAD renderings of the found solutions can be found in Appendix A.12.

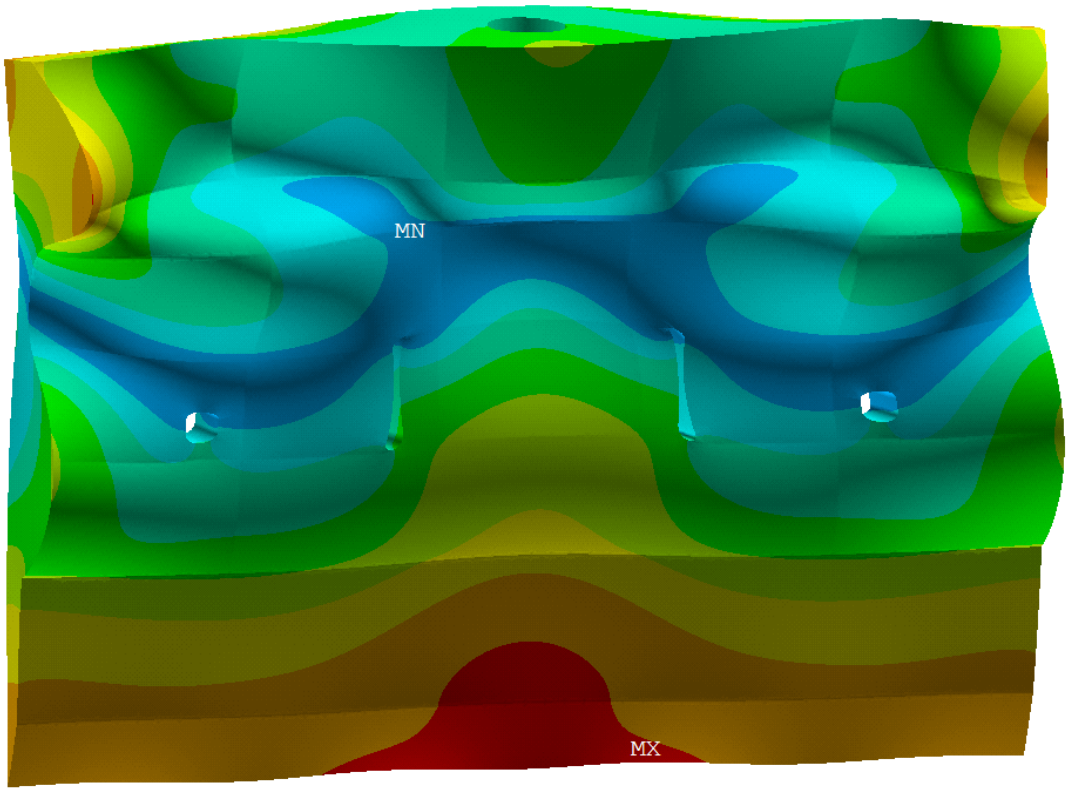

Figure 3.11: Solution for the cutting knife for longitudinal ultrasonic vibration assisted cutting. Colors indicate total nodal displacement for the mode shape (modal analysis) with blue being the lowest value ($6.84\,\mu m$) and red the highest ($83.76\,\mu m$), with linear distribution between.

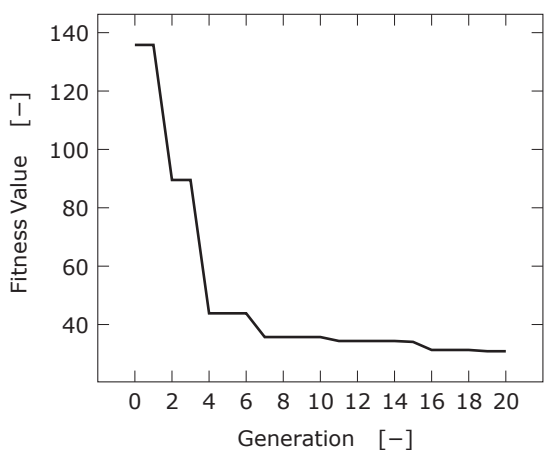

(a) Fitness function from the GA optimization of the lateral ultrasonic vibration assisted cutting knife.

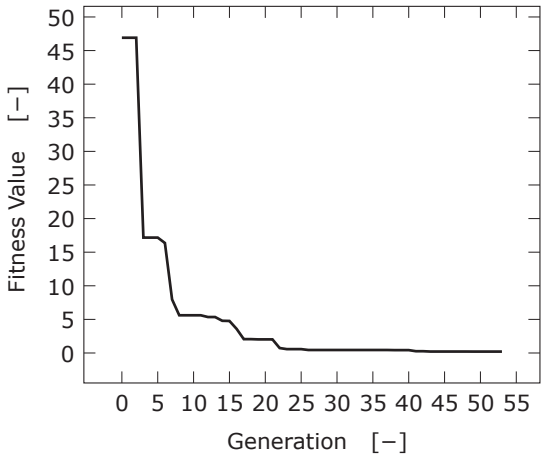

(b) Fitness function from the GA optimization of the longitudinal ultrasonic vibration assisted cutting knife.

Figure 3.12: Fitness functions of the GA optimizations.

4 Models of Vibration Assisted Guillotining of Stacks

In this chapter, a dynamic model regarding the longitudinal vibration assisted guillotining of stacked thin material and a quasi-static energy based analytical model regarding the lateral vibration assisted guillotining of stacked thin material are developed. The dynamic model is one-dimensional and assumes the paper material to fail at a specific cutting force. Empirically determined material parameters represent the stack. From its interaction with the applied load from the cutting knife, the dynamic behavior during longitudinal vibration assisted cutting and the resulting cutting forces are analyzed. Cutting forces and friction forces are not separately discussed.

In regard to lateral vibration assisted cutting, cutting forces and friction forces in vertical and slicing (lateral) direction are derived. The analytical model assumes that material failure occurs at a constant specific energy (work). This specific energy is provided by the combination of slice-push cutting. Total observed cutting forces are the sum of the specific cutting force and friction force. Since the cutting tool may never separate from the workpiece, no dynamic model is necessary. Thus, the energy based model is purely analytical and sufficiently represents the slice-push cutting process.

Both models only focus on the interaction between cutting tool and workpiece. Hence, only the cutting edge of the tool is relevant for the following considerations. The previously optimized tools are later used for the experimental model verification.

4.1 Observed Cutting Forces for Longitudinal Vibration Assisted Cutting

Prior to going into details of modeling the dynamic behavior of the stacked thin material to completely calculate cutting forces, an analytical approach is made. First, the dynamics of the used force sensors is discussed. With that information, the theoretical forces of longitudinal vibration assisted cutting are determined. Consequently, the need for an dynamic model for longitudinal vibration assisted cutting will become apparent.

4.1.1 Stack and Force Sensor Behavior

Before interpreting the measurement data from the force sensor, the frequency response needs to be investigated. To accomplish this, the following procedure was carried out: conducting an experimental modal analysis, identifying the transfer function of the system, and mathematically model how the measurement data is recorded by the sensor. The system that needs to be identified is the stack on top of the sensors with excitation at the knife contacting the stack. It is of main interest, because the cutting force at the top sheet

Parameter	Value
K_p	1
T_w	0.0037
ς	0.32

Table 4.1: Parameters for the identified transfer function of the paper stack.

is here equivalent to the input of the system, and the force acting upon the force sensor is the equivalent to the output of the system. Figure 4.1 shows the schematic measurement setup for the experimental modal analysis. The cutting knife is in contact with the precut stack, but only pushes down with its weight (approx. 10 N). For stability, it is handheld during the experiments. Thus, damping values will be higher than they actually are. Stack total height is 50 mm, and it is partially cut by 20 mm. Figure 4.2 shows the system response, Nyquist plot, and Bode plot. Assuming the surrounding structure as perfectly rigid, it becomes clear that it may be regarded as a second order system. Thus, the transfer function is derived as

$$\mathcal{X}(s) = \frac{K_p}{1 + 2\varsigma T_w s + (T_w s)^2} \tag{4.1}$$

where K_p is the gain, T_w is the period of the resonance frequency, and ς is the damping coefficient. Table 4.1 lists the values for the transfer function found through system identification. With these values, a theoretical second order system may be simulated. Since the transfer function is now known, the output of the system at a given input may be calculated, as it is done in the next section. The general equation is

$$F_S(s) = \mathcal{X}(s)O(s) \tag{4.2}$$

where F_S is the output of the system, and $O(s)$ is the input of the system in the frequency domain.

As the cutting process progresses, the stack changes as a system up to the point where it disappears and the oscillating knife directly impacts the force sensors. Thus, an experimental modal analysis of the force sensor is also necessary. Figure 4.3 shows the system response of the force sensors without stack or knife (for experimental reasons, the knife was removed, because it is still regarded as perfectly rigid). From the experimental data, the system including the sensors can no longer be easily identified, nor can be it be regarded as perfectly rigid. However, it is assumed that it behaves as a second order system as well.

4.1.2 Parallel Vertical Cutting with Longitudinal Vibration

The cutting force for guillotining with longitudinal vibration can be simply calculated from equation (2.1). With the findings presented in section 2.5.1, and assuming an ideal rigid-plastic material for the workpiece, the cutting force in vertical direction for an asymmetrical cutting knife becomes

$$F_C = \begin{cases} e_{fr} w + F_F \sin\beta & \text{if tool in contact with workpiece during } t_c \\ 0 & \text{if tool out of contact with workpiece during } (T - t_c) \end{cases} \tag{4.3}$$

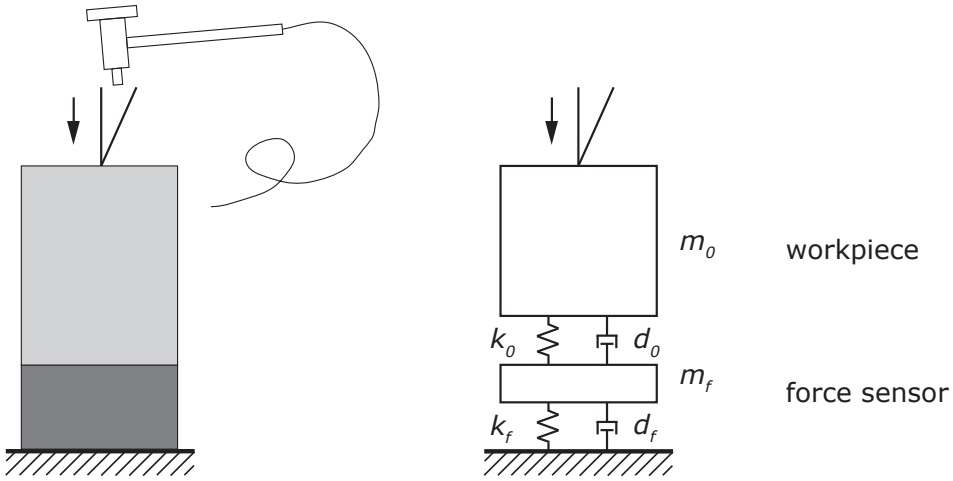

Figure 4.1: Schematic experimental setup for determining the dynamic behavior of the sheet stack. Excitation is initiated at the top of the cutting knife, which is handheld during the experiment.

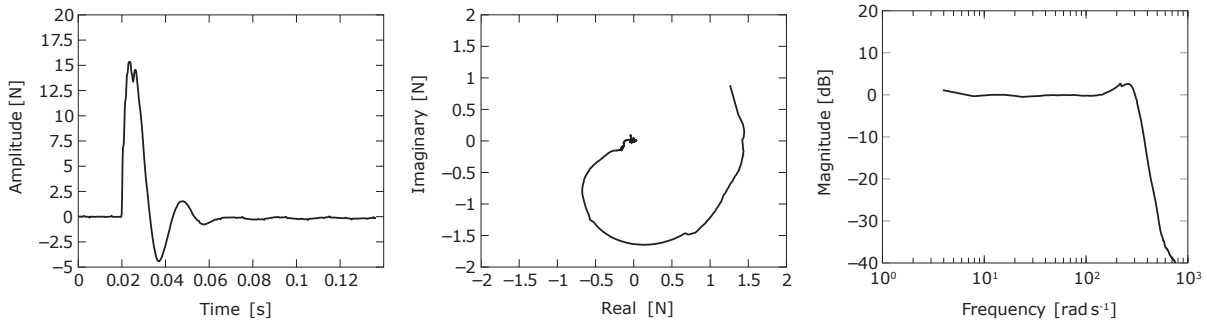

(a) System Response. **(b)** Nyquist. **(c)** Bode.

Figure 4.2: Dynamic Response of the Stack as determined through the system response analysis.

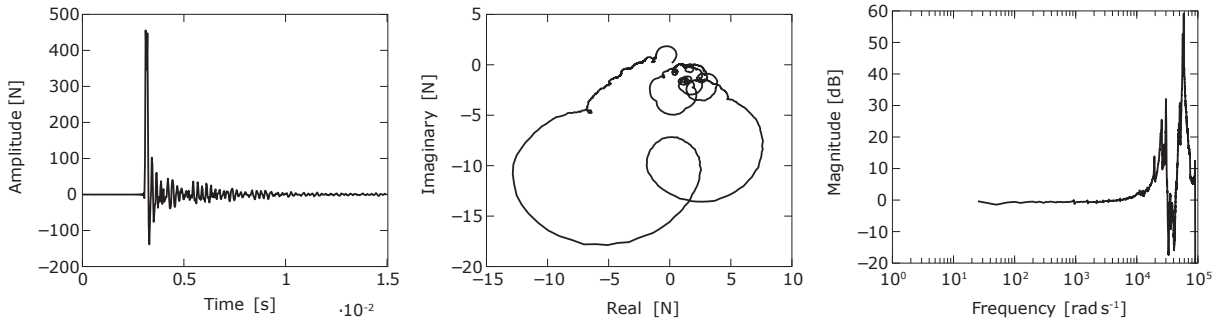

(a) System Response. **(b)** Nyquist. **(c)** Bode.

Figure 4.3: Dynamic Response of the Force Sensor as determined through the system response analysis.

where F_F is the friction force solely on the cutoff side. However, the measured cutting force may not represent the true cutting force at the cutting edge. Hence, the previously describe model of the force sensor is used to calculate the measured cutting force. Assuming a rectangular pulse force input represents the vibration assisted cutting of an ideal rigid-plastic material, the following considerations are made: A single rectangular pulse in the time domain is written as [130]

$$q(t) = a_P(\Lambda(t)) \tag{4.4}$$

with

$$\Lambda(t) = \begin{cases} 1 & \text{if} \quad 0 < t \leq t_c \\ 0 & \text{else} \end{cases} \tag{4.5}$$

where a_P is the input amplitude, and T is the period of the pulse. Periodically occurring rectangular pulses as shown in Figure 4.4 are written as

$$o(t) = \sum_{n=0}^{\infty} q(t - nT) \tag{4.6}$$

in the time domain. As stated before, the output of a system depends on the input and transfer function, hence

$$F(t) = \mathcal{X}(s)O(\omega t) \tag{4.7}$$

It becomes clear that for an input containing a series of pulses, the output of the second order system depends on its dynamic parameters. To give a rough estimate of what the output of a given system results in the time domain, the periodically occurring rectangular pulses or pulse wave are transformed with the Fourier series expansion (see A.2). The Fourier series expansion of a pulse wave is

$$\hat{o}(t) = \mathcal{F}(o(t)) = a_P \left(\frac{t_c}{T} + \sum_{n=1}^{\infty} \frac{2}{n\pi} \sin\left(\frac{\pi n t_c}{T}\right) \cos\left(\frac{2\pi n}{T} t\right) \right) \tag{4.8}$$

With the theory of the frequency response of an asymptotically stable system [131, 132], equation (4.8) allows the output $F(t)$ to be expressed as

$$F(t) = a_P \left[\frac{t_c}{T} \mathcal{X}(j0) + \sum_{n=1}^{\infty} \frac{2}{n\pi} \sin\left(\frac{\pi n t_c}{T}\right) \left| \mathcal{X}\left(j\frac{2\pi n}{T}\right) \right| \cos\left(\frac{2\pi n}{T} t + \angle \mathcal{X}\left(j\frac{2\pi n}{T}\right)\right) \right] \tag{4.9}$$

where j is the imaginary unit, $||$ indicates the amplitude of the transfer function, and $\angle$ indicates the phase of the transfer function. Whether or not a specific frequency can be output by the system depends on the absolute value of $\mathcal{X}$. If

$$\left| \mathcal{X}\left(j\frac{2\pi n}{T}\right) \right| \ll 1 \tag{4.10}$$

the amplitude of the input frequency is much reduced at the output. Regarding the previously determined parameters of the second order system, for a very high input frequency, the output will simply become

$$F(t) \approx a_P \frac{t_c}{T} \mathcal{X}(j0) \approx a_P \frac{t_c}{T} \tag{4.11}$$

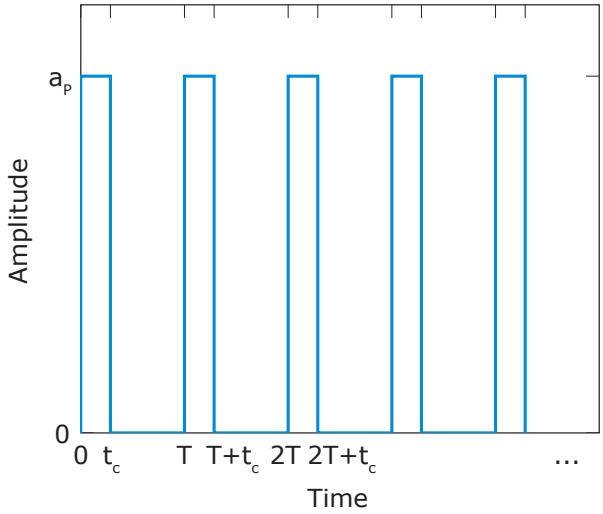

Figure 4.4: Periodically occurring rectangular pulses or pulse wave described by equation (4.6).

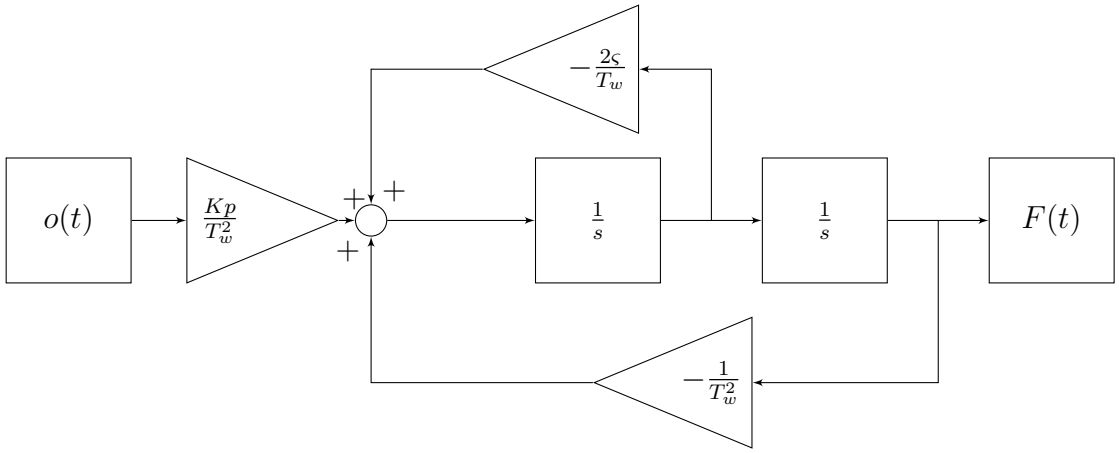

Figure 4.5: Block diagram of the Simulink model to determine the output of the second-order system at a periodic input.

Thus, it seems appropriate to use the average force resulting from measurements of high frequency loading when comparing results of the dynamic model to the experimental data. To test these findings, a simple model in MATLAB Simulink was created as shown in Figure 4.5. When using the parameters listed in Table 4.1, defining $\frac{t_c}{T} = 0.3$, and letting the knife oscillate at 35 kHz or 10 Hz, the dynamic behavior shown in Figure 4.6 can be seen. If the maximum force value is 1000 N, the average force becomes 300 N at high frequency after 40 ms. For 10 Hz the second order system does not decrease the input amplitude of the vibration, so the oscillating force is visible. It should be emphasized again that the input amplitude remains the same when oscillating at 35 kHz, but the input signal is not properly transmitted to the output and therefore an average value can be formed. Similar observations can be made, when simply holding an ultrasonic vibration assisted cutting device (e.g. scalpel, drill). The user's arm, as a second order system, filters out the high frequenting impacts and thus a lower force is felt.

However, the dynamic model does not discuss aa ideal rigid-plastic material, but rather a nonlinear elastic material. From [59] it is known that paper is actually nonlinear or-

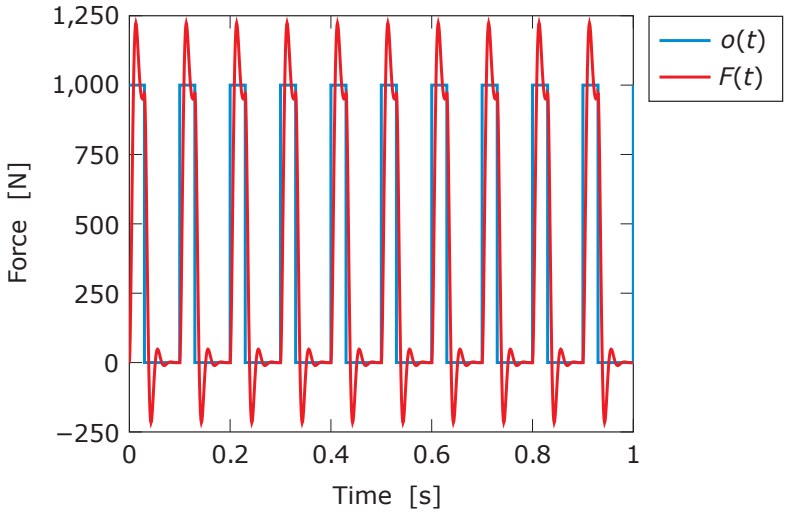

(a) $\frac{1}{T} = 1/10\,\mathrm{s}^{-1}$.

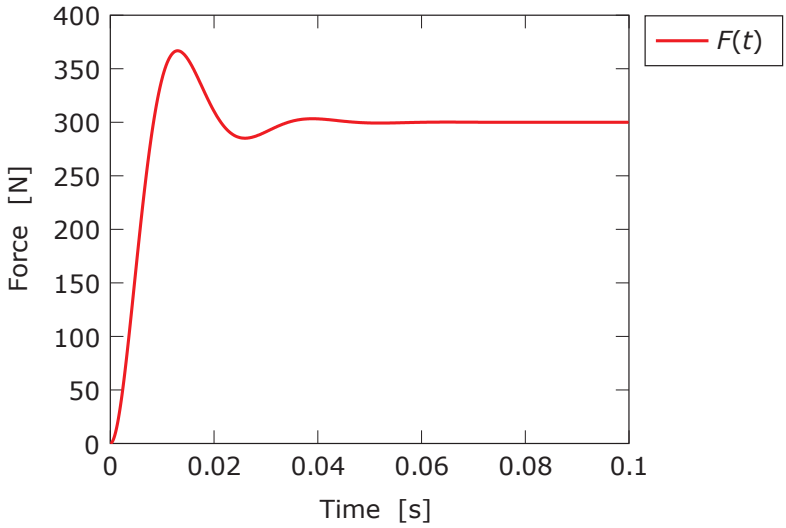

(b) $\frac{1}{T} = 1/35\,000\,\mathrm{s}^{-1}$.

Figure 4.6: Results from Simulink model (Figure 4.5) with Parameters taken from Table 4.1 and $\frac{t_c}{T} = 0.3$. Input is a square wave function with $0\,\mathrm{N}$ and $1000\,\mathrm{N}$.

thotropic material, but it is simplified to isotropic here. For the presented dynamic model, the force acting upon the cutting knife will be calculated from

$$F_R = \begin{cases} e_{fr}w & \text{if } F_C \geq e_{fr}w \quad \text{during } t_c \\ k(\varepsilon)\Delta u_z + d(\varepsilon)\Delta \dot{u}_z & \text{if } F_C < e_{fr}w \quad \text{during } t_c \\ 0 & \text{during } (T - t_c) \end{cases} \tag{4.12}$$

where $k(\varepsilon)$ is the stiffness of the stack, $d(\varepsilon)$ is the damping of the stack, and ε is the compression ratio of the stack. Friction is not separately addressed, here. This model and these parameters are discussed in details in section 4.2.

4.2 Dynamic Model - Basic Physical Characterization

Considering the discussion in the previous sections, it becomes clear that for longitudinal ultrasonic vibration assisted cutting, a more detailed model is necessary. To understand the effects of longitudinal ultrasonic vibrations when guillotining stacked thin materials, a physical model needs to be defined. Especially the discontinuous contact between a rigid blade and soft workpiece requires a detailed consideration of the contact and separation phases. With the force model and the previously discussed energy balances, the dynamic process of vibration assisted sheet cutting can be examined. The cutting of a stack of thin sheet material can be split up into three separate actions:

1. Compression of the stack
2. Cutting of the material once the specific cutting force is reached
3. Displacing of the cut material

Figure 4.7 shows the cutting process with these three separate actions of a stacked thin material. Therefore, the physical model will be subdivided into compression of the stack (dynamic characterization) and cutting of the sheets within the stack. The displacement phase is neglected. The previously introduced model of an ideal rigid-plastic material or the calculations of cutting forces for an elastic-plastic material (equation (2.41)) will not sufficiently model the stack of thin material. To better characterize the dynamics of the stacked thin material, a system of serial stringed mass-spring-dampers is introduced as model for the behavior of the stack. A definition of how a single sheet of paper is cut allows the model to simulate the cutting process. Stiffness and damping values are then taken from experiments and are used in the dynamic model to properly represent the material behavior. The dynamics of the model are discussed to highlight the specific dynamic behavior occurring during vibration assisted cutting. Finally, the simulated compression ratio and the resulting stiffness and damping values during the simulation are identified, to give a clear indication on the effects occurring in longitudinal vibration assisted cutting.

4.2.1 Cutting Knife Motion

A simple asymmetrical blade, represented by a point of motion, cuts into the stack. It starts with an initial free space between the cutting edge and top sheet of the stack, and moves downwards into the stack. The knife's motion will be translated into an external

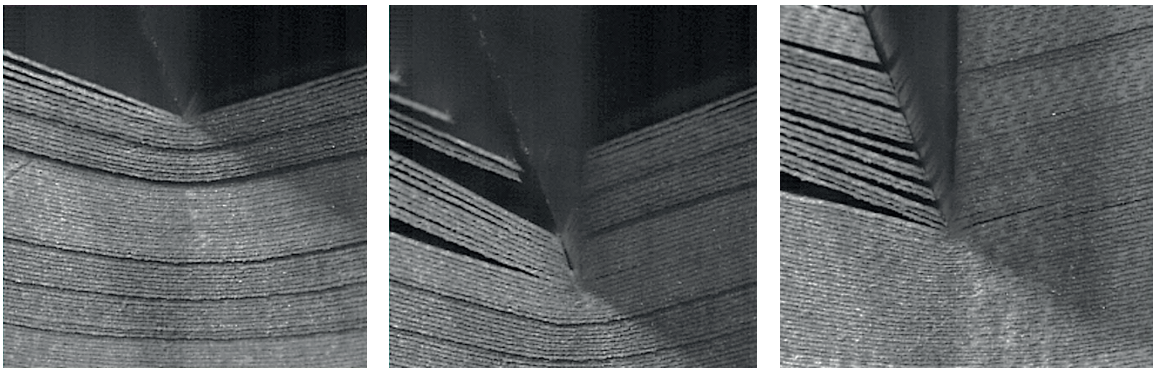

Figure 4.7: Freeze frames from high-speed video recording. Visible from left to right are the three separate actions when cutting a stack of thin paper material.

force once it is in contact with the stack (see next sections). The movement, velocity, and acceleration of the cutting knife are expressed by

$$z_b = v_c t + a_v \sin(\omega t) \tag{4.13}$$

$$\dot{z}_b = v_c + \omega a_v \cos(\omega t) \tag{4.14}$$

$$\ddot{z}_b = -\omega^2 a_v \sin(\omega t) \tag{4.15}$$

The cutting edge angle ($\beta = 24°$), which is irrelevant to this simulation, will be regarded as infinitely long.

4.2.2 Representation of the Paper Stack

A discrete serial stringed mass-spring-damper system with external forces is used to model the paper stack. Each individual mass-spring-damper system represents one single sheet of the stack as shown in Figure 4.8. Hence, the stack and its sheets are modeled according to the Kelvin-Voigt material model [133, 134]. The stiffness and damping of the paper sheets depend on the compression or position of the top sheet. With the differential ordinary equation

$$\boldsymbol{M}\ddot{\boldsymbol{u}}(t) + \boldsymbol{K}(\varepsilon)\boldsymbol{u}(t) + \boldsymbol{D}(\varepsilon)\dot{\boldsymbol{u}}(t) = \boldsymbol{F}(t) \tag{4.16}$$

or

$$\begin{bmatrix} m_1 & 0 & \cdots & 0 & 0 \\ 0 & m_2 & \cdots & 0 & 0 \\ \vdots & \vdots & \ddots & \vdots & \vdots \\ 0 & 0 & \cdots & m_{n-1} & 0 \\ 0 & 0 & \cdots & 0 & m_n \end{bmatrix} \begin{bmatrix} \ddot{u}_1 \\ \ddot{u}_2 \\ \vdots \\ \ddot{u}_{n-1} \\ \ddot{u}_n \end{bmatrix}$$
$$+ \begin{bmatrix} k_1(\varepsilon) + k_2(\varepsilon) & -k_2(\varepsilon) & \cdots & 0 & 0 \\ -k_2(\varepsilon) & k_2(\varepsilon) + k_3(\varepsilon) & \cdots & 0 & 0 \\ \vdots & \vdots & \ddots & \vdots & \vdots \\ 0 & 0 & \cdots & k_{n-1}(\varepsilon) + k_n(\varepsilon) & -k_n(\varepsilon) \\ 0 & 0 & \cdots & -k_n(\varepsilon) & k_n(\varepsilon) \end{bmatrix} \begin{bmatrix} u_1 \\ u_2 \\ \vdots \\ u_{n-1} \\ u_n \end{bmatrix}$$
$$+ \begin{bmatrix} d_1(\varepsilon) + d_2(\varepsilon) & -d_2(\varepsilon) & \cdots & 0 & 0 \\ -d_2(\varepsilon) & d_2(\varepsilon) + d_3(\varepsilon) & \cdots & 0 & 0 \\ \vdots & \vdots & \ddots & \vdots & \vdots \\ 0 & 0 & \cdots & d_{n-1}(\varepsilon) + d_n(\varepsilon) & -d_n(\varepsilon) \\ 0 & 0 & \cdots & -d_n(\varepsilon) & d_n(\varepsilon) \end{bmatrix} \begin{bmatrix} \dot{u}_1 \\ \dot{u}_2 \\ \vdots \\ \dot{u}_{n-1} \\ \dot{u}_n \end{bmatrix} = \begin{bmatrix} F_1 \\ F_2 \\ \vdots \\ F_{n-1} \\ F_n \end{bmatrix} \tag{4.17}$$

the motion of the stack and its sheets is described, where $\boldsymbol{M}$ is the mass matrix, $\boldsymbol{K}(\varepsilon)$ is the stiffness matrix, $\boldsymbol{D}(\varepsilon)$ is the damping matrix, and $\boldsymbol{F}(t)$ is the external load vector. While the force sensor is represented by a mass-spring-damper system as well (illustrated in Figure 4.8), its stiffness is much larger than the stiffness of paper and will therefore play no role in the dynamic model. However, it is relevant for the calculation of the cutting force as discussed in section 4.1.2. The stack is impacted by the cutting knife. If the knife is in contact with the stack, the cutting knife acts upon the top sheet as an external force $F_b(t)$. Thus, $\boldsymbol{F}(t)$ consists of the gravity force and $F_b(t)$ for the top sheet. Throughout the entire process, the general expression

$$F_b(t) = k_b \Delta u + d_b \Delta \dot{u} \quad \text{during } \Delta t_c \tag{4.18}$$

gives the loading at the top sheet during contact, where k_b is the stiffness and d_b is the damping between cutting edge and top sheet. The stiffness is determined through contact mechanics between two cylinders with parallel axes [135]. The combination of the two materials Young's Moduli E_1, E_2 and Poisson Ratios ν_1, ν_2, and length of the contact L, the stiffness calculates to

$$k_b = \frac{\pi}{4} L \left(\frac{1 - \nu_1^2}{E_1} + \frac{1 - \nu_2^2}{E_2} \right)^{-1} \tag{4.19}$$

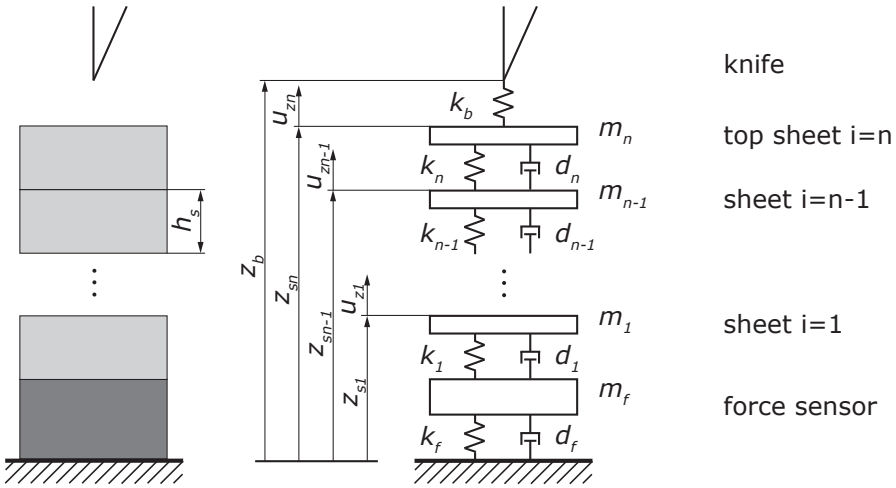

Figure 4.8: Stack model for cutting. Each sheet of paper is expressed by a mass-spring-damper system.

Since the Young's Modulus of the knife's material is much higher than of paper, the contact stiffness may be approximated with the stiffness of paper [136]. The damping d_b is interpreted as material damping when elastic deformation occurs. Its value is chosen as fixed to the damping value occurring at the continuous cutting process. Nonlinearities during the impact phase are not represented with the Kelvin-Voigt material model, and will be neglected here as well. The stiffness and damping of the lowest sheet represents the material contact between force sensor (steel) and paper, and is therefore also simplified to a fixed value equivalent to the parameters used for the blade stiffness and damping.

4.2.3 Cutting of Single Paper Sheet

To allow the cutting process to be simulated, the dynamic model needs to be capable of simulating the stack behavior while cutting individual sheets within the stack. This is defined by allowing the cutting knife to penetrate the stack once a specific critical cutting force is reached. The overall cutting process parameters are summarized in Figure 4.9 and are discussed as follows. In order to cut a single sheet of paper at a critical force, the resulting force of the top sheet's stiffness and damping or force acting at the cutting edge is considered. As the force acting upon the cutting blade reaches the critical value

$$F_b \geq F_{crit} \tag{4.20}$$

the cutting blade starts penetrating the top sheet. The force at the blade is specifically calculated at each time step by

$$F_b = k_b(z_c - \Delta z_b) + d_b(\dot{u}_{top} - \dot{u}_b) \tag{4.21}$$

where z_c is the cutting depth, Δz_b is the relative blade position to the top of the stack, $\dot{u}_{top}$ is the velocity of the top sheet, and $\dot{u}_b$ is the velocity of the cutting blade. The length of penetration or cutting, while the knife is in contact with the top sheet at critical cutting force, is defined by

$$|z_c| = (n_n - n_c)h_s + u_{top} - z_b \tag{4.22}$$

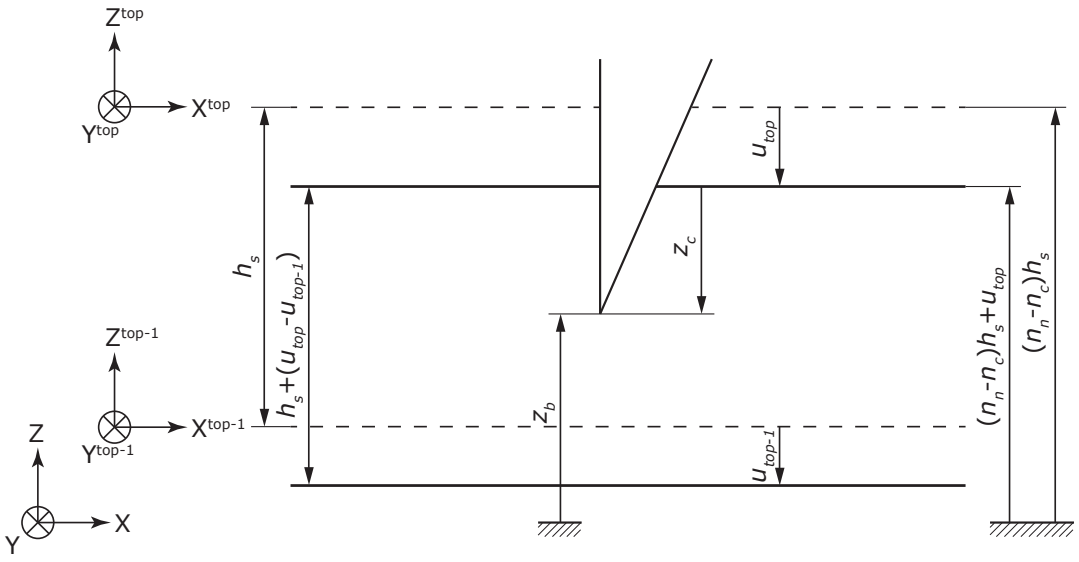

Figure 4.9: Parameters describing the continuously increasing cutting depth during the cutting process. u_{top} and u_{top-1} are defined within the respective local coordinate system of each sheet. Their values are also valid within the global X-Y-Z coordinate system.

where n_n is the number of sheets in the stack, n_c is the amount of sheets already cut, and h_s is the height of a single sheet. It will increase until the top sheet of the stack is completely cut. The inequality $|z_c| \leq h_s$ is always kept during the cutting procedure of a single sheet. Consequently the ratio of how much a sheet is cut can be obtained by

$$r_c = \frac{|z_c|}{h_s} \tag{4.23}$$

Considering the compression of the stack, the cut ratio could also be calculated with respect to the actual sheet height during the compression. However, for simplification, a single sheet is regarded as floppy material and thereby the cut parts of the sheet cannot store elastic energy [137]. Calculating the cutting ratio with respect to the original height also allows the cutting depth to increase monotonously. During the cutting process, the cutting for initiated from the cutting blade is kept constant at

$$F_b = F_{crit} \tag{4.24}$$

and is therefore limited. This definition is derived from the assumption that no hardening of the material occurs while the knife penetrates the current sheet being cut.

4.2.4 Partial Motion of Stack at Detaching

Depending on the parameters of the vibration assisted cutting, the knife can detach from the stack for a short time during the upward movement of the longitudinal vibration. It is essential to model this behavior, because the top sheet no longer experiences any loading from the knife and the stack may oscillate freely. The top sheet can also relax when the loading of the knife is reduced or reaches zero. However, it is important to note that the relaxation or free motion of the stack may not be faster then the motion of the cutting

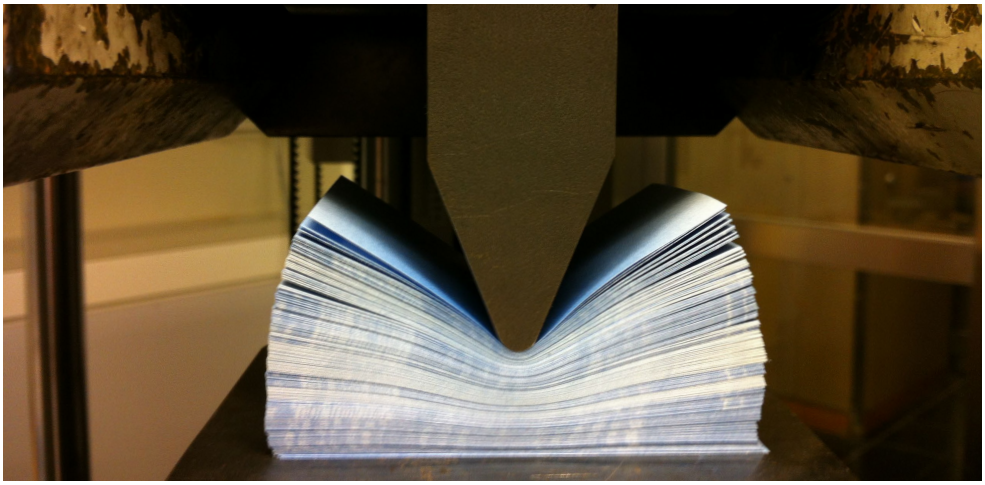

Figure 4.10: Experimental setup for determining the stack stiffness. A blunted edge (radius of 3 mm) is driven into the stack without cutting any sheets.

knife, while contact exists. The cutting knife will always limit any free motion once the top sheet comes into contact with it. Thus, the velocity of relaxation may not exceed the velocity of the knife motion

$$\dot{u}_{top} \leq \dot{z}_b \tag{4.25}$$

The calculation of the cutting depth during the detached phase (stack is free or relaxing with the upward speed of the cutting knife) is

$$|z_c'| = r_c \left(h_s + (u_{top} - u_{top-1})\right) \tag{4.26}$$

Thus, the cutting depth is "corrected" with $r_c(u_{top} - u_{top-1})$ while the relaxation process occurs. Considering the previous assumption that the cut part of the sheet cannot store any elastic energy, and the relative position of the two top sheets may indicate compression or tension, it is not clear how much the cutting depth changes due to elastic deformation. However, in the system of ordinary differential equations, the mass does not change during the cutting of a single sheet. Therefore, the cut part of the sheet should be able to move relative to its local displacement.

4.2.5 Material and Model Parameters

Stack Stiffness and Damping

As already discussed in section 2.2.2, the compressive behavior of paper is nonlinear correlated to the applied load and small number of sheets within the stack. However, for the previous described model stiffness and damping of the sheets need to be defined. Therefore, compression-dependent stiffness and overall damping need to be experimentally investigated for large stacks (many sheets within the stack), to create an empirical model describing the compressive behavior. This empirical model is then used by the dynamic model to correctly calculate the stiffness and damping.

Figure 4.10 shows the experimental setup for the parameter identification. Experiments are simply carried out by compressing (without cutting) three stacks with different amount of sheets of paper at two different speeds, while recording force and position. To avoid

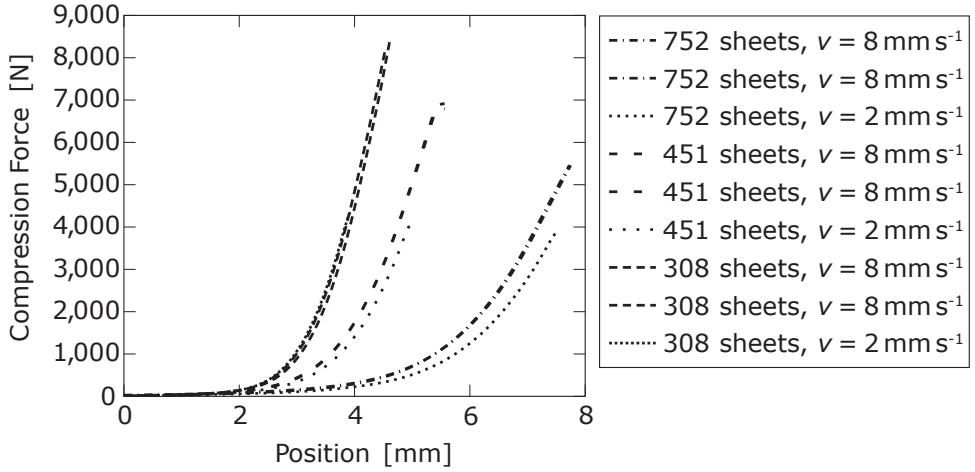

Figure 4.11: Experimental results from compressive tests of three different stacks at two different speeds.

any negative influence from the stack memory effect and relaxation, each experiment and its repetition are done with individual stacks. Prior to compression with a blunt cutting knife, the starting position was determined by pre-pressing with 30 N. This allowed a fairly good comparable starting position with regard to number of sheets within the stack, and the usage of a different stack for each experiment. Pre-pressing the stack also allows good repeatability for this experimental setup. Section 6.1 lists the material parameters of the paper used. For the empirical investigation of stiffness and damping, stacks of 50 mm length and 40 mm width were used. The height of a single sheet of paper is 60 µm.

Before determining the stiffness and damping of a stack of thin material, the following assumptions are found. The measured force is a combination of stiffness force and damping force, as stated by

$$F_{exp} = F_k + F_d \tag{4.27}$$

where F_{exp} is the measured force, F_k is the stiffness force, and F_d is the damping force. Furthermore, it is assumed that these two forces may be calculated by

$$F_k = k(u)u \tag{4.28}$$
$$F_d = d(u)\dot{u} \tag{4.29}$$

where $k(u)$ and $d(u)$ are assumed to dependent on the position of the top sheet. Instead of using the relative position of the sheet, which is related to the position of the upper part of the sheet, the compression ratio ε may be used. For the experiments, the compression ratio of the entire stack is

$$\varepsilon = \frac{z_{press}}{h_s n_n} \tag{4.30}$$

with z_{press} as the measured compression. Within the dynamic model, the compression ratio is calculated with

$$\varepsilon = \frac{|u_{top}|}{(n_n - n_c)\, h_s} \tag{4.31}$$

It is assumed that the compression per sheet is homogeneous, and thus equal to the compression ratio of the stack.

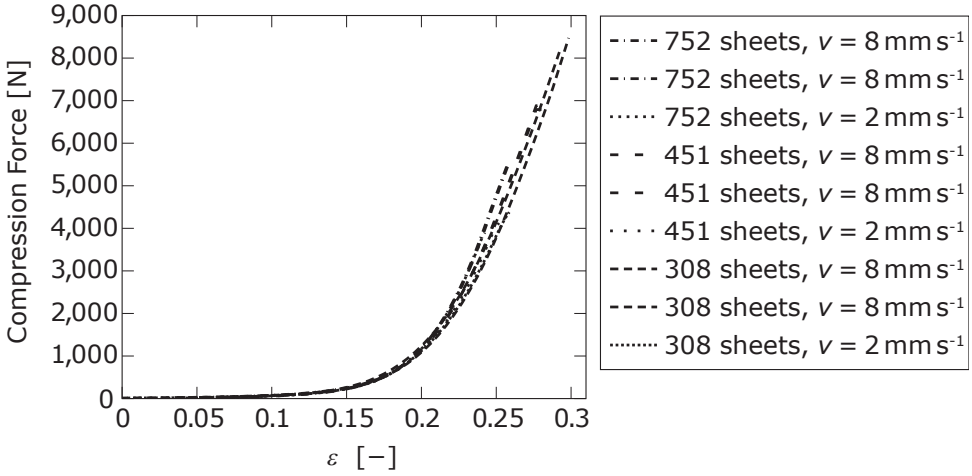

Figure 4.12: Experimental results from compressive tests of three different stacks at two different speeds, with z_{press} divided by the number of sheets in the stack. The relation of F_{exp} is plotted over the compression ratio ε.

First, the overall stack behavior during compression is analyzed. When compressing stacks of different amount of sheets at two speeds, a difference in F_{exp} can be observed as shown Figure 4.11. It is dependent on the amount of sheets and compression speed. From two experiments run at different compression speeds of $2\,\mathrm{mm\,s^{-1}}$ and $8\,\mathrm{mm\,s^{-1}}$, an increase in F_{exp} at higher speeds is observed for larger stacks. This difference is less significant for smaller stacks. To test the observed behavior on its correlation on number of sheets, the position data of each experiment is divided by the number of sheets in the stack. This may be done under the assumption that the compression of each single sheet is uniform within the stack. From Figure 4.12, it becomes apparent that at lower compression forces, the compressive behavior per single sheet may be regarded as independent from the number of total sheets per stack. In addition, the dependency on compression speed is negligible for low compression ratios ($F_{exp} < 2000\,\mathrm{N}$). Due to the discrepancy between blunt knife and actual cutting knife regarding the contact area (radius), experiments with different radii at the blunt edge are carried out. Figure 4.13 shows the results of these compression experiments. No significant correlation between the radii and compression force can be seen.

Thus, the stiffness per sheet may be determined by

$$k(\varepsilon) = \frac{\partial F_{exp}(\varepsilon)}{\partial z_{press}(\varepsilon)} \tag{4.32}$$

where $F_{exp}(\varepsilon)$ is the experimentally recorded compression force and $z_{press}(\varepsilon)$ may be regarded as the position of the top sheet. In order to derive a stiffness function from the force-elongation data, an appropriate function is fitted to the empirical data.

$$F\left(\frac{z_{press}}{n_n}\right) = \overset{*}{a}_k \exp\left(\frac{z_{press}}{n_n}\overset{*}{b}_k\right) + \overset{*}{c}_k \tag{4.33}$$

was determined through fitting methods and gives the empirical correlation between stiffness and compression. Table 4.2 shows the parameters for the empirical equation. The overall best values, which fit the stiffness function into all the measurement data, are used

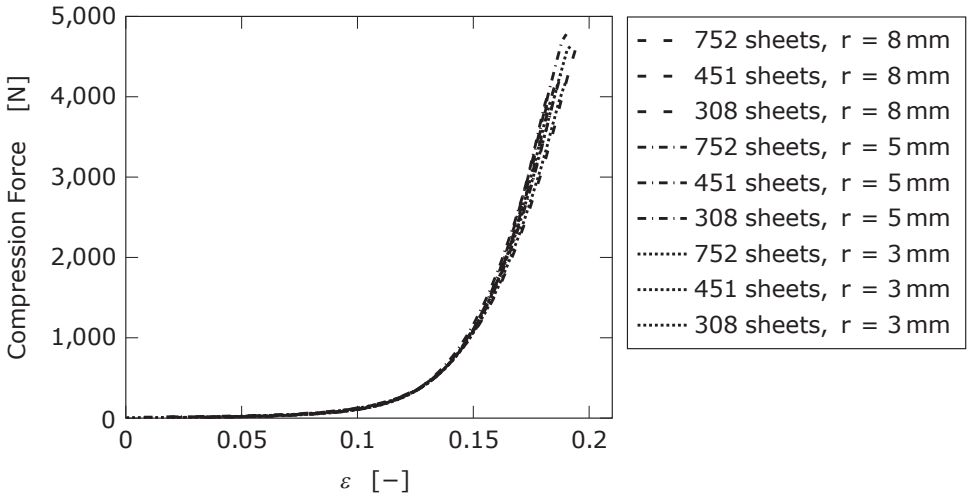

Figure 4.13: Experimental results from compressive tests with three different radii of the blunt edge of three different stacks. z_{press} is divided by the number of sheets in the stack. The relation of F_{exp} is plotted over the compression ratio ε.

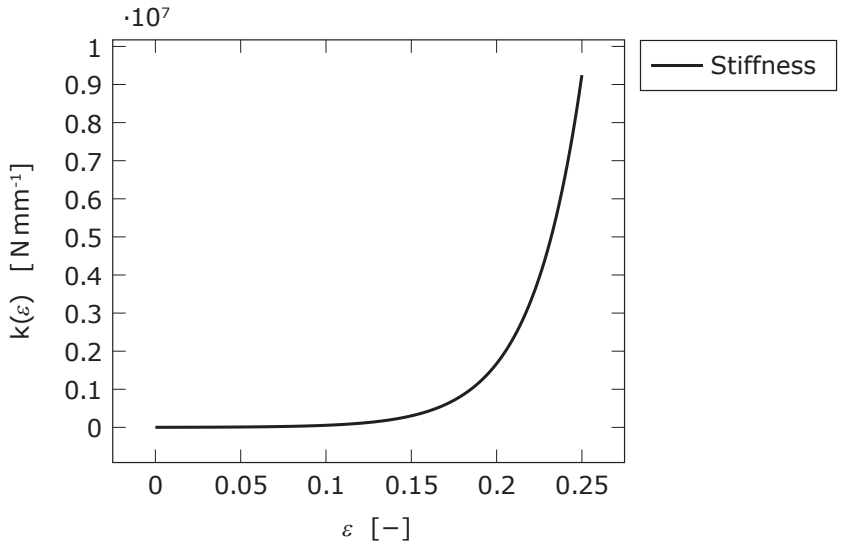

Figure 4.14: Trend of the stiffness function according to equation (4.34).

# of sheets	$\overset{*}{a}_k$	$\overset{*}{b}_k$	$\overset{*}{c}_k$
752	3.78	564.95	0
451	11.73	468.77	0
308	16.922	432.52	0
overall best	3.14	570	0

Table 4.2: Parameters for the empirical stiffness equations for various stack heights and the overall best fit for all measurement data.

from now on. To obtain a function regarding the stiffness of the stack, the derivative of equation (4.33) is calculated as

$$k(\varepsilon) = \overset{*}{a}_k \overset{*}{b}_k \exp\left(\overset{*}{b}_k \varepsilon\right) \tag{4.34}$$

with $k(\varepsilon)$ being the stiffness depending on the compression of the stack, which is assumed to be evenly distributed. It is displayed in Figure 4.14.

Second, the damping behavior of the stack needs to be analyzed. Since the compression experiments do not show a clear velocity dependency per sheet in the region of small compression ratio, the damping parameters need to be determined through an experimental modal analysis. In order to accomplish this, the experimental setup shown in Figure 4.15 is used. A variable mass is placed upon the blunt cutting knife (see Figure 4.10), which is in contact with the stack containing 451 sheets. Excitation occurs at the top of the variable mass and the response of the force measurement sensor below the stack is recorded. Deformation within the stack for each experiment is assumed to be homogeneous. Different experimental modal analyses are carried out with different masses to vary the compression of the stack. For each system response in the time domain, a Fast Fourier transform (FFT) [138] is performed to allow the determination of the resonance frequency and its damping ratio. Based on the frequency spectrum from the FFT, the damping ratio is calculated with the full width at half power method (see Figure A.3) [139, 140]. At the resonance frequency peak

$$D = \frac{\lambda}{\omega_0} = \frac{\frac{d}{2m}}{\frac{\omega_0}{2}} = \frac{\frac{\Delta\omega}{\omega_0}}{2} = \frac{\frac{\omega_b - \omega_a}{\omega_0}}{2} \qquad \text{at} \quad \frac{a_{Pmax}}{\sqrt{2}} \tag{4.35}$$

is calculated from the experimental results to identify the damping ratio D, where ω_0 is the resonance frequency, λ is the decay constant, d is damping coefficient, m is the variable mass, ω_a and ω_b are the frequencies where the amplitude is $\frac{a_{Pmax}}{\sqrt{2}}$. Figure 4.16 shows the damping ratio and resonance frequency for each mass (denoted as the gravity force). From the identified parameters, the physical damping (viscous) is calculated with

$$d = 2D\omega_0 m \tag{4.36}$$

where the parameters depend on the experiment. To obtain the damping values per sheet, it is assumed that the correlation of the damping to the number of sheets within a large stack is linear. Therefore, the identified damping values are multiplied with 451 (series connection of dashpots). Next, the dependency to the compression ratio needs to be found. Since no significant damping is seen in the compression experiments, the applied load force resulting from the mass on top of the blunt knife is used to calculate the compression with equation (4.33). It is assumed that the deformation of the stack is linearly distributed, as in a homogeneous material. Thus, the dependency of the damping value to compression of the stack is found as displayed in Figure 4.17. Through curve fitting,

$$d(\varepsilon) = \overset{*}{a}_d \exp\left(\overset{*}{b}_d \varepsilon\right) + \overset{*}{c}_d \tag{4.37}$$

gives the correlation between compression ratio and damping.

Through the empirical stiffness equation and its corresponding parameters, and the damping results of the experimental modal analysis, the dynamic model can appropriately simulate the stack's compressive behavior. Table 4.3 summarizes the identified parameters.

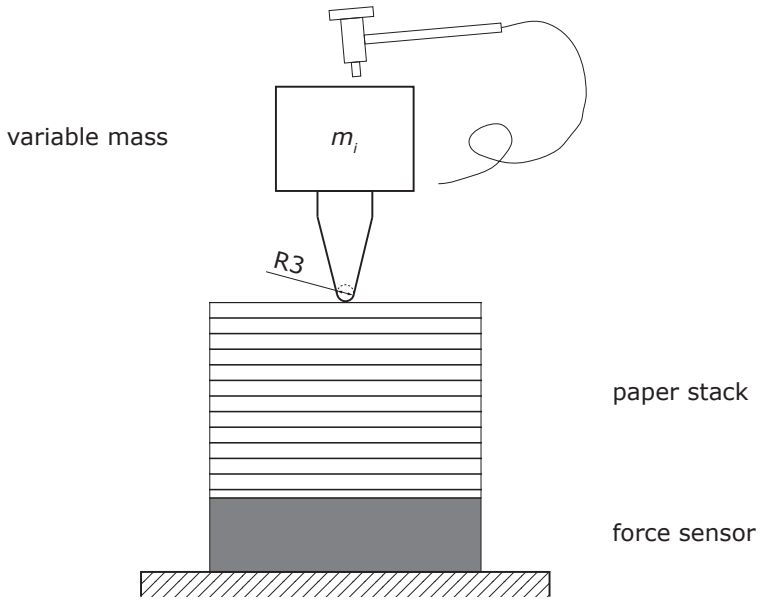

Figure 4.15: Experimental setup for determining the damping of a sheet stack with 451 sheets. Mass on top of the blunt knife is varied according to the experimental procedure to cause different compression ratios.

	Stiffness	Damping
$\overset{*}{a}$	3.14	14.5
$\overset{*}{b}$	570	405
$\overset{*}{c}$	–	-14

Table 4.3: Parameters for the empirical stiffness and damping equations.

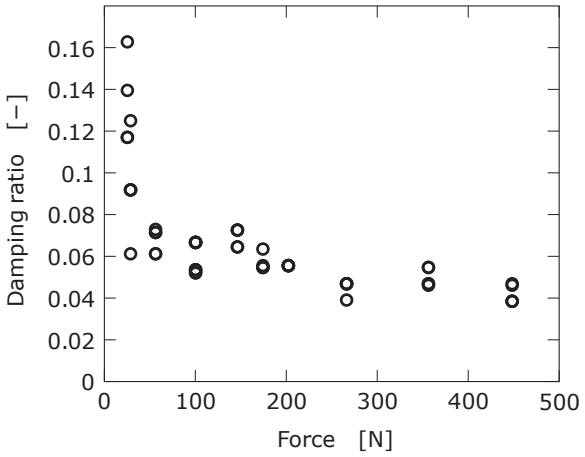

(a) Damping ratio at different loads.

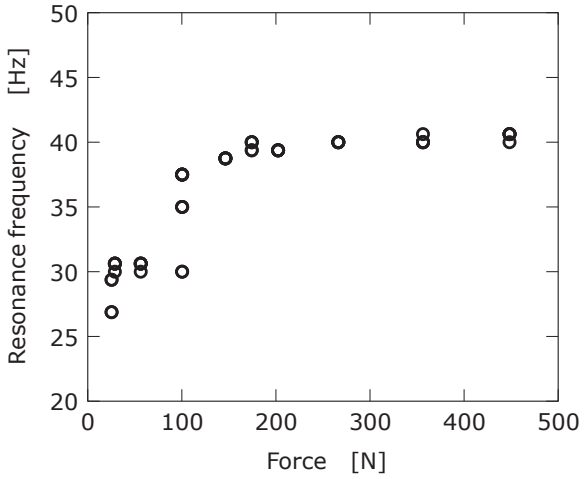

(b) Resonance frequency at different loads.

Figure 4.16: Damping ratio and resonance frequency for the different masses applied to the blunt knife. Each experiment is run 5 times and individually displayed here.

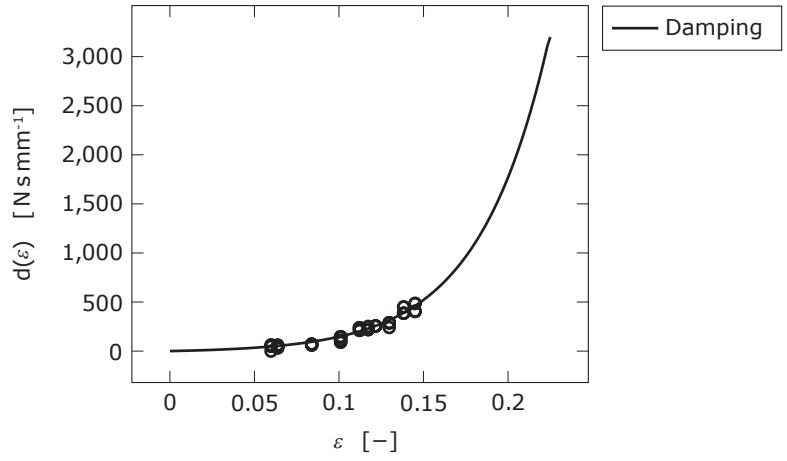

Figure 4.17: Trend of the damping function according to equation (4.37). Damping values from the experimental modal analysis are shown.

4.2.6 Results

To test the dynamic model, simulations at no and high oscillating frequency are carried out. Feed rate 750 mm min^{-1}, vibration amplitude 4 µm, and vibration frequency 0 kHz and 35.0 kHz are the parameters used in the simulated cutting of 21 sheets. For an overview, Figure A.4 shows the procedure within the dynamic model. For damping and stiffness, the found empirical equations are used. Compression distribution as discussed in [40] is neglected, because the expansion of the compressed area is asymptotic and not relevant to this simulation. The critical cutting force, empirically obtained from a simple guillotining test, is virtually set to 12.5 N mm^{-1}. Stiffness between top sheet and blade is set to $k_b = 4.26 \cdot 10^5$ N mm^{-1}, and damping between top sheet and blade is set to $d_b = 694$ N s mm^{-1}. These values are taken from the steady-state condition when the compression force equals the specific cutting force.

Dynamic Behavior

In this section, the dynamic behavior of the introduced model is analyzed. It will help to determine whether or not it is suitable for simulating the longitudinal vibration assisted cutting process. Beginning with the overall blade movement and its impact on the stack, Figure 4.18 shows the change in position over time for conventional and vibration assisted cutting, with highlighted cutting start and stop points of a single sheet. While the knife continuously penetrates the stack during the conventional cutting, the oscillation during vibration assisted cutting can clearly be seen. The elastic behavior caused by the stiffness parameter and the relaxation during the detachment phase caused by the damping parameter are outlined by the zoomed in window.

Next, the stiffness and damping depending on stack compression are considered. In Figure 4.19, the compression ratio during the simulation with oscillating movement of the blade is shown. As the knife progresses, the compression is increased and becomes overall steady as the cutting of the sheets commences. The compression ratio is approx. 10 % lower when applying vibrations to the cutting knife, indicating that the specific cutting force is reached quicker than without vibration. Small relaxations can be observed during the upward motion of the knife. The discontinuities in the curves are due to the finished cutting and following spontaneous relaxation of the stack, caused by the missing remaining material of the previously top sheet, which is completely cut in the preceding time step. From the compression, the stiffness and damping over time may be derived as shown in Figure 4.20 and Figure 4.21. The lower compression ratio and consequentially lower stiffness and damping values indicate an increased damping force due to the higher velocity during impact. Figure 4.22 shows the average damping force per top sheet for the cutting process. It becomes clear that the high velocity of the cutting edge causes failure of the material at a lower compression of the stack. It explains a key advantage of vibration assisted cutting: high velocity impact.

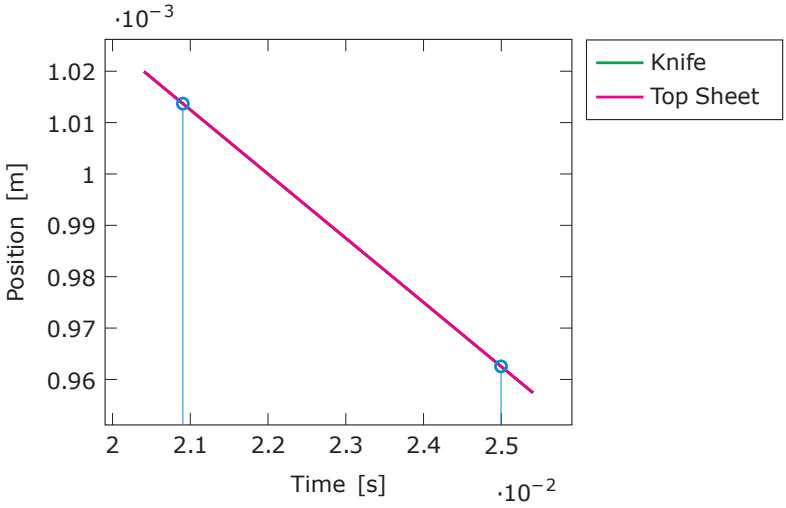

(a) Conventional cutting process.

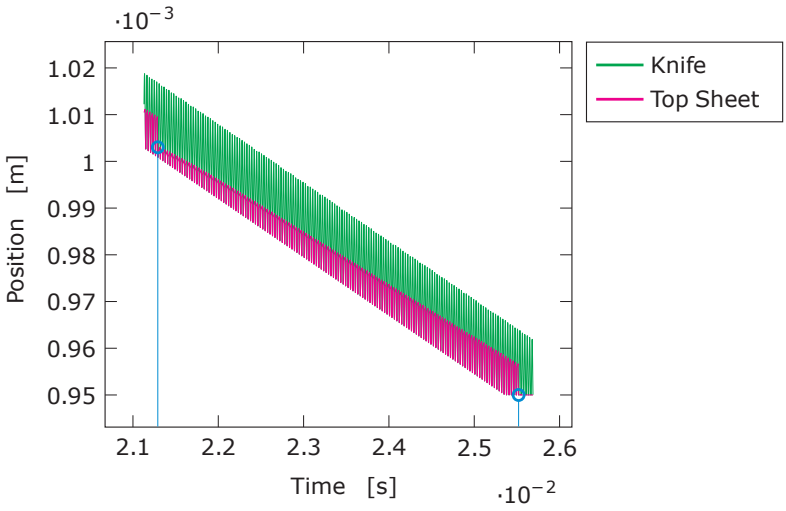

(b) Vibration assisted cutting process.

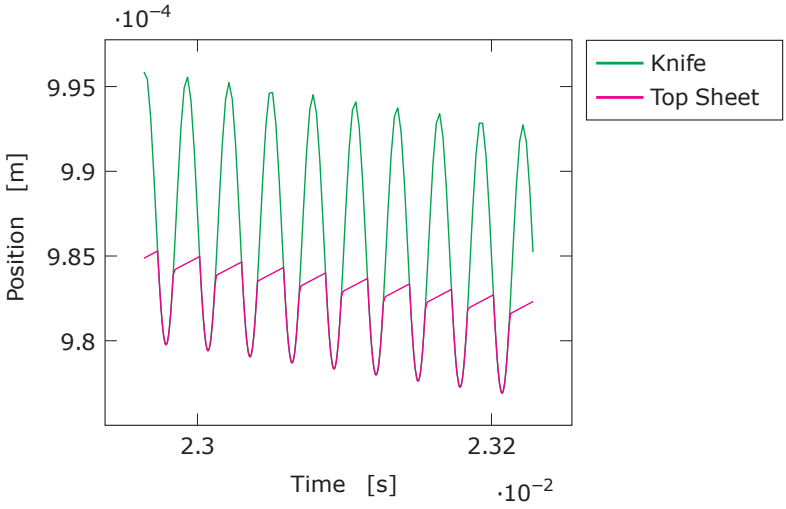

(c) Zoom in from (b).

Figure 4.18: Motion of the cutting knife and displacement of the top sheet during simulation. ○ indicates the completely cut sheet.

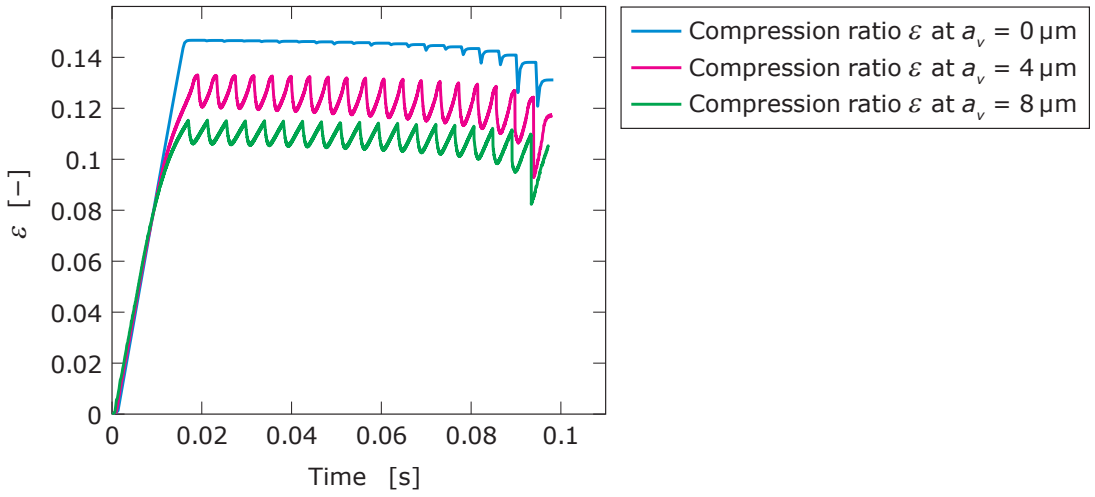

Figure 4.19: Simulation results of the compression ratio during cutting without and with vibration at $35\,\mathrm{kHz}$ and indicated vibration amplitudes.

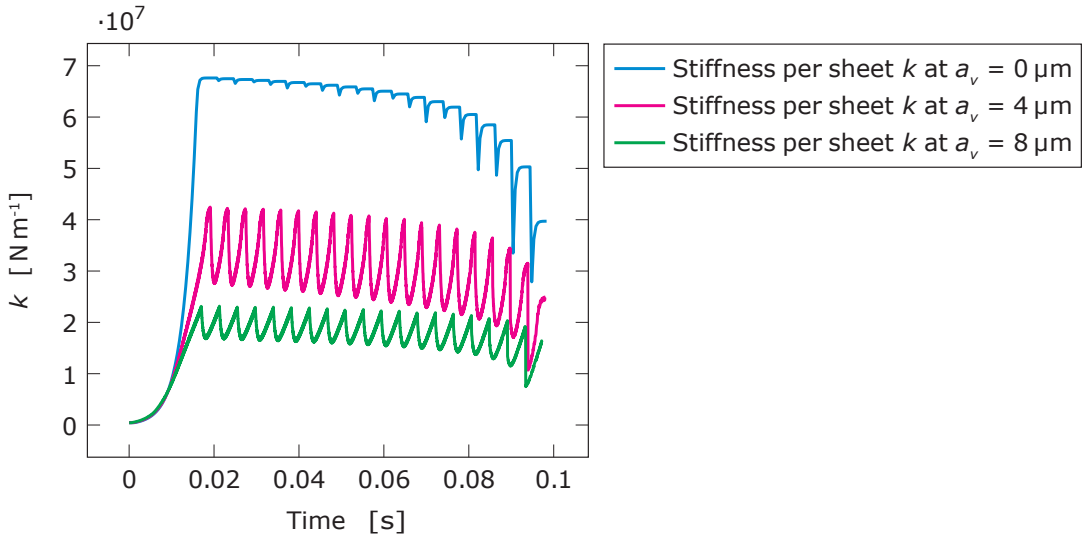

Figure 4.20: Simulation results of the stiffness during cutting without and with vibration at $35\,\mathrm{kHz}$ and indicated vibration amplitudes.

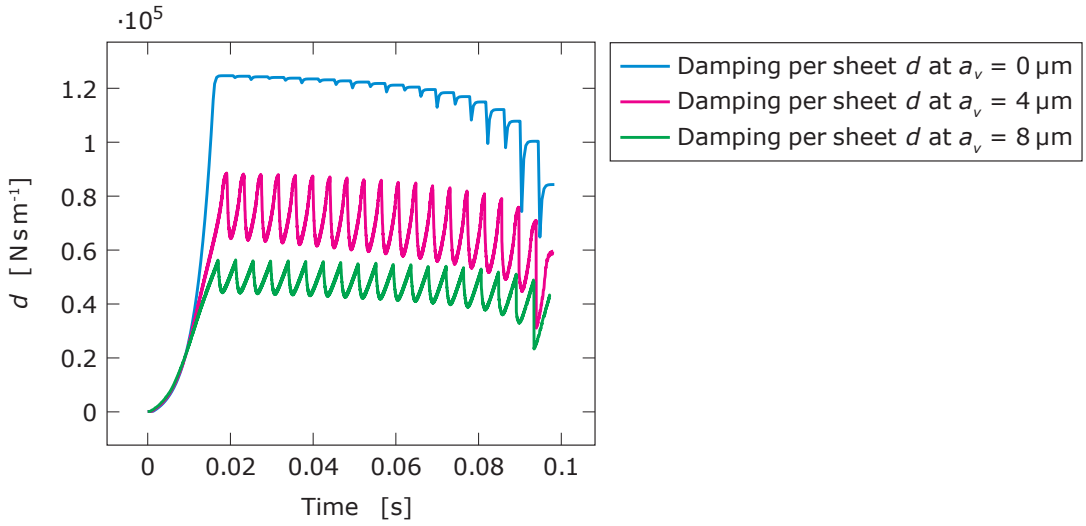

Figure 4.21: Simulation results of the damping during cutting without and with vibration at $35\,\mathrm{kHz}$ and indicated vibration amplitudes.

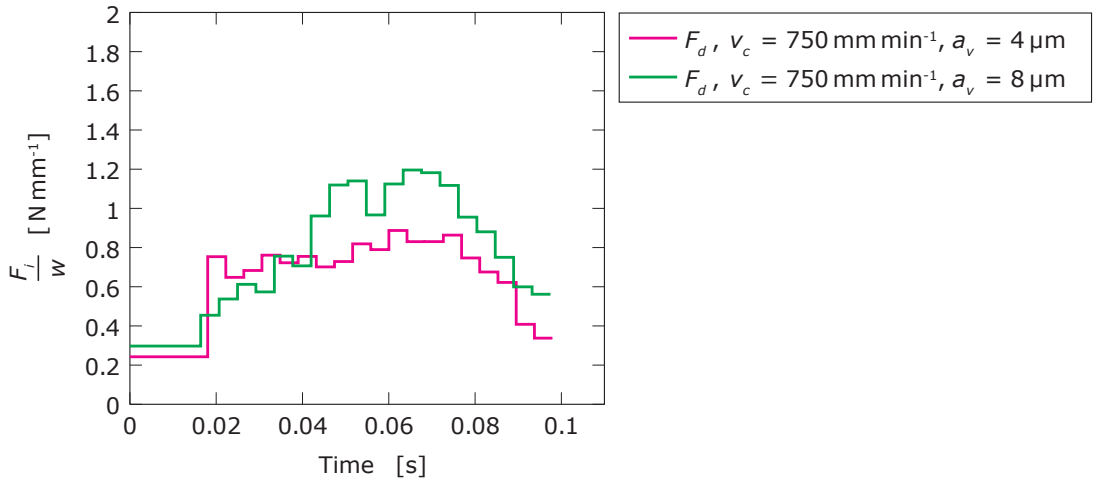

Figure 4.22: Simulation results of the dynamic forces (or damping forces) during cutting with vibration at $35\,\mathrm{kHz}$ and indicated vibration amplitudes. Results for cutting without vibration are omitted here, because they are simply 0.

4.3 Parallel Vertical Cutting with Lateral Vibration

Some parts of the following content have been published by the author in [B.v]. Calculating the forces for guillotining with assisting lateral vibration is done based on the model introduced in section 2.3.1 and theory of reciprocating blades [60]. Cutting edges oscillating laterally also comprise a slice-push ratio, but unlike continuously moving blades, the slice-push ratio changes with the position of the stroke. There is a maximum slice-push ratio at mid-stroke and zero slice-push ratio at the ends of the stroke. Regarding a lateral sinusoidal oscillation (stroke) of the cutting edge, where the motion is calculated by

$$\mathrm{d}u_Y = \mathrm{d}u_{Ymax} \sin(\omega t) \tag{4.38}$$

with du_{Ymax} being the maximum lateral (horizontal) motion or amplitude of the oscillation, ω being the frequency of the oscillation, and t being time. The slice push ratio can be written as

$$\zeta = \frac{\mathrm{d}u_{Ymax}}{\mathrm{d}u_Z} \sin(\omega t) \tag{4.39}$$

For the sake of simplification and consistency, the slice-push ratio will be based on the velocity components from now on. Consequently, ζ is expressed by

$$\zeta = \frac{v_Y}{v_Z} \sin(\omega t) = \frac{\omega a_v}{v_Z} \sin(\omega t) \tag{4.40}$$

Thus, the vertical and lateral frictionless cutting forces (see section 2.3.1) can be written as

$$\frac{F_Z}{e_{fr} w} = \frac{\zeta}{1+\zeta^2} = \frac{v_Z \omega a_v \sin(\omega t)}{v_Z^2 + (\omega a_v \sin(\omega t))^2} \tag{4.41}$$

$$\frac{F_Y}{e_{fr} w} = \frac{1}{1+\zeta^2} = \frac{v_Z^2}{v_Z^2 + (\omega a_v \sin(\omega t))^2} \tag{4.42}$$

and the resulting force becomes

$$\frac{F_R}{e_{fr} w} = \sqrt{\frac{1}{1+\zeta^2}} = \sqrt{\frac{1}{1+\left(\dfrac{\omega a_v \sin(\omega t)}{v_Z}\right)^2}} \tag{4.43}$$

With a known specific cutting force e_{fr}, vibration amplitude a_v, vibration frequency ω, and feed rate v_Z, these forces can be directly calculated. In a next step, the friction forces of the cutting process are considered.

To include the friction forces occurring at the cutting edge, the model introduced in section 2.3.2 is expanded from a two-dimensional to a three-dimensional consideration. Figure 4.23 illustrates the new friction forces impacting the cutting edge. Since the cutting edge movement now includes a velocity component in y-direction, the friction force at the cutting edge requires a force component in y-direction as well. This is realized by introducing the angle γ between the downward velocity along the cutting edge $v_Z/\cos\beta$ and resulting velocity v_R. The angle γ helps calculate the vertical and lateral forces [141] and is defined by

$$\tan\gamma = \frac{\dfrac{v_Y}{v_Z}}{\cos\beta} = \zeta \cos\beta \tag{4.44}$$

$$\text{resp.} \quad \gamma = \arctan(\zeta \cos\beta) \tag{4.45}$$

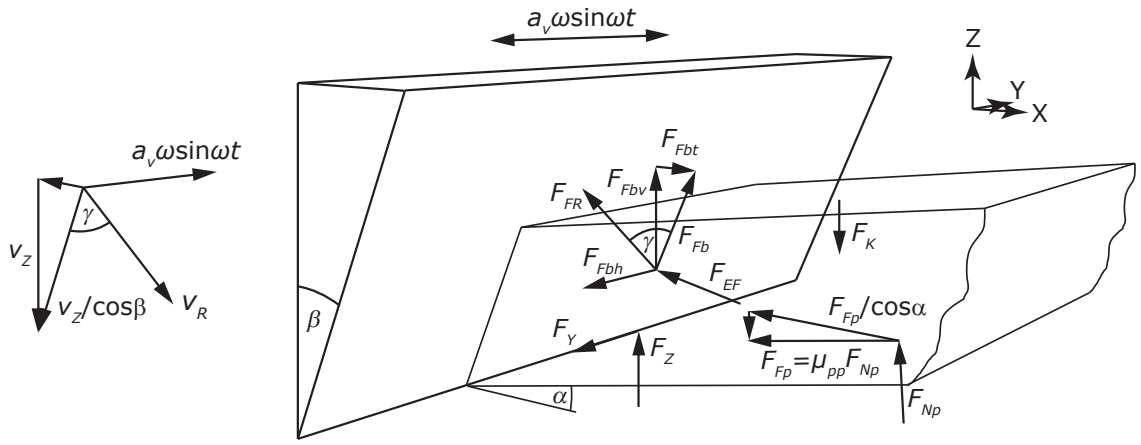

Figure 4.23: Cutting forces in y- and z-direction. Friction forces in x-y-z-direction. Angle γ is described by equation (4.44).

It can be seen that γ also depends on ζ and is therefore not constant. This becomes obvious in Figure 4.23, where the resulting velocity v_R changes direction with its y- and z-components. Next, the components of the friction forces acting upon the cutting edge are derived. The normal force F_{EF} is caused by the paper stack being cut and creates a friction force F_{FR}

$$F_{FR} = F_{EF}\mu_b \tag{4.46}$$

pointing opposite of v_R along the cutting edge. Analogous to the cutting forces, the resulting friction force comprises of tangential and lateral friction forces. While considering γ, these friction forces are

$$F_{Fbh} = \sin\gamma F_{EF}\mu_b \tag{4.47}$$
$$F_{Fb} = \cos\gamma F_{EF}\mu_b \tag{4.48}$$

The tangential friction force F_{Fb} can be further divided into vertical and transversal components as

$$F_{Fbt} = \sin\beta\cos\gamma F_{EF}\mu_b \tag{4.49}$$
$$F_{Fbv} = \cos\beta\cos\gamma F_{EF}\mu_b \tag{4.50}$$

With these equations, the friction forces in lateral, vertical, and transversal direction can be calculated. Figure 4.24 plots the friction forces over ζ. The lateral friction force reaches a maximum, depending on the parameters (here at $\zeta = 4.5$), before it asymptotically decreases. It is important to keep in mind that the normal force F_{EF} acting upon the cutting blade changes with the slice-push ratio as well. This is realized by including γ in equation (2.26), resulting in

$$F_{EF} = F_K \frac{\sin\alpha + \mu_{pp}\cos\alpha}{\left[\begin{array}{l}(\cos\beta - \mu_b\cos\gamma\sin\beta)(\cos\alpha - \mu_{pp}\sin\alpha) \\ \quad -(\sin\beta + \mu_b\cos\gamma\cos\beta)(\sin\alpha + \mu_{pp}\cos\alpha)\end{array}\right]} \tag{4.51}$$

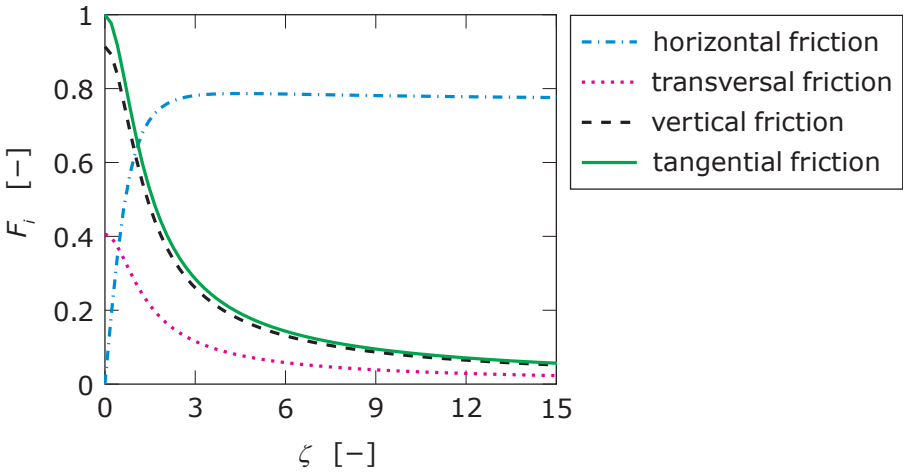

Figure 4.24: Normalized friction forces as a function of ζ.

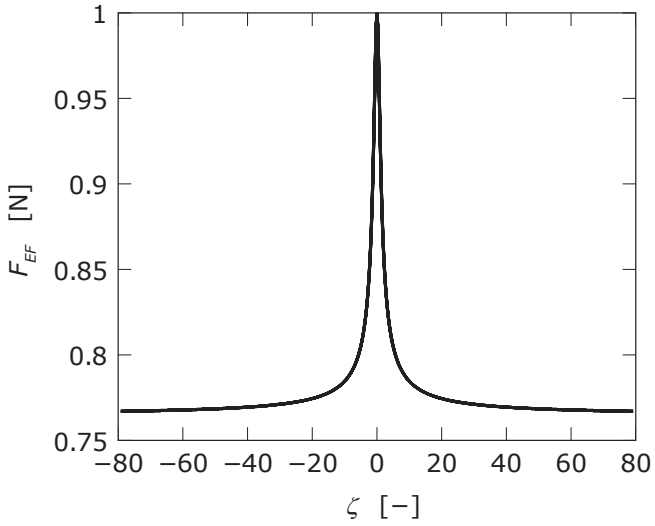

Figure 4.25: Normalized normal force acting against the cutting edge as a function of ζ. Here, $\mu_b = 0.25$, $\mu_{pp} = 0.35$, and $\beta = 24°$.

Thus, F_{EF} depends on γ and consequently the slice-push ratio. Since the normal force acting upon the cutting edge is a result from friction effects along the face of the cutting edge, this correlation is obvious. Figure 4.25 shows an asymptotically decreasing F_{EF} for high slice push ratios. Taking equation (4.50) into account, the reduction of friction forces in z-direction is significant, because F_{Fbv} itself and F_{EF} decrease with an increasing ζ. If $\zeta \to \infty$, equation (4.51) simplifies to

$$\lim_{\zeta \to \infty} F_{EF} = F_K \frac{\sin\alpha + \mu_{pp}\cos\alpha}{\cos\beta\,(\cos\alpha - \mu_{pp}\sin\alpha) - \sin\beta\,(\sin\alpha + \mu_{pp}\cos\alpha)} \tag{4.52}$$

To calculate the friction occurring during ultrasonic lateral vibration assisted guillotining, the average vertical friction force needs to be calculated. Based on the findings in the previous section, it becomes apparent that any friction or force reduction for high frequency oscillation is due to the dynamic behavior of sensors or structures. Calculating

the average friction force at the cutting edge is similar to the determination of the friction force during perpendicular oscillation to the macroscopic movement as derived in [142]. When expanding equation (4.50) to

$$F_{Fbv}(t) = \cos\beta F_{EF}\mu_b \cos\left(\arctan\left(\frac{v_{Ymax}\sin(\omega t)}{\frac{v_Z}{\cos\beta}}\right)\right) \tag{4.53}$$

and using the previously introduced slice-push ratio, equation (4.53) is simplified to

$$F_{Fbv}(t) = \cos\beta F_{EF}\mu_b \cos\left(\arctan\left(\zeta\sin(\omega t)\cos\beta\right)\right) \tag{4.54}$$

Calculating the average vertical friction force $\bar{F}_{Fbv}$ is done by integration over one oscillation period. Following shows this integration with invariant F_{EF}.

$$\begin{aligned}\bar{F}_{Fbv}(t) = \frac{1}{T}\int_0^T F_{Fbv}(t)\mathrm{d}t =& \frac{1}{2\pi}\int_0^{2\pi} F_{Fbv}(\omega t)\mathrm{d}(\omega t)\\ =& \frac{1}{2\pi}\cos(\beta)F_{EF}\mu_b\int_0^{2\pi}\cos\left(\arctan\left(\zeta\sin(\omega t)\cos\beta\right)\right)\mathrm{d}(\omega t)\\ =& \frac{1}{2\pi}\cos(\beta)F_{EF}\mu_b\int_0^{2\pi}\frac{1}{\sqrt{\zeta^2\cos^2(\beta)\sin^2(\omega t)+1}}\mathrm{d}(\omega t)\end{aligned} \tag{4.55}$$

The present integral is a complete elliptical integral of the first kind in the standard form

$$F(\phi|m) = \int\frac{\mathrm{d}\phi}{\sqrt{1-m\sin^2(\phi)}} \tag{4.56}$$

which cannot be described by an elementary function. When looking at the values of equation (4.50) over time, it becomes apparent that it is symmetrical across $\frac{\pi}{2}$. Hence the average value of one period of 2π can also be represented by the average over a quarter period $\frac{\pi}{2}$. This allows the simplification to

$$\bar{F}_{Fbv}(t) = \frac{2}{\pi}\cos(\beta)F_{EF}\mu_b\int_0^{\frac{\pi}{2}}\frac{1}{\sqrt{\zeta^2\cos^2(\beta)\sin^2(\omega t)+1}}\mathrm{d}(\omega t) \tag{4.57}$$

which contains a complete elliptical integral K_{ell} and can be computed with help of a numerical method. After integration, the average vertical friction force is obtained as

$$\bar{F}_{Fbv}(\zeta) = \frac{1}{\sqrt{\zeta^2\cos^2(\beta)+1}}\frac{2}{\pi}\cos(\beta)F_{EF}\mu_b K_{ell}\left(\frac{\zeta\cos\beta}{\sqrt{\zeta^2\cos^2(\beta)+1}}\right)\mathrm{sgn}(\zeta) \tag{4.58}$$

K_{ell} is the notation for complete elliptical integral of the first kind (term inside of K_{ell} must be squared for MATLAB). To examine the friction reduction through lateral vibration, the

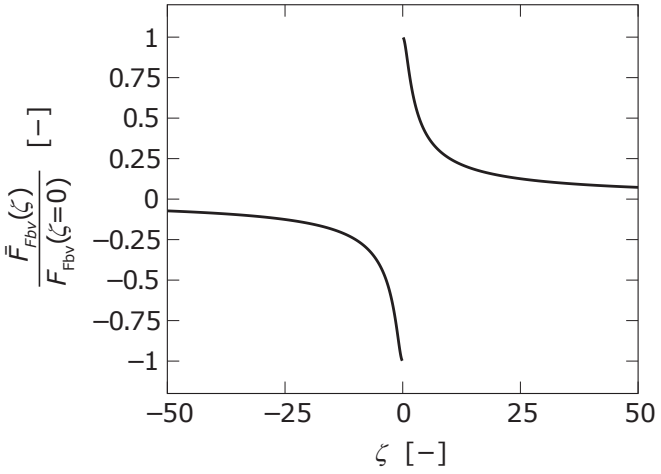

Figure 4.26: Average vertical friction force reduction as a function of ζ with invariant F_{EF}.

above equation can be divided by equation (4.54) to calculate the relative friction reduction as

$$\frac{\bar{F}_{Fbv}(\zeta)}{F_{Fbv}(\zeta=0)} = \frac{1}{\sqrt{\zeta^2\cos^2(\beta)+1}}\frac{2}{\pi}K_{ell}\left(\frac{\zeta\cos\beta}{\sqrt{\zeta^2\cos^2(\beta)+1}}\right)\operatorname{sgn}(\zeta) \tag{4.59}$$

Figure 4.26 shows this relative reduction graphically. For $\zeta \to \infty$, the velocity of the oscillation becomes $v_{Ymax} \to \infty$, resulting in maximum friction reduction or no friction in vertical direction. For $\zeta \to 0$, the velocity of the oscillation becomes $v_{Ymax} \to 0$, resulting in no friction reduction or maximum friction in vertical direction.

Finally, the cutting forces and friction forces (general equations) are added to calculate the total forces observed in y and z direction (lateral and vertical) at the cutting edge. Equation (4.41) and equation (4.50) for the force in y-direction, and equation (4.42) and equation (4.47) for the force in z-direction become

$$\begin{aligned} F_Z =& \frac{1}{1+\zeta^2}e_{fr}w + \cos\beta\cos\gamma F_{EF}\mu_b \\ =& \frac{1}{1+\zeta^2}e_{fr}w + \cos\beta\cos\left(\arctan\left(\zeta\cos\beta\right)\right)F_{EF}\mu_b \\ =& \frac{1}{1+\zeta^2}e_{fr}w + \frac{\cos\beta}{\sqrt{\cos^2(\beta)\zeta^2+1}}F_{EF}\mu_b \end{aligned} \tag{4.60}$$

$$\begin{aligned} F_Y =& \frac{\zeta}{1+\zeta^2}e_{fr}w + \sin\gamma F_{EF}\mu_b \\ =& \frac{\zeta}{1+\zeta^2}e_{fr}w + \sin\left(\arctan\left(\zeta\cos\beta\right)\right)F_{EF}\mu_b \\ =& \frac{\zeta}{1+\zeta^2}e_{fr}w + \frac{\zeta\cos\beta}{\sqrt{\cos^2(\beta)\zeta^2+1}}F_{EF}\mu_b \end{aligned} \tag{4.61}$$

and the resulting force is

$$F_R = \sqrt{\left(\frac{1}{1+\zeta^2}e_{fr}w + \cos\beta\cos\gamma F_{EF}\mu_b\right)^2 + \left(\frac{\zeta}{1+\zeta^2}e_{fr}w + \sin\gamma F_{EF}\mu_b\right)^2} \tag{4.62}$$

The above equations only depend on the specific cutting force e_{fr}, slice-push ratio ζ, cutting angle β, the normal force acting upon the cutting edge F_{EF}, and friction coefficient μ_b between stack and cutting edge.

Looking the entire process from a global point of view, the equations derived above need to accommodate the total resulting force acting upon the cutting knife, to e.g. allow comparison with measurement data. It is assumed that the stack rests upon a fixed boundary. Hence, for cutting the stack, the vertical component of the normal force acting upon the cutting edge need to be included in the equation, because it exerts a force on the cutting knife as well. The normal force acting against the knife is caused by the normal force between the sheets, caused by the compression. Since the stack undergoes large deformation, the assumption of the cutting process to be truly asymmetrical is no longer valid (see Figure 4.7), because the workpiece completely surrounds the cutting edge. Thus, the equations for the forces in the direction of large deformation need to be assumed to be similar to symmetrical cutting as shown in Figure 4.27. Due to the knife being asymmetrical, F_{EF} (equation (2.26)) will be different for both sides. On the cut off side, F_{EFc} depends on cutting angle and stack angle, as well as both friction coefficients. On the workpiece side, F_{EFw} depends only on the stack angle. Therefore, equation (4.60) is extended to

$$F_Z = \frac{1}{1+\zeta^2} e_{fr} w + \frac{\cos\beta}{\sqrt{\cos^2(\beta)\zeta^2+1}} F_{EFc}\mu_b + \sin\beta F_{EFc} + \sin\alpha F_{EFw} \tag{4.63}$$

where the last two terms correct for the vertical part of F_{EFc} and F_{EFw}, with

$$F_{EFc} = F_K \frac{\sin\alpha + \mu_{pp}\cos\alpha}{\left[\begin{array}{c}(\cos\beta - \mu_b\cos\gamma\sin\beta)(\cos\alpha - \mu_{pp}\sin\alpha) \\ -(\sin\beta + \mu_b\cos\gamma\cos\beta)(\sin\alpha + \mu_{pp}\cos\alpha)\end{array}\right]} \tag{4.64}$$

$$F_{EFw} = F_K \frac{\sin\alpha + \mu_{pp}\cos\alpha}{(\cos\alpha - \mu_{pp}\sin\alpha) - \left(\frac{\mu_{pp}(\cos\alpha + \sin\alpha)}{\sqrt{\zeta^2+1}}\right)} \tag{4.65}$$

Friction resulting from F_{EFw} is very small ($\beta = 0°$) and thus not included here. The lateral friction force obtained through equation (4.61) does not need to be adjusted, because the friction from the backside may be neglected as it is much smaller. Thus, the two parameters that need to be adjusted for fitting the experimental data are the specific cutting force e_{fr} and normal force between sheets F_K. In section 6.5, the above equations are experimentally verified for low ζ.

For ultrasonic vibration assisted cutting, the sensors incapability to recorded the high frequency oscillation of the vertical cutting force needs to be accommodated. An example of the resulting continuously changing slice-push ratio is shown in Figure 4.28. Figure 4.29a shows the overall trend of the normalized lateral cutting force and Figure 4.29b shows the overall trend of the normalized vertical cutting force for an oscillating ζ over two periods. While the velocity and consequently the slice-push ratio increases, the lateral force F_Y initially increases and asymptotically decreases until the maximum slice-push ratio is reached. The vertical force F_Z decreases asymptotically while the slice-push ratio increases. However, at high frequency oscillation, the force sensor cannot output the true values due to the dynamics of the stack and sensor. To calculate the time average of a

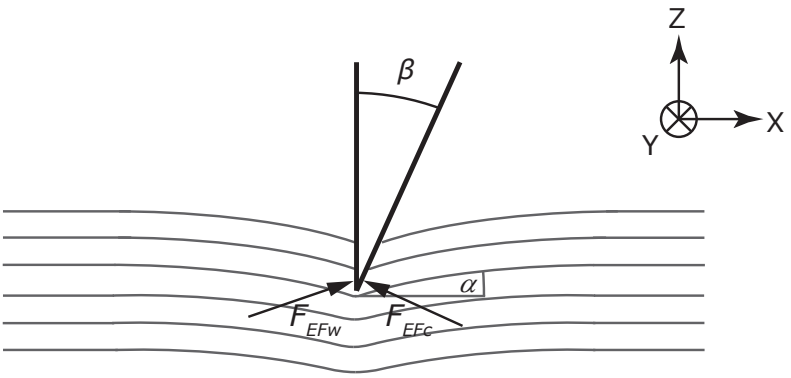

Figure 4.27: F_{EFc} and F_{EFw} acting against the cutting knife. F_{EFw} is caused by the large deformation due to the compression. α is the angle of the current sheet being cut.

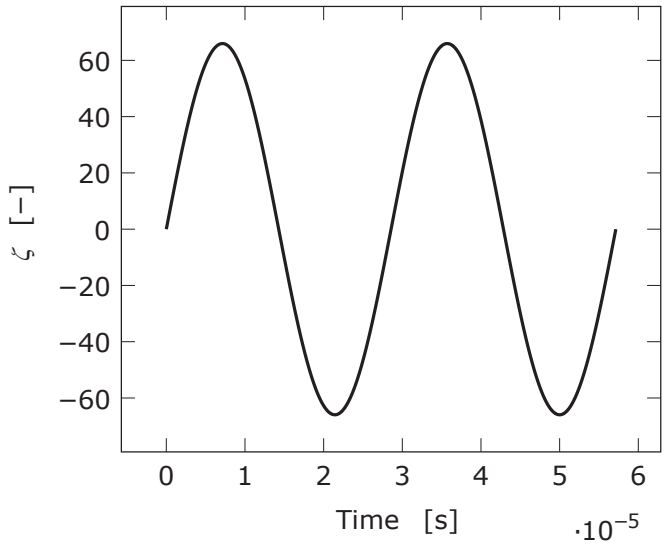

Figure 4.28: Slice-push ratio ζ over time for oscillation of $\omega = 35\,\mathrm{kHz}$ and $a_v = 5\,\mu\mathrm{m}$ of two periods, with $v_Z = 1000\,\mathrm{mm\,min^{-1}}$.

quarter period, the complete elliptic integral is used again. Calculating the time average of F_Z through the use of the complete elliptic integral is more complex and can be achieved through numerical computation.

Another theoretical approach is to define the friction occurring at the cutting edge as shear friction [143]. It is included here for comparison purposes and chosen over the previously introduced Coulomb model (section 2.3.1), because it models the friction effect as a separate variable independent of the cutting force. Shear friction allows modeling of friction forces of floppy materials, where there is no normal contact stress against the cutting edge [60]. Since Coulomb friction is inappropriate in the absence of normal contact stress, a constant shear stress τ_F acting over length L is introduced. Thus, the friction force becomes

$$F_F = L\tau_F w \tag{4.66}$$

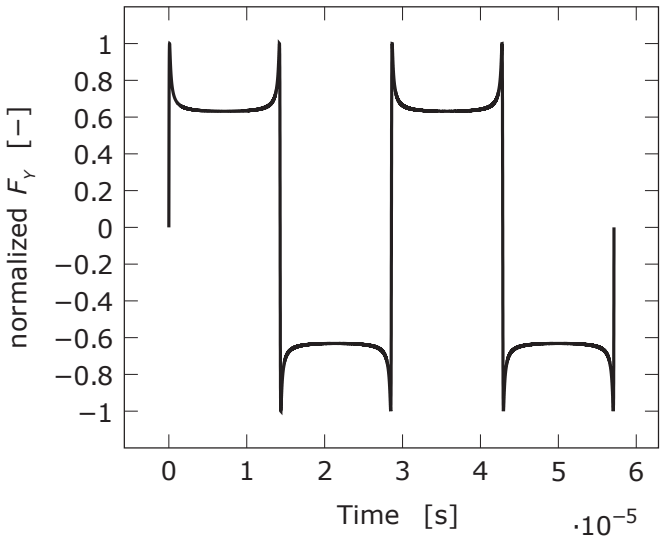

(a) F_Y over time for two periods of the oscillating slicing motion. The curve's shape depends on the material parameters. It is calculated from equation (4.61).

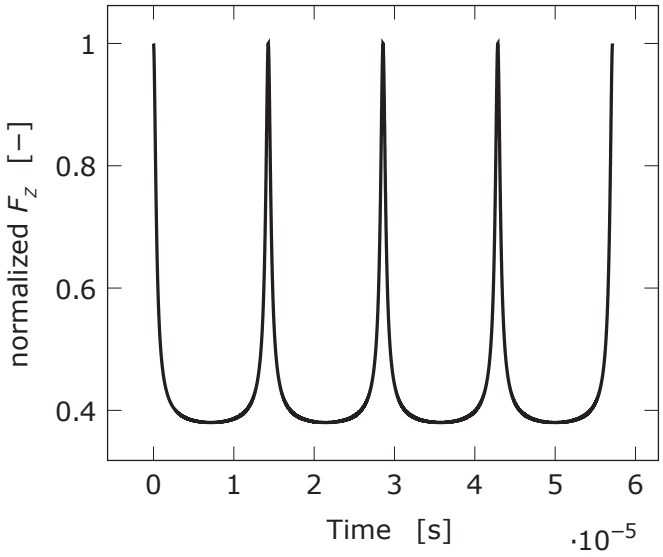

(b) F_Z over time for two periods of the oscillating slicing motion. The curve's shape depends on the material parameters. It is calculated from equation (4.63).

Figure 4.29: Forces over time for two periods of the oscillating slicing motion.

and the total forces in y- and z-direction is calculated to

$$F_Z = \frac{1}{1+\zeta^2} e_{fr} w + \frac{1}{\sqrt{1+\zeta^2}} L \tau_F w = \frac{1}{1+\zeta^2} e_{fr} w \left(1 + M\sqrt{1+\zeta^2}\right) \tag{4.67}$$

$$F_Y = \frac{\zeta}{1+\zeta^2} e_{fr} w + \frac{\zeta}{\sqrt{1+\zeta^2}} L \tau_F w = \frac{\zeta}{1+\zeta^2} e_{fr} w \left(1 + M\sqrt{1+\zeta^2}\right) \tag{4.68}$$

as in [60] with $M = \frac{L\tau_F}{e_{fr}}$. The shear force, which acts as friction force, increases the total force necessary for cutting. Values for the parameters e_{fr}, and M are unknown and will be fitted into the measurement data in section 6.5.

Here, the equilibrium of forces needs to be extended for a global consideration. In case the extended version of the shear friction model proves to be true, the original shear friction model is not appropriate to use for calculating the cutting forces, because it originally assumes a floppy material. Hence, the friction occurring during the guillotining of stacked paper sheets causes contact stress and requires Coulomb friction. As it is the case above, the vertical force needs to include some force that causes the friction at the cutting blade. Here, the vertical force is adjusted by

$$F_Z = \frac{1}{1+\zeta^2} e_{fr} w \left(1 + M\sqrt{1+\zeta^2}\right) + \frac{F_{add}}{1+\zeta^2} + F_{bdd} \tag{4.69}$$

with the last two terms adding a slice-push ratio dependent additional force and constant force. As before, these forces represent the force acting from the workpiece side onto the cutting knife.

Through the calculations for deriving the analytical model, it becomes apparent that the observed force reduction at the cutting edge is not only an effect from the combination of push cutting and slice cutting, which both contribute to material failure, but especially the friction force reduction in push cutting (vertical) direction.

5 Fracture Model of Slice-Push Cutting

In this chapter, the separation process of paper sheets during cutting with slice-push movement of the knife is analyzed by methods from fracture mechanics. In contrast to the previously discussed energy based model, the fracture mechanics model assumes fracture toughness to indicate material failure. Furthermore, the cutting of the stack is sideways (90° rotated), allowing proper crack propagation during cutting. Starting with the derivation of stress state at the cut edge, a fracture-mechanical model is build. Based on the analysis of the stress in push- and slice-direction, the cutting forces are derived while considering the point of fracture toughness. The following model will highlight the friction effects at the cutting edge during slice-push cutting. The FEM simulations carried out in this chapter were done with ABAQUS.

5.1 State of Stress at the Cut Edge

To start with the analysis of the stresses at the cut edge, a local coordinate system ($X'Y'Z'$) is introduced as shown in Figure 5.1, which is rotated around the Y-axis of the global coordinate system (XYZ) at an angle of β (angle of the cutting edge). Thus, the X'-axis is normal to the cutting face, and the Z'-axis is tangential to the cutting face. Within the new coordinate system, the tangential and normal stresses are calculated. In normal direction, the cutting edge is pushing into the cut edge of the material, resulting in a contact pressure p, causing a stress in X' direction as

$$\sigma_{X'X'} = -p \tag{5.1}$$

The tangential stress is the resulting friction along the cut edge, with its direction matching the relative velocity $\boldsymbol{v}_{r'}$ between cutting edge and cut edge with its components $v_{Y'}$ and $v_{Z'}$. Thus, it be can be said that

$$\boldsymbol{v}_{r'}^{X'Y'Z'} = \begin{pmatrix} 0 \\ v_{Y'} \\ v_{Z'} \end{pmatrix} = v_{r'} \begin{pmatrix} 0 \\ \dfrac{v_{Y'}}{v_{r'}} \\ \dfrac{v_{Z'}}{v_{r'}} \end{pmatrix} = v_{r'} \begin{pmatrix} 0 \\ \dfrac{v_{Y'}}{\sqrt{v_{Y'}^2 + v_{Z'}^2}} \\ \dfrac{v_{Z'}}{\sqrt{v_{Y'}^2 + v_{Z'}^2}} \end{pmatrix} \tag{5.2}$$

The previously introduced slice-push ratio can also be used here. With

$$\zeta = \frac{v_{Y'}}{v_{Z'}} \tag{5.3}$$

and

$$v_{Z'} = \frac{v_Z}{\cos\beta}, \quad \beta \in \left[0, \frac{\pi}{2}\right) \tag{5.4}$$

$$v_{Y'} = v_Y \tag{5.5}$$

the slice-push ratio along the flank plane can be rewritten as

$$\zeta' = \frac{v_{Y'}}{v_{Z'}} = \zeta \cos\beta \tag{5.6}$$

allowing the relative velocity to be expressed in the local coordinate system with the local slice-push ratio by

$$\boldsymbol{v}_{r'}^{X'Y'Z'} = v_{r'} \begin{pmatrix} 0 \\ \frac{v_{Y'}}{\sqrt{v_{Y'}^2 + v_{Z'}^2}} \frac{\frac{1}{v_{Z'}}}{\frac{1}{v_{Z'}}} \\ \frac{v_{Z'}}{\sqrt{v_{Y'}^2 + v_{Z'}^2}} \frac{\frac{1}{v_{Z'}}}{\frac{1}{v_{Z'}}} \end{pmatrix} = v_{r'} \begin{pmatrix} 0 \\ \frac{\zeta'}{\sqrt{1+\zeta'^2}} \\ \frac{1}{\sqrt{1+\zeta'^2}} \end{pmatrix} \tag{5.7}$$

Next, the tangential stress is derived. Assuming Coulomb friction, the resulting tangential stress becomes

$$\tau = \mu p \tag{5.8}$$

with μ being the friction coefficient between cutting edge and cut edge. From equation (5.8), it can be seen that effects in normal and tangential direction are correlated. Therefore, with the normal vector $\boldsymbol{n}^{X'Y'Z'} = (-1, 0, 0)^T$ the stress vector at the cut edge within the local coordinate system calculates to

$$\boldsymbol{s}^{X'Y'Z'}\boldsymbol{n} = -\begin{pmatrix} \sigma_{X'X'} \\ \tau_{X'Y'} \\ \tau_{X'Z'} \end{pmatrix} = p \begin{pmatrix} 1 \\ \frac{\mu\zeta'}{\sqrt{1+\zeta'^2}} \\ \frac{\mu}{\sqrt{1+\zeta'^2}} \end{pmatrix} \approxeq p \begin{pmatrix} 1 \\ \frac{\mu\zeta}{\sqrt{1+\zeta^2}} \\ \frac{\mu}{\sqrt{1+\zeta^2}} \end{pmatrix} \tag{5.9}$$

with the linear approximation $\zeta \approxeq \zeta'$ for small β. The resulting error is approximately 2.4 % for an angle of 12.5°, and 8.7 % for an angle of 24°. Therefore, the following cutting forces are slightly overestimated. Now, the stress vector needs to be transformed into the global coordinate system with the transformation matrix $\boldsymbol{\Upsilon}$, which is formed by constituting the basis vector of the local coordinate system in the global coordinate system by

$$\boldsymbol{\Upsilon} = \begin{pmatrix} \cos\beta & 0 & -\sin\beta \\ 0 & 1 & 0 \\ \sin\beta & 0 & \cos\beta \end{pmatrix} \tag{5.10}$$

Since it is assumed again that the cutting angle is very small, the transformation matrix may be linearized with the linear term of the Taylor series, resulting in

$$\boldsymbol{\Upsilon} = \begin{pmatrix} 1+\mathcal{O}(\beta^2) & 0 & -\beta+\mathcal{O}(\beta^2) \\ 0 & 1 & 0 \\ \beta+\mathcal{O}(\beta^2) & 0 & 1+\mathcal{O}(\beta^2) \end{pmatrix} \approxeq \begin{pmatrix} 1 & 0 & -\beta \\ 0 & 1 & 0 \\ \beta & 0 & 1 \end{pmatrix} \tag{5.11}$$

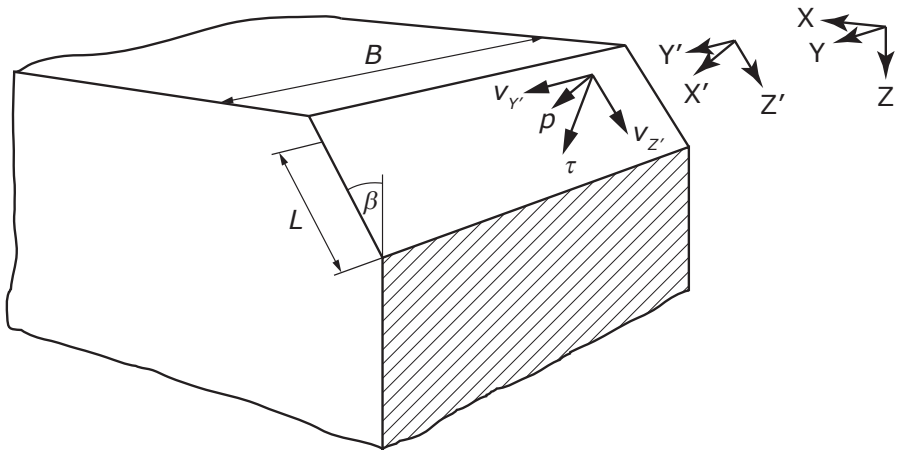

Figure 5.1: Asymmetrical cut. B is the material thickness, and L is the contact length between cutting edge and material. The local coordinate system is represented by $(X'Y'Z')$, and the global coordinate system is defined by (XYZ).

With the transformation matrix, the stress vector in the global coordinate system can be obtained as

$$\boldsymbol{s}^{XYZ} = p \begin{pmatrix} 1 & 0 & -\beta \\ 0 & 1 & 0 \\ \beta & 0 & 1 \end{pmatrix} \begin{pmatrix} 1 \\ \frac{\mu\zeta}{\sqrt{1+\zeta^2}} \\ \frac{\mu}{\sqrt{1+\zeta^2}} \end{pmatrix} = p \begin{pmatrix} 1 - \frac{\beta\mu}{\sqrt{1+\zeta^2}} \\ \frac{\mu\zeta}{\sqrt{1+\zeta^2}} \\ \beta + \frac{\mu}{\sqrt{1+\zeta^2}} \end{pmatrix} \tag{5.12}$$

5.2 Determination of the Stress Intensity Factors

5.2.1 Symmetrical Cutting Edge

In section 2.4, the concept of the stress intensity factors was briefly introduced to describe fracture mechanics at a crack tip. The stress intensity factors can be calculated by the limit value of the stress field near the crack tip. However, these definitions are of a general nature and cannot be solely used for finding an analytical description for loading at a specific workpiece. For specific fracture mechanical problems, known equations and tables or FEM need to be used. Here, the fracture mechanics example for mode I and mode II from [63] (Table 4.1) is applied. It assumes an infinite plane with a semi-infinite crack with all forces acting concentrated on one line near the crack tip (see Figure 5.2). To extend the known model with a mode III opening, FEM simulations were conducted to find an analogous mathematical relation. The FEM model is based on a sufficiently large fixed plate consisting of 4-node shell elements [144]. A slit in the middle of the plate with three quarters of the plate length and no lateral displacement is modeled. Forces are applied in small discrete steps (much smaller than size of the plate) along the slit and the crack is

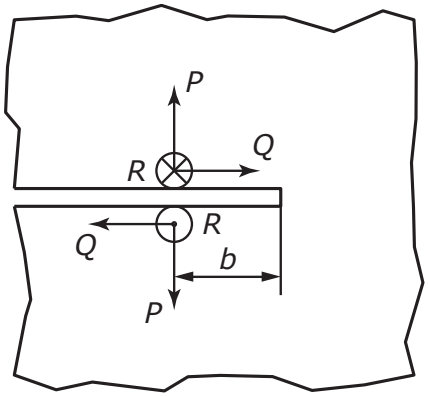

Figure 5.2: Forces at the crack tip (similar to case 4 in Table 4.1 of [63]).

gradually elongated (steps smaller than element length). The mesh is not changed with exception at the crack tip. This procedure is also called virtual crack extension [64]. To calculate the stress intensity factors, the total elastic energy within the plate was analyzed. The energy release rate defined by

$$\mathcal{G} = \frac{1}{B}\frac{\partial U}{\partial a} \tag{5.13}$$

is approximated by relating the elastic energy U to the crack elongation a and dividing the slope of the regression curve by the plate thickness B. From the energy release rate, the stress intensity factors

$$K_I = \sqrt{\mathcal{G}E}, \quad K_{II} = \sqrt{\mathcal{G}E}, \quad K_{III} = \sqrt{\mathcal{G}2G} \tag{5.14}$$

were derived [63], with E being Young's Modulus and $G = \frac{E}{2(1+\nu)}$ being the shear modulus with ν as the Poisson ratio. It should be pointed out that equation (5.14) is only valid for pure modes and not mixed loads. The numerical model was verified with the analytical formulas [63]

$$K_I = \frac{2P}{\sqrt{2\pi b}}, \quad K_{II} = \frac{2Q}{\sqrt{2\pi b}} \tag{5.15}$$

for the first two crack modes as shown in Figure 5.3. For the simulations of the third modulus, a slightly different correlation between load distance b and stress intensity was found. While for modes I and II, the K-factor is negatively correlated to the square root of the load distance, it is positively correlated to the K-factor for mode III. Through dimensional analytical considerations, a parameter in mm^{-1} units is introduced. This is accomplished by including the plate thickness, which is verified through the FEM simulation as shown in Figure 5.4. The formula

$$K_{III} = c\frac{R\sqrt{b}}{B} \tag{5.16}$$

gives the stress intensity factor for mode III in this specific case, where B is plate thickness, R is the loading force, and $c \approxeq 2.8$ as identified with the FEM results.

As mentioned before, equations (5.15) and (5.16) are valid for line loads and need to be integrated to allow for area loading under the assumption of linear elasticity. When considering $P \to p$,

$$\mathrm{d}K_I = \frac{2p\mathrm{d}z}{\sqrt{2\pi z}} \tag{5.17}$$

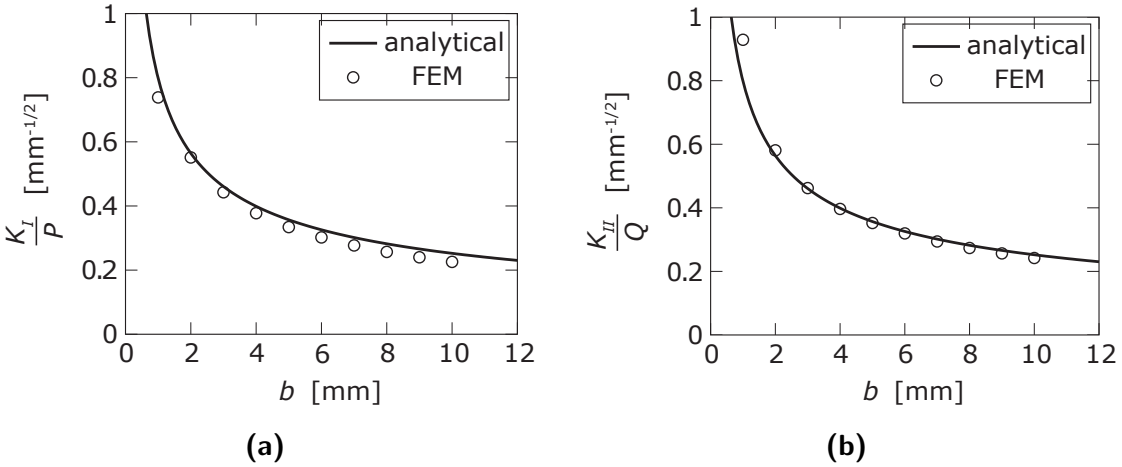

Figure 5.3: Comparison between FEM and analytical calculations of the stress intensity factors for modes I and II within a plane (see Figure 5.2). K-factors are normalized with the line loading P and Q. The 2D FEM model is used.

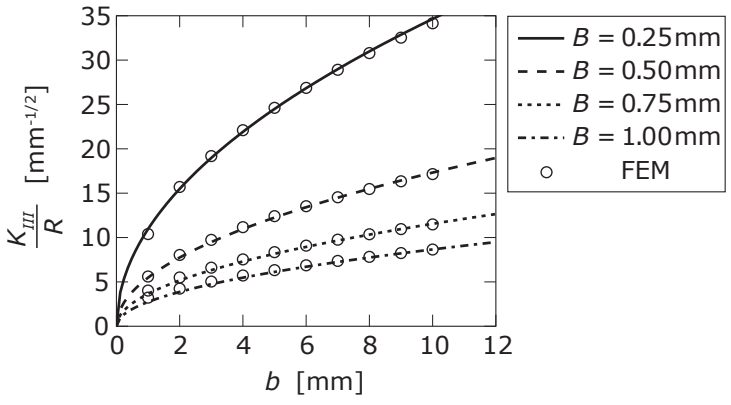

Figure 5.4: Numerically calculated stress intensity factor K_{III} and fitted curves for different plate thickness B. Normalized by the applied line load R.

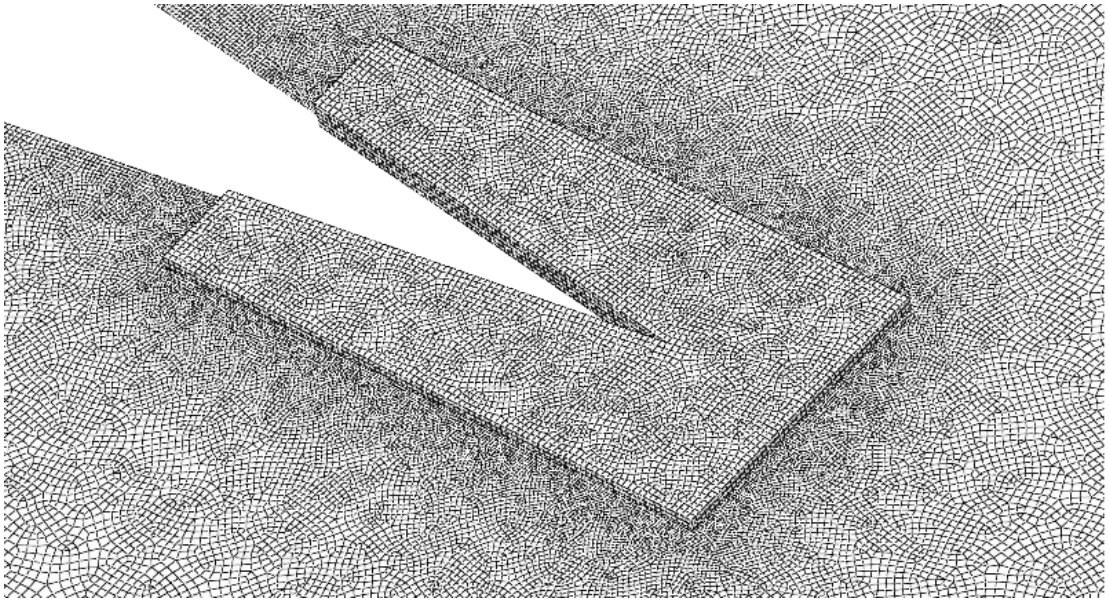

Figure 5.5: FEM Model for stress intensity factors [144]. The region around the crack tip is meshed with three-dimensional elements, and the surrounding area with two-dimensional elements (boundaries not visible).

is valid for an infinitesimal part along the crack edge, and results in

$$K_I = \int_{b_0}^{b_1} \frac{2p\mathrm{d}z}{\sqrt{2\pi z}} = \frac{4p}{\sqrt{2\pi}} \left[\sqrt{b_1} - \sqrt{b_0}\right] \tag{5.18}$$

where b_0 is the distance from the crack tip to the front of the applied load, and b_1 is the distance from the crack tip to the back of the applied load. Assuming that $b_0 \ll b_1$, the equation can be further simplified. With $Q \to \tau_{YZ}$ and $R \to \tau_{YX}$, the K-factors

$$K_I = \frac{4p}{\sqrt{2\pi}}\sqrt{L}, \quad K_{II} = \frac{4\tau_{YZ}}{\sqrt{2\pi}}\sqrt{L}, \quad K_{III} = \frac{2}{3}c\frac{\tau_{YX}\sqrt{L^3}}{B} \tag{5.19}$$

are obtained with L being the contact length of the cutting edge (see Figure 5.1).

Because the cutting angle is not a negligible value, the previously mentioned FEM model was refined to allow proper representation of the three dimensional problem: the region near the crack tip consists of three dimensional cube elements, and the rest of the plate consists of shell elements as shown in Figure 5.5; the displacement between the two parts are locked. Furthermore, the model no longer calculates the elastic energy as it is done previously, but directly calculates the stress intensity factors (which is actually done via energy as explained in [64]).

The hybrid model formulation is again used to verify the above stated equations for modes I and II and obtain an analytical equation for mode III. However, for the symmetrical cutting edge only mode I is valid and thus it is solely considered here. Figure 5.6 plots the results of the analytical equation and numerical simulation for K_I. It can be seen that the stress intensity factor does not significantly change with larger cutting angles. Therefore, the first equation of correlation (5.19) will be used for further considerations of symmetrical cutting.

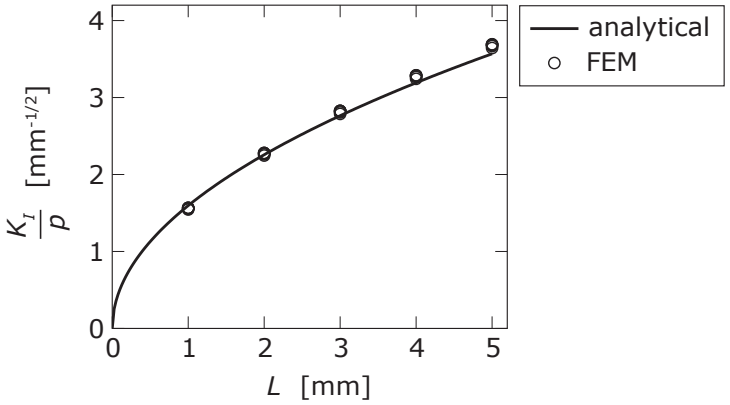

Figure 5.6: Numerically calculated stress intensity factor K_I with the hybrid FEM model and symmetrical cutting edge, depending on the actual contact length L, for $\beta = 0°$, $2.5°$, $5°$, $7.5°$, $10°$ and $12.5°$. The curve represents the analytical result of the first equation of (5.19) at $\beta = 0$, normalized by the pressure p.

5.2.2 Asymmetrical Cutting Edge

To obtain the stress intensity factors for asymmetrical loading, the new hybrid simulation model with volume elements around the crack tip is used. Unlike in the symmetrical case, only the single side rotated by β is under loading. The side parallel oriented to the cutting direction was defined as fixed, meaning boundary conditions do not allow any displacement. In addition, area loading was directly applied to obtain correlations similar to (5.19). An example for this is the slicing of sheet material while guiding it on one side parallel to the cutting process. For the first mode, a similar behavior to the symmetrical case was observed as shown in Figure 5.7. Small angles do not significantly impact K_I. For the second mode, the stress intensity changes with approximately the sine of the cutting angle as visible in Figure 5.8. However, the global trend of functions matches the one of K_I as in the symmetrical case. For the third mode, a completely different behavior is observed as shown in Figure 5.9. The stress intensity factor increases linearly with the length of the area under loading, and decreases linearly with an increasing cutting angle. Hence, two additional proportionality factors need to be introduced. These are, unlike for the first two crack modes, not dimensionless. The stress intensity factors for asymmetrical loading

$$K_I = pc_I\sqrt{L}, \quad K_{II} = \tau_{Y'Z'}c_{II}\sqrt{L}\,(1-\beta)\,, \quad K_{III} = \tau_{Y'X'}\frac{L}{B}\,(c_{III_1} + c_{III_2}\beta) \tag{5.20}$$

are calculated, with $c_I = c_{II} = 0.871$, $c_{III_1} = 4.11\,\mathrm{mm}^{1/2}$, and $c_{III_2} = -2.39\,\mathrm{mm}^{1/2}$ obtained through numerical calculations.

5.3 Cutting Forces

From section 5.1, the stress at the cutting edge is known as a function of friction and slice-push ratio, and from section 5.2, the correlation between stress and stress intensity factors is outlined. From these two considerations, the cutting forces in y-direction (lateral) and z-direction (vertical) direction are now derived.

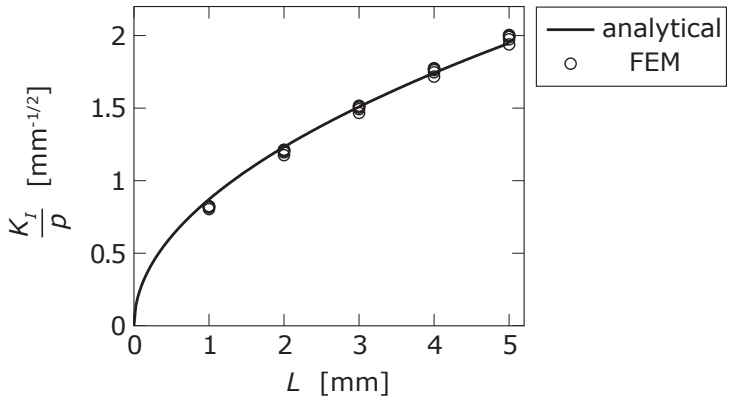

Figure 5.7: Numerically calculated stress intensity factor K_I with the hybrid FEM model and asymmetrical cutting edge, depending on the actual contact length L, for $\beta = 0°, 2.5°, 5°, 7.5°, 10° \text{ and } 12.5°$. The curve represents the analytical result of (5.20) at $\beta = 0$, normalized by the pressure p.

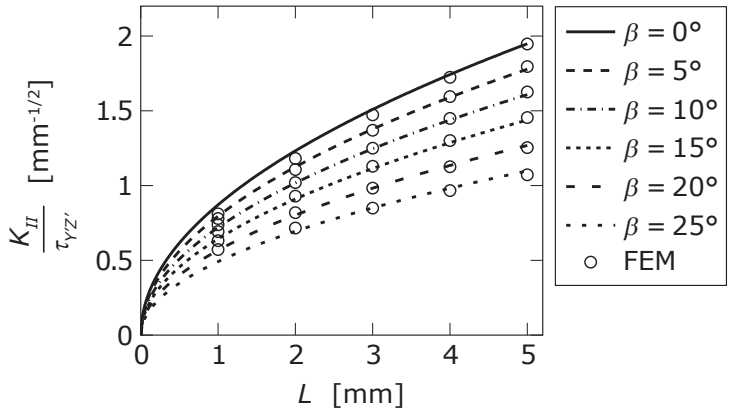

Figure 5.8: Numerically calculated stress intensity factor K_{II} with the hybrid FEM model and asymmetrical cutting edge, depending on the actual contact length L, for $\beta = 0°, 2.5°, 5°, 7.5°, 10° \text{ and } 12.5°$. The curves represents the analytical result of (5.20), normalized by the shear stress $\tau_{Y'Z'}$.

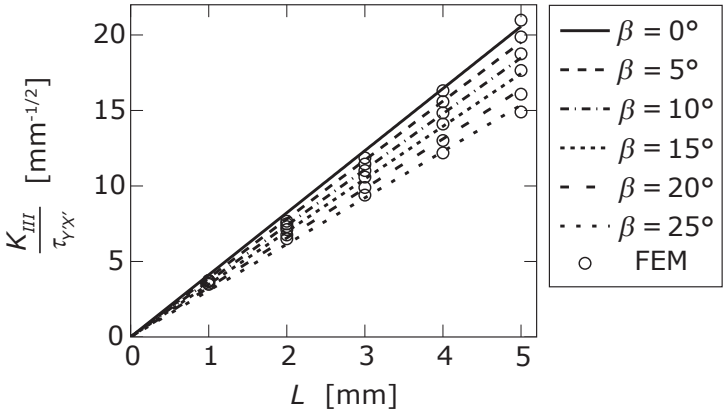

Figure 5.9: Numerically calculated stress intensity factor K_{III}, depending on the actual contact length L, for $\beta = 0°$, 2.5°, 5°, 7.5°, 10° and 12.5°. The curves represents the analytical result of (5.20), normalized by the shear stress $\tau_{Y'X'}$. Hybrid FEM model and asymmetrical cutting edge.

5.3.1 Symmetrical Cutting Edge

When multiplying the stress from (5.12) with the plate thickness B and the effective length L along the cutting edge, the force acting upon the knife can be obtained, assuming the compressive stress is uniformly distributed. Starting with a single side of the cut edge: for the quasi static condition, the vertical cutting force is in equilibrium with the projected area loading and the projected shear stress in z-direction, each multiplied with contact area BL. Hence, the stress vector may be simple multiplied with the unit vector indicating the direction of the force. For the symmetrical cutting edge,

$$F_Z = 2BLp(\boldsymbol{s})^T \boldsymbol{e}_z = 2BLp \begin{pmatrix} 1 - \dfrac{\beta\mu}{\sqrt{1+\zeta^2}} \\ \dfrac{\mu\zeta}{\sqrt{1+\zeta^2}} \\ \beta + \dfrac{\mu}{\sqrt{1+\zeta^2}} \end{pmatrix}^T \begin{pmatrix} 0 \\ 0 \\ 1 \end{pmatrix} = 2BLp\left(\beta + \frac{\mu}{\sqrt{1+\zeta^2}}\right) \tag{5.21}$$

is calculated. This function is an asymptotic monotonously decreasing function with ζ (positive parameters) as shown in Figure 5.10. To analyze the effect of ζ, the limit values are considered. Without any slicing, the vertical cutting force becomes

$$\lim_{\zeta \to 0} F_Z = 2BLp(\beta + \mu) \tag{5.22}$$

and with maximum slicing, it becomes

$$\lim_{\zeta \to \infty} F_Z = 2BLp(\beta) \tag{5.23}$$

Based on these limit values, it is clear that the vertical cutting force changes significantly at constant area loading (pressure at the cutting edge), with the factor

$$\frac{\lim_{\zeta\to\infty} F_Z}{\lim_{\zeta\to 0} F_Z} = \frac{\beta}{\beta+\mu} = \frac{1}{1+\frac{\mu}{\beta}} = \frac{1}{1+\varpi} \tag{5.24}$$

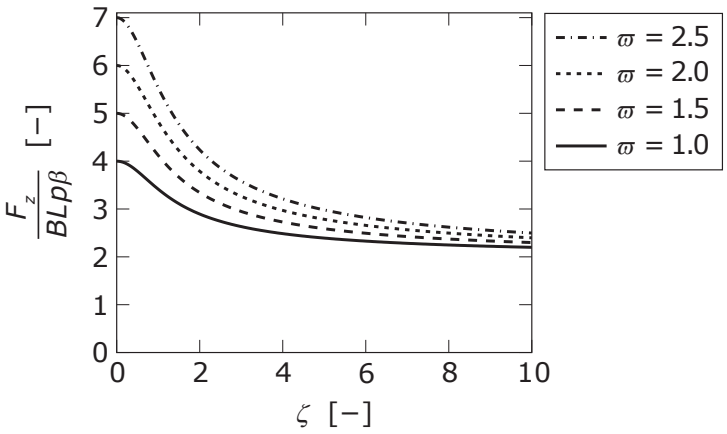

Figure 5.10: Trend of the vertical cutting force (normalized by contact pressure, contact area, and cutting angle), depending on slice-push ratio ζ for various ϖ, taken from (5.21).

with

$$\varpi = \frac{\mu}{\beta} \tag{5.25}$$

Thus, the vertical cutting force solely depends on the relation between friction coefficient and cutting angle. This effect is more distinct with a higher friction coefficient and smaller cutting angle. With $\mu \approxeq \beta$ (with β in [rad]), a 50 % decrease in the vertical force can be observed, when cutting with a slice-push motion.

The physical explanation of this phenomenon is simple: With an increasing slice-push ratio, the shear stress acts more in y-direction and does not need to be overcome by the vertical force (advance force) in z-direction, but by the horizontal force in y-direction.

Next, the horizontal cutting force and its dependency on ζ is considered. Again, the stress vector is multiplied with the contact area and unit vector, resulting in

$$F_Y = 2BLp(\boldsymbol{s})^T \boldsymbol{e}_y = 2BLp \begin{pmatrix} 1 - \dfrac{\beta\mu}{\sqrt{1+\zeta^2}} \\ \dfrac{\mu\zeta}{\sqrt{1+\zeta^2}} \\ \beta + \dfrac{\mu}{\sqrt{1+\zeta^2}} \end{pmatrix}^T \begin{pmatrix} 0 \\ 1 \\ 0 \end{pmatrix} = 2BLp\frac{\mu\zeta}{\sqrt{1+\zeta^2}} \tag{5.26}$$

As expected, the horizontal force or slicing force increases with the slice-push ratio and friction coefficient. It is displayed in Figure 5.11. Again, the limit values are considered, resulting in

$$\lim_{\zeta\to 0} F_Y = 0 \tag{5.27}$$

$$\lim_{\zeta\to\infty} F_Y = 2BLp\mu \tag{5.28}$$

whereat $\lim_{\zeta\to\infty} \sqrt{1+\zeta^2} = \zeta$ was used. The resulting cutting force is calculated through

$$F_R = \sqrt{F_Y^2 + F_Z^2} = 2BLp\sqrt{\frac{\left(\beta\sqrt{1+\zeta^2}+\mu\right)^2 + (\mu\zeta)^2}{1+\zeta^2}} \tag{5.29}$$

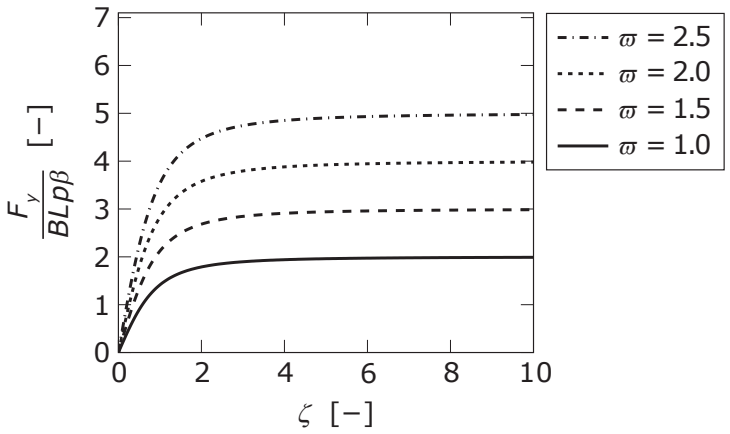

Figure 5.11: Trend of the horizontal cutting force (normalized by contact pressure, contact area, and cutting angle), depending on slice-push ratio ζ for various ϖ, taken from (5.26).

shown in Figure 5.12 and its limit values are

$$\begin{aligned}\lim_{\zeta\to 0} F_R &= \sqrt{\left(\lim_{\zeta\to 0} F_Y\right)^2 + \left(\lim_{\zeta\to 0} F_Z\right)^2} \\ &= \sqrt{0 + \left(2BLp(\beta+\mu)\right)^2} = 2BLp(\beta+\mu)\end{aligned} \tag{5.30}$$

$$\begin{aligned}\lim_{\zeta\to \infty} F_R &= \sqrt{\left(\lim_{\zeta\to \infty} F_Y\right)^2 + \left(\lim_{\zeta\to \infty} F_Z\right)^2} \\ &= \sqrt{\left(2BLp\mu\right)^2 + \left(2BLp\beta\right)^2} = 2BLp\sqrt{\mu^2+\beta^2}\end{aligned} \tag{5.31}$$

Again, the quotient of the two limit values yields

$$\frac{\lim_{\zeta\to\infty} F_R}{\lim_{\zeta\to 0} F_R} = \frac{2BLp\sqrt{\mu^2+\beta^2}}{2BLp(\beta+\mu)} = \frac{\sqrt{1+\left(\frac{\mu}{\beta}\right)^2}}{1+\left(\frac{\mu}{\beta}\right)} = \frac{\sqrt{1+\varpi^2}}{1+\varpi} \tag{5.32}$$

indicating that the ratio between friction coefficient and cutting angle is the essential factor. Unlike for the vertical cutting force, this correlation is no longer monotonous as shown in Figure 5.13. It contains a minimum at $\varpi = 1$ and thus a maximum resulting force reduction of 30 % may be obtained. It should be pointed out again that these effects solely consider friction along the cutting edge, making this a dissipative process.

Finally, the balance of forces and the fracture mechanical consideration shall be combined to allow the calculation of the required cutting forces based on the fracture toughness K_{Ic}. Assuming an elastic material, the cutting occurs at the point where the fracture toughness (critical stress intensity factor) is reached. For symmetrical cutting, equation (5.19) becomes

$$p = \frac{K_{Ic}\sqrt{2\pi}}{4\sqrt{L}} \tag{5.33}$$

Inserting this into equations (5.21) and (5.26) with the definition of ϖ, the cutting forces

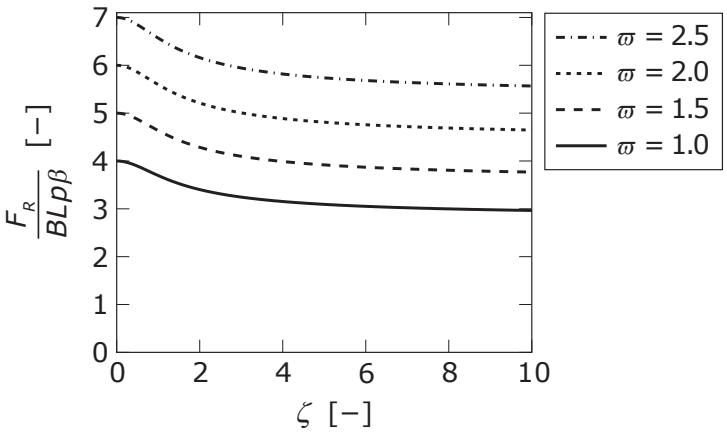

Figure 5.12: Trend of the resulting cutting force (normalized by contact pressure, contact area, and cutting angle), depending on slice-push ratio ζ for various ϖ, taken from (5.29).

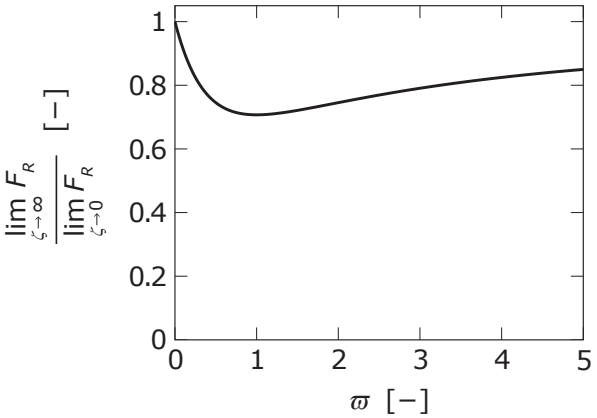

Figure 5.13: Ratio between resulting cutting force for infinity slice-push ratio and zero slice-push ratio, depending on ζ for various ϖ as stated in (5.32).

are calculated with

$$F_Z = B\sqrt{L}K_{Ic}\beta\frac{\sqrt{2\pi}}{2}\left(1+\frac{\varpi}{\sqrt{1+\zeta^2}}\right) \tag{5.34}$$

$$F_Y = B\sqrt{L}K_{Ic}\beta\frac{\sqrt{2\pi}}{2}\frac{\varpi\zeta}{\sqrt{1+\zeta^2}} \tag{5.35}$$

5.3.2 Asymmetrical Cutting Edge

When cutting with an asymmetrical cutting knife, only one cutting face is assumed to be in contact with the workpiece. This simple removes the factor 2 from the symmetrical considerations. However, during asymmetrical cutting, the asymmetrical fracture modes II and III may occur, resulting in a variable pressure loading at the cutting face. Consequently, a criterion including mixed loading must be found. According to [64], the energy release rate may be calculated from the stress intensity factors

$$\mathcal{G} = \frac{K_I^2}{E}+\frac{K_{II}^2}{E}+\frac{K_{III}^2}{2G} \tag{5.36}$$

With a known fracture toughness,

$$\mathcal{G}_c = \frac{K_{Ic}^2}{E} \tag{5.37}$$

is defined. Inserting this into equation (5.36), gives

$$K_I^2+K_{II}^2+K_{III}^2(1+\nu) = K_{Ic}^2 \tag{5.38}$$

as the necessary condition for crack propagation, with $G = \frac{E}{2(1+\nu)}$, and the assumption that the overall fracture toughness is dominated by K_{Ic}. As stated in [64], K_{IIc} and K_{IIIc} are generally much larger than K_{Ic}. Inserting (5.20) into (5.12) gives

$$\begin{aligned} K_I &= c_I p\sqrt{L}, \\ K_{II} &= c_{II}(1-\beta)\underbrace{p\frac{\mu}{\sqrt{1+\zeta^2}}}_{\tau_{Y'Z'}}\sqrt{L}, \\ K_{III} &= (c_{III_1}+c_{III_2}\beta)\underbrace{p\frac{\mu\zeta}{\sqrt{1+\zeta^2}}}_{\tau_{Y'X'}}\frac{L}{B}. \end{aligned} \tag{5.39}$$

Hence,

$$p\sqrt{L}\sqrt{(c_I)^2+\left(c_{II}(1-\beta)\frac{\mu}{\sqrt{1+\zeta^2}}\right)^2+\left((c_{III_1}+c_{III_2}\beta)\frac{\mu\zeta}{\sqrt{1+\zeta^2}}\frac{\sqrt{L}}{B}\right)^2(1+\nu)} = K_{Ic} \tag{5.40}$$

Assuming $\mu \ll 1$ allows the second term to be negligible: Mode II becomes insignificant. For the third term (Mode III) the same argument holds, except for very small values of B.

However, the case of very small B is exempted here. The critical contact pressure is thus defined by

$$p_c = \frac{K_{Ic}}{\sqrt{L} c_I} \tag{5.41}$$

Inserting this into equations (5.21) and (5.26), omitting factor 2 due to asymmetrical cutting, and with the definition of ϖ from equation (5.25), the cutting forces are calculated with

$$F_Z = B\sqrt{L} K_{Ic} \beta \frac{1}{c_I} \left(1 + \frac{\varpi}{\sqrt{1+\zeta^2}} \right) \tag{5.42}$$

$$F_Y = B\sqrt{L} K_{Ic} \beta \frac{1}{c_I} \frac{\varpi \zeta}{\sqrt{1+\zeta^2}} \tag{5.43}$$

with $\frac{1}{c_I} \approxeq 1.15$ (numerically calculated from FEM results). In the next chapter, these findings are experimentally verified.

6 Vibration Assisted Guillotining of Paper Stacks - Model Verification

Some parts of the following content have been published by the author in [B.v].

6.1 Experimental Setups

To verify the various findings of the above discussed models, three test stands were setup as shown in Figure 6.1, Figure 6.2, and Figure 6.3. The purpose of the first setup is to vertically cut stacks at different feed rates and vibration amplitudes. Knives are connected to the z-carriage, which moves CNC controlled in z-direction. Stacks of different height and width may be placed below it on the table. Forces are measured below the stack with two parallel Kistler pressure force sensors 9323A. During the process, position of the z-carriage, and power output of the ultrasonic generator feeding the transducer are synchronously measured with the force data. The generator providing power to the ultrasonic transducer has an operating frequency of $35.0\,\mathrm{kHz} \pm 0.5\,\mathrm{kHz}$. The generator output power ranges from 0 W to 1200 W, with 900 W being the maximum power for continuous operation. Sampling rate of the recording device is 350 kHz, which is chosen for the dynamic verification of the model.

The second setup (Figure 6.2) provides the possibility to measure the lateral and vertical forces when cutting with low slice-push ratios. A three axial force measurement platform is placed on the table of a three-axis machine tool (CNC), and a asymmetrical cutting knife is inserted in a rotationally blocked spindle. By overlaying different linear paths in vertical and lateral direction, various slice-push ratios can be defined. Feed rate is kept constant for all experiments. Stacks of different size and width may be fixed on top of the platform by either directly fixating it or blocking specific degrees of freedom. This setup is slightly reconfigured for the verification of the fracture mechanic model, which requires a 90° rotated paper stack.

The third experimental setup (Figure 6.3) allows the measurement of the cutting force when using the newly created cutting knife for lateral ultrasonic vibration assisted cutting. The cutting knife is mounted at the nodal points onto the CNC controlled z-carriage, and the ultrasonic transducer provides the necessary operation frequency. A three axial force measurement platform is placed below the paper stack to record the vertical cutting force. The feedrate is chosen to achieve a very high slice-push ratio during the cutting process.

The material used as workpiece for the experiments is printed label paper with an average thickness of 0.06 mm and an area density of $68\,\mathrm{g\,m^{-2}}$. The upper side of the paper contains typical printing for beer bottles, while the lower side is without printing or coating. Stack width is 37 mm and its height 50 mm. The paper stack is stabilized for handling with a carton board underneath. The thickness of the cardboard is 1 mm.

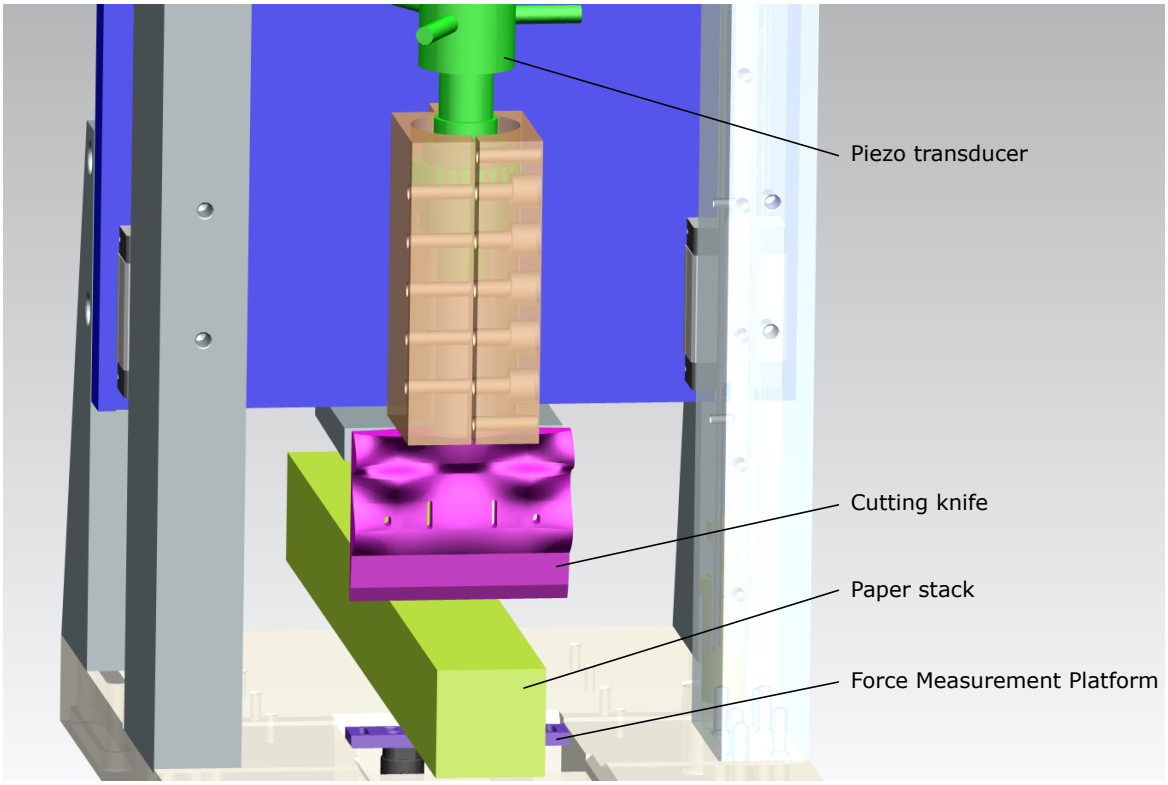

Figure 6.1: Schematic drawing of the experimental setup for determining the cutting forces for longitudinal ultrasonic vibration assisted cutting and verification of the dynamic model. Total nodal displacement FEM solution for the cutting knife is shown in Figure 3.11.

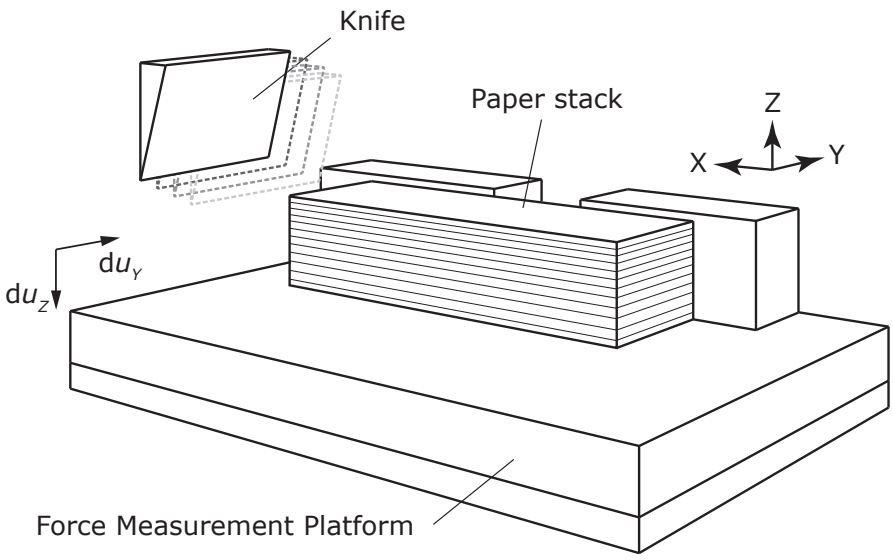

Figure 6.2: Schematic drawing of the experimental setup for determining the cutting forces for various slice-push ratios.

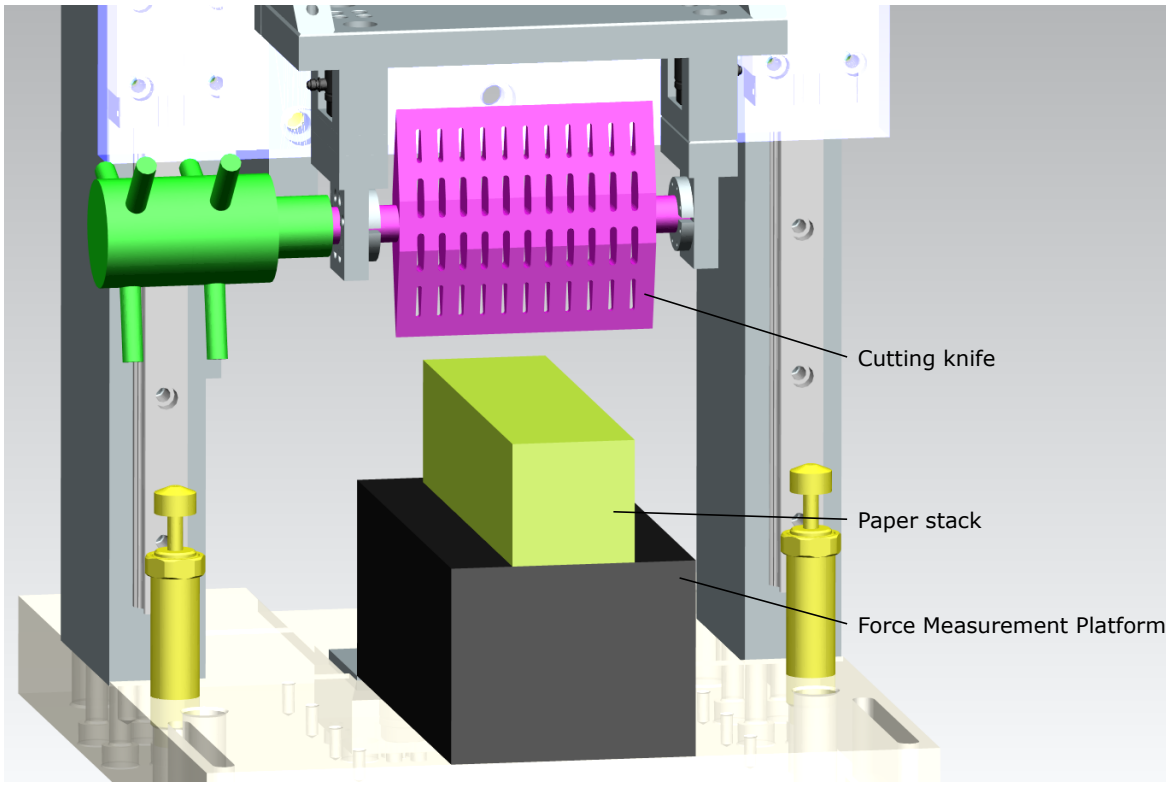

Figure 6.3: Schematic drawing of the experimental setup for determining the cutting forces for lateral ultrasonic vibration assisted cutting. Total nodal displacement FEM solution for the cutting knife is shown in Figure 3.10.

6.2 Proof of Concept for Structural Optimized Longitudinal Cutting Knife

To test whether the optimization methodology is capable of providing the desired mode shape at the specified resonance frequency, the asymmetrical cutting knife for longitudinal ultrasonic vibration assisted cutting (Figure 3.11) is experimentally verified using a two-dimensional laser-vibrometer. This requires a unique experimental setup, where the cutting edge is severely blunted by shortening the overall height of the knife from the cutting edge. Due to the shortened height, the operating frequency will be higher and the mode shape slightly changed. The blunt edge's diffuse reflecting capability is enhance by applying a special diffuse reflection tape. Measurements with transducer excitation at 100 volts are carried out at 25 evenly distributed measurement points along the cutting edge in x- and z-direction. The measured displacement of the cutting edge in x-direction is shown in Figure 6.4a and the measured displacement in z-direction is shown in Figure 6.4b. The bending mode and longitudinal mode are clearly visible. Since the cutting knife is overall shortened, the bending mode may be considered to be larger than when using the unaltered cutting knife. Overall, the optimization methodology for designing the cutting knives seems to deliver appropriate results. Consequently, the designed cutting knives are eligible to be used in the following experiments.

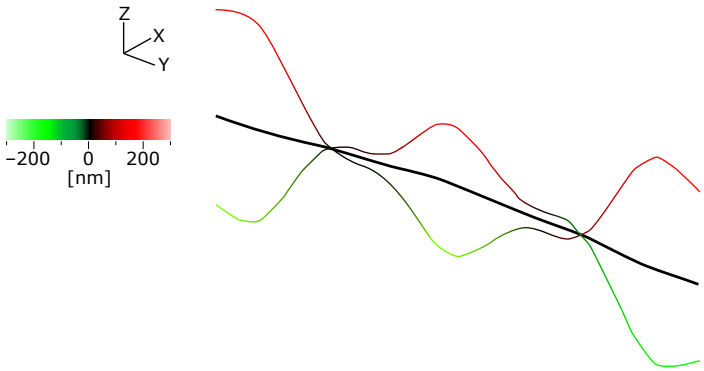

(a) Laser-Vibrometer Measurement at the blunt cutting edge in x-direction. Total displacement shown.

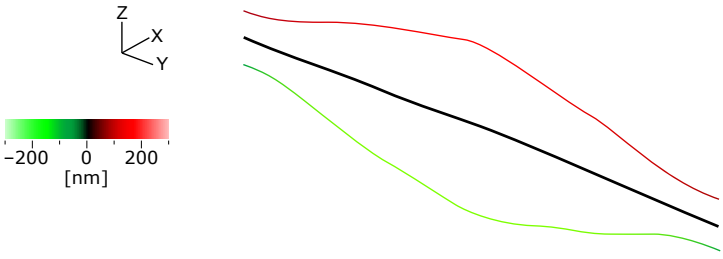

(b) Laser-Vibrometer Measurement at the blunt cutting edge in z-direction. Total displacement shown.

Figure 6.4: Laser-Vibrometer Measurements of the optimized longitudinal ultrasonic vibration assisted cutting knife shown in Figure 3.11. Bending mode amplitude is increased due to the prerequisite blunting of the cutting edge. Operation frequency is 36.2 kHz.

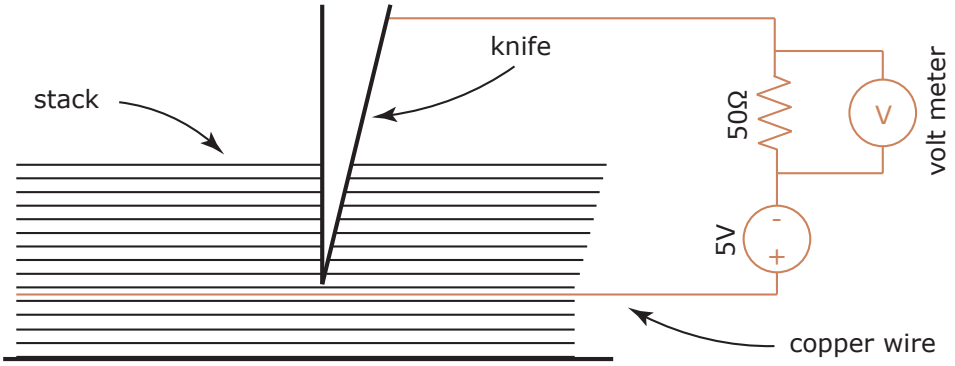

Figure 6.5: Measurement setup for determining the contact time between knife and paper stack.

6.3 Dynamic Model Verification and Results

6.3.1 Dynamic Model Settings

To verify the previously introduced dynamic model for vibration assisted guillotining of stacks, the following settings were selected for the experiments and simulations:

- Feed rate of 750 mm min^{-1} and 1000 mm min^{-1}
- Vibration frequency of 35 kHz or none
- Vibration amplitude of 0 µm, 4 µm, and 8 µm
- Stiffness and Damping from section 4.2.5
- For the simulation: 21 sheets of paper

6.3.2 Dynamic Behavior

To verify the dynamic behavior of the dynamic model, it is practical to test whether the cutting knife detaches from the stack at high frequency vibration. The out-of-contact time is mainly dependent on vibration amplitude, frequency, feed forward, stiffness, and damping of the material. Therefore, the contact time between cutting knife and stack was determined using the measurement setup schematically depicted in Figure 6.5. Copper wires with a diameter of 0.2 mm were inserted at three different levels (Table 6.1) within the stack, and attached to one terminal of a 5 V source. The other terminal was connected to the cutting knife. Contact between cutting knife and stack is determined by the current in the wire. Every time the knife comes into contact with one of the copper wires, the voltage jumps from 0 V to 5 V.

Figure 6.6 shows the results for one experiment. The peaks indicating contact between cutting knife and stack can be clearly seen. At the beginning of each contact measurement, the voltage oscillates between 0 V to 5 V, indicating discontinuous contact. After some time, the voltage stays constant at 5 V due to the wire now continuously touching the back

Wire	Position
1	$\approx 42\,\mathrm{mm}$
2	$\approx 27\,\mathrm{mm}$
3	$\approx 15\,\mathrm{mm}$

Table 6.1: Placement of the copper wires within the stack for contact time measurements. Uncompressed stack height is $\approx 50\,\mathrm{mm}$.

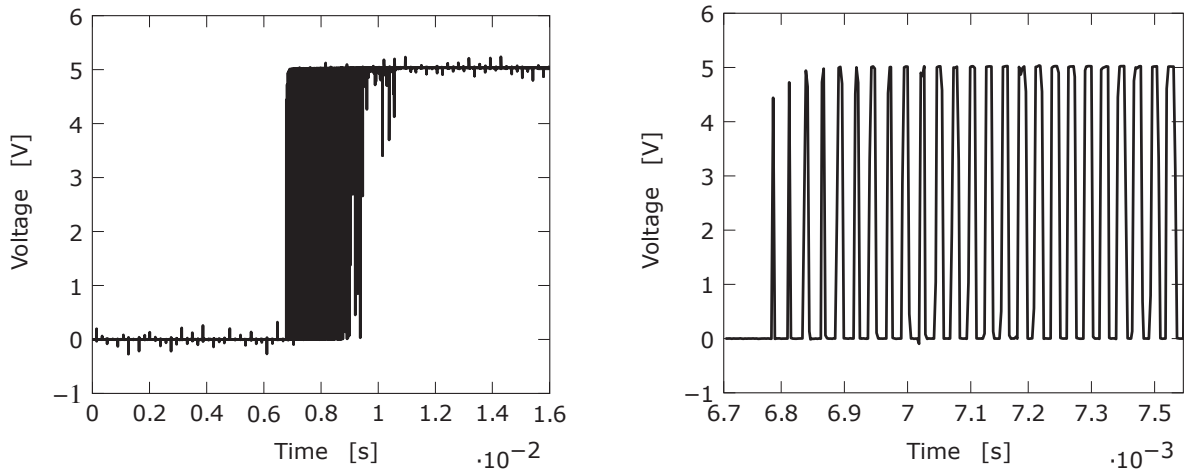

(a) Example for discontinuity. **(b)** Zoom in from (a).

Figure 6.6: Voltage output during discontinuous contact phase of the longitudinal vibration assisted cutting process.

face of the cutting knife without loosing contact. To determine the contact ratio during the discontinuous cycle of the process, the contact ratio is calculated by

$$r_{con} = \frac{t_c}{t_c + t_{noc}} \tag{6.1}$$

where t_c is the time of contact between wire and knife, and t_{noc} is the time of no contact between wire and knife. The average contact ratio is obtained with

$$\bar{r}_{con} = \frac{1}{n} \sum_{i=1}^{n} r_{con}(i) \tag{6.2}$$

Figure 6.7 shows the contact ratio of the experiments and Figure 6.8 shows the contact ratio of the simulation for comparison. In contrast to the experimental cutting of a stack with 50 mm height, the simulation runs only with 21 sheets to save computing time. Regarding the average contact ratio, the simulation closely matches the average contact ratio of the experiments. The same can be seen in Figure 6.9 and Figure 6.10 for a higher feed rate. Thus, the experiments indicate overall proper simulation of the stack's dynamic behavior. In the experiments, the cutting knife detaches from the stack as well as in the simulation. Next, the dependency of the contact ratio to the cutting depth is considered. It can be seen that at contact start, the contact ratio is low and increases with the number of

contacts (= cutting depth) until it reaches 1. This is simply caused by the shorter distance between upper position of the knife during the oscillation and the wire. Eventually, the feed rate has moved the knife farther into the wire than the value of vibration amplitude, causing constant contact. The amount of contacts from contact start to continuous contact between stack and knife increases with the lower wires in the experiments and sheets in the simulation. This is caused by the increase in total stiffness of the stack, lowering the total deformation of the stack. Some deviations are also caused by discrepancy between real stiffness and damping parameters with those used in the simulation. Since the total number of contacts is lower in the simulation, the stiffness and damping parameters per sheets are slightly higher than they are in the real stack during the decompression phase. It can be argued that the material behavior during compression and decompression is not linearly correlated. However, this does not seem to significantly impact the average contact ratio and therefore the simulation remains fairly accurate.

Overall, the dynamic behavior of the model is in good accordance with the experimental verification. Apart from measurement uncertainties impacting the experiments and input data of the model, these differences can be additionally caused by the copper wire's higher stiffness and thickness.

6.3.3 Cutting Forces for Longitudinal Vibration Assisted Cutting

In order to verify the dynamic model including the reduction in forces due to discontinuous high frequency vibration, a series of experiments were conducted. Parameters changed are listed in section 6.3.1. Figure 6.11 shows the experimental results for cutting with and without vibration at $750\,\mathrm{mm\,min^{-1}}$. A reduction in the cutting force is clearly visible, which can also be seen by the results of the dynamic model displayed in Figure 6.12. It should be pointed out again, that the force output by the model is the average cutting force as discussed in the previous chapter. With an increase in amplitude, which is controlled by the increase of power output of the generator, the cutting force is reduced even more. Again, the simulation model matches closely the experimental results, verifying two key aspects: the cutting force is not reduced, but the material fails quicker due to the higher damping force caused by the high velocity as discussed in section 4.2.6. The same observations can be made in Figure 6.13 and Figure 6.14 for a feed rate of $1000\,\mathrm{mm\,min^{-1}}$.

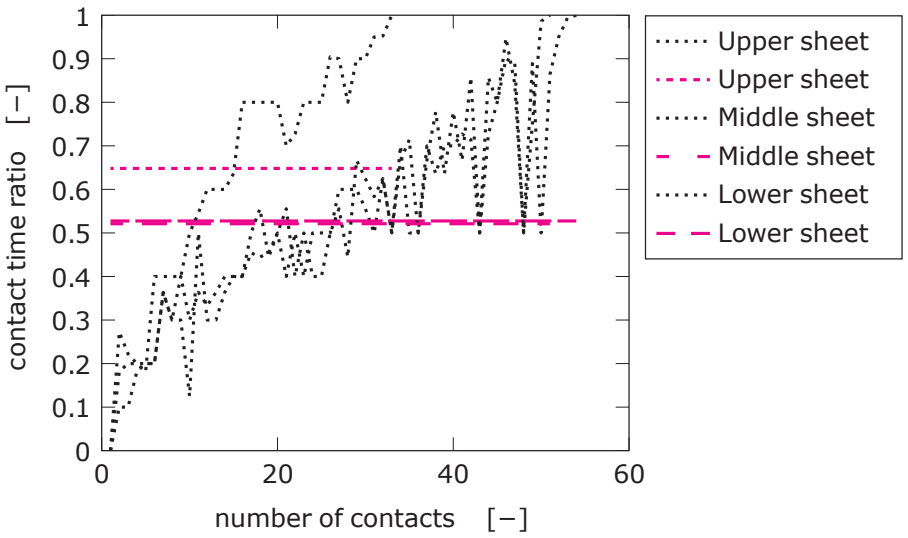

Figure 6.7: Measurement results of the contact ratio for longitudinal ultrasonic vibration assisted cutting. Wire positions are indicated by the sheets with their position listed in Table 6.1. Feedrate is $750\,\mathrm{mm\,min^{-1}}$ and vibration amplitude is $8\,\mu\mathrm{m}$.

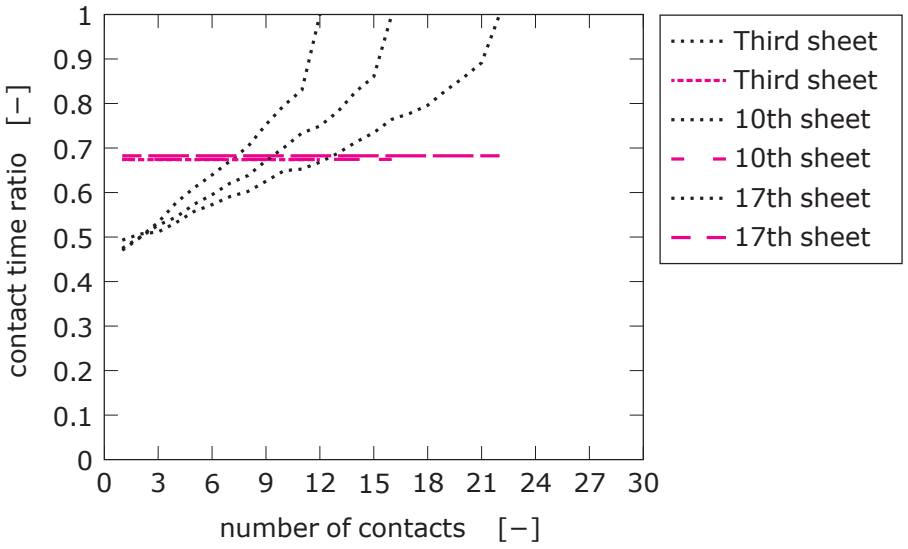

Figure 6.8: Simulation results of the contact ratio taken from three different sheets. Feedrate is $750\,\mathrm{mm\,min^{-1}}$ and vibration amplitude is $8\,\mu\mathrm{m}$.

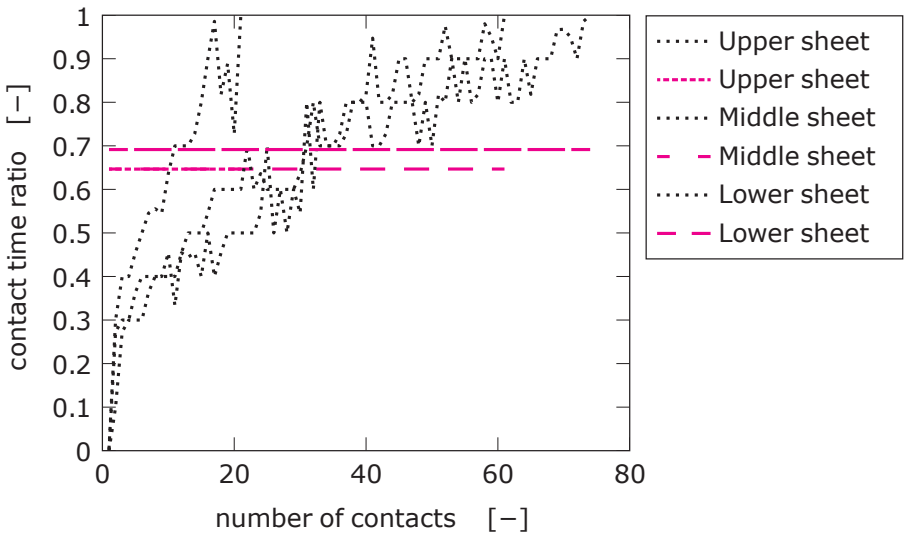

Figure 6.9: Measurement results of the contact ratio for longitudinal ultrasonic vibration assisted cutting. Wire positions are indicated by the sheets with their position listed in Table 6.1. Feedrate is $1000\,\mathrm{mm\,min^{-1}}$ and vibration amplitude is $8\,\mu\mathrm{m}$.

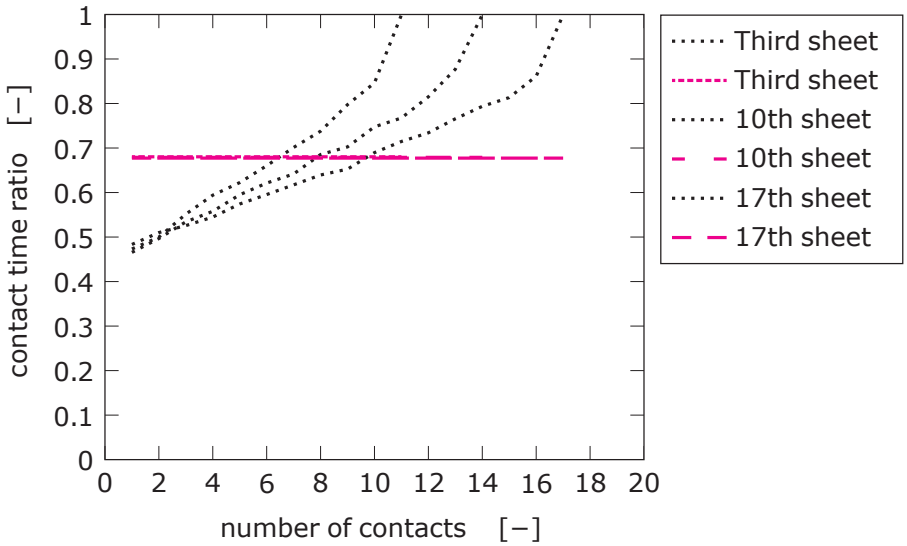

Figure 6.10: Simulation results of the contact ratio taken from three different sheets. Feedrate is $1000\,\mathrm{mm\,min^{-1}}$ and vibration amplitude is $8\,\mu\mathrm{m}$.

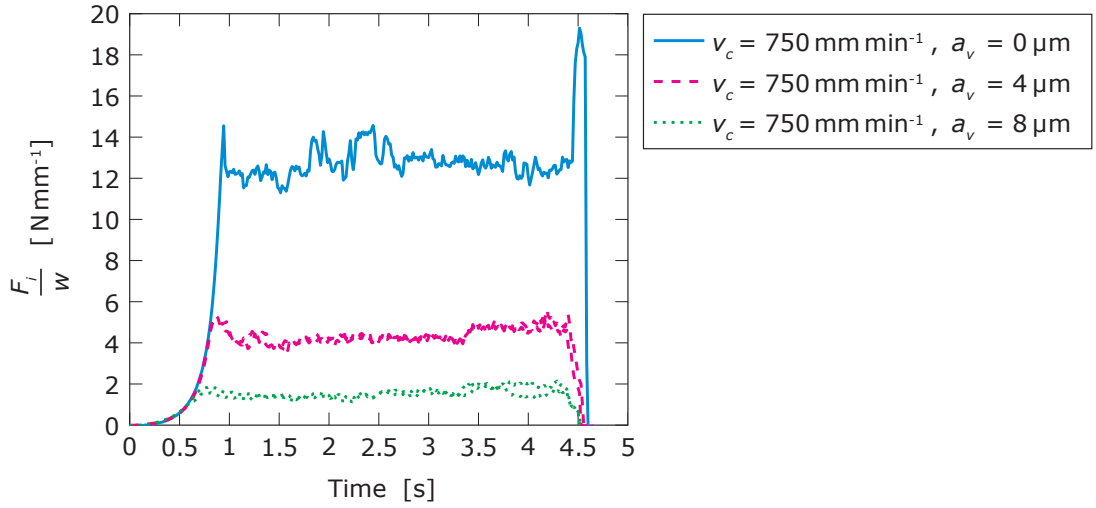

Figure 6.11: Measurement results for cutting with and without vibration at $35\,\mathrm{kHz}$ longitudinal oscillation. Vibration amplitude is changed. Feedrate is kept constant at $750\,\mathrm{mm\,min^{-1}}$. For the experiments with vibration two runs are shown.

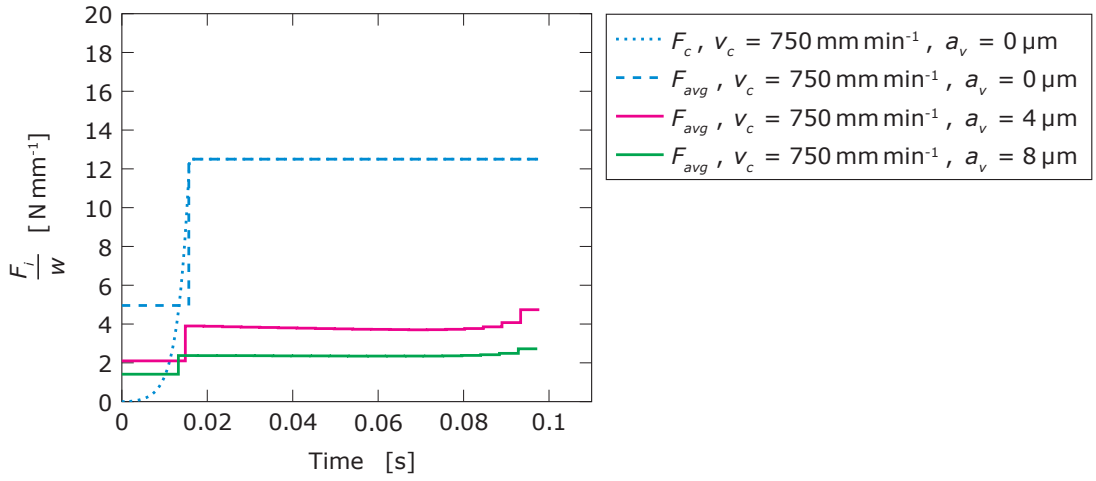

Figure 6.12: Simulation results for cutting with and without vibration at $35\,\mathrm{kHz}$ longitudinal oscillation. Parameters changed are listed in section 6.3.1. Feedrate is $750\,\mathrm{mm\,min^{-1}}$. F_C shows the computed conventional force without averaging. Index avg indicates averaged computed forces.

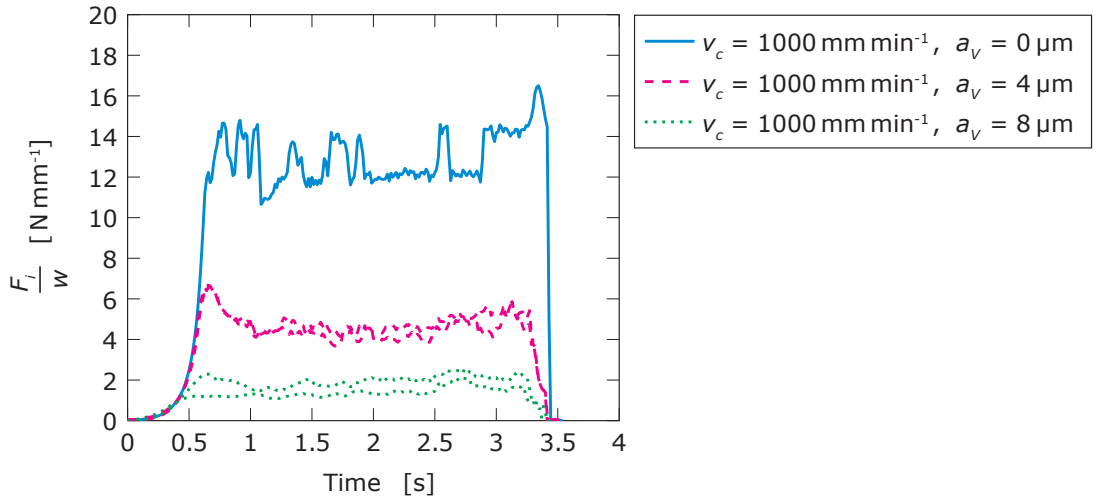

Figure 6.13: Measurement results for cutting with and without vibration at $35\,\mathrm{kHz}$ longitudinal oscillation. Vibration amplitude is changed. Feedrate is kept constant at $1000\,\mathrm{mm\,min^{-1}}$. For the experiments with vibration two runs are shown.

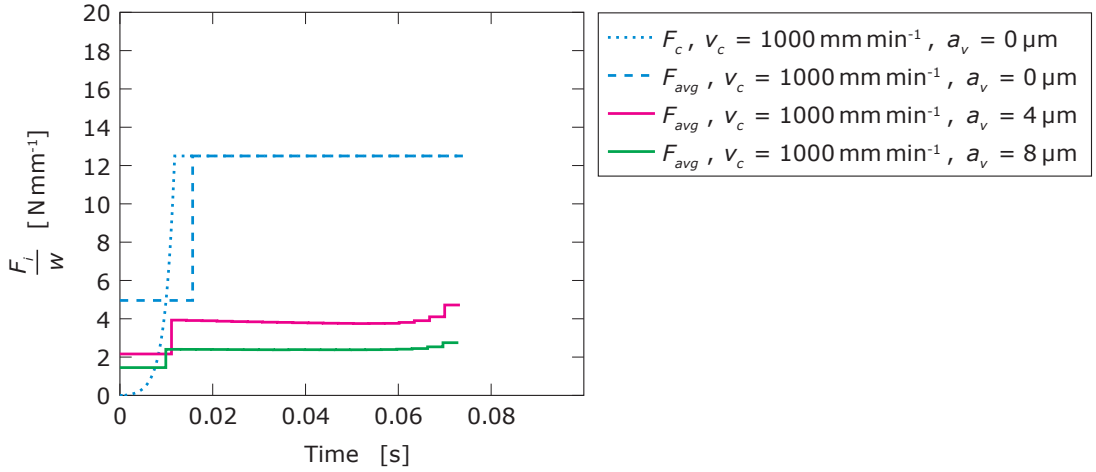

Figure 6.14: Simulation results for cutting with and without vibration at $35\,\mathrm{kHz}$ longitudinal oscillation. Parameters changed are listed in section 6.3.1. Feedrate is $1000\,\mathrm{mm\,min^{-1}}$. F_C shows the computed conventional force without averaging. Index avg indicates averaged computed forces.

6.4 Friction Coefficients

Any friction effects for the following discussed models assume Coulomb friction. The experiments are therefore designed to record the appropriate factors. Friction coefficients are determined by sliding a mass of 550 g over a sheet of paper. Normal force and friction force are measured with a three-axis measurement platformed placed underneath the testing area. For the friction coefficient between sheets, an additional sheet is fixed under the sliding mass. The resulting friction coefficients are $\mu_b = 0.25$ for the friction between cutting blade and paper sheet, and $\mu_{pp} = 0.35$ for the friction between paper sheets.

6.5 Cutting Forces for Lateral Vibration Assisted Cutting

To verify the analytical equations (4.61) and (4.63) of the lateral vibration assisted cutting forces, a series of experiments with various slice-push ratios were conducted on the test stand in Figure 6.2. The paper stack was oriented to allow cutting along the width of the stack, with variation of the lateral movement resulting in different slice-push ratios ζ. The movement in vertical direction is kept unchanged. There are two different ways to fix the paper stack on top of the three axial measurement platform. The first setup is to freely lay the stack on the platform wile locking its movement in lateral direction. Prior to cutting, the knife compresses the paper stack and the cut away sheets can only be displaced in transversal direction. The second setup is to fix the paper stack on the measurement platform by clamping it down from the top on the flat side of the cutting knife with approximately 1000 N. Consequently, the stack is compressed and cannot move in any direction except being compressed further. Before cutting, the knife only slightly increases the compression of the stack. Here, the cut away sheets can freely fall anywhere. The stack angle $\alpha \cong 20°$ on the cutoff side was determined through visual analysis of the high speed camera recordings. It remained constant throughout the experiments.

Figure 6.15 shows the results for cutting at various slice-push ratios for the freely placed stack. For $\zeta = 0$, the vertical force shows its maximum value and decreases with an increasing ζ. The lateral force is 0 at $\zeta = 0$ and increases to its maximum at $\zeta \approx 1.5{-}2$. The curves calculated by the analytical equations are fitting well into the measurement data. Higher slice-push ratios could not be achieved, because single sheets were pushed away instead of being cut. With regard to the identified compression force $F_K = 4.86\,\mathrm{N\,mm^{-1}}$, the displacement of the sheets instead of cutting is logical. With $\mu_{pp} = 0.35$ and $F_K = 4.86\,\mathrm{N\,mm^{-1}}$ as a normal force, the resulting friction force is $1.70\,\mathrm{N\,mm^{-1}}$, which is lower than the lateral cutting force (assuming only lateral movement). Hence, the friction force between the cut sheet and sheet below it must be larger than the force necessary for separating the material.

Figure 6.16 shows the results for cutting at various slice-push ratios for the fixed stack. Again, for $\zeta = 0$, the vertical force shows its maximum value and decreases with an increasing ζ. However, the descent is larger than in the freely placed stack. This is mainly caused by the compression, which decreases the angle α on the workpiece side, lowering the vertical forces at higher ζ, and increases the overall compression force near the cutting path, causing an increase in the vertical force at lower ζ. The lateral force is 0 at $\zeta = 0$ and increases to its maximum at $\zeta \approx 1.5 - 2$, and then decreases slightly at higher ζ.

At $\zeta = 1.33$ is the maximum of F_Y calculated by the model, which is close to the

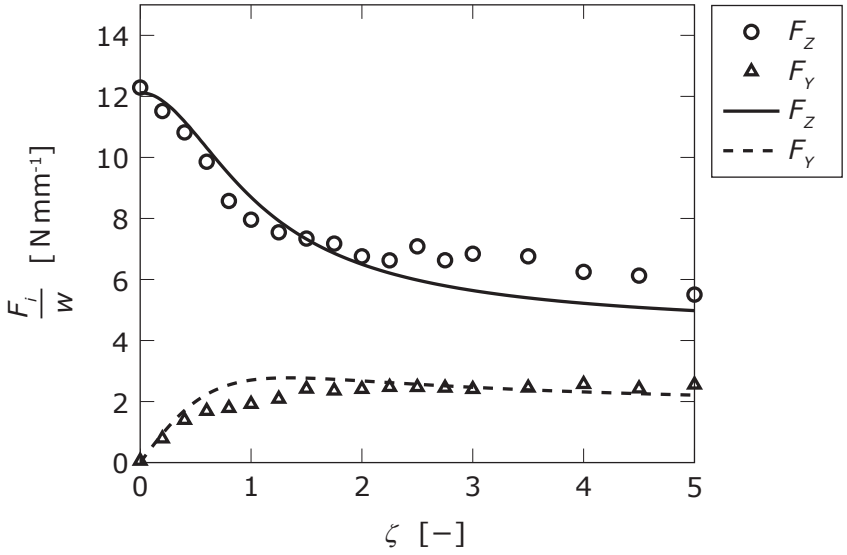

Figure 6.15: Experimental results of the normalized vertical (F_Z) and lateral (F_Y) cutting forces during cutting of the freely placed stack. Curves show the fitted analytical model with equations (4.60) and (4.61). $e_{fr} = 1.76\,\mathrm{N\,mm^{-1}}$ $F_K = 4.86\,\mathrm{N\,mm^{-1}}$, $\beta = 24°$, $\alpha = 20°$, $\mu_b = 0.25$, and $\mu_{pp} = 0.35$.

	New Model		Shear Stress Model			
	e_{fr}	F_K	e_{fr}	M	F_{bdd}	F_{cdd}
Free	$1.76\,\mathrm{N\,mm^{-1}}$	$4.86\,\mathrm{N\,mm^{-1}}$	$1.76\,\mathrm{N\,mm^{-1}}$	1.171	$3.51\,\mathrm{N\,mm^{-1}}$	$4.84\,\mathrm{N\,mm^{-1}}$
Fixed	$1.76\,\mathrm{N\,mm^{-1}}$	$4.86\,\mathrm{N\,mm^{-1}}$	$1.76\,\mathrm{N\,mm^{-1}}$	1.171	$3.51\,\mathrm{N\,mm^{-1}}$	$4.84\,\mathrm{N\,mm^{-1}}$

Table 6.2: Fitting parameters of the analytical equations for the slice-push cutting experiments regarding the new model containing coulomb friction compared with the modified shear stress model.

maximum of the measurement data of both sets of experiments.

As already introduced, the shear friction model may also be used to describe the experimental data. Figures 6.17 and 6.18 show the trends of equations (4.68) and (4.69) of the freely placed and compressed stacks, with minimum, maximum and fitted M values. For a complete overview, Table 6.2 lists the parameters that were used for fitting the equations into the experimental data, using the least squares method. Since the additional forces F_{bdd} and F_{cdd} are $\neq 0$, there is contact stress at the cutting edge. Therefore, the regular shear stress model cannot correctly calculate the forces in vertical (z) direction. The value of F_{cdd} also indicates, that a minimum compression is necessary to allow slice-push cutting of the stack.

From the above results, the specific cutting force necessary for separation of the paper material is calculated to $e_{fr} = 1.76\,\mathrm{N\,mm^{-1}}$. The remaining force acting against the cutting edge is caused by the friction effects. With the help of the J contour integral, this specific cutting force is verified in section 6.6.2. With the present findings, it becomes clear that the main contributor to the overall cutting force is due to the friction effects between the

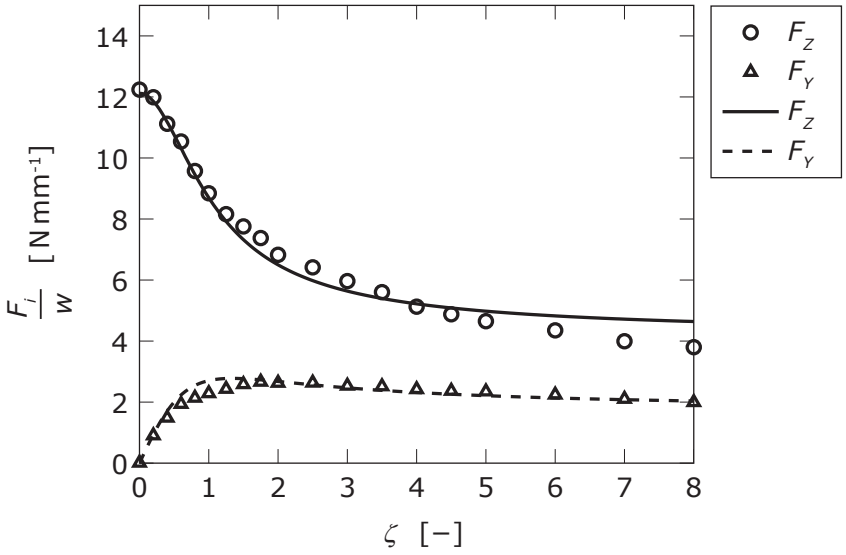

Figure 6.16: Experimental results of the normalized vertical (F_Z) and lateral (F_Y) cutting forces during cutting of the fixed stack. Curves show the fitted analytical model with equations (4.60) and (4.61). $e_{fr} = 1.76\,\mathrm{N\,mm^{-1}}$ $F_K = 4.86\,\mathrm{N\,mm^{-1}}$, $\beta = 24°$, $\alpha = 20°$, $\mu_b = 0.25$, and $\mu_{pp} = 0.35$.

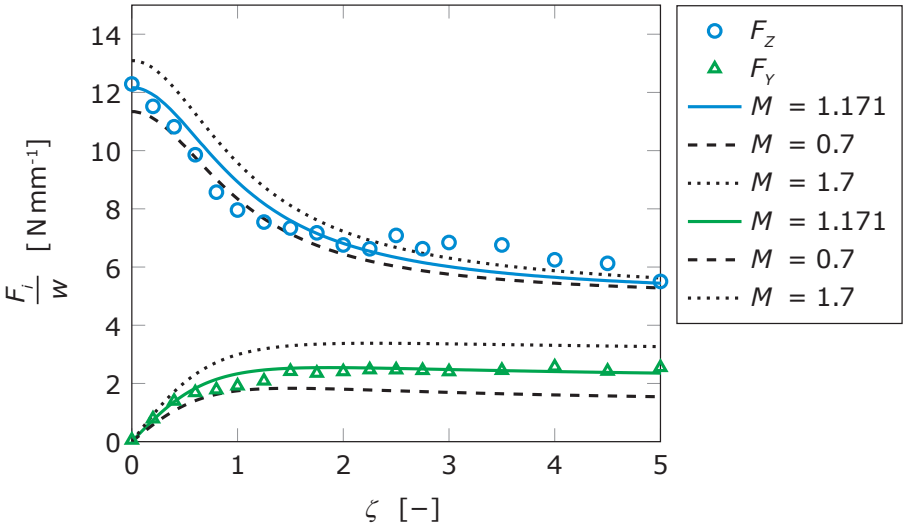

Figure 6.17: Experimental results of the normalized vertical (F_Z) and lateral (F_Y) cutting forces during cutting of the freely placed stack. Curves show the fitted analytical model with equations (4.68) and (4.69). $e_{fr} = 1.76\,\mathrm{N\,mm^{-1}}$, and $M = 1.171\,\mathrm{N}$ as best fit.

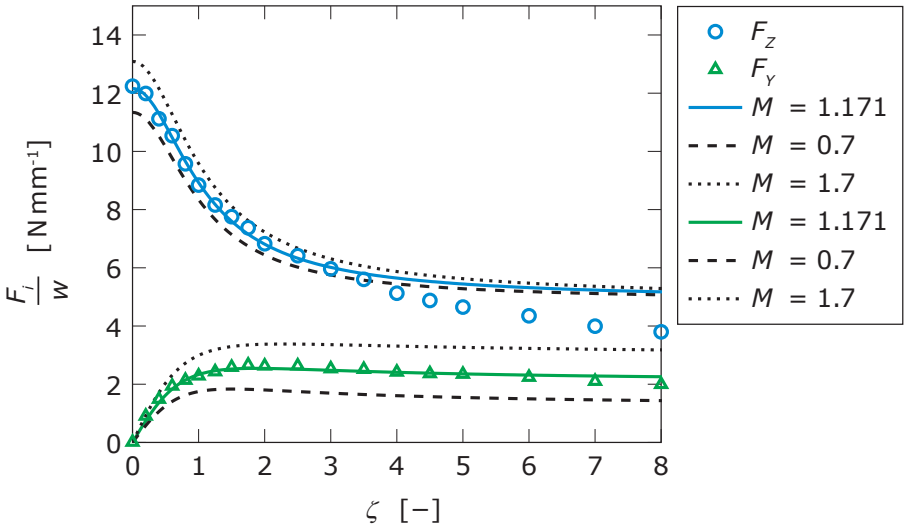

Figure 6.18: Experimental results of the normalized vertical (F_Z) and lateral (F_Y) cutting forces during cutting of the fixed stack. Curves show the fitted analytical model with equations (4.68) and (4.69). $e_{fr} = 1.76\,\mathrm{N\,mm^{-1}}$, and $M = 1.171\,\mathrm{N}$ as best fit.

ζ	F_{EFc}	F_{EFw}
0	$13.62\,\mathrm{N\,mm^{-1}}$	$5.00\,\mathrm{N\,mm^{-1}}$
1	$10.85\,\mathrm{N\,mm^{-1}}$	$4.65\,\mathrm{N\,mm^{-1}}$
2	$9.00\,\mathrm{N\,mm^{-1}}$	$4.38\,\mathrm{N\,mm^{-1}}$
3	$8.26\,\mathrm{N\,mm^{-1}}$	$4.26\,\mathrm{N\,mm^{-1}}$
4	$7.89\,\mathrm{N\,mm^{-1}}$	$4.19\,\mathrm{N\,mm^{-1}}$
5	$7.67\,\mathrm{N\,mm^{-1}}$	$4.15\,\mathrm{N\,mm^{-1}}$

Table 6.3: Values for F_{EFc} and F_{EFw} with respect to ζ. $F_K = 4.86\,\mathrm{N\,mm^{-1}}$, $\beta = 24°$, $\alpha = 20°$, $\mu_b = 0.25$, and $\mu_{pp} = 0.35$.

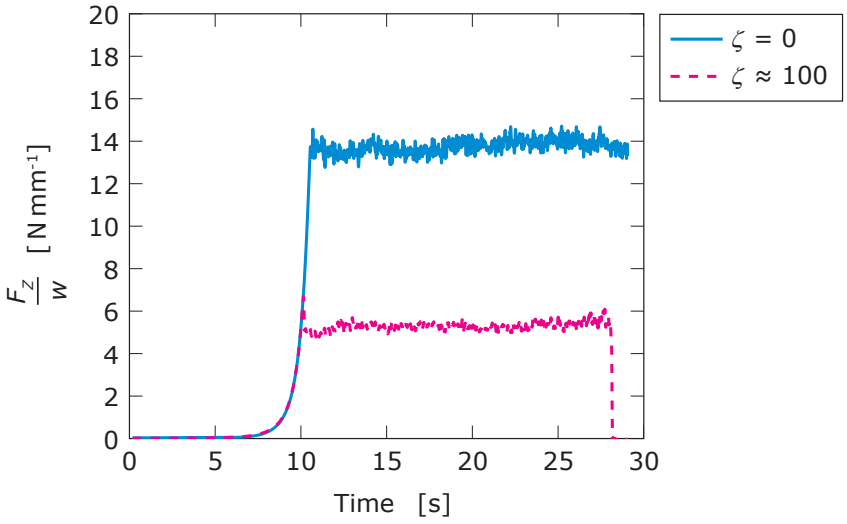

Figure 6.19: Experimental results of the normalized vertical (F_Z) cutting force during lateral ultrasonic vibration assisted cutting of the paper stack.

sheets and the cutting blade.

To analyze the cutting force when using the previously created cutting knife for lateral ultrasonic vibration assisted cutting, the experimental setup in Figure 6.3 is used. With the ultrasonic cutting knife, very high slice-push ratios can be achieved. This will help to verify the model for slice-push cutting, because the vertical force F_Z shows an asymptotic trend. According to the introduced model,

$$F_Z(\zeta \to \infty) = 4.15\,\mathrm{N\,mm^{-1}} \tag{6.3}$$

is the predicted lowest vertical force during slice-push cutting. Since the actual cutting force occurring at the top sheet of the stack oscillates between maximum and minimum value, and considering the previously discussed dynamic behavior, the time average value of the vertical force from the model is $4.40\,\mathrm{N\,mm^{-1}}$. With the measured force of $5\,\mathrm{N\,mm^{-1}}$ from the experiment at $\zeta \approx 100$ shown in Figure 6.19, the model is fairly accurate. Horizontal forces cannot be measured and are therefore excluded from the comparison. Theoretically, the limit value of F_Y with the current experimental parameters is

$$F_Y(\zeta \to \infty) = 1.71\,\mathrm{N\,mm^{-1}} \tag{6.4}$$

Since at $\zeta \to \infty$ the observed cutting force in y-direction corresponds to $F_{EF}\mu_b = 1.71\,\mathrm{N\,mm^{-1}}$ (the term containing e_{fr} becomes zero), the remaining force is only caused by friction.

6.6 Verification of Fracture Mechanics Model for Lateral Slice-Push Cutting

To verify the Fracture Mechanic Model introduced in section 5, two types of experiments need to be conducted. To obtain material properties, a fracture test is performed. The results are inserted into the analytical equations to obtain a proper cutting force simulation. Next, cutting experiments at various slice-push ratios are conducted to verify the calculated cutting forces of the introduced model.

6.6.1 Tensile Test

In order to utilize the fracture mechanics model, the workpiece material needs to qualify according to the assumptions of the linear fracture mechanics considerations. This means that the material under loading is linear elastic or assumed to be linear elastic and shows brittle fracture when failing. For defining these parameters, the stress-strain curve of the workpiece material needs to be determined. Due to the production processes of paper, the specimen may be oriented in machining direction (MD) or perpendicular to the machining direction, also called cross direction (CD). The material is therefore transversely isotropic (also called normal anisotropic). In [59], paper is described as an orthotropic material. Hence transverse isotropy is a special case of orthotropy, because it behaves like an isotropic material in the plane perpendicular to the main direction. Thus, tensile tests need to be conducted along and perpendicular to the machining direction (which lie in the same plane). This is done with the help of an uniaxial tensile specimen. Figure 6.20 shows the force-elongation curve of the material for both directions. Brittle fracture is clearly visible, which indicates that the linear fracture mechanical model as previously detailed is eligible, when disregarding the nonlinear behavior. Since the cutting process occurs at the point of failure, the disregard of the plastic/irreversible part at other points of operation is acceptable.

Since paper shows a nonlinear elastic-plastic behavior with a nearly linear elastic part, similar to polymers, the Ramberg and Osgood (1943) [145] model is used (as in [64])

$$\epsilon = \left(\frac{\sigma}{\sigma_0} + \alpha \left(\frac{\sigma}{\sigma_0} \right)^n \right) \frac{\sigma_0}{E}, \tag{6.5}$$

where ϵ is the nominal strain, σ is the nominal stress, σ_0 is the yield stress, and E is the Young's modulus. α and n are dimensionless constants. The first term in the parentheses can be regarded as the linear elastic part, and the second term can be regarded as the (nonlinear) plastic part. Exponent n is much larger than 1 to keep the nonlinear part smaller than the linear part as long as the nominal stress is lower than the yield stress. In the present experimental data, there is no clear yield stress, which leads to the linear part being a small section at the start. Since the viscoelastic behavior of paper shown in Figure 6.21 is neglected due to the cutting process occurring at a much higher speed than the tensile test, the application of the Ramberg and Osgood model is feasible. The parameters are determined by fitting the above equation onto the experimental data of the tensile test with the least squares method.

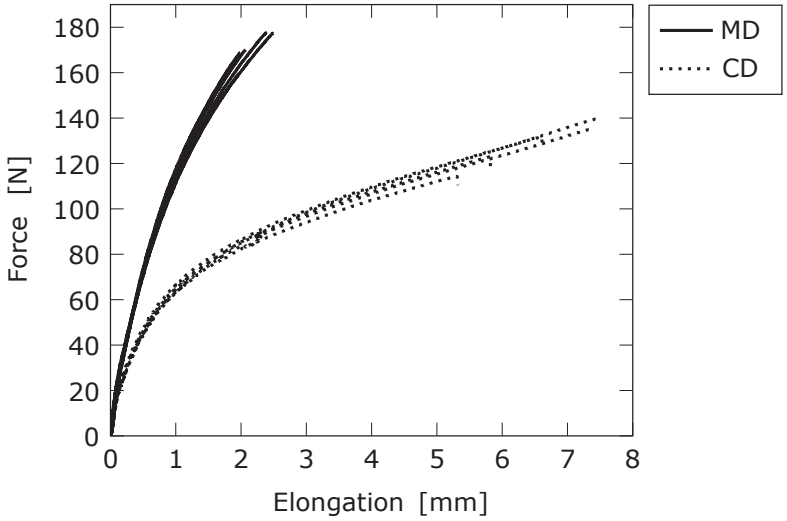

Figure 6.20: Experimental results from the tensile test in machining direction (MD) and cross direction (CD). $w = 50\,\mathrm{mm}$, $B = 6\,\mu\mathrm{m}$. Curves indicated brittle fracture of the material. Loading is continuously applied with $1\,\mathrm{N\,s^{-1}}$.

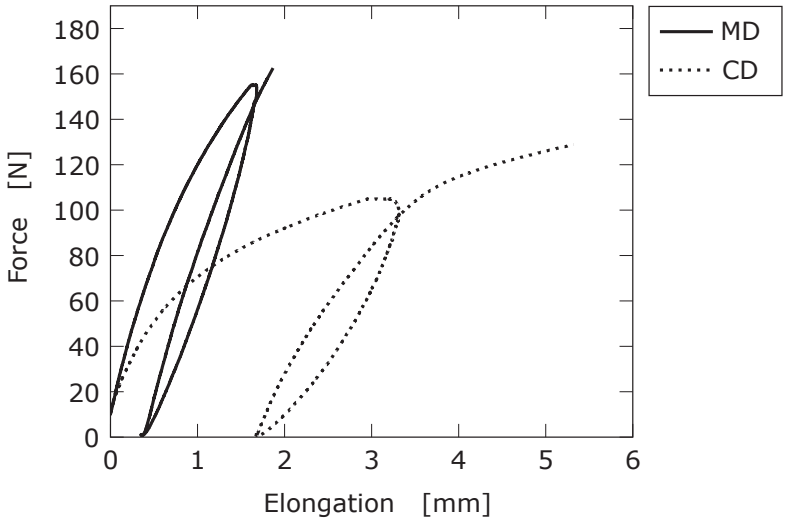

Figure 6.21: Experimental results from the tensile test with one loading cycle in machining direction (MD) and cross direction (CD). $w = 50\,\mathrm{mm}$, $B = 6\,\mu\mathrm{m}$. Holding force in MD is $155\,\mathrm{N}$ for $5\,\mathrm{s}$ and in CD is $105\,\mathrm{N}$ for $5\,\mathrm{s}$. The holding force is approximately between $80\,\%$ to $90\,\%$ of the critical value. Elongation during holding is $0.064\,\mathrm{mm}$ in MD and $0.29\,\mathrm{mm}$ in CD. Loading is continuously applied with $1\,\mathrm{N\,s^{-1}}$.

Tensile Test	E	σ_0	α	n
MD	$6512.59\,\mathrm{MPa}$	$17.86\,\mathrm{MPa}$	0.123	2.97
CD	$4710.89\,\mathrm{MPa}$	$15.31\,\mathrm{MPa}$	0.386	3.61

Table 6.4: Parameters determined through fitting equation (6.5) onto the data of the tensile tests. Paper material with $w = 50\,\mathrm{mm}$ is used.

DENT Test	K_{Ic} (MD)	K_{Ic} (CD)
$a = 5\,\mathrm{mm}$	$110\,\mathrm{MPa\,mm^{-1/2}}$	$83\,\mathrm{MPa\,mm^{-1/2}}$
$a = 10\,\mathrm{mm}$	$120\,\mathrm{MPa\,mm^{-1/2}}$	$92\,\mathrm{MPa\,mm^{-1/2}}$
$a = 15\,\mathrm{mm}$	$119\,\mathrm{MPa\,mm^{-1/2}}$	$89\,\mathrm{MPa\,mm^{-1/2}}$
average	$116\,\mathrm{MPa\,mm^{-1/2}}$	$88\,\mathrm{MPa\,mm^{-1/2}}$

Table 6.5: K_{Ic} determined through DENT tests. Paper material with $w = 50\,\mathrm{mm}$ is used.

6.6.2 DENT

As introduced in section 2.2.2, paper is a nonlinear orthotropic viscoelastic material. In order to find the fracture toughness as limiting value in linear elastic fracture mechanics, the material should show brittle fracture during the failure phase. The nonlinear irreversible behavior will be neglected, because only the fracture toughness at the final sudden failure is relevant. There are various analytical ways to determine the fracture toughness of a material [63]. Since sheets of paper are relatively thin, causing failure due to tension with a tensile test machine is most suitable. To investigate the fracture mechanical properties of the paper sheets using a tensile test machine, a symmetrical specimen is required. Generally, the so called Double-Edge-Notched-Tension specimen is best used for such investigations as shown in Figure 6.22. The notches in the sample were created by slitting with a cutter, thereby causing an initial crack. From the force-elongation curve of the DENT sample, the critical value K_{Ic} is determined according to the procedure detailed in [64]. With the help of

$$\begin{aligned} K_I = & \frac{F}{B\sqrt{w}} \frac{\sqrt{\frac{\pi a}{2w}}}{\sqrt{1-\frac{a}{w}}} \left[1.122 - 0.561 \left(\frac{a}{w}\right) \right. \\ & \left. - 0.205 \left(\frac{a}{w}\right)^2 + 0.471 \left(\frac{a}{w}\right)^3 + 0.190 \left(\frac{a}{w}\right)^4 \right] \end{aligned} \tag{6.6}$$

where F is the force acting upon the DENT sample, and the other parameters from Figure 6.22, K_I may be calculated (Table 2.4 of [64]). Hence, K_{Ic} is simply calculated from the critical force F_{crit} at the brittle fracture point. Figure 6.23 shows the force-elongation curves for three sets of results of the DENT experiments with varying notch depth. Each set of experiments is run five times and the maximum force at the fracture of the samples is extracted to calculate K_{Ic} with equation (6.6).

While it is difficult to experimentally record the pure cutting force without any friction effects for soft materials like paper sheet stacks, the critical force at which the cutting knife penetrates the paper sheet is investigated with the help of the J contour integral [64]. The overall energy necessary for cutting may be defined by

$$dW = J_c dA = J_c dB w \tag{6.7}$$

where W is the cutting work, J_c is the critical J-integral value, and A is the newly created area. Therefore, the J contour integral needs to be obtained from the DENT results

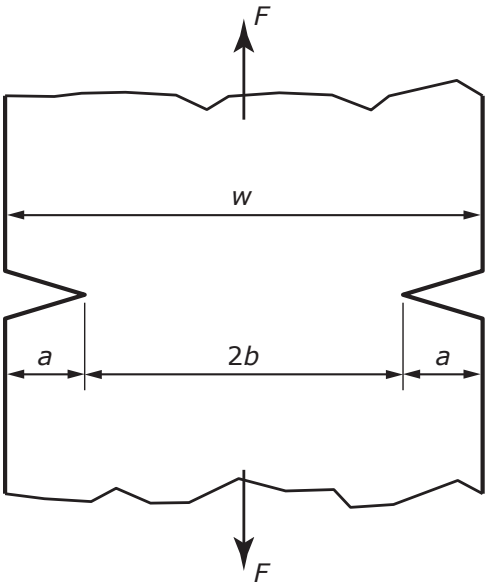

Figure 6.22: Double-Edge-Notched-Tension (DENT) sample for determining the fracture toughness K_{Ic}.

while considering the nonlinear elastic behavior. The procedure detailed below is based on Anderson's book [64]. The J contour integral can be regarded as the energy release rate for nonlinear materials [64], which is

$$J = \left(\frac{\partial U_K}{\partial A}\right)_F \tag{6.8}$$

under load control (indicated by the index F), where U_K is the complementary deformation energy, and A is the crack area. Since the used DENT specimen actually has two crack areas, $A = 2Ba$ is calculated. The complimentary deformation energy U_K is obtained from

$$U_K = \int_0^F u dF \tag{6.9}$$

with F being the applied load, and u the displacement of the contact point. Both above equations can be combined and with switching integration and differentiation

$$J = \left(\frac{\partial}{2B\partial a}\int_0^F u dF\right)_F = \frac{1}{2B}\int_0^F \left(\frac{\partial u}{\partial a}\right)_F dF \tag{6.10}$$

is obtained. Since the remaining length of the DENT sample is more relevant, because the energy release rate is defined through crack area, not crack length, it is inserted in the above equation with $b = \frac{w}{2} - a$. Thus the equation becomes

$$J = -\frac{1}{2B}\int_0^F \left(\frac{\partial u}{\partial b}\right)_F dF \tag{6.11}$$

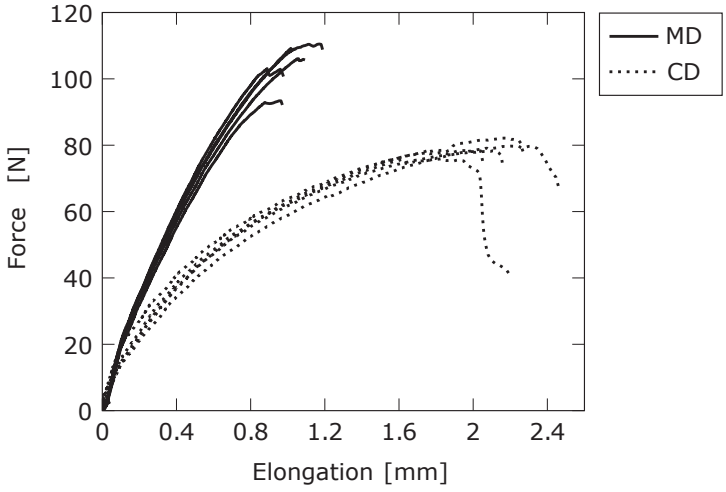

(a) $a = 5\,\mathrm{mm}$, $w = 50\,\mathrm{mm}$, $B = 6\,\mu\mathrm{m}$.

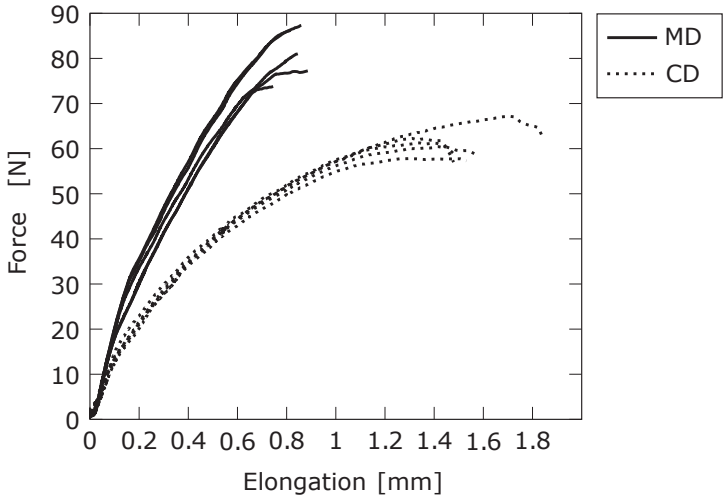

(b) $a = 10\,\mathrm{mm}$, $w = 50\,\mathrm{mm}$, $B = 6\,\mu\mathrm{m}$.

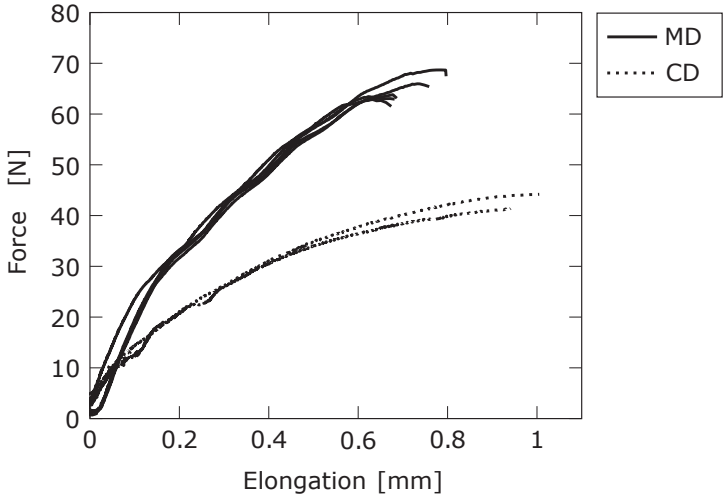

(c) $a = 15\,\mathrm{mm}$, $w = 50\,\mathrm{mm}$, $B = 6\,\mu\mathrm{m}$.

Figure 6.23: Force-Elongation curve of the Double-Edge-Notched-Tension (DENT) tests in machining direction (MD) and cross direction (CD). Notches are created by incision with a cutter blade. Each experiment is repeated five times.

DENT Test	J_c (MD)	J_c (CD)
$a = 5\,\mathrm{mm}$	$1.819\,\mathrm{N\,mm^{-1}}$	$1.424\,\mathrm{N\,mm^{-1}}$
$a = 10\,\mathrm{mm}$	$2.204\,\mathrm{N\,mm^{-1}}$	$1.756\,\mathrm{N\,mm^{-1}}$
$a = 15\,\mathrm{mm}$	$2.149\,\mathrm{N\,mm^{-1}}$	$1.285\,\mathrm{N\,mm^{-1}}$
average	$2.057\,\mathrm{N\,mm^{-1}}$	$1.488\,\mathrm{N\,mm^{-1}}$

Table 6.6: J_c determined through DENT tests. Paper material with $w = 50\,\mathrm{mm}$ is used.

With regard to linear elastic fracture mechanics, the displacement u is assumed to be mainly elastic. Hence, the above equation is equal to the energy release rate, allowing the simplification to

$$J = \mathcal{G} = \frac{K_I^2}{E} \tag{6.12}$$

for the plain-stress state. Consequently, the critical J-integral value J_C can be determined using the above provided values for K_{Ic} and E. Table 6.6 lists the various J_c values for MD and CD of the paper material. The average value of J_c in CD matches the fitted value determined from the analytical model for lateral cutting, where the cutting knife penetrates the stack along CD over the entire sheet width.

6.6.3 Cutting Forces

Cutting forces were experimentally tested with the measurement setup shown in Figure 6.24. It is very similar to the previously introduced measurement setup, except the sideways oriented sheet stack. Hence, the sheets are synchronously cut from top to bottom. A clamp firmly fixes the sideways oriented stack to the force measurement platform. Force sensor, cutting knife, and sheet stack were all aligned to each other along the y-axis to allow proper slicing of the sheet material. Sheets are cut in cross direction (MD), which creates a fracture in MD, requiring the K_{Ic} of CD, assuming isotropy. Nonlinearities and the orthotropic behavior are neglected.

Since the previously introduced fracture model for slice-push cutting does not contain the initial incision of the material, the sheets were slightly precut with a very high slice-push ratio. For the actual experiments, the cutting knife started its motion a few mm above the workpiece, and moved along a linear path downwards. The slope of this path was determined through the desired slice-push ratio.

Figure 6.25 shows the results of the experiments. Three tests were run for every slice-push ratio, with 50 and 100 sheets per stack. Slice-push ratios $\zeta < 0.75$ could not be realized, because the separation process proved to be more of ripping nature than actual cutting, and $\zeta \geq 6$ were not necessary as the asymptotic trend is already visible.

With the known fracture toughness from the DENT experiments, the trend of the cutting forces was easily determined by solely fitting the contact length L into the data using the least square method. In general, the contact length L was unknown for all experiments and could only be roughly estimated. With the friction coefficient of $\mu_b = 0.25$, contact length of approximately $L = 0.10\,\mathrm{mm}$ for 50 sheets and $L = 0.17\,\mathrm{mm}$ for 100 sheets was found.

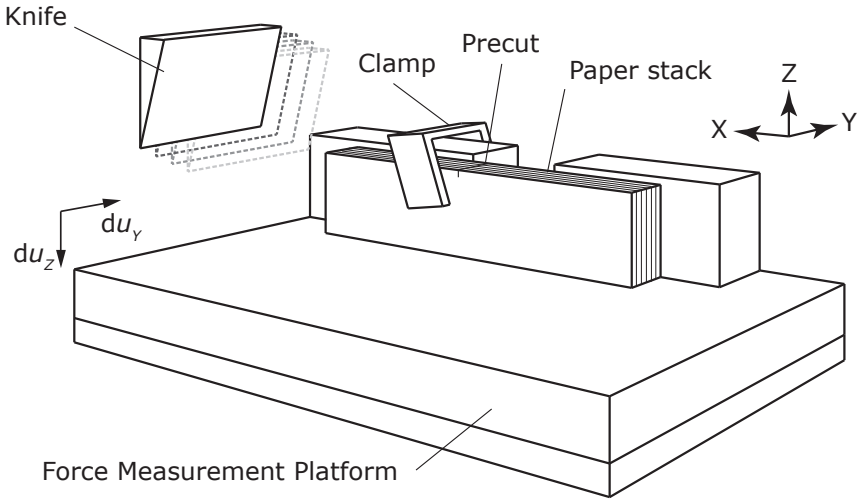

Figure 6.24: Schematic drawing of the experimental setup for determining the cutting forces for various slice-push ratios.

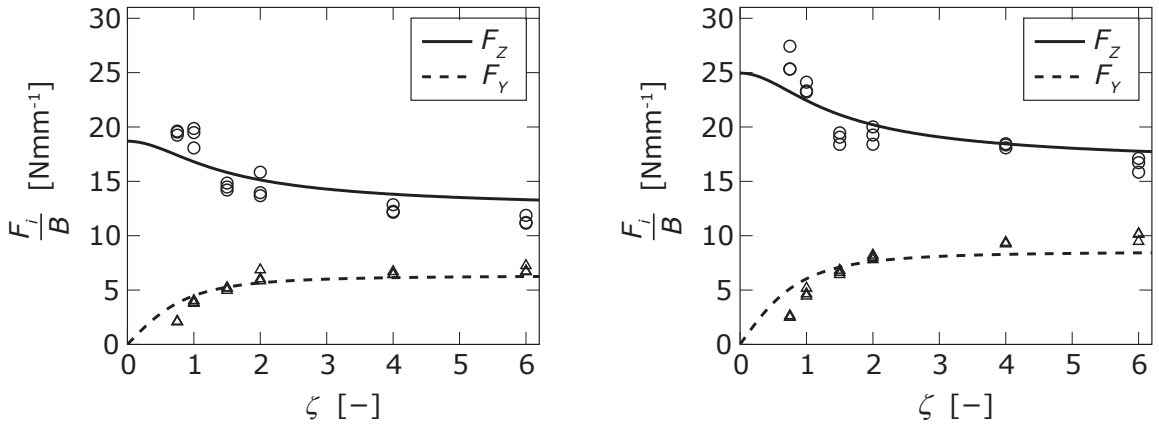

(a) 50 sheets, $B = 3\,\mathrm{mm}$. **(b)** 100 sheets, $B = 6\,\mathrm{mm}$.

Figure 6.25: Experimental results of cutting with slice-push motion of 50 and 100 sheets of paper oriented sideways. Curves shown results of analytical model calculated with equations (5.42) and (5.43). $K_{Ic} = 88\,\mathrm{MPa\,mm^{-1/2}}$, $\beta = 24°$, and $\mu_b = 0.25$ with L being fitted.

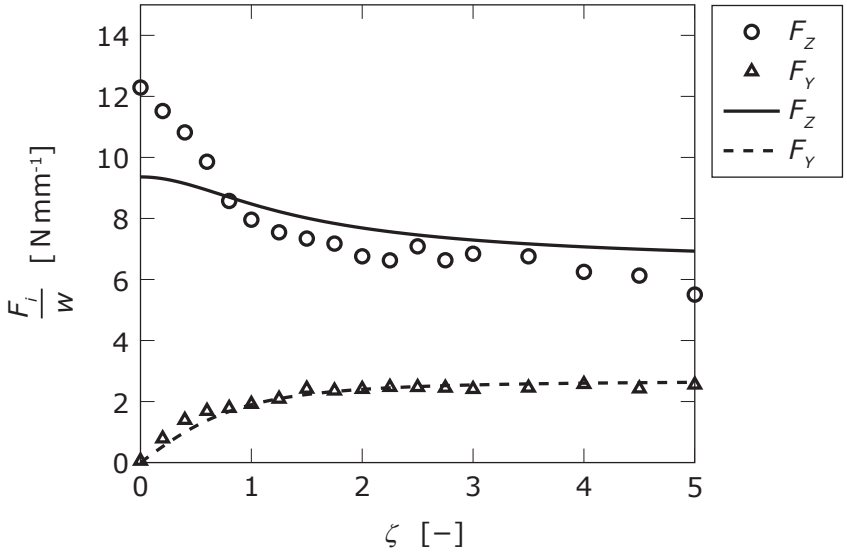

Figure 6.26: Experimental results of cutting a large paper stack with slice-push motion. Curves shown results of analytical model calculated with equations (5.34) and (5.43). $K_{Ic} = 88\,\mathrm{MPa\,mm^{-1/2}}$, $\beta = 24°$, and $\mu_b = 0.25$ with $L \approx 0.016\,\mathrm{mm}$ being fitted.

6.6.4 Applying Model to Lateral Cutting of Stack

Now the possibility whether or not the fracture mechanical model can properly predict cutting forces when slice-push cutting a stack as in Figure 6.2 is discussed. While the energy based model does not include crack propagation within the material, the fracture mechanical model does not include the friction effects between the layered materials. While the cutting of the paper sheets within the stack is not regarded as a continuous process, because each sheet is cut individually, the propagation of a crack in the uncut material was already stated in [36], which allows the overall considerations, here. Figure 6.26 shows the experimental data of the freely placed stack with the fitted analytical equations of the vertical and lateral forces. Since large deformations in z-direction occur due to the compression of the stack prior to cutting, the symmetrical case for the vertical force (equation (5.34)) and asymmetrical case for the lateral force (equation (5.43)) is considered. It can be seen that equation (5.34) qualitatively models the z-force behavior but cannot correctly quantitatively represent the measured values. Since the fracture mechanical model does not included the complex friction interaction between paper sheets during the cutting process, the very high cutting force in vertical (z) direction at low slice-push ratio cannot be represented. For the lateral force in y-direction, the fracture mechanical model predicts the occurring force well for small ζ. However, the maximum at $\zeta \approx 1.5 - 2$ and the force reduction at large ζ are not included due to the same reason as previously stated. The reduction due to variable friction forces is not included in the fracture mechanics model. Hence, there is no maximum value, but only the terminal value of the asymptotic trend. In addition, in the fracture mechanics model, the slicing motion does not contribute towards failure.

7 Conclusion and Outlook

The hybrid process of vibration assisted guillotining of stacked thin material is an enhancement of the conventional cutting process by adding oscillations to the cutting edge. The two discussed vibration directions, longitudinal and lateral, have an impact on the cutting force when cutting the stacked material. With very high vibration frequency, the cutting forces can be reduced when applying either vibration direction. However, the specific cutting force stays constant, making the force reduction observed during ultrasonic longitudinal vibration assisted cutting a phony effect.

The phony force reduction of ultrasonic longitudinal vibration assisted cutting is simply caused by the dynamic of the surrounding structure. The transfer function between tool and further distant structural components affects the observed amplitude of the vibration. The value of the reduced force is simply the time average of the force during contact time between tool and workpiece and the zero value during out of contact time. On the up side, the high impact velocity creates high damping forces or dynamic forces, which abets failure. This effect is beneficial, because the required compression prior to cutting is reduced. Proper modeling of the process has been accomplished and supports the findings by matching the experimental results.

On the contrary, the ultrasonic lateral vibration assisted cutting can clearly reduce the observed cutting forces due to splitting up the specific work necessary for separation into vertical and horizontal components. Slice-push cutting of stacked material can reduce observed forces with increasing slice-push ratio. This effect is mainly caused by distributing the friction effects in an other direction than cutting of the material. For the cutting of paper stacks, the friction occurring at the cutting edge is very significant and accounts for most of the observed forces. With the assumption of constant work necessary for failure, the cutting forces can be analytically calculated. The J contour integral and ultrasonic dynamic cutting experiments verify the presented model. For the slice-push cutting of stacks, infinitely increasing the slice-push ratio does not result in infinitely small forces, due to the asymptotic trend caused by the minimal required compression force.

The introduced fracture mechanics model for slice-push cutting at low slice-push ratios supports the findings on friction reduction during the cutting process. However, mode I is still the main failure effect at the crack tip, even though an asymmetrical cutting knife, which enables all three failure modes, is used. Due to the complex friction effects occurring during the regular stack cutting, the fracture mechanics model can only properly predict the vertical and horizontal cutting forces during sideways cutting. For the fracture mechanics model, the normal force acting against the face of the cutting edge remains constant.

Through the outlined optimization methodology, a step-by-step design strategy of ultrasonic cutting tools is created. Combining the intuitive ideas of the decision maker and the mathematical approach of the optimization algorithms, allows an effective search for new and improved designs for structures required to posses specific dynamic properties. Since ultrasonic devices should resonate with a desired mode shape, the optimization methodology can be applied. The inventive designs of the presented ultrasonic knives are

tested under real cutting conditions.

Based on the presented findings, various new horizons can be approached. Applying the optimization methodology on designing other manufacturing tools dedicated for ultrasonic vibration assisted machining may allow new and innovative tools. Through the proper design of tools, new hybrid processes can be accomplished.

The presented dynamic model can be modified to simulate similar ultrasonic longitudinal vibration assisted manufacturing processes. The introduced Kelvin-Voigt material model may be expanded to include more complex material behavior. Introducing other oscillation directions to the dynamic model allows to simulate multi directional cutting forces. More detailed analysis of the effect of high impact forces on material failure may further enhance the performance of the model, allowing the discussion on the beneficial effect of longitudinal ultrasonic vibration assisted machining. Including fracture mechanics in the dynamic model presents an interesting possibility to study crack propagation during high momentum impacts.

With the energy based model and fracture mechanics model, more investigations on slice-push cutting can be done. Other materials undergoing large deformations prior to cutting can be tested. Searching for methods to reduce friction during the cutting process are of high interest. Describing cutting forces of any process in terms of fracture mechanics enables the formulation of models based on material based properties. Differentiating between initial incision and continuous cutting may also be modeled. Extending the fracture mechanics model to include the J integral may allow a wider application. The cutting of materials with high friction between tool and workpiece also needs to be tested for mixed mode failure. Finally, the fracture mechanics model needs to be extended by including blade sharpness, material deformation, and tool wear.

A Appendix

A.1 Alternative Expression of the Transfer Function for 2nd Order System

$$\begin{aligned}\mathcal{X}(s) =& \frac{K_p}{1+2\varsigma T_w s+(T_w s)^2} = \frac{K_p}{1+2\varsigma T_w s+(T_w s)^2}\frac{\frac{1}{T_w^2}}{\frac{1}{T_w^2}} \\ =& \frac{K_p\frac{1}{T_w^2}}{\frac{1}{T_w^2}+2\varsigma\frac{1}{T_w}s+s^2} = \frac{K_p\omega_0^2}{\omega_0^2+2\delta\omega_0 s+s^2}\end{aligned} \tag{A.1}$$

with $\frac{1}{T_w}=\omega_0$ and $\varsigma=\delta$.

A.2 Fourier Series of Pulse Wave

A pulse wave (duty cycle, pulse train) can be expressed with equation (4.6), but for multiplying with the transfer function it needs to be expressed as a Fourier series. Following are the mathematical steps to obtaining this Fourier series. A periodic function may be expressed as [146]

$$\hat{o}(t) = \frac{a_0}{2} + \sum_{n=1}^{N}\left[a_n\cos\left(\frac{2\pi n}{T}t\right) + b_n\sin\left(\frac{2\pi n}{T}t\right)\right] \tag{A.2}$$

where the first part in the sum the symmetrical terms and the second part in the sum the asymmetrical terms represent (relative to the origin). For simplification, the pulse wave depicted in Figure 4.4 is shifted left by $\frac{t_c}{2}$, to make it symmetrical around the origin (this is allowed, because it is periodic and its shape is time invariant). Therefore, the above equation becomes

$$\hat{o}(t) = \frac{a_0}{2} + \sum_{n=1}^{\infty}\left[a_n\cos\left(\frac{2\pi n}{T}t\right)\right] \tag{A.3}$$

with $N\to\infty$, which only leaves a_0 and a_n as

$$a_n = \frac{2}{T}\int_0^T \hat{o}(t)\cos\left(\frac{2\pi n}{T}t\right)\mathrm{d}t \tag{A.4}$$

$$a_0 = \lim_{n\to 0} a_n \tag{A.5}$$

In regard to the shifted pulse wave, the integration steps are as follows

$$a_n = \frac{2a_P}{T}\int_0^{\frac{t_c}{2}} \cos\left(\frac{2\pi n}{T}t\right)\mathrm{d}t + \frac{2a_P}{T}\int_{T-\frac{t_c}{2}}^{T} \cos\left(\frac{2\pi n}{T}t\right)\mathrm{d}t \tag{A.6}$$

$$= \frac{a_P}{\pi n}\sin\left(2\pi n\frac{t_c}{2T}\right) + \frac{a_P}{\pi n}\left(-\sin\left(2\pi n\frac{T-\frac{t_c}{2}}{T}\right)\right) \tag{A.7}$$

with

$$\sin\left(2\pi n\frac{T-\frac{t_c}{2}}{T}\right) = \sin\left(2\pi n - \frac{2\pi n t_c}{2T}\right) = -\sin\left(\frac{\pi n t_c}{T}\right) \tag{A.8}$$

it becomes

$$a_n = 2\frac{a_P}{\pi n}\sin\left(\pi n\frac{t_c}{T}\right) = \frac{2a_P}{\pi n}\sin\left(\pi n\frac{t_c}{T}\right) \tag{A.9}$$

and inserting it into equation (A.3)

$$\hat{o}(t) = \frac{a_0}{2} + \sum_{n=1}^{\infty}\left[\frac{2a_P}{\pi n}\sin\left(\pi n\frac{t_c}{T}\right)\cos\left(\frac{2\pi n}{T}t\right)\right] \tag{A.10}$$

Now a_0 is simply calculated as

$$a_0 = \lim_{n\to 0}\frac{2A}{\pi n}\sin\left(\pi n\frac{t_c}{T}\right) \tag{A.11}$$

$$= 2a_P\frac{t_c}{T} \tag{A.12}$$

which gives

$$\hat{o}(t) = \mathcal{F}(o(t)) = a_P\left(\frac{t_c}{T} + \sum_{n=1}^{\infty}\frac{2}{n\pi}\sin\left(\frac{\pi n t_c}{T}\right)\cos\left(\frac{2\pi n}{T}t\right)\right) \tag{A.13}$$

A.3 UVA Cutting with Rigid Plastic and Ideal Elastic Plastic Material Model

Figure A.1 depicts the UVA cutting of a rigid plastic material, and Figure A.2 depicts the UVA cutting of an ideal elastic plastic material.

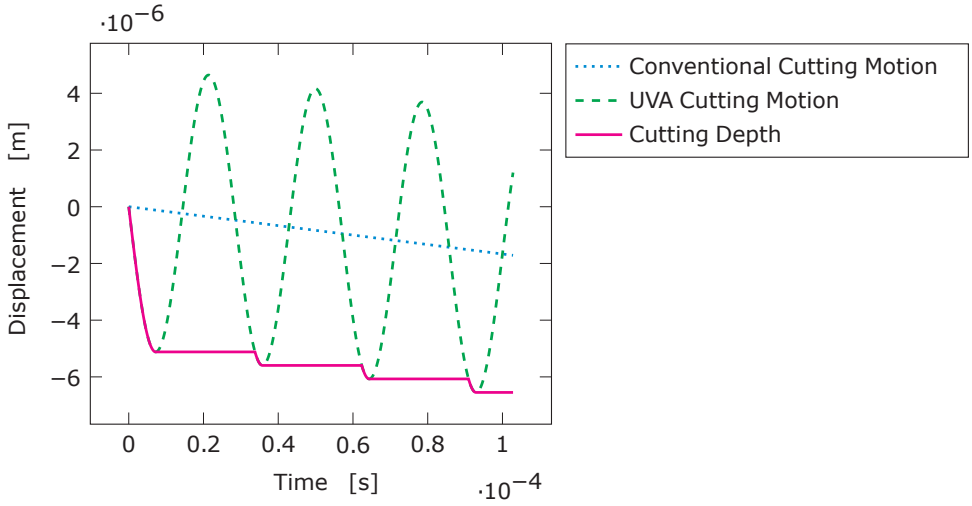

Figure A.1: Rigid plastic model of vibration-assisted cutting.

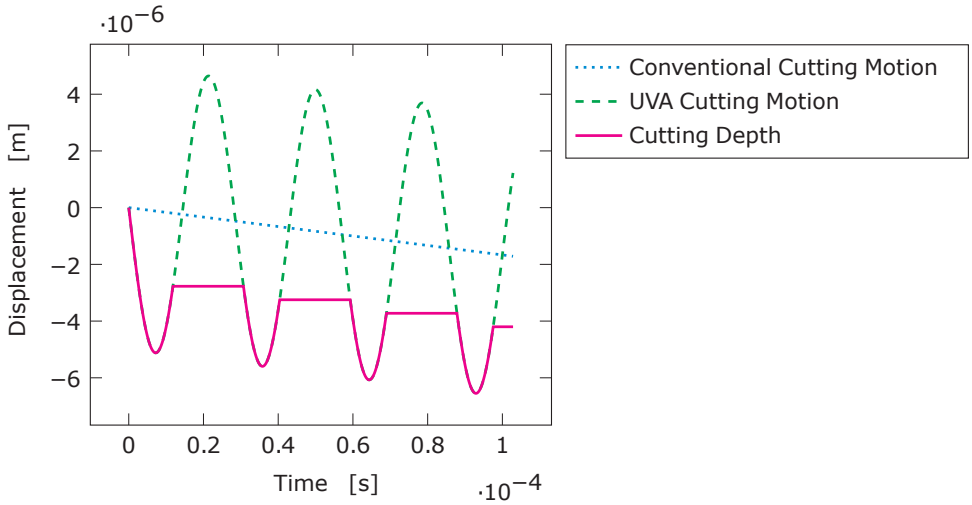

Figure A.2: Ideal Elastic plastic model of vibration-assisted cutting.

A.4 Calculation of Damping - graphically

Figure A.3 shows how to calculate according to the full width at half power method. Equations are listed in the respective section in this dissertation.

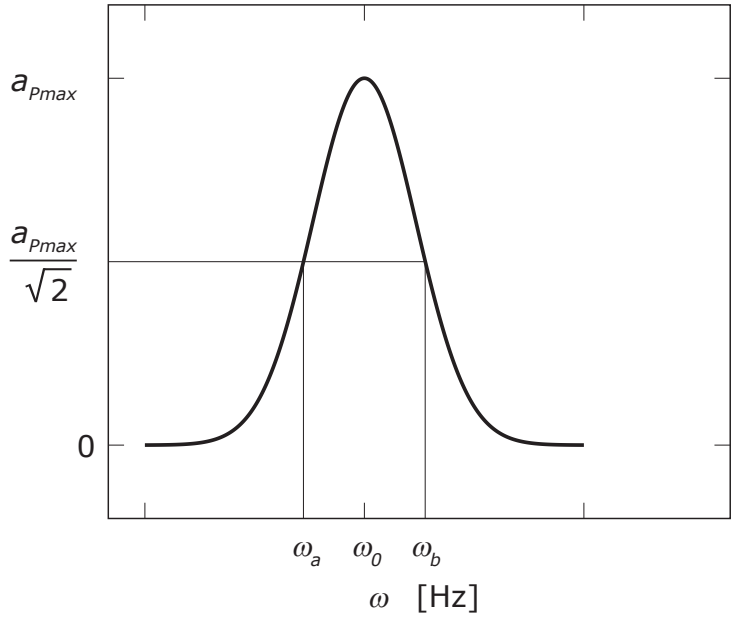

Figure A.3: Full Width at Half Power.

A.5 Flow diagram for the dynamic model

Figure A.4 shows a flow diagram for the calculations within the dynamic model.

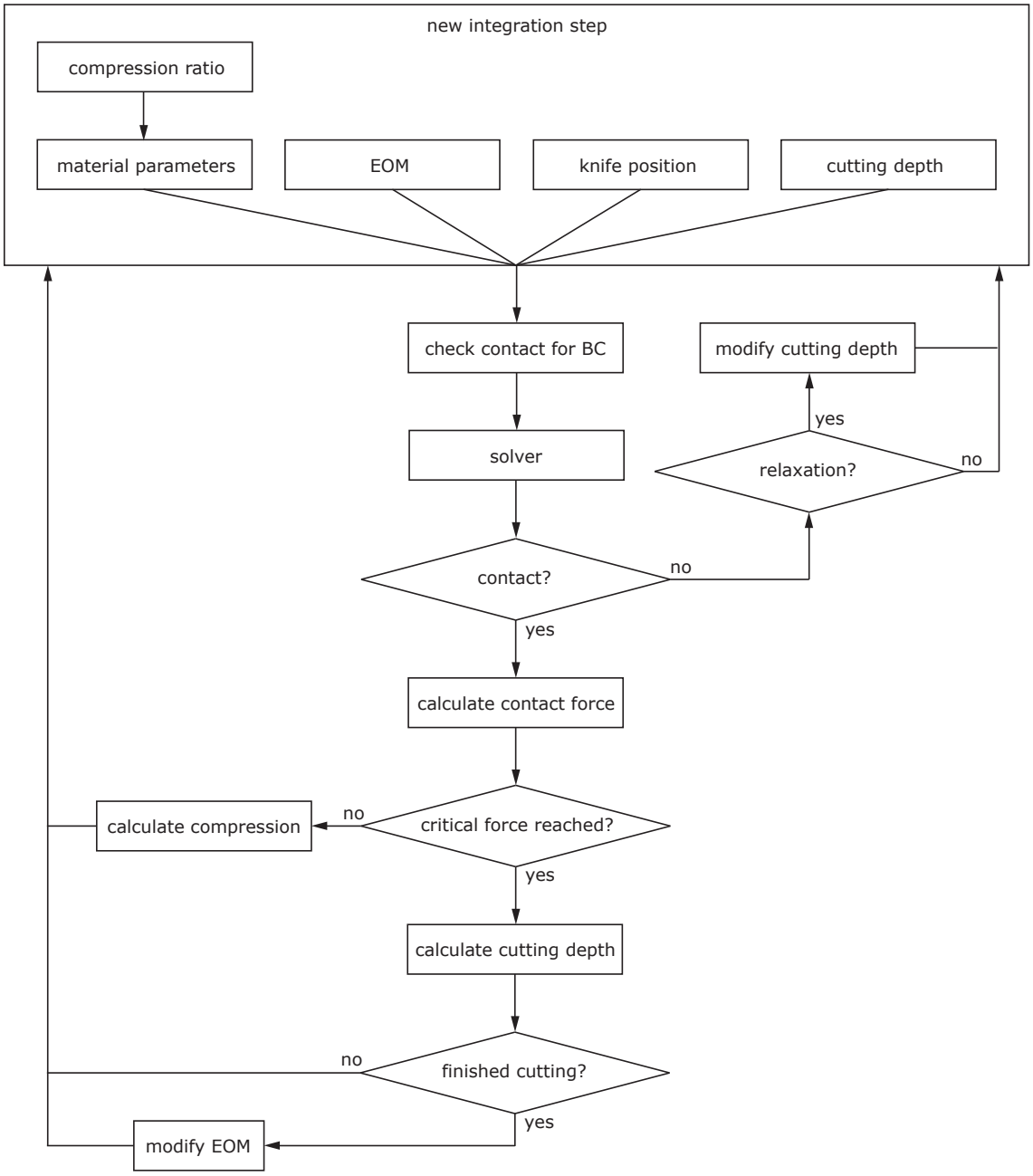

Figure A.4: Steps of the dynamic model. EOM stands for equation of motion (equation 4.16).

A.6 Integration Steps for F_Z

Since the force sensor is incapable of reproducing the true cutting force, the time average of the vertical cutting force $F_Z(t)$ needs to be calculated. To understand which mathematical steps are required, $F_Z(t)$ is completely expanded here.

$$
\begin{aligned}
F_Z(t) =& \frac{e_{fr} w}{1+\zeta^2 \sin^2(\omega t)} + \frac{\cos\beta F_{EFc} \mu_b}{\sqrt{\cos^2(\beta)\zeta^2 \sin^2(\omega t)+1}} + \sin\beta F_{EFc} + \sin\alpha F_{EFw} \\
=& \frac{e_{fr} w}{1+\zeta^2 \sin^2(\omega t)} \\
&+ \frac{\cos\beta}{\sqrt{\cos^2(\beta)\zeta^2 \sin^2(\omega t)+1}} \frac{F_K \mu_b (\sin\alpha + \mu_{pp}\cos\alpha)}{(\cos\beta - \mu_b \cos\gamma \sin\beta)(\cos\alpha - \mu_{pp}\sin\alpha) \\
&\qquad - (\sin\beta + \mu_b \cos\gamma \cos\beta)(\sin\alpha + \mu_{pp}\cos\alpha)} \\
&+ \frac{\sin\beta F_K (\sin\alpha + \mu_{pp}\cos\alpha)}{(\cos\beta - \mu_b \cos\gamma \sin\beta)(\cos\alpha - \mu_{pp}\sin\alpha) \\
&\qquad - (\sin\beta + \mu_b \cos\gamma \cos\beta)(\sin\alpha + \mu_{pp}\cos\alpha)} \\
&+ \frac{\sin\alpha F_K (\sin\alpha + \mu_{pp}\cos\alpha)}{(\cos\alpha - \mu_{pp}\sin\alpha) - \left(\frac{\mu_{pp}(\cos\alpha + \sin\alpha)}{\sqrt{\zeta^2 \sin^2(\omega t)+1}}\right)} \\
=& \frac{e_{fr} w}{1+\zeta^2 \sin^2(\omega t)} + \frac{\cos\beta}{\sqrt{\cos^2(\beta)\zeta^2 \sin^2(\omega t)+1}} \\
&\cdot \frac{F_K \mu_b (\sin\alpha + \mu_{pp}\cos\alpha)}{\left(\cos\beta - \frac{\mu_b \sin\beta}{\sqrt{\zeta^2 \sin^2(\omega t)\cos^2(\beta)+1}}\right)(\cos\alpha - \mu_{pp}\sin\alpha) \\
&\qquad - \left(\sin\beta + \frac{\mu_b \sin\beta}{\sqrt{\zeta^2 \sin^2(\omega t)\cos^2(\beta)+1}}\right)(\sin\alpha + \mu_{pp}\cos\alpha)} \\
&+ \frac{\sin\beta F_K (\sin\alpha + \mu_{pp}\cos\alpha)}{\left(\cos\beta - \frac{\mu_b \sin\beta}{\sqrt{\zeta^2 \sin^2(\omega t)\cos^2(\beta)+1}}\right)(\cos\alpha - \mu_{pp}\sin\alpha) \\
&\qquad - \left(\sin\beta + \frac{\mu_b \sin\beta}{\sqrt{\zeta^2 \sin^2(\omega t)\cos^2(\beta)+1}}\right)(\sin\alpha + \mu_{pp}\cos\alpha)} \\
&+ \frac{\sin\alpha F_K (\sin\alpha + \mu_{pp}\cos\alpha)}{(\cos\alpha - \mu_{pp}\sin\alpha) - \left(\frac{\mu_{pp}(\cos\alpha + \sin\alpha)}{\sqrt{\zeta^2 \sin^2(\omega t)+1}}\right)}
\end{aligned}
\tag{A.14}
$$

shows several terms that upon integration may be transformed into a complete elliptical integral of the first kind. Since most of the factors are material dependent, we can reduce

the expanded equation into the generic form

$$\begin{aligned} F_Z(t) =& \mathring{e}K_{ell1}^2 + \mathring{A}_{1'}K_{ell2} \\ & \cdot \frac{1}{\mathring{B}_{1'} - \mathring{C}_{1'}K_{ell2}} \\ & + \frac{\mathring{A}_{2'}}{\mathring{B}_{1'} - \mathring{C}_{1'}K_{ell2}} \\ & + \frac{\mathring{A}_{3'}}{\mathring{B}_{2'} - \mathring{C}_{2'}K_{ell2}} \end{aligned} \tag{A.15}$$

or

$$F_Z(t) = \mathring{e}K_{ell1}^2 + \mathring{A}_1\frac{K_{ell2}}{1 - \mathring{B}_1K_{ell2}} + \mathring{A}_2\frac{1}{1 - \mathring{B}_1K_{ell2}} + \mathring{A}_3\frac{1}{1 - \mathring{B}_2K_{ell2}} \tag{A.16}$$

Now, $F_Z(t)$ can be integrated with

$$\begin{aligned} \bar{F}_Z =& \frac{1}{T}\int_0^T F_Z(t)\mathrm{d}t = \frac{1}{2\pi}\int_0^{2\pi} F_Z(\omega t)\mathrm{d}(\omega t) \\ =& \frac{2}{\pi}\int_0^{\frac{\pi}{2}} F_Z(\omega t)\mathrm{d}(\omega t) \\ =& \frac{2}{\pi}\mathring{e}\int_0^{\frac{\pi}{2}} \mathring{e}K_{ell1}^2\mathrm{d}(\omega t) + \frac{2}{\pi}\mathring{A}_1\int_0^{\frac{\pi}{2}} \frac{K_{ell2}}{1 - \mathring{B}_1K_{ell2}}\mathrm{d}(\omega t) \\ & + \frac{2}{\pi}\mathring{A}_2\int_0^{\frac{\pi}{2}} \frac{1}{1 - \mathring{B}_1K_{ell2}}\mathrm{d}(\omega t) + \frac{2}{\pi}\mathring{A}_3\int_0^{\frac{\pi}{2}} \frac{1}{1 - \mathring{B}_2K_{ell2}}\mathrm{d}(\omega t) \end{aligned} \tag{A.17}$$

The integrals can be separately integrated, resulting in the average cutting force in z-direction. Alternatively, the complete equation can be simply numerically integrated for the desired result.

A.7 Vertical Friction Reduction with respect to ξ

In some contributions, the slice-push ratio for ultrasonic vibration assisted machining is defined as (see section 2.5.2)

$$\xi = \frac{v_c}{\hat{v}} \tag{A.18}$$

(literally push-slice ratio), which results in a slight different graph in regard to the vertical friction reduction as shown in Figure A.5. Equations can be found in [142].

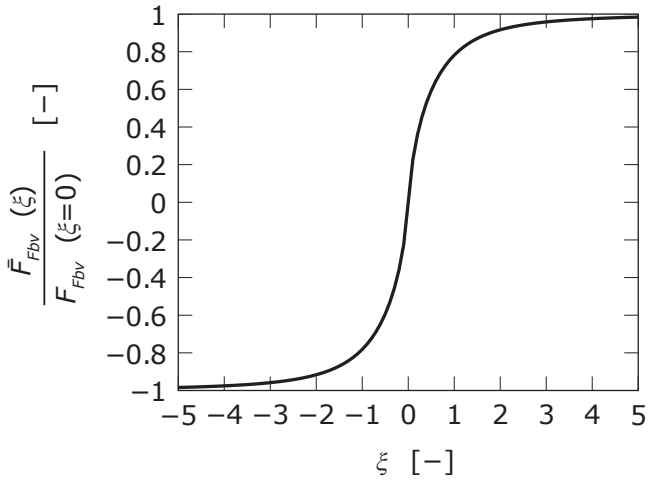

Figure A.5: Vertical friction force reduction as a function of ξ with invariant F_{EF}.

A.8 J_c for Nonlinear Elastic Plastic Materials

If the DENT test is performed with linear elastic materials showing significant plastic (nonlinear) deformation, the calculation of J_c needs to include the necessary energy. Hence, the calculation following equation (6.11) are continued as following (based on [64]). The previously introduced displacement u can be split up into elastic and plastic parts with

$$u = u_{el} + u_{pl} \tag{A.19}$$

allowing the integral to be written as

$$J = -\frac{1}{2B}\int_0^F \left(\left(\frac{\partial u_{el}}{\partial b}\right) + \left(\frac{\partial u_{pl}}{\partial b}\right)\right)_F \mathrm{d}F \tag{A.20}$$

The first term contains the energy release rate from the linear elastic fracture mechanics, which allows the simplification to

$$J = \frac{K_I^2}{E} - \frac{1}{2B}\int_0^F \left(\frac{\partial u_{pl}}{\partial b}\right)_F \mathrm{d}F \tag{A.21}$$

With the obtained K_{Ic} from the previously carried out DENT tests, and the Young's Modulus E from curve fitting of the tensile test, the elastic term can easily be determined. The challenge is the evaluation of the plastic term of the integral. With the help of a few mathematical transformations, this challenge can be overcome. To begin with, the plastic deformation is replaced by

$$u_{pl} = b\mathring{H}\left(\frac{F}{Bb}\right) \tag{A.22}$$

where $\mathring{H}()$ is a generic auxiliary function, requiring stress as an argument and giving back a dimensionless return value. It is essentially the force-elongation or stress-strain curve of the material, where force or stress is the input and strain is the return value. Since the displacement u_{pl} is in the dimension of length, the multiplication with b is necessary (assuming b is significantly smaller than w, and thus the sample only plasticizes between the crack tips). Using the product rule and chain rule for the differentiation,

$$\begin{aligned}\left(\frac{\partial u_{pl}}{\partial b}\right)_F &= \mathring{H}\left(\frac{F}{Bb}\right) + b\mathring{H}'\left(\frac{F}{Bb}\right)\frac{\partial}{\partial b}\left(\frac{F}{Bb}\right) = \mathring{H}\left(\frac{F}{Bb}\right) - b\mathring{H}'\left(\frac{F}{Bb}\right)\frac{F}{Bb^2} \\ &= \mathring{H}\left(\frac{F}{Bb}\right) - \mathring{H}'\left(\frac{F}{Bb}\right)\frac{F}{Bb}\end{aligned} \tag{A.23}$$

where $\mathring{H}'$ is the first derivative of the function $\mathring{H}$ with respect to its sole argument. This can be found by deriving with respect to F instead of b as stated in

$$\left(\frac{\partial u_{pl}}{\partial F}\right)_b = b\mathring{H}'\left(\frac{F}{Bb}\right)\frac{\partial}{\partial F}\left(\frac{F}{Bb}\right) = b\mathring{H}'\left(\frac{F}{Bb}\right)\frac{1}{Bb} = \frac{1}{B}\mathring{H}'\left(\frac{F}{Bb}\right) \tag{A.24}$$

Inserting this result and the definition of the auxiliary function into the derivative with respect to b,

$$\left(\frac{\partial u_{pl}}{\partial b}\right)_F = \frac{u_{pl}}{b} - B\left(\frac{\partial u_{pl}}{\partial F}\right)_b\frac{F}{Bb} = \frac{1}{b}\left(u_{pl} - F\left(\frac{\partial u_{pl}}{\partial F}\right)_b\right) \tag{A.25}$$

is obtained. Inserting the above equation into equation (A.21), and partial integration, J is calculated as

$$J = \frac{K_I^2}{E} - \frac{1}{2Bb}\int_0^F \left(u_{pl} - F\left(\frac{\partial u_{pl}}{\partial F}\right)_b\right) \mathrm{d}F$$
$$= \frac{K_I^2}{E} - \frac{1}{2Bb}\left[\int_0^F u_{pl}\mathrm{d}F - \underbrace{\int_0^F F\left(\frac{\partial u_{pl}}{\partial F}\right)\mathrm{d}F}_{Fu_{pl}\big|_{F=0}^{F=F} - \int_0^F u_{pl}\mathrm{d}F}\right] = \frac{K_I^2}{E} - \frac{1}{2Bb}\left[2\int_0^F u_{pl}\mathrm{d}F - Fu_{pl}\right] \quad \text{(A.26)}$$

([64] contains a sign error). To numerically determine the value of the J-integral at a specific force, the force value and elongation value must be recorded throughout the entire DENT test. Consequently, J_c is simply numerically calculated with equation (A.26) at the critical force of DENT sample failure. To allow proper sudden critical failure, the DENT test should be carried out with loading control.

A.9 DENT Testing of Paper (illustrating photos)

Figure A.6 shows how the DENT testing is carried out with paper sheets. Initial incisions and crack propagation are visible.

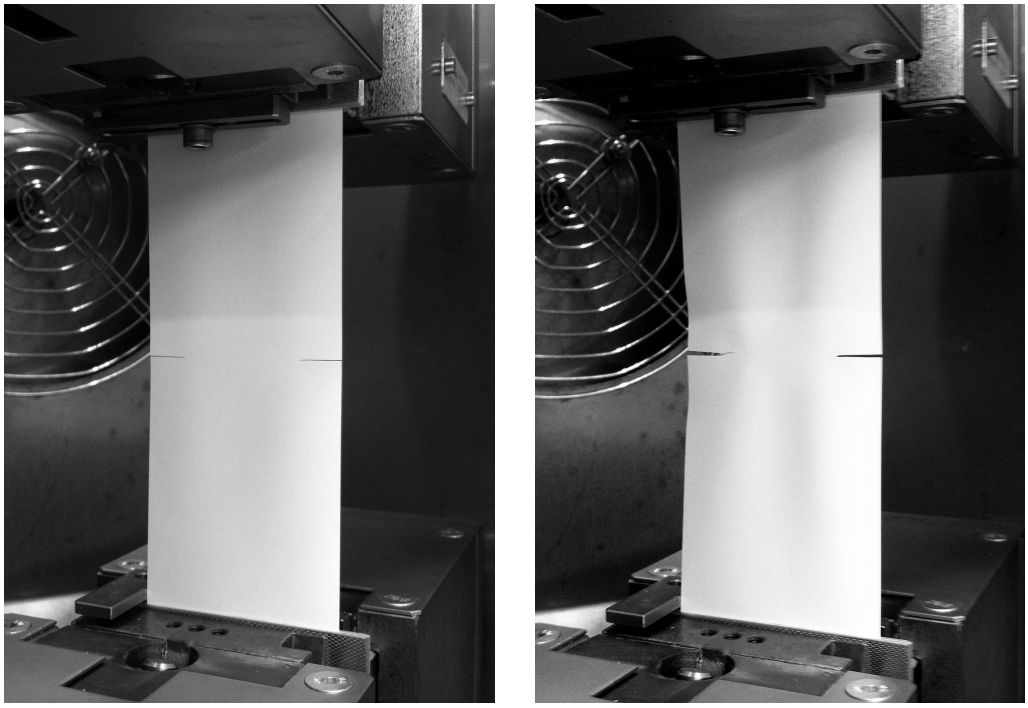

(a) Initial Condition, with no force applied. Incision for edge notch done with a cutter knife.

(b) DENT sample near critical force before failure. Growing crack on left notch clearly visible.

Figure A.6: Illustrating Photos for DENT testing of paper sheets, with $a = 10\,\mathrm{mm}$.

A.10 Length of Axially Symmetric Devices

Considering a uniform rod with in-plane displacements being excited along the axis of rotation, a longitudinal mode occurs. If u is the displacement at x, then the displacement at $x + dx$ will be $u + (\partial u/\partial x)dx$. Then the element dx in the new position has changed in length by $(\partial u/\partial x)dx$, and thus the strain of the element is $\partial u/\partial x$ as shown in Figure A.7 [121]. With Hooke's law

$$\sigma = E\epsilon \tag{A.27}$$

with σ being the stress in the element, ϵ being the strain, and E being Young's modulus, for a uniform rod with a cross-sectional area A and applied force F it can be stated that

$$\frac{\partial u}{\partial x} = \frac{F}{AE} \tag{A.28}$$

By differentiating it with respect to x,

$$AE\frac{\partial^2 u}{\partial x^2} = \frac{\partial F}{\partial x} \tag{A.29}$$

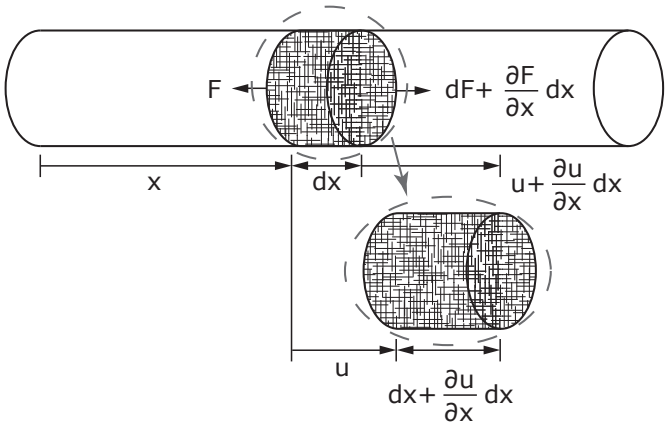

Figure A.7: Displacement of rod element [121].

By applying Newton's second law (laws of motion) for the element and equating the unbalanced force to the product of the mass and acceleration of the element,

$$\frac{\partial F}{\partial x}dx = \rho A dx \frac{\partial^2 u}{\partial t^2} \tag{A.30}$$

with ρ being the density of the rod. Substituting $\partial F/\partial x$ in equation (A.30) with equation (A.29), the partial differential equation

$$\frac{\partial^2 u}{\partial t^2} = \left(\frac{E}{\rho}\right)\frac{\partial^2 u}{\partial x^2} \tag{A.31}$$

or

$$\frac{\partial^2 u}{\partial x^2} = \frac{1}{c^2}\frac{\partial^2 u}{\partial t^2} \tag{A.32}$$

is obtained, where c is the displacement propagation velocity within the rod.

$$c = \sqrt{\frac{E}{\rho}} \tag{A.33}$$

Solving partial differential equations may be done with the separation of variables and the solution of the form

$$u(x,t) = G(x)H(t) \tag{A.34}$$

and equation (A.32) becomes

$$\frac{1}{G}\frac{\mathrm{d}^2 G}{\mathrm{d}x^2} = \frac{1}{c^2}\frac{1}{H}\frac{\mathrm{d}^2 H}{\mathrm{d}t^2} \tag{A.35}$$

Because the left side of this equation is independent of t, whereas the right side is independent of x, it follows that each side must be a constant. Letting this constant be $-(\omega/c)^2$, two ordinary differential equations (ODE) can be obtained

$$\frac{\mathrm{d}^2 G}{\mathrm{d}x^2} + \left(\frac{\omega}{c}\right)^2 G = 0 \tag{A.36}$$

$$\frac{\mathrm{d}^2 H}{\mathrm{d}t^2} + \omega^2 H = 0 \tag{A.37}$$

with the general solution being

$$G(x) = A\sin\left(\frac{\omega}{c}x\right) + B\cos\left(\frac{\omega}{c}x\right) \tag{A.38}$$

$$H(t) = C\sin(\omega t) + D\cos(\omega t) \tag{A.39}$$

The arbitrary constants A, B, C, D depend on the boundary conditions and the initial conditions. The general solution is

$$u(x,t) = \left(A\sin\left(\frac{\omega}{c}x\right) + B\cos\left(\frac{\omega}{c}x\right)\right)(C\sin(\omega t) + D\cos(\omega t)) \tag{A.40}$$

Regarding the free uniform rod with a longitudinal mode, the stress at the ends must be zero. Thus the natural frequency of vibration is given as

$$\omega_n = \frac{n\pi}{l}\sqrt{\frac{E}{\rho}} \tag{A.41}$$

with n presenting the order of the mode and l the total length of the rod. Equation (A.41) is only accurate for low order modes and when the length is much greater than the diameter.

Non-uniform but axis-symmetrical geometries can also be analytically designed using the Webster Horn Equation [147].

$$\frac{\partial^2 u}{\partial x^2} + \frac{1}{A(x)}\frac{dA(x)}{dx}\frac{\partial u}{\partial x} = \frac{1}{c^2}\frac{\partial^2 u}{\partial t^2} \tag{A.42}$$

where $A(x)$ is the cross sectional area dependent on position x. With this formula, simple axis-symmetrical horns can be tuned according to a specific excitation frequency. However, more complex geometries are necessary for most manufacturing processes.

A.11 Basic Equations for Dynamic Analysis using FEM

Following FEM equations are taken from [148].

A.11.1 Modal Analysis

Modal Analysis of a structure is used to determine its mode shapes and frequencies. For an undamped system, the equation of motion is

$$\boldsymbol{M}\ddot{\boldsymbol{u}} + \boldsymbol{K}\boldsymbol{u} = \boldsymbol{0} \tag{A.43}$$

Since no time dependent forces are impacting the modal analysis, the linear system motion can be described as free harmonic vibrations, stated by

$$\boldsymbol{u} = \boldsymbol{\Theta}_i \cos(\omega_i t) \tag{A.44}$$

where $\boldsymbol{\Theta}_i$ is the eigenvector, representing the mode shape of the i^{th} natural frequency, and (ω_i is the i^{th} natural circular frequency. Inserting equation A.44 into equation A.43 gives the non-trivial solution

$$\det\left(\boldsymbol{K} - \omega^2\boldsymbol{M}\right) = 0 \tag{A.45}$$

This solution is an eigenvalue problem and can be solved for up to n values of ω^2, where n are the degrees of freedom.

A.11.2 Harmonic Analysis

The Harmonic Analysis allows the solution of the time dependent equation of motion of a linear structure undergoing steady-state vibrations. It is stated by

$$\boldsymbol{M}\ddot{\boldsymbol{u}} + \boldsymbol{K}\boldsymbol{u} + \boldsymbol{D}\dot{\boldsymbol{u}} = \boldsymbol{F} \tag{A.46}$$

It is assumed that all parts of the structure move with the same frequency Ω. Due to the damping of the structure, phase shift ι may occur. Displacement and applied load are introduced as

$$\boldsymbol{u} = (\boldsymbol{u_1} + i \cdot \boldsymbol{u_2})\, e^{i\Omega t} \tag{A.47}$$

$$\boldsymbol{F} = (\boldsymbol{F_1} + i \cdot \boldsymbol{F_2})\, e^{i\Omega t} \tag{A.48}$$

because they may be different for every degree of freedom. Inserting these vectors into the equation of motion gives

$$\left(\boldsymbol{K} - \Omega^2 \boldsymbol{M} + i\Omega \boldsymbol{D}\right)(\boldsymbol{u_1} + i \cdot \boldsymbol{u_2}) = \boldsymbol{F_1} + i \cdot \boldsymbol{F_2} \tag{A.49}$$

where

$$\boldsymbol{u_1},\ \boldsymbol{F_1} = \boldsymbol{u_{max}} \cdot \cos\iota,\ \boldsymbol{F_{max}} \cdot \cos\iota \tag{A.50}$$

$$\boldsymbol{u_2},\ \boldsymbol{F_2} = \boldsymbol{u_{max}} \cdot \sin\iota,\ \boldsymbol{F_{max}} \cdot \sin\iota \tag{A.51}$$

A.12 Additional Figures of the Optimization Results

Figure A.8 and Figure A.9 show examples of starting designs of the GA optimization. Figure A.10 and Figure A.11 show CAD drawings of the final solution for the geometry of the lateral ultrasonic vibration assisted cutting knife. Figure A.12, Figure A.13a, and Figure A.13b show CAD drawings of the final solution for the geometry of the longitudinal ultrasonic vibration assisted cutting knife.

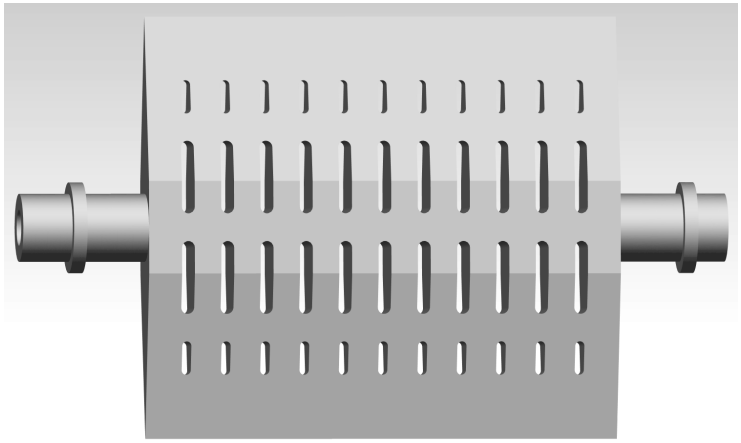

Figure A.8: An example of a random starting geometry for the lateral ultrasonic vibration assisted cutting knife.

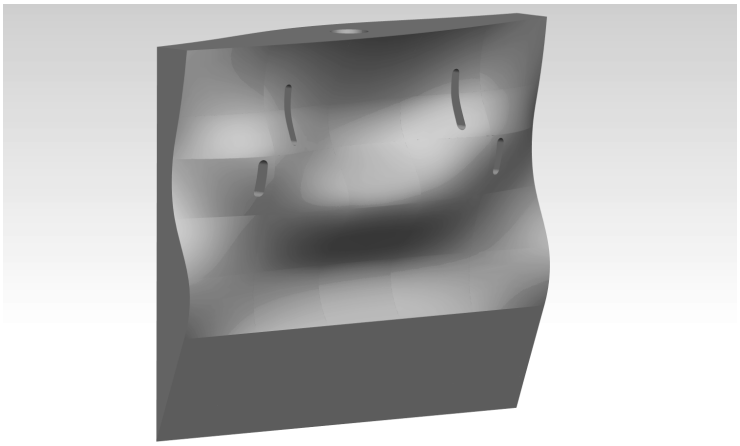

Figure A.9: An example of a random starting geometry for the longitudinal ultrasonic vibration assisted cutting knife.

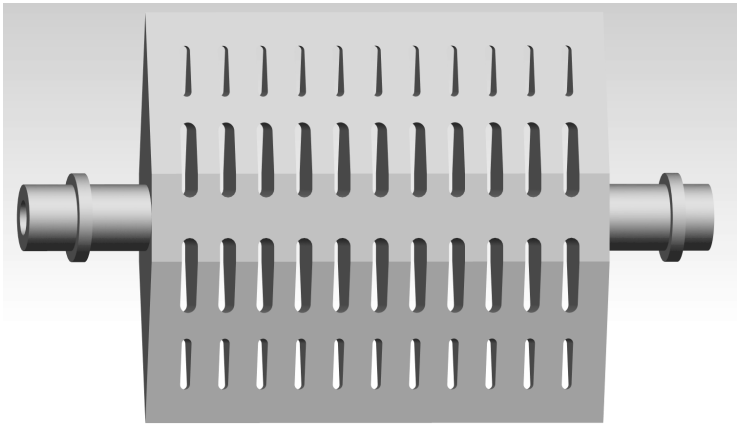

Figure A.10: Front view of the final geometry for the lateral ultrasonic vibration assisted cutting knife.

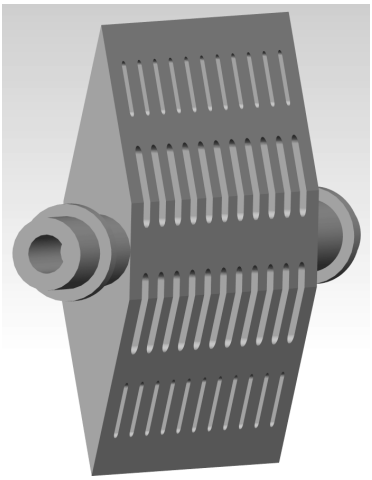

Figure A.11: Side view of the final geometry for the lateral ultrasonic vibration assisted cutting knife.

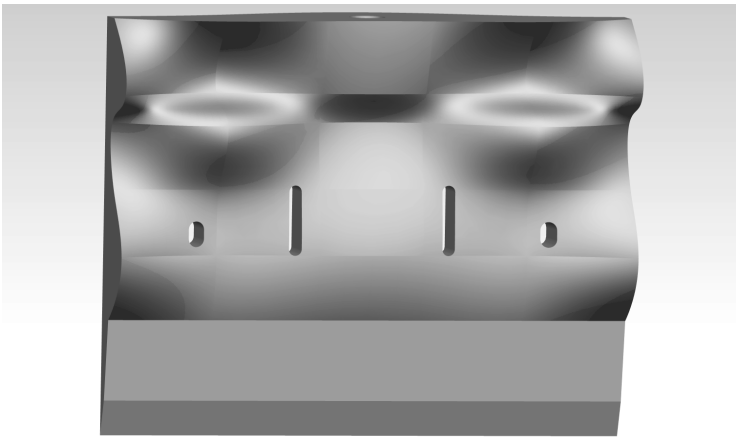

Figure A.12: Front view of the final geometry for the longitudinal ultrasonic vibration assisted cutting knife.

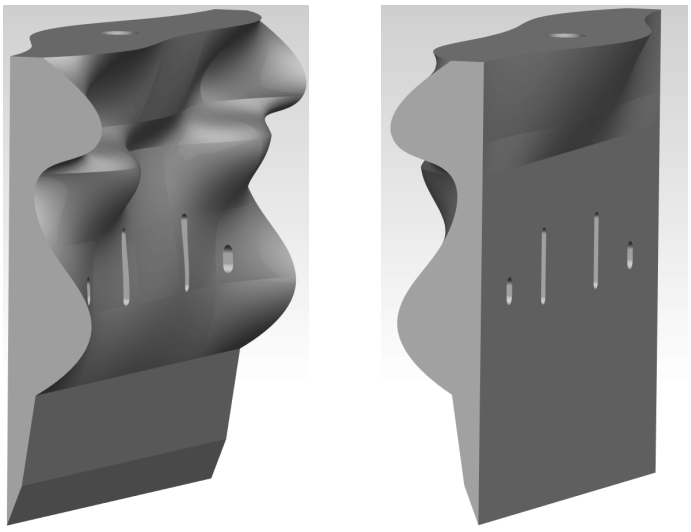

(a) **(b)**

Figure A.13: Side views of the final geometry for the longitudinal ultrasonic vibration assisted cutting knife.

A.13 Reflection Electron Microscope (REM) Images of the Paper Sheets

Figure A.14 shows REM images of the paper sheets using the experiments. All sheets were cut with vertical slide cutting (no vibration).

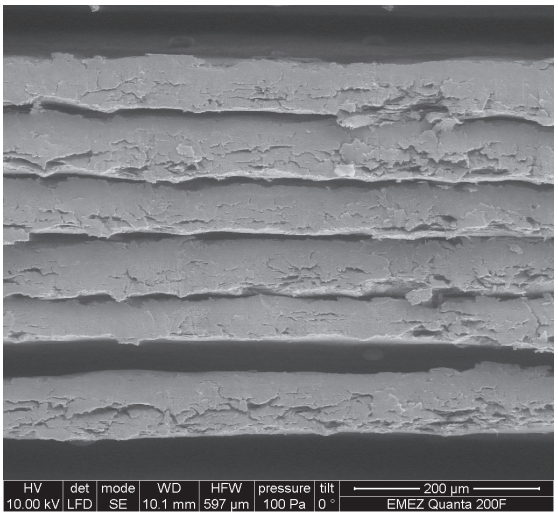

(a) Front view.

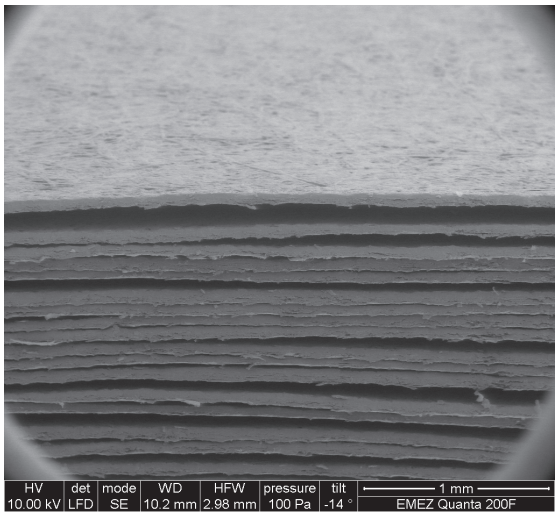

(b) Bottom tilted view.

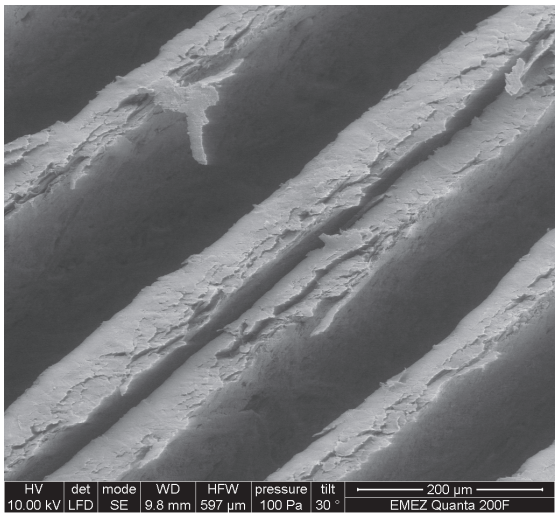

(c) Front tilted view.

Figure A.14: REM images of the paper sheets used in the experiments. The patches on top of the fibers are parts of the printing ink.

A.14 Sheets scaling off after cutting and self-locking cutting angle

When cutting a stack of sheets, it can be observed that at a small length of the cut of part, the top cut sheets do not touch the knife in section III but scale off at a certain cutting

depth, because the normal force of the lower sheet cannot physically support the cut sheets. Hence the position x_N of the normal force F_{Np} is defined in Figure 2.8. To calculate the stack height h_s at which sheets no longer scale off, the equilibrium of moments for $\alpha = 0$ at point z_1 is considered by

$$\sum M_{z_1} = 0 = F_{EF1}\frac{h_p}{2\cos\beta} + F_{G1}\frac{b}{2} + F_{Np1}x_{N1} \tag{A.52}$$

that can be rearranged to

$$x_{N1} = \frac{\mu_{pp}\frac{h_p}{2\cos\beta} + \frac{b}{2}\left(\cos\beta - \mu_b\sin\beta - \mu_{pp}\sin\beta - \mu_b\mu_{pp}\cos\beta\right)}{\cos\beta - \mu_b\sin\alpha} \tag{A.53}$$

and simplified under the assumption that $F_{Npn} = n \cdot F_{Np}$ and $F_{G1} = F_{G2} = ... = F_{Gn}$,

$$x_{Nn} = x_{N1} + \frac{n-1}{2}h_p\left(\mu_{pp} + \tan\beta\right) \tag{A.54}$$

as the general expression for x_{Nn}, where h_p is the thickness of one sheet, and $b/2$ is the center of gravity per sheet. x_{Nn} increases with the cutting depth of the knife. When $x_N = b$, the cut sheets scale off. Thus h_s can be obtained:

$$h_s = 2\frac{b - x_{n1}}{\mu_{pp} + \tan\beta} - h_p \tag{A.55}$$

Equations (A.53), (A.54), and (A.55) can be rewritten for $\alpha > 0$ to

$$x_{N1} = \frac{\frac{\mu_{pp}\cos\alpha + \sin\alpha}{\Psi}\frac{h_p}{2\cos\beta} + \frac{b}{2}\cos\alpha}{\frac{\cos\beta - \mu_b\sin\beta}{\Psi}} \tag{A.56}$$

$$x_{Nn} = x_{N1} + \frac{n-1}{2}h_p\left(\mu_{pp} + \tan(\beta+\alpha)\right) \tag{A.57}$$

$$h_s = 2\frac{b - x_{n1}}{h_p\mu_{pp} + \tan(\beta+\alpha)} - h_p \tag{A.58}$$

with

$$\Psi = \left(\cos\beta - \mu_b\sin\beta\right)\left(\cos\alpha - \mu_{pp}\sin\alpha\right) - \left(\sin\beta + \mu_b\cos\beta\right)\left(\sin\alpha + \mu_{pp}\cos\alpha\right) \tag{A.59}$$

for equation (A.56). To determine the cutting angle β_L at which self-locking occurs, equation (A.59) is set to zero. Hence, the self-locking angle calculates to

$$\beta_L = \arctan\frac{1 - (\mu_b + \mu_{pp})\tan\alpha - \mu_b\mu_{pp}}{(1 - \mu_b\mu_{pp})\tan\alpha + \mu_b + \mu_{pp}} \tag{A.60}$$

A.15 Additional Photos of the Guillotining Test Stand

Figure A.15 shows further photos of the guillotining test stand.

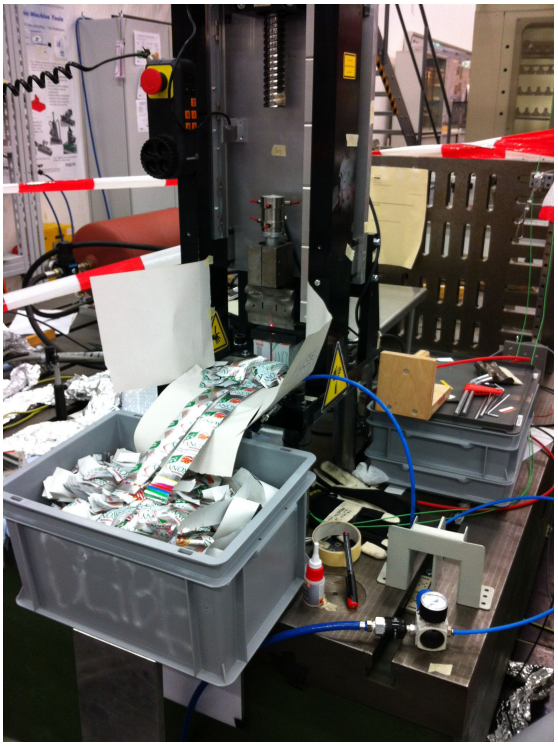

(a)

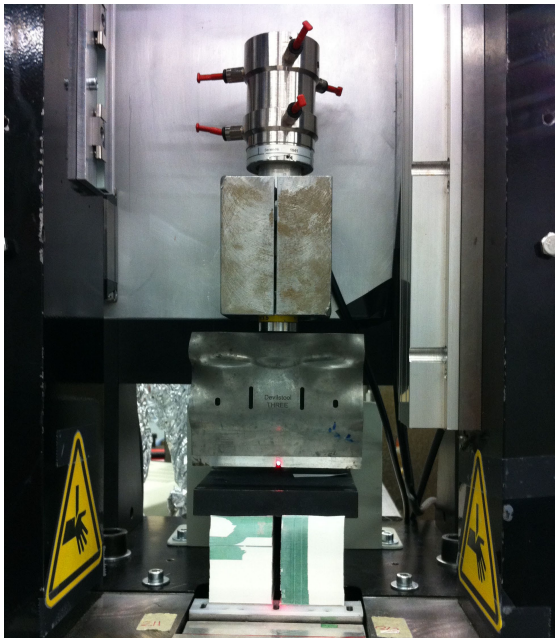

(b)

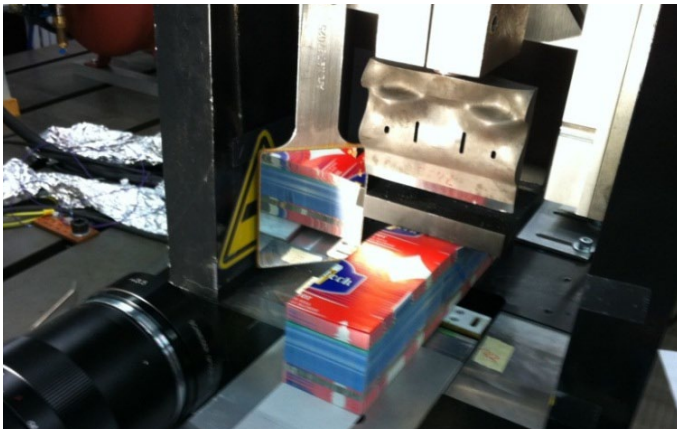

(c)

Figure A.15: Additional images of the guillotining test stand.

B List of Publications

i K.-R. Deibel, J. Boos, K. Wegener. Friction Effects between Ultrasonic Cutting Blade and Sheet Stack. *2012 IEEE International Ultrasonics Symposium*, Pages 2663-2666, 2012, Dresden, Germany. ISBN 978-1-4673-4561-3, ISSN 1948-5719, DOI http://dx.doi.org/10.1109/ULTSYM.2012.0667.

ii K.-R. Deibel, J. Boos, S. Weikert, K. Wegener. Correlation of Cutting Force and Power Consumption for Ultrasonic-Vibration-Assisted Cutting of Label Paper Stacks. *ASME 2012 International Mechanical Engineering Congress & Exposition*, Volume 3, Pages 1421-1428, 2012, Houston, USA. ISBN 978-0-7918-4519-6.

iii K.-R. Deibel, K. Wegener. Methodology for Shape Optimization of Ultrasonic Amplifier using Genetic Algorithms and Simplex Method. *Proceedings of the North American Manufacturing Research Institution of SME*, Volume 41, 2013, Madison, Wisconsin, USA. ISBN 087263874-x, ISSN 2161-220X.

iv K.-R. Deibel, K. Wegener. Methodology for Shape Optimization of Ultrasonic Amplifier using Genetic Algorithms and Simplex Method. *Journal of Manufacturing Systems*, 32(4): 523-528, 2013. DOI http://dx.doi.org/10.1016/j.jmsy.2013.05.010.

v K.-R. Deibel, S. Lämmlein, K. Wegener. Model of Slice-Push Cutting Forces of stacked thin Material. *Journal of Materials Processing Technology*, 214(3): 667-672, 2013. DOI http://dx.doi.org/10.1016/j.jmatprotec.2013.10.009.

vi (K.-R. Deibel, C. Raemy, K. Wegener. Modeling Slice-Push Cutting Forces of a Sheet Stack based on Fracture Mechanics. *Journal of Engineering Fracture Mechanics*, 2013. Under Review.)

vii (K.-R. Deibel, F. Kaiser, R. Zimmermann, L. Meier, P. Bolt, K. Wegener. Longitudinal Ultrasonic Vibration Assisted Guillotining of Stacked Paper. *Ultrasonics*, 2013. Under Review.)

C List of supervised Theses

The following theses (unpublished) were supervised by the author:

i P. Bolt. Modellieren von Reibung und Materialverhalten beim Vibration unterstützten Schneiden von gestapelten Materialien. Master Thesis. 2013.

ii S. Müller. Untersuchungen zu Verbindungsstellen und Schwingungsübertragung beim vibrationsunterstützten Bohren/Schneiden. Master Thesis. 2013.

iii F. Kaiser. Energieeffizienz beim Hybrid-Schneiden. Bachelor Thesis. 2013.

iv S. Lämmlein. Konstruktion von neuem Messer zum UVA Sägeschneiden, experimenteller Verifikation und energetischer Beurteilung. Bachelor Thesis. 2013.

v C. Raemy. Modellierung des Schneidprozesses beim Hybridschneiden - Versagen und Bruch. Semester Project. 2013.

vi M. Schneider. Weiterführende Arbeiten zur Konstruktion via Strukturoptimierung eines Niederkraftbohrers. Bachelor Thesis. 2013.

vii R. Zimmermann. Modelling of Vibration Assisted Guillotining and Experimental Verification. Master Thesis. 2013.

viii U. Lemann. Konstruktion via Strukturoptimierung eines Gesteinsbohrers für planetarische Operationen und Niederkraftbohrer. Bachelor Thesis. 2012.

ix N. Furrer. Weiterführende Arbeiten (Konstruktion, Simulation) zu einem VA chirurgischen Messer aus der Medizinaltechnik. Semester Project. 2012.

x D. Stone. Strukturoptimierung (TOPO) und Fertigung eines Cutters zum Hybrid-Schneiden von HT-Fasermaterialien. Semester Project. 2012.

xi L. Meier. Konstruktion eines neuen Prüfstands zum vibrationsunterstützten Schneiden und Experimenten. Bachelor Thesis. 2012.

xii R. Wäspi. Konstruktion und Untersuchungen zu einem ultraschallunterstützten chirurgischen Messer aus der Medizinaltechnik. Bachelor Thesis. 2012.

Bibliography

[1] E. W. Wood and Alfred L. Loomis. The physical and biological effects of high-frequency soundwaves of great intensity. *Philosophical Magazine Series 7*, 4:417–436, 1927.

[2] Shaul Katzir. Who knew piezoelectricity? Rutherford and Langevin on submarine detection and the invention of sonar. *Notes and Records of the Royal Society*, 2012.

[3] J. Farrer. Method of abrading, 1948. Patent 602801, Great Britain.

[4] Vladimir K. Astashev and Vladimir I. Babitsky. *Ultrasonic Processes and Machines*. Springer, 2007.

[5] L. D. Rozenberg and V. F. Kazantsev. *Ultrasonic Cutting*. Consultants Bureau, 1964.

[6] D. E. Brehl and T. A. Dow. Review of vibration-assisted machining. *Precision Engineering*, 32:153–172, 2008.

[7] Jochen Matauschek. *Einführung in die Ultraschalltechnik*. VEB Verlag Technik, 1961.

[8] Rudolf Millner. *Ultraschalltechnik: Grundlagen und Anwendungen*. Physik-Verlag, 1987.

[9] DIN 8588. DIN 8588 Fertigungsverfahren Zerteilen. Deutsches Institut für Normung e.V., 2003.

[10] Alfred Herbert Fritz; Günter Schulze. *Fertigungstechnik*. Springer, Berlin, 10th edition, 2012.

[11] DIN 8580. DIN 8580 Fertigungsverfahren. Deutsches Institut für Normung e.V., 2003.

[12] Collège International pour l'Etude Scientifique des Techniques de Production Mécanique. *Dictionary of Production Engineering 1*. Springer, 2nd edition, 1997.

[13] Collège International pour l'Etude Scientifique des Techniques de Production Mécanique. *Dictionary of Production Engineering 2*. Springer, Berlin, 1st edition, 2004.

[14] Collège International pour l'Etude Scientifique des Techniques de Production Mécanique. *Dictionary of Production Engineering 3*. Spring, 1st edition, 2004.

[15] *Cutting Paper and Board*. Seminar of the British Paper and Board Industry Federation, Bristol, January 1978.

[16] Fritz Hesse and Hans-Jürgen Tenzer. *Grundlagen der Papierverarbeitung*, volume 2. VEB Verlag für Buch- und Bibliothekswesen, Leipzig, 1963.

[17] Helmut Kipphan. *Handbuch der Printmedien*. Springer, 2000.

[18] Reimund Neugebauer, Bernd Arnold, Dieter Schmoeckel, and Nikolai Geissler. *Einflüsse auf die Schnitteilqualität beim Schneiden von Blechen auf Tafelscheren*. Europäische Forschungsgesellschaft für Blechverarbeitung e.V., 1999.

[19] Erhard Hennemann. Das Messer im Schnellschneider. *Papier+Kunststoff-Verarbeiter*, 1:17–20, 1982.

[20] DIN 8869. DIN 8869 Langmesser für Papierschneidemaschinen. Deutsches Institut für Normung e.V., 1964.

[21] Dittrich. Die zum Schnitt erforderlichen Kräfte an Schneidemaschinen. *Buchbinderei und Papierverarbeitung*, 5,6:65–67,91–93, 1959.

[22] Wolfgang Rösner and Wilfried Schulz. *Theoretische und experimentelle Untersuchungen zur Optimierung des Schneidprozesses von Papierstapeln*. Dissertation, Technische Hochschule Karl-Marx-Stadt, 1974.

[23] Hans Jürgen Schneider and Ernst Erich Kottsieper. Maschinenmesser - Qualitätswerkzeuge für das Schneiden von Papier und Kunststoff. *Papier+Kunststoff-Verarbeiter*, 5 and 6:30–44 and 92–98, 1982.

[24] Erhard Hennemann. Scharf und sauber. *Papier+Kunststoff-Verarbeiter*, 6:100–102, 1982.

[25] Claudia Treffert. Der gute Schnitt. *Papier+Kunststoff-Verarbeiter*, 10:30–34, 1996.

[26] R Wilken, B. Hartmann, and J. Forster. Zum Stanzen von Etiketten. *Etiketten*, 1-2:9–14 and 4–8, 1994.

[27] Helmut Hofer und Volker Würth. Stanzkraft und Messerverschleiss beim Stanzen von Wellpappe. *Papier+Kunststoff-Verarbeiter*, 8 and 10:11–13 and 33–38, 1994.

[28] Wolfgang Grebe and Rolf Sinn. Zurichtungsfreies Stanzen - keine Utopie mehr? *Papier+Kunststoff-Verarbeiter*, 4:50–54, 1997.

[29] Erdinc Agirbas and Eugen Herzau. Untersuchung zur Bestimmung der Stanzkraft in Abhängigkeit von den Stanzguteigenschaften. *Papier+Kunststoff-Verarbeiter*, 7/8:22–28, 1998.

[30] Hans Klingelhöffer. Schneidkraft und Schneidarbeit beim Scherschnitt. *Allgemeine Papierrundschau (APR)*, 23:1190, 1961.

[31] Helmut Hofer. Stanzen von Karton und Wellpappe in Theorie und Praxis. *Papier+Kunststoff-Verarbeiter*, 2:28–33, 1997.

[32] Hans Klingelhöffer. Schneiddruck von Kreismessern. *Allgemeine Papierrundschau (APR)*, 17:972, 1963.

[33] Reinhold Schable. Fehlerhafte Schneidwinkeleinstellungen verursachen schlechte Schnittqualität. *Papier+Kunststoff-Verarbeiter*, 1:20–26, 1994.

[34] Reinhold Schable. Die Wichtigkeit der Messereinstellungen beim Scherenschnitt. *Papier+Kunststoff-Verarbeiter*, 9:34–38, 1994.

[35] Hans Klingelhöffer. Ziehender Schnitt. *Allgemeine Papierrundschau (APR)*, 14:760, 1962.

[36] B. M. Mordowin. *Buchbindereimaschinen I.* VEB Verlag Technik, Berlin, 1st edition, 1962.

[37] Schneidemaschinen für Papier und andere blättrige Stoffe. *Papier-Zeitung*, 90:1684–1691, 1936.

[38] Thomas Hülsmann. *Verschleissvorgänge beim Querschneiden dünner Bahnen.* Dissertation, Universität Stuttgart, 1988.

[39] Andrzej Dowgiallo. Cutting force of fibrous materials. *Journal of Food Engineering*, 66(1):57 – 61, 2005.

[40] Michael Desch. *Der Einfluss der Schneidlage auf den effektiven Keilwinkel des Messers - eine methodische Untersuchung an Schnellschneidern.* PhD thesis, Technische Universität Darmstadt, August 2012.

[41] Hans Klingelhöffer. Spannungsverteilung und Schnittgüte beim Scherschnitt. *Allgemeine Papierrundschau (APR)*, 15:498, 1967.

[42] K. Weyl. Schnittkräfte an Papier-Schneidemaschinen. *Allgemeiner Anzeiger für Buchbindereien*, 2-5:64–65 and 124–140 and 240–254 and 336–339, 1962.

[43] Rudi Cwiklinski. Fachkunde für den Buchbinder. *Buchbinderei und Papierverarbeitung*, 4:63–64, 1959.

[44] Hugo Klein. Querschneider-Technologie. *Papier+Kunststoff-Verarbeiter*, 1 and 2 and 4 and 5:28–32 and 28–34 and 26–30 and 56–60, 1981.

[45] S. I. Cavlin and B. Edholm. Der Einfluss von Papiereigenschaften und Korrugierungsbedingungen auf die Rissbildung beim Stanzen. *Papier+Kunststoff-Verarbeiter*, 11:58–66, 1989.

[46] D. L. T. Chapman and J. D. Peel. Calendering processes and the compressibility of paper (part 1). *Paper Technology*, 10:T24–T32, 1969.

[47] H. J. Hohmann. Biegesteifigkeit von Pappe und Karton. *Verpackungs-Rundschau*, 5:41–45, 1971.

[48] U. Höke and L. Göttsching. Stauchfestigkeiten von Papier, Wellpappe und Schachteln. *Das Papier*, 10A:V65–V73, 1985.

[49] Richard E. Mark, Jr. Charles C. Habeger, Jens Borch, and M. Bruce Lyne, editors. *Handbook of Physical Testing of Paper*, volume 1. Marcel Dekker, Inc., New York, 2nd edition, 2002.

[50] Walter Brecht and Martin Schädler. Über neue Messungen der Kompressibilität von Papieren. *Das Papier*, 10A:626–634, 1963.

[51] H. Grossmann and H. L. Baumgarten. Zum Verhalten von Papier und Karton in der Kompressionsphase des Messerschnittes. *Das Papier*, 10A:V74–V82, 1985.

[52] H. L. Baumgarten. Zustandsänderungen der Gase in porösen Materialien bei deren dynamischer Kompression am Beispiel Papier. *Das Papier*, 2:45–51, 1979.

[53] H.-J. Schaffrath and L. Göttsching. Modellierung der Kompression von Papier in z-Richtung bei niedriger Flächenpressung. *Das Papier*, 7:350–355, 1992.

[54] H.-J. Schaffrath and L. Göttsching. Das Kompressionsverhalten von Papier in z-Richtung. *Das Papier*, 10A:V74–V81, 1992.

[55] J. Blechschmidt and L. Burchardt. Grundlagen, Möglichkeiten und Grenzen der Berechenbarkeit von Festigkeitseigenschaften ein- und mehrlagiger Papiere auf empirischen Weg. *Das Papier*, 7:356–360, 1992.

[56] Emil Wolf. *Theoretische und experimentelle Grundlagenuntersuchungen zum Scherschneiden von Papier*. Dissertation, Ruhr-Universität Bochum, 2005.

[57] Georg Jayme. Neue Beiträge zur Theorie der Entstehung der Blattfestigkeit. *Das Papier*, 10A:581–603, 1961.

[58] Walter Brecht and Rudolf Wanka. Die Querkontraktion von Papieren. *Das Papier*, 4:141–147, 1963.

[59] Robert Paetow. *Über das Spannungs-Verformungs-Verhalten von Papier*. PhD thesis, Technische Hochschule Darmstadt, 1991.

[60] Tony Atkins. *The Science and Engineering of Cutting*. Butterworth-Heinemann, Oxford, 1st edition, July 2009.

[61] Nils Furrer and Karl-R. Deibel (supervisor). Weiterführende Arbeiten (Konstruktion, Simulation) zu einem VA chirurgischen Messer aus der Medizinaltechnik. Semester Project (unpublished), March 2013.

[62] Wolfgang Rösner and Wilfried Schulz. Zu Fragen des Schneidens von Materialien der buchbinderischen Weiterverarbeitung. *Papier und Druck*, 27:23–29, 1978.

[63] D. Gross and T. Seelig. *Bruchmechanik Mit Einer Einführung In Die Mikromechanik*. Springer, 2011.

[64] T.L. Anderson. *Fracture Mechanics: Fundamentals and Applications*. CRC Press, 2005.

[65] Susann Zahn. *Ultraschallschneiden von Lebensmitteln*. PhD thesis, Technische Universität Dresden, 2009.

[66] S.M. Goh, M.N. Charalambides, and J.G. Williams. On the mechanics of wire cutting of cheese. *Engineering Fracture Mechanics*, 72(6):931 – 946, 2005.

[67] Ludwig Gerhard Reinhard Neder. *Technologie des Schneidens von Prepregs mit ultraschultraschall Klingen*. PhD thesis, Rheinisch-Westfälischen Technischen Hochschule Aachen, 1990.

[68] Debao Zhou, M.R. Claffee, Kok-Meng Lee, and G.V. McMurray. Cutting, 'by pressing and slicing', applied to the robotic cut of bio-materials. II. Force during slicing and pressing cuts. In *Robotics and Automation, 2006. ICRA 2006. Proceedings 2006 IEEE International Conference on*, pages 2256–2261, 2006.

[69] D. Zhou and G. McMurray. Modeling of blade sharpness and compression cut of biomaterials. *Robotica*, 28:311–319, 2 2010.

[70] E. Reyssat, T. Tallinen, M. Le Merrer, and L. Mahadevan. Slicing Softly with Shear. *Phys. Rev. Lett.*, 109:244–301, Dec 2012.

[71] M. Feiler. *Ein Beitrag zur Klärung der Vorgänge beim Schneiden dünner flächiger Materialien*. PhD thesis, Universität Stuttgart, 1970.

[72] Yiu-Wing Mai Anthony George Atkins. *Elastic and plastic fracture: metals - polymers - ceramics - composites - biological materials*. Ellis Horwood, 1985.

[73] M. Mahvash, L.M. Voo, Diana Kim, K. Jeung, J. Wainer, and A.M. Okamura. Modeling the Forces of Cutting With Scissors. *Biomedical Engineering, IEEE Transactions on*, 55(3):848–856, 2008.

[74] C.T. McCarthy, M. Hussey, and M.D. Gilchrist. On the sharpness of straight edge blades in cutting soft solids: Part I - indentation experiments. *Engineering Fracture Mechanics*, 74(14):2205 – 2224, 2007.

[75] C.T. McCarthy, A. Ní Annaidh, and M.D. Gilchrist. On the sharpness of straight edge blades in cutting soft solids: Part II - Analysis of blade geometry. *Engineering Fracture Mechanics*, 77(3):437 – 451, 2010.

[76] T. Chanthasopeephan, J.P. Desai, and A.C.W. Lau. Determining Fracture Characteristics in Scalpel Cutting of Soft Tissue. In *Biomedical Robotics and Biomechatronics, 2006. BioRob 2006. The First IEEE/RAS-EMBS International Conference on*, pages 899–904, 2006.

[77] J.G. Williams, Y. Patel, and B.R.K. Blackman. A fracture mechanics analysis of cutting and machining. *Engineering Fracture Mechanics*, 77(2):293 – 308, 2010.

[78] Willy Heckers. *Bruchmechanische Untersuchungen an Papier*. PhD thesis, Technische Hochschule Darmstadt, 1982.

[79] Chandra Nath and M. Rahman. Effect of machining parameters in ultrasonic vibration cutting. *International Journal of Machine Tools and Manufacture*, 48:965–974, 2008.

[80] W. Littmann, H. Storck, and J. Wallaschek. Sliding friction in the presence of ultrasonic oscillations: superposition of longitudinal oscillations. *Archive of Applied Mechanics*, 71(8):549–554, 2001.

[81] Walter Littmann, Heiner Storck, and Joerg Wallaschek. Reduction of friction using piezoelectrically excited ultrasonic vibrations. *Proceedings of SPIE, Smart Structures and Materials: Damping and Isolation*, 4331:302–311, 2001.

[82] Yvonne Schneider. *Einsatz von Ultraschall zur Modifikation lebensmitteltechnischer Grundoperationen am Beispiele des Schneidens*. PhD thesis, Technische Universität Dresden, 2007.

[83] Yvonne Schneider, Susann Zahn, and Harald Rohm. Qualitative process evaluation for ultrasonic cutting of food. *Engineering in Life Sciences*, 2:153–157, 2002.

[84] T. Brown, J. S. James, and G. L. Purnell. Cutting forces in food: Experimental measurement. *Journal of Food Engineering*, 70:165–170, 2005.

[85] Susann Zahn, Yvonne Schneider, and Harald Rohm. Ultrasonic cutting of foods: Effects of excitation magnitude and cutting velocity on the reduction of cutting work. *Innovative Food Science & Emerging Technologies*, 7(4):288 – 293, 2006.

[86] Yvonne Schneider, Susann Zahn, and Harald Rohm. Power requirements of the high-frequency generator in ultrasonic cutting of foods. *Journal of Food Engineering*, 86(1):61–67, 2008.

[87] G. Arnold, L. Leiteritz, S. Zahn, and H. Rohm. Ultrasonic cutting of cheese: Composition affects cutting work reduction and energy demand. *International Dairy Journal*, 19(5):314–320, 2009.

[88] Wolfgang Feil. *Ultrasonic Energy for Cutting, Coagulating, and Dissecting*. Thieme, 2005.

[89] Mauro Labanca, Flavio Azzola, Raffaele Vinci, and Luigi F. Rodella. Piezoelectric surgery: Twenty years of use. *British Journal of Oral and Maxillofacial Surgery*, 46(4):265 – 269, 2008.

[90] Franz Friedrich, Robert Lockhart, and Danick Briand. Silicon micromachined ultrasonic transducer with improved power transfer for cutting applications. *2012 IEEE International Ultrasonics Symposium Proceedings*, pages 1169–1172, 2012.

[91] R. Bäckmann. Moderne Trenn- und Schneidtechnologien für technische Textilien. *Kettenwirk-Praxis*, 21:29–33, 1987.

[92] R. Bäckmann. Ultraschall - Handwerkzeuge, Automaten, Roboter. *Mode, Bekleidung, Technik*, 1:4–7, 1991.

[93] R. Bäckmann. Thermische Schneid- und Verbindungstechniken für Vliesstoffe. *Melliand Textilberichte*, 6:427–431, 1982.

[94] Ludwig Neder. Schneiden mit ultraschultraschall Messer, HGF-Kurzbericht. *Industrie-Anzeiger*, 107:25–26, 1985.

[95] W. König und L. Neder. Bessere Schnittflächen mit Ultraschall. *Plastverarbeiter*, 37:41–50, 1986.

[96] Jeong-Du Kim and Eun-Sang Lee. A study of the ultrasonic-vibration cutting of carbon-fiber reinforced plastics. *Journal of Materials Processing Technology*, 43(2-4):259 – 277, 1994.

[97] V.I. Babitsky, A.N. Kalashnikov, A. Meadows, and A.A.H.P. Wijesundara. Ultrasonically assisted turning of aviation materials. *Journal of Materials Processing Technology*, 132(1-3):157–167, 2003.

[98] F J Ma, D M Guo, R K Kang, and Y J Ren. Surface quality of carbon/carbon composite after ultrasonic assisted turning. *Proceedings of the Institution of Mechanical Engineers, Part B: Journal of Engineering Manufacture*, 225:2144–2148, 2011.

[99] D. B. Downey. *The Cutting and Slitting of Paper*. PhD thesis, University of Bath, 1975.

[100] Ma Li'e, Hou Yupeng, Chen Yunchun, and Wu Jimei. Research on the vibration cutting and the simulation. *Advanced Materials Research*, 174:286–289, 2011.

[101] G. Sinn, B. Zettl, H. Mayer, and S. Stanzl-Tschegg. Ultrasonic-assisted cutting of wood. *Journal of Materials Processing Technology*, 170(1-2):42 – 49, 2005.

[102] Gerhard Sinn, Herwig Mayer, and Stefanie Stanzl-Tschegg. Surface properties of wood and MDF after ultrasonic-assisted cutting. *Journal of Materials Science*, 40:4325–4332, 2005.

[103] K. H. W. Seah, Y. S. Wong, and L. C. Lee. Design of tool holders for ultrasonic machining using FEM. *Journal of Materials Processing Technology*, 37:801–816, 1993.

[104] S.G. Amin, M.H.M. Ahmed, and H.A. Youssef. Computer-aided design of acoustic horns for ultrasonic machining using finite-element analysis. *Journal of Materials Processing Technology*, 55(3?4):254 – 260, 1995.

[105] Shuyu and Lin. Study on the longitudinal-torsional composite mode exponential ultrasonic horns. *Ultrasonics*, 34(7):757 – 762, 1996.

[106] Jiromaru Tsujino. Ultrasonic motor using a one-dimensional longitudinal-torsional vibration converter with diagonal slits. *Smart Materials and Structures*, 7(3):345, 1998.

[107] Stewart Sherrit, Steven A. Askins, Mike Gradziol, Benjamin P. Dolgin, Xiaoqi Bao, Zensheu Chang, and Yoseph Bar-Cohen. Novel horn designs for ultrasonic/sonic cleaning, welding, soldering, cutting, and drilling. In *Proceedings of SPIE*, volume 4701, pages 353–360. SPIE, 2002.

[108] M. Badescu, S. Stroescu, S. Sherrit, J. Aldrich, X. Bao, Y. Bar-Cohen, Z. Chang, W. Hernandez, and A. Ibrahim. Rotary hammer ultrasonic/sonic drill system. In *Robotics and Automation, 2008. ICRA 2008. IEEE International Conference on*, pages 602–607, May 2008.

[109] Vinod Yadava and Aniruddha Deoghare. Design of horn for rotary ultrasonic machining using the finite element method. *The International Journal of Advanced Manufacturing Technology*, 39:9–20, 2008.

[110] Andrea Cardoni, Patrick Harkness, and Margaret Lucas. Ultrasonic rock sampling using longitudinal-torsional vibrations. *Physics Procedia*, 3(1):125–134, 2010.

[111] L. Parrini. New techniques for the design of advanced ultrasonic transducers for wire bonding. *Electronics Packaging Manufacturing, IEEE Transactions on*, 26(1):37 – 45, January 2003.

[112] Yongqiang Qiu, Zhihong Huang, Alan Slade, and Gareth Thomson. Optimization of Ultrasonic Tool Performance in Surgery. In *4th European Conference of the International Federation for Medical and Biological Engineering*, volume 22 of *IFMBE Proceedings*, pages 899–902. Springer Berlin Heidelberg, 2009.

[113] Andrea Cardoni and Margaret Lucas. Enhanced vibration performance of ultrasonic block horns. *Ultrasonics*, 40(1-8):365 – 369, 2002.

[114] Anurag Sharma, Shoji Mishiro, Kiyoshi Suzuki, Tomoyasu Imai, Tetsutaro Uematsu, and Manabu Iwai. A New Longitudinal Mode Ultrasonic Transducer with an Eccentric Horn for Micro Machining. *Key Engineering Materials*, 238 - 239:147–152, 2003.

[115] Alan MacBeath, Andrea Cardoni, Lorna Smith, and Margaret Lucas. Ultrasonic Cutting with High-Gain Blades. *Applied Mechanics and Materials*, 1-2:45–50, 2004.

[116] Erkki Heikkola, Kaisa Miettinen, and Paavo Nieminen. Multiobjective optimization of an ultrasonic transducer using NIMBUS. *Ultrasonics*, 44(4):368 – 380, 2006.

[117] B. Fu, T. Hemsel, and J. Wallaschek. Piezoelectric transducer design via multiobjective optimization. *Ultrasonics*, 44, Supplement(0):e747 – e752, 2006.

[118] José Manuel Fernandez and Yves Perriard. Sensitivity Analysis and Optimization of a Standing Wave Ultrasonic Linear Motor. *IEEE Transaction on Ultrasonics, Ferroelectrics amd Frequency Control*, 53(7):1352–1361, 2006.

[119] Ioan Călin Roşca, Sergiu T. Chiriacescu, and Nicolae Constantin Creţu. Ultrasonic horns optimization. *Physics Procedia*, 3(1):1033 – 1040, 2010.

[120] D. Porto, A. Bourquard, and Y. Perriard. Genetic Algorithm optimization for a surgical ultrasonic transducer. In *Ultrasonics Symposium, 2008. IUS 2008. IEEE*, pages 1457 –1460, nov. 2008.

[121] William T. Thomson and Marie Dillon Dahleh. *Theory of Vibration with Applications*. Prentice Hall, New Jersey, 5th edition, 1998.

[122] Euan McCulloch. *Experimental and Finite Element Modelling of Ultrasonic Cutting of Food*. PhD thesis, University of Glasgow, March 2008.

[123] Hans A. Eschenauer, Niels Olhoff, and Walter Schnell. *Applied Structural Mechanics*. Springer, 1997.

[124] Gerhald Kress and David Keller. Structural Optimization. Lecture Notes (unpublished), 2007.

[125] James C. Spall. *Introduction to Stochastic Search and Optimization*. Wiley-Interscience, 2003.

[126] D.H. Wolpert and W.G. Macready. No Free Lunch Theorems for Optimization. *Evolutionary Computation, IEEE Transactions on*, 1(1):67–82, April 1997.

[127] G. R. Hext W. Spendley and F. R. Himsworth. Sequential Application of Simplex Designs in Optimisation and Evolutionary Operation. *Technometrics*, 4:441–461, 1962.

[128] A. Ravindran, K. M. Ragsdell, and G. V. Reklaitis. *Engineering Optimization - Methods and Applications*. John Woley and Sons, 2nd edition, 2006.

[129] Lothar Harzheim. *Strukturoptimierung*. Harri Deutsch, 2008.

[130] Thomas Frey and Martin Bossert. *Signal- und Systemtheorie*. Vieweg+Teubner, 2nd edition, 2008.

[131] Lino Guzzella. *Analysis and Synthesis of Single-Input Single-Output Control Systems*. vdf Hochschulverlag AG, 2007.

[132] Konrad Rudin. Fourier series of pulse wave. Privat Correspondance, 2013.

[133] Richard M. Christensen. *Theory of Viscoelasticity: An Introduction*. Academic Press, New York, 1971.

[134] A. C. Pipkin. *Lectures on Viscoelasticity Theory*. Springer-Verlag, New York, 2nd edition, 1986.

[135] Valentin L. Popov. *Contact Mechanics and Friction*. Springer, 2010.

[136] Remo Zimmermann and Karl-R. Deibel (supervisor). Modelling of Vibration Assisted Guillotining and Experimental Verification. Master Thesis (unpublished), March 2013.

[137] Fabian Kaiser and Karl-R. Deibel (supervisor). Energieeffizienz beim vibrationsunterstützten Schneiden. Bachelor Thesis (unpublished), June 2013.

[138] E. Oran Brigham. *FFT Schnelle Fourier-Transformation*. R. Oldenbourg Verlag, 5th edition, 1992.

[139] Allan G. Piersol and Thomas L. Paez. *Harris' shock and vibration handbook*. McGraw-Hill, New York, 6th edition, 2010.

[140] Fredy Kuster. Messung dynamischer Grössen bei Produktionsanlagen. Lehrschrift (unpublished), January 2012.

[141] Sarah L. Lämmlein and Karl-R. Deibel (supervisor). Konstruktion eines neuen Messers zum UVA Sägeschneiden. Experimentelle Verifikation und energetische Beurteilung. Bachelor Thesis (unpublished), June 2013.

[142] H. Storck, W. Littmann, J. Wallaschek, and M. Mracek. The effect of friction reduction in presence of ultrasonic vibrations and its relevance to travelling wave ultrasonic motors. *Ultrasonics*, 40(1-8):379 – 383, 2002.

[143] Thomas Childs, Katsuhiro Maekawa, Toshiyuki Obikawa, and Yasuo Yamane. *Metal Machining: Theory and Applications*. Arnold, 2000.

[144] Christian Raemy and Karl-R. Deibel (supervisor). Modellierung des Schneidprozesses beim Hybrid-Schneiden - Versagen und Bruch. Semester Project (unpublished), June 2013.

[145] Walter Ramberg and William R. Osgood. Description of Stress-Strain Curves by Three Parameters. *National Adivsory Committee for Aeronautics*, (902), 1943.

[146] I. N. Bronstein, K. A. Semendjajew, G. Musiol, and H. Mühlig. *Taschenbuch der Mathematik*. Verlag Harri Deutsch, 5th edition, 2001.

[147] E. Eisner. Complete Solutions of the "Webster" Horn Equation. *Acoustical Society of America Journal*, 41:1126, 1967.

[148] ANSYS Inc. Theory Reference for the Mechanical APDL and Mechanical Applications, 2009. Release 12.0, Pages 1029-1042.